Delft University of Technology

Improving the Flying Qualities of the HORUS Spaceplane

Master of Science Thesis

J. A. Reijne

TU Delft

Improving the Flying Qualities of the HORUS Spaceplane

Master of Science Thesis

by

J. A. Reijne

in partial fulfillment of the requirements for the degree of

Master of Science
in Aerospace and Mechanical Engineering

at Delft University of Technology
to be defended publicly on Friday February 25, 2022 at 9:30

Student number:	4481747	
Supervisors:	dr. ir. E. Mooij,	TU Delft
	dr. ir. R. Pecnik,	TU Delft
Committee members:	dr. ir. E. Mooij,	TU Delft
	dr. ir. R. Pecnik,	TU Delft
	dr. S. Cazaux,	TU Delft
	ir. P. C. Boldini,	TU Delft

TU Delft

Preface

After a long journey of studying in the fields of mechanical and aerospace engineering, I may complete my study with this very interesting subject. The dream to become an engineer with a structural overview in many subjects that are involved in engineering is almost achieved. I enjoyed my studies very much and cannot wait to start my career as an engineer. This thesis report is the last step to finalize my study program. The thesis is conducted in the name of the Delft University of Technology for the courses AE5810 and ME55035.

The double degree master program, which required some determination and effort, gave me the opportunity to create a path to follow my interests. The programs of both faculties resulted into the chosen subject of re-entry vehicles. The subject combines the gained knowledge of both my masters and applies this to my passion of spaceflight. Therefore, I want to express my gratitude to the people who made this double degree program and therefore my study path possible.

It is a privilege to perform research in the field of re-entry vehicles, something that every space enthusiast (like me) relates with the amazing history of the Space Shuttle program. In this study I have the possibility to investigate the shape of a gliding re-entry vehicle with the use of big data which is fascinating to me. I find it interesting to research in a structured, efficient and accurate manner whether the shape of the spaceplane can be improved. The features that are involved in this study are part of what I want to improve in myself as an engineer.

This global pandemic of the COVID-19 virus, in which I preformed my thesis, is another additional challenge. At this moment the university is closed, which makes my living space also my research environment. However, the supervising professors Dr.ir. E. Mooij and Dr.ir. R. Pecnik make this possible by communicating by e-mail or video call, this way I am still able to perform my thesis.

I want to give special thanks to a large number of people that helped me with this last part of my study program. First of all the track coordinators Mr. Tighe and Mr. Noomen and the study advisors, who helped me to set up the double degree program, in which the general combined thesis subject and regulations to participate to the double degree program were clarified. Another special thanks to the exam committees of both faculties to give me the approval to follow my interests. Also, I want to express my gratitude to my friends around me, who made me relax when I needed it. And lastly, the most important people for this research, my two supervisors who agreed to supervise me. They helped me in finding an overlap to satisfy the double degree requirements. And most importantly, they helped me learn key features to improve myself in doing research.

J. A. Reijne
Delft, January 2022

Abstract

The spaceplane vehicle is a promising concept for the future of spaceflight. What makes the spaceplane attractive is the possibility to reuse the transport system for multiple missions. This will lower the costs and satisfies the demands for more frequent transportation to space. For such a vehicle it is necessary to fulfil the flying qualities for a safe, stable and controlled flight. But, this is easier said than done, because the spaceplane vehicle has to endure many different flight conditions. While re-entering the atmosphere, the speeds and therefore the temperatures become so high that the vehicle design has to be devoted to this hypersonic flight phase. This phase results in the distinctive spaceplane design that contains a blunt nosecone and blunt wing leading edges, which detaches the shockwaves and therefore lowers the wall temperatures for materials to withstand. The downside of these design features is that when the operating speeds are lower, the reduced streamlined shape creates instability in the flow, which results in flight instability. This especially occurs in the range of Mach 2.5 until 0.8, what is called the terminal area energy management (TAEM) phase of the re-entry. Improving the flying qualities in this flight phase is important to make sure that the spaceplane is operating safely. This subject is leading to the main research question:

Which HORUS-2B shape modifications can improve the flying qualities in the supersonic till subsonic flow regime of the re-entry trajectory, without exceeding the thermo-mechanical loads of higher flow regimes?

To investigate the flying qualities of a spaceplane, the equations of motion are derived and linearized. These equations contain many input variables including the aerodynamic characteristics of the spaceplane. The linearized equations are converted to a state-space form, which creates the opportunity to derive the eigenmotions of the spaceplane. These eigenmotions are showing the dynamic stability of the spaceplane for certain manoeuvres, among of which the longitudinal short period oscillation, the phugoid and the lateral short period oscillation. For these eigenmodes there are military requirements to make sure that the flight is safe and controllable.

To optimise the shape for these eigenmodes a model is created which is able to generate shapes depending on input parameters which are dimensions of the spaceplane. The generated shape is used in an aerodynamic simulation, that requires a mesh grid around the spaceplane which defines points representing the air, where the flow properties can be determined. To reduce computational time there is looked into the efficiency and accuracy performance of the mesh and computational fluid dynamic (CFD) simulations. The fluid model and mesh quality combination is optimised to stay within 60 seconds of simulation time for one simulation and resulted into an average deviation of approximately 20%. The aerodynamic characteristics of each spaceplane are determined by adjusting the attitude or velocity with flow conditions along the reference trajectory. The whole process is automated and driven by the program Matlab which determines the eigenmodes and visualizes the results.

The most unstable eigenmotion is the phugoid manoeuvre, which can be improved by: lowering the fuselage height, increasing the fuselage width, increasing the wing span, enlarging the winglets upwards and make the wingspan larger. Hereby the phugoid motion becomes less unstable with the downside that the longitudinal short period oscillation becomes a little less stable. Overall, the phugoid eigenmode is difficult to make stable with the available parameters and there scopes. The lateral short period oscillation is within the level 3 military requirement and is slightly improved in the supersonic regime as well as in the hypersonic regime. With a more advanced optimising method it is likely that a level 2 requirement will be achieved. The other eigenmodes are negligible small and are mostly stable. The static stability of the yaw moment affected of the side-slip-angle, which is also unstable for the original spaceplane shape, is improved (but still unstable) by the same shape modifications used for improving the eigenmodes. Other smaller modifications such as: the wing thickness or changing the corner of the wing did not influence the results much.

For further research a better optimisation algorithm would increase the performance capabilities of each modification parameter. And more computational capacity would likely increase the accuracy of the aerodynamic characteristics. For a full investigation of the flying qualities, the controllability performance should be investigated, to show the capability to artificially stabilize the spaceplane for a safe and controllable flight back from space.

List of Symbols

Symbol	Description	Units
$\mathbf{A}$	System matrix	-
$\mathbf{B}$	Control matrix	-
b_{ref}	Reference width	m
c_{ref}	Reference length	m
D	Diameter	m
D_s	Particle hard shell diameter	m
e	Internal energy	J
g	Local gravity acceleration	ms^{-2}
h	Altitude	m
I_{ij}	Inertia tensor components (i and j = $\{x, y, z\}$), referenced to the body frame	kgm^2
k	Thermal conductivity	$Wm^{-1}K^{-1}$
Kn	Knudsen number	-
L	Representative length scale	m
M	Mach number	-
m	Mass of spaceplane	kg
P	Period	s
p_c	Critical pressure	Nm^{-2}
p_r	Pressure reduction	Nm^{-2}
p_s	Static pressure	Nm^{-2}
p_t	Total pressure	Nm^{-2}
$\tilde{q}$	Dynamic pressure	Nm^{-2}
R	Ideal gas constant, 287.05 for air	$Jkg^{-1}K^{-1}$
R	Modulus of position vector	m
Re	Reynolds number	-
$\mathbf{R}_s$	Position vector	m
S_{ref}	Reference area	m^2
$S_{i,j}$	Strain rate tensor	s^{-1}
t	Time	s
T	Temperature	K
$T_{1/2}$	Halve time	s
T_2	Doubling time	s
T_c	Critical temperature	K
T_r	Temperature reduction	K
T_s	Static temperature	K
T_t	Total temperature	K
$\mathbf{u}$	Velocity vector fluid flow theory	ms^{-1}
u_τ	Friction velocity	ms^{-1}
$\mathbf{V}_s$	Velocity vector	ms^{-1}
V	Speed	ms^{-1}
y^+	A non-dimensional distance of the mesh nodes	-
Z	Compressibility factor	-
Z	Magnitude complex value	-

Greek symbols

Symbol	Description	Units
α	Angle-of-attack	rad
β	Side-slip angle	rad
γ	Flight-path angle	rad
γ	Heat capacity ratio	-
δ	Latitude	rad
δ_b	Body flap deflection angle	rad
$\delta_{e,l}$	Left elevon deflection angle	rad
$\delta_{e,r}$	Right elevon deflection angle	rad
$\delta_{r,l}$	Left rudder deflection angle	rad
$\delta_{r,r}$	Right rudder deflection angle	rad
ζ	Damping ratio	-
θ	Angle of the complex value	rad
μ	Dynamic viscosity	Pas
ν	Kinematic viscosity	m^2s^{-1}
ρ	Density	kgm^{-3}
σ	Bank angle	rad
σ_B	Boltzmann constant, 1.38×10^{-23}	$m^2kgs^{-2}K^{-1}$
τ	Longitude	rad
χ	Heading angle	rad
ω	Earth's rotation rate	$rads^{-1}$
ω_n	Natural frequency	$rads^{-1}$

Aerodynamic symbols

Symbol	Description	Units
C_D	Drag force coefficient	-
C_{D_0}	Nominal drag force coefficient	-
ΔC_{D_b}	Increment in the drag force coefficient due to the change in the body flap angle	rad^{-1}
ΔC_{D_h}	Increment in the drag force coefficient due to the change in the altitude	-
ΔC_{D_M}	Increment in the drag force coefficient due to the change in the Mach number	-
$\Delta C_{D_{r,l}}$	Increment in the drag force coefficient due to the change in rudder angle	rad^{-1}
$\Delta C_{D_{r,r}}$	Increment in the drag force coefficient due to the change in rudder angle	rad^{-1}
$\Delta C_{D_{w,l}}$	Increment in the drag force coefficient due to the change in left wing angle	rad^{-1}
$\Delta C_{D_{w,r}}$	Increment in the drag force coefficient due to the change in right wing angle	rad^{-1}
C_L	Lift force coefficient	-
C_{L_0}	Nominal lift force coefficient	-
ΔC_{L_b}	Increment in the lift force coefficient due to the change in body flap angle	rad^{-1}
ΔC_{L_M}	Increment in the lift force coefficient due to the change in the Mach number	-
$\Delta C_{L_{w,l}}$	Increment in the lift force coefficient due to the change in the left wing angle	rad^{-1}
$\Delta C_{L_{w,r}}$	Increment in the lift force coefficient due to the change in the right wing angle	rad^{-1}
C_l	Roll moment coefficient	-
ΔC_{l_β}	Increment in the roll moment coefficient due to the change in the side-slip-angle	rad^{-1}
$\Delta C_{l_{\delta a}}$	Increment in the roll moment coefficient due to the change in the the aileron angle	rad^{-1}
$\Delta C_{l_{\delta r}}$	Increment in the roll moment coefficient due to the change in the rudder angle	rad^{-1}
$\Delta C_{l_{w,l}}$	Increment in the roll moment coefficient due to the change in the left wing angle	rad^{-1}
$\Delta C_{l_{w,r}}$	Increment in the roll moment coefficient due to the change in the right wing angle	rad^{-1}

Symbol	Description	Units
C_m	Pitch moment coefficient	-
C_{m_0}	Nominal pitch moment coefficient	-
ΔC_{m_α}	Increment in the pitch moment coefficient due to the change in the angle-of-attack	rad^{-1}
$\Delta C_{m_{\dot{\alpha}}}$	Increment in the pitch moment coefficient due to the change in the pitch rate	rad^{-2}
$\Delta C_{m_{\delta b}}$	Increment in the pitch moment coefficient due to the change in the body flap angle	rad^{-1}
$\Delta C_{m_{\delta e}}$	Increment in the pitch moment coefficient due to the change in the elevon angle	rad^{-1}
ΔC_{m_b}	Increment in the pitch moment coefficient due to the change in the body flap angle	rad^{-1}
ΔC_{m_M}	Increment in the pitch moment coefficient due to the change in the Mach number	-
ΔC_{m_q}	Increment in the pitch moment coefficient due to the change in dynamic pressure	-
$\Delta C_{m_{w,l}}$	Increment in the pitch moment coefficient due to the change in the left wing angle	rad^{-1}
$\Delta C_{m_{w,r}}$	Increment in the pitch moment coefficient due to the change in the right wing angle	rad^{-1}
C_n	Yaw moment coefficient	-
ΔC_{n_β}	Increment in yaw moment coefficient due to the change in the side-slip-angle	rad^{-1}
$\Delta C_{n_{\beta,dyn}}$	Increment in the dynamic yaw moment coefficient due to the change in the side-slip-angle	rad^{-2}
$\Delta C_{n_{\delta a}}$	Increment in yaw moment coefficient due to the change in the aileron angle	rad^{-1}
$\Delta C_{n_{\delta r}}$	Increment in yaw moment coefficient due to the change in the rudder angle	rad^{-1}
$\Delta C_{n_{r,l}}$	Increment in yaw moment coefficient due to the change in the left rudder angle	rad^{-1}
$\Delta C_{n_{r,r}}$	Increment in yaw moment coefficient due to the change in the right rudder angle	rad^{-1}
$\Delta C_{n_{w,l}}$	Increment in yaw moment coefficient due to the change in the left wing angle	rad^{-1}
$\Delta C_{n_{w,r}}$	Increment in yaw moment coefficient due to the change in the right wing angle	rad^{-1}
C_S	Side force coefficient	-
ΔC_{S_β}	Increment in the side force coefficient due to the change in the side-slip-angle	rad^{-1}
$\Delta C_{S_{r,l}}$	Increment in the side force coefficient due to the change in the left rudder angle	rad^{-1}
$\Delta C_{S_{r,r}}$	Increment in the side force coefficient due to the change in the right rudder angle	rad^{-1}
$\Delta C_{S_{w,l}}$	Increment in the side force coefficient due to the change in the left wing angle	rad^{-1}
$\Delta C_{S_{w,r}}$	Increment in the side force coefficient due to the change in the right wing angle	rad^{-1}
F_D	Drag force	N
F_S	Side force	N
F_L	Lift force	N
F_X	X force (body fixed reference frame)	N
F_Y	Y force (body fixed reference frame)	N
F_Z	Z force (body fixed reference frame)	N
$\mathcal{L}$	Roll moment	Nm
$\mathcal{M}$	Pitch moment	Nm
$\mathcal{N}$	Yaw moment	Nm
p	Roll rate	$rads^{-1}$
q	Pitch rate	$rads^{-1}$
r	Yaw rate	$rads^{-1}$

List of Abbreviations

CAD	Computer aided design
CFD	Computational fluid dynamics
CNES	Centre National D'Études Spatiales
CPU	Central processing unit
ESA	European Space Agency
GNC	Guidance navigation and control
HORUS	Horizontal upper stage
ISS	International Space Station
LEO	Low earth orbit
LTI	Linear time-invariant
NASA	National Aeronautics and Space Administration
RPD	Relative Percent Difference
SSO	Space Shuttle Orbiter
TAEM	Terminal area energy management
TM	Technical Memorandum
US	United States

Contents

1 Introduction

Spaceplanes are becoming part of the next generation vehicles in the spaceflight industry. The idea of combining the features of an aircraft with a spacecraft has led to these new designs. The spaceplane can operate similarly as a normal spacecraft in space. But, when re-entering an atmosphere, it uses the lift force for a slow and controlled descent. A spaceplane is a safe, reusable and efficient transportation system. The ability to steer the vehicle towards the desired runway creates the possibility for a quick inspection and re-fuel that is required for the next mission. This lowers the mission costs and creates the opportunity for more frequent flying. Overall the re-usability makes the spaceplane concept very innovative and sustainable.

There is a demand for inexpensive vehicles that can reach Earth's orbit. Such that resupplying, satellite reparation or de-orbiting, futuristic rocket re-fueling and space tourism become cheaper. That is also the reason why commercial companies are joining the spaceflight industry [Heracleous et al., 2019]. A fully re-usable vehicle will be likely to dominate this field of technology. Hence, the spaceplane concept is very promising. But, the re-entry trajectory of the spaceplane vehicle has difficulties to guarantee a safe and controlled descent. Therefore, the flying qualities of the spaceplane has to be satisfied by comparing them with military standards to make sure the re-entry is safe. This thesis will investigate those flying qualities and improve these in critical areas.

To investigate these flying qualities a study and evaluation of the stability and control characteristics has to be performed. Those qualities ensure that the flight is safe and controllable in steady flight and during flight manoeuvres. Thus, by satisfying the flying qualities associated with vehicle type, it can be ensured that the mission will be a success. These qualities change depending on the flight conditions and therefore the phases of the re-entry trajectory. The qualities involve the following aspects [Mooij, 1985]:

- The ability to generate manoeuvres or maintain steady equilibrium states over the whole flight range.
- The capability to create control forces to induce a state change.
- These forces are linked to the manoeuvrability from one steady-state condition to another.
- The reaction speed of the system after a command response, i.e., response characteristics.
- The capability to maintain equilibrium conditions with constant speed and angle-of-attack if the control system is not operating.

1.1. Problem statement

The first analysis of the flying qualities dates back to the first manned flight with a motorised airplane. To understand how to balance, steer and control the airplane appeared to be important from the very first moment. A similar approach to determine the flying qualities of the spaceplane concept, because the vehicles are more or less the same. The only difference is that the spaceplane performs an unpowered descent and is therefore gliding. However, this is not effecting the fundamentals to describe the motion of the vehicle.

Whereas different re-entry vehicles, like capsules, descent semi-ballistically, spaceplanes perform a gliding re-entry trajectory. The gliding trajectory is complex, because the spacecraft has to stay within the limits of the entry corridor during the descent. The lower limit in the entry corridor is defined by the maximum

thermo-mechanical loads. This constraint indicates that the spaceplane's velocity cannot be too high, because the heat flux or the mechanical stresses will have disastrous consequences. If the velocity at a certain altitude is too low, the upper limit will be exceeded. This upper limit is called the equilibrium glide, which defines the limit before the spaceplane will perform a skipping flight trajectory. This basically means that the spaceplane is bouncing off the atmosphere, because the lift force exceeds the gravity force, resulting in an upwards acceleration. Skipping flight trajectory is considered unsafe and therefore undesired. The re-entry trajectory contains different phases where the objectives are different. The thermo-mechanical loads are the number one priority in the beginning of the descent. However, later when these loads are less in magnitude, the landing accuracy becomes more important.

To stay within these boundaries, spaceplanes use a guidance, navigation and control (GNC) system [Roenneke and Cornwell, 1993]. (This system changes for different phases of the re-entry.) By changing the magnitude and direction of the forces acting on the vehicle, the spaceplane can be steered and the velocity controlled. To change the aerodynamic forces, the system adjusts the spaceplane's attitude. Which is possible by actuating the attitude control thrusters and the deflection surfaces. The thrusters create an additional force, whereas the deflection surfaces adjust the pressure distribution in a certain area around the vehicle which creates the force. By this action the force/moment equilibrium is disturbed and the state (attitude) changes to a new equilibrium. This leads to the following definitions: stability and controllability.

The dynamic and static stability of a vehicle is very important. Static stability is indicating that the spaceplane creates a moment (when at an unsteady state) forcing the spaceplane's attitude to the desired attitude state. The dynamic stability is indicating that perturbations around the steady state are damped. When the attitude is changed to stay within the entry corridor limits or to perform a manoeuvre, the spaceplane must become stable afterwards. This means that the perturbations in the forces are damped and the system moves to a steady equilibrium. The stability characteristics of a vehicle are mostly determined by the stationary spaceplane shape. The controllability is the ability to perform the manoeuvres. In other words, being able to steer the vehicle as desired at all flight conditions. These control characteristics are indirectly determined by the deflection surfaces relative to the main body. (Or determined by the thrusters in space.) Because the induced force in combination with the spaceplanes inertia and the control system determines the controllability. These two definitions are the basics for the flying qualities of the spaceplane.

From hypersonic aerodynamics it is known that to counter the heat problems in the beginning of the re-entry, the nosecone and the leading edges of the spaceplane have to be blunt [Detra and Hidalgo, 1961]. Otherwise the heat flux will be too high to withstand for present-day materials. Increasing the bluntness of the nosecone will result in an increasing distance between the shockwave and the nose tip. The detached shockwave will result in more energy staying within the airflow and less energy dissipation into the materials of the spaceplane. Therefore a blunt nosecone and blunt leading edges are required features of the spaceplane concept. However, the blunt nose creates flow separation and therefore dynamic instability. This makes a safe and controlled re-entry harder to accomplish. These two aspects of the spaceplane concept are counteracting and therefore make its design very complex. Thus, the nosecone feature to withstand the heat flux in the beginning of the re-entry influences the flying qualities at the end of the re-entry. Leading to a compromised vehicle shape to fulfill the requirements of the whole re-entry flight.

One great example of such a designed vehicle is the retired Space Shuttle, which will be used to explain relevant fundamentals, because of its rich history and available literature. However, there are also smaller vehicles with such an aerodynamically controlled re-entry. One of those is the HORUS-2B (abbreviation for Horizontal Upper Stage) conceptual design. This spaceplane has been studied since the 1960s by the Messerschmitt-Bölkow-Blohm (MBB). The HORUS-2B spaceplane was initially designed to be an unpowered reusable spaceplane as a second stage of the Ariana 5 rocket. Later it was redesigned with a rocket propulsion system and it became a potential second stage of the Sänger hypersonic aircraft. The HORUS-2B is equipped with both reaction-control thrusters and aerodynamic-control surfaces. The control surfaces comprise two rudders, two elevons and one body flap. The elevons combine the elevator and the ailerons. By symmetrically or asymmetrically deflecting them, they can introduce a pitch or roll motion respectively. Furthermore, a deflection of the rudders will introduce a yaw motion. The limitation of the rudders is that they can only move outwards, which means that for the yaw motion only one rudder is active. This limitation results in weak yaw control capabilities, because the rudder deflection angle is quickly maximised (saturated rudder deflection) [Mooij, 2018]. Therefore the assisting yaw thrusters are necessary over the whole flight domain, which is not desired.

Previous studies have also shown that the controllability and stability of the HORUS-2B vehicle are poor [Viavattene and Mooij, 2019]. These controllability and stability problems originate from the vehicle design.

The shape restrictions due to the thermo-mechanical load limits leads to sensitive controllability and bad stability. The lack of stability is most important in the lower flight velocity regime where the dynamic pressure is low. At this moment, a robust control system needs to be applied to make the system as insensitive to uncertainties as possible. By means of a double-sensitivity analysis, the presence of uncertainties can be counteracted to minimise the performance influence.

Thus, the aerodynamic coefficients of the vehicle body shape and control-surfaces should be enhanced. This might eliminate the need for the reaction thrusters over the whole flight domain, and cause improvement in the control performance and stability. Which is important for achieving a safe flight to the planned landing location. This leads us to the main research objective. The research objective is to improve the flying qualities, which involve the controllability and stability performance, of the HORUS-2B spaceplane while re-entering the Earth's atmosphere, by investigating the aerodynamic behaviour of different vehicle shapes in the subsonic and supersonic flow regime, given that the thermo-mechanical loads from the beginning of the re-entry phase (where a higher flow velocity regime is valid) are not exceeded.

In this study, the controllability and stability performance of this specific vehicle are analysed. Moreover, this study can also be applied to spaceplanes in general. The impact of the shape modifications will give insights that will be useful for designing spaceplanes, whereby the original HORUS-2B vehicle is a reference vehicle to validate the data. Besides the investigation of the flying qualities, a complete aerodynamic simulation study, which is required for determining the aerodynamic characteristics, is also performed. Finally, the aerodynamics are determined in an efficient manner.

1.2. Research questions

Based on the research objective, the main research questions are formulated and stated below.

Which HORUS-2B shape modifications can improve the flying qualities in the supersonic till subsonic flow regime of the re-entry trajectory, without exceeding the thermo-mechanical loads of higher flow regimes?

1. What are the vehicle shape limitations and their consequences due to the thermo-mechanical load constraints in the beginning of the re-entry trajectory?

2. Which vehicle shape modifications can be applied and will improve the controllability and stability for the lower Mach regimes?

3. What are the effects of the subsonic and supersonic improved shape on the flying qualities in the hypersonic regime?

To answer the main research question and sub-research questions the thesis report is structured in the following way. In Chapter 2, the foundation of the research study is stated. Starting with a solving strategy, giving a road map of how the problem will be solved. Followed by an investigation of previous designed spaceplanes with respect to shape, stability and controllability. To give insight in the design trade offs that have been made in the past. But, the mission heritage will also show methods to analyse the aerodynamics, controllability and stability. This will lead to the mission design, restrictions and requirements. In Chapter 3, the flight mechanics are explained. The flight mechanics is one of the key elements to determine the research questions. Starting with the equations of motion which are required to describe the motion of an object. These mathematical descriptions of the equations of motion require reference frames which is another subsection of this chapter. With the equations of motion a state-space model is created, which determines the flight qualities of the spaceplane. This chapter will end with the flight modes and stability characteristics. In Chapter 4, the aerodynamic theory is explained, which is another key aspect of this study. This chapter starts with explaining atmospheric influence and the required assumptions necessary for the determination of the flow field. Followed by flow phenomena which occur during the re-entry. All the features of the different Mach regimes are explained. Besides the theoretical explanation of these flow regimes, the field of numerical simulations is used to verify the observations. The small side study gives confirmation of the ability to simulate the different flow regimes with the chosen software. After which the HORUS simulation setup and flow observations are explained. These simulations also require a more in dept explanation of the mesh creation. In Chapter 5, the architectural design is discussed. The architectural design is a road map which describes how the different elements are connected and automated to perform the whole analysis. The focus is on the software which creates the possibility for automation. Besides the main elements; determination of the flying qualities and aerodynamics, the tools required before, in between and after those analysis are

explained. Leading to an overview of software which leads to a model which can generate the results of this research. In Chapter 6, a validation and verification of the model are discussed. With the use of the reference aerodynamic data of the HORUS-2B and the relevant studies about the flying quality, the validation of the model is investigated. In Chapter 7, the results of the model are explained in full detail. These results contain the aerodynamic characteristics, stability performance, effects on the flying qualities and a comparison with military requirements of different spaceplane shapes. In the last chapter, Chapter 8, the conclusions and recommendations of this research are expressed and discussed.

2

Mission heritage

In this chapter the mission heritage of the spaceplane concept, the shape and involved flying qualities, controllability and methodologies to investigate this problem will be discussed. Starting with previous designed vehicles, which give more insight in the purpose of the vehicle shape. The spaceplane shape in combination with the aerodynamic characteristics will help understand the general flying qualities of this vehicle type. Some specific shape features which are necessary for this type of vehicle will be analysed in more depth. Also, relevant spaceplane shape optimisation studies will be discussed, which creates a solid foundation for this research. Another important aspect of this study are the aerodynamic simulations. These simulations require research to generate optimal, efficient and accurate results. This chapter ends with the reference vehicle and the mission and system requirements. These requirements are stated to define the specifications which the model should comply with to be able to answering the research question.

2.1. Solving Methodology

The strategy to solve this problem starts with the heritage of the spaceplane concept. To study how previous engineers have designed spaceplanes based on aerodynamics due to the main body and the control surfaces, combined with the related subject of the controllability and stability performances. The design phase is an iterative process, because if something in the shape is changed, other related properties such as the controllability and stability are also adjusted. This leads to new shape adjustments and therefore the process repeats itself. Hence, this design process is very difficult. It is very helpful for this research to investigate which methods previous studies have used for analysing these features. One important spaceplane is the Space Shuttle (SSO) which was very successful and rich in available literature. There are also other spaceplanes such as the HERMES (concept) and X-38, these are smaller designs with less payload capacity compared to the Space Shuttle. Still, they will also provide insights in the shape contours and related flying qualities. The more different spaceplane shapes, control deflection surfaces, and control and stability performances are discussed, the more insight in possible improvements can be found. Based on these findings in the mission heritage of spaceplanes, the system requirements of the reference vehicle and the mission of this research can be defined. When the mission requirements and restrictions are well stated, the aerodynamic performance can be specified for the mission.

2.2. Space Shuttle Orbiter design

For the Americans the foundation of the spaceplane concept started with the X-series, which were experimental aircraft created by governmental institutions. These aircraft were experiments that investigated how to deal with different flight speeds, heat related issues, stability and controllability demands. Among of which hypersonic vehicles, which created the foundation of the Space Shuttle (visualisation in Figure 2.1). The Space Shuttle operated from 1981 till 2011 and was designed to deliver huge volumetric payloads into space. There was a demand to put large satellites and a residence (ISS and Mir) into Earth's orbit. Because mankind wanted to study, such as, deep space and the harsh space environment. To do so, a more frequent space transportation vehicle was required. Hence, the partly reusable Space Shuttle became the first step towards re-usability.

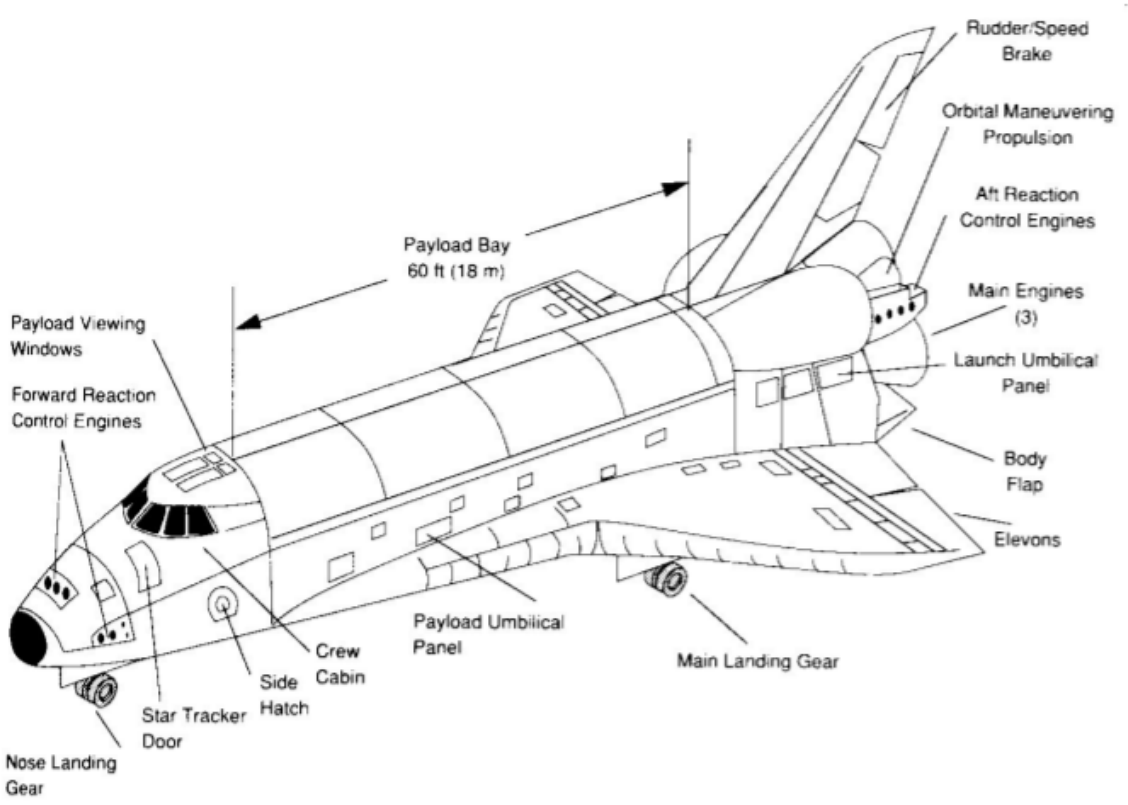

Figure 2.1: Space Shuttle design [Weiland, 2014].

2.2.1. Nosecone influence

A lot of research was required to design the Space Shuttle. A compilation of analytical studies, experimental wind tunnel testing and vehicle data (X-series) were used in the design considerations [Camarda, 2014]. The X-15 was conceived to understand and overcome the hypersonic related thermal barrier. Because the materials could (and still can) not withstand the heat load. In these tests it became clear that for hypersonic speeds the heating rate was a function of the radius. To decrease the stagnation heat flux, the radii of the nose caps and leading edges had to be increased. Because this feature increases the distance between the shock and the vehicle itself. As a result of this, most energy stays within the airflow instead of dissipating inside the materials. Another idea to decrease the stagnation heat flux is to increase the angle-of-attack, which increases the lift coefficient and therefore lowers the descent speed. For that reason, the angle-of-attack of the Space Shuttle is roughly 40 degrees at the beginning of the re-entry . (The blunt nose feature and coming back into the atmosphere with high angle-of-attack is used on all spaceplanes.)

However, as already briefly indicated, the blunt nosecone creates a negative effect on the dynamic stability in the lower velocity regimes (between high subsonic and low supersonic). This effect is extensively described in [Kazemba et al., 2012]. In supersonic flow about a blunt body, a bow shockwave follows the nose of the vehicle. Flow downstream of the bow shock stagnates on and accelerates around the forebody. The large turning angle of the shoulder induces the formation of expansion waves and leads to separation of the flow. This creates a low-pressure region behind the body characterized by an unsteady recirculation region in the near wake. Further downstream, the wake flow converges, stagnates and forms a trailing recompression shock. The core of the wake is viscous and often partially subsonic, while the outer wake is typically inviscid and supersonic. These factors combine to result in a flow with a time-varying pressure field and is a function of axial and radial position relative to the forebody. This flow phenomenon is visualised in Figure 2.2. Thus, the dynamic instability occurs, because the flow separation induced force on the aft body is dependent upon the crossflow at the separation source, which originated at an earlier time instant [Ericsson and Reding, 1969]. For instance, if the spaceplane returns to zero angle-of-attack, it has a residual

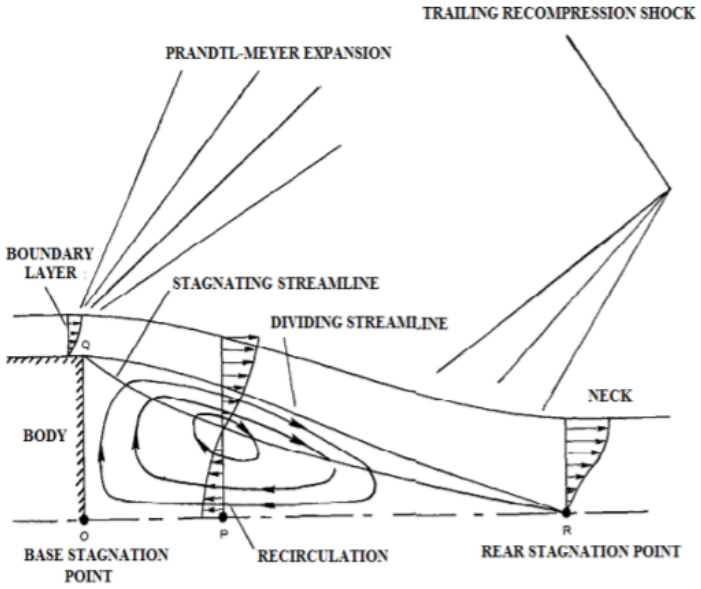

Figure 2.2: Flow separation at the aft body of a blunt object [Kazemba et al., 2012].

generated pitch motion force that is lacking behind. If the separation inducted force is statically stabilising (nose downwards), the effect will continue to drive the motion at zero angle-of-attack and therefore results in undamped stability effects.

The phenomenon described above has the opposite effect on the static stability. The static stability becomes stronger in the subsonic and transsonic regime. This is due to the separation and subsequent reattachment of the flow on the body, resulting in increased static stability. This has a positive effect on the stable and steady flight aspect of the flying qualities, but the downside is that there is more effort necessary for manoeuvres.

The dynamic pitching coefficient as a function of Mach number is plotted in Figure 2.3 for two blunt objects [Ericsson and Reding, 1969]. These two objects have two different radii at the shoulder and are oscillating free around an angle-of-attack of zero degrees. The dynamic pitching coefficient consists of two parts (C_{m_q} and $C_{m_{\dot{\alpha}}}$), these are the moment coefficient due to the pitch rate and the moment coefficient due to the rate of change of angle-of-attack. In the hypersonic regime, the damping remains relatively constant and is typically stable or neutrally stable. After hypersonic speeds, into supersonic the damping becomes stronger and therefore more dynamically stable. Then, as can be seen in the graph, the peak with lowest dynamic damping occurs around the transonic speeds. At this point the object tends to become unstable because the positive pitching damping coefficient shows instability. Next, the damping increases again as the vehicle decelerates through subsonic speeds. Similar results can be seen for a flared cylinder shape. The instability is related to the pressure coefficient. When the vehicle is decelerating from Mach 2.5 or higher, the aftbody pressure coefficient decreases at a faster rate compared to the forebody pressure coefficient. However, from Mach 2.5 or lower this phenomena reverses. This crossover point is the reason for the instability peak. In Figure 2.4 the influence of the angle-of-attack on the damping coefficient is plotted for a flared cylinder with different oscillating ranges (at a constant Mach number of 0.65). With increasing angle-of-attack the damping increases and therefore the body becomes more dynamically stable. These figures show the general effects of a blunt nosecone.

2.2.2. Aerodynamic characteristics

During major portions of the flight, the Space Shuttle is longitudinally and laterally statically stable [Young et al., 1981]. In flight regimes where the Space Shuttle is unstable, stability is artificially provided by the flight control system. This means that the control system uses the deflection surfaces or attitude control thrusters to stabilize the spaceplane. In the case of the yaw motion, the deflection surface (mainly rudder) was not sufficient for maneuvering and therefore yaw thrusters were necessary. These yaw thrusters also create an additional roll moment, which requires a counter moment from the ailerons and roll thrusters. (The thrust

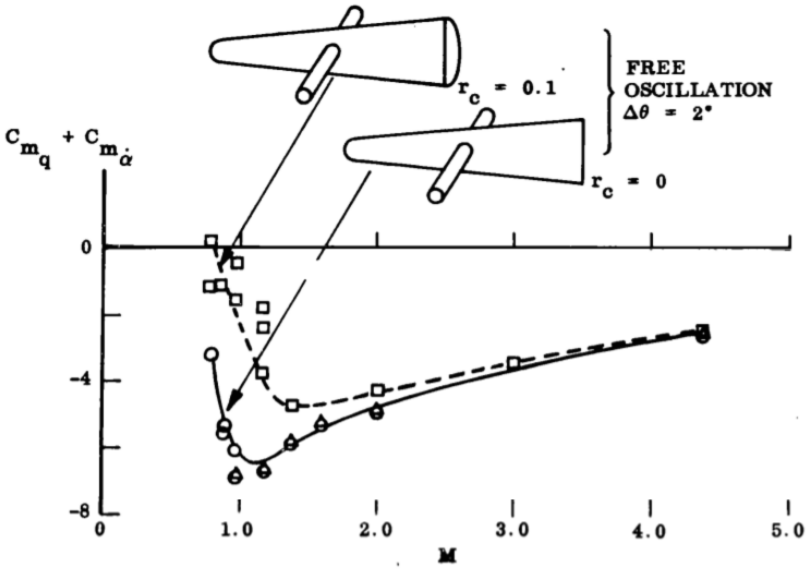

Figure 2.3: Effect of the Mach number on the dynamic pitch motion of two different base shoulder objects ($\alpha = 0°$) [Ericsson and Reding, 1969].

moment required from the roll thrusters is relatively small compared to the thrust from the yaw thrusters.) The yaw thrusters are used from the entry interface till Mach 1, which is obviously undesired because of additional propellant mass.

A few static longitudinal stability parameters can be determined from Figure 2.5 which can be found in the source [Hirschel and Weiland, 2009]. The upper left figure shows that the $dC_L/d\alpha$ shows linear behaviour until an angle-of-attack of 20 degrees. With increasing Mach number the gradient reduces substantially. This behaviour is usual for all spaceplanes. An increase of angle-of-attack creates more lift force, because the spaceplane defelcts the air more downwards. The highest line is for Mach 1.1, which is inside the transonic regime. The reason for this behaviour is the induced wave drag due to the fundamental changes in the pressure distribution. In the upper right figure of Figure 2.5, the $dC_D/d\alpha$ is shown. The drag quadratically increases with increasing angle-of-attack, because the spaceplane is deflecting more air. In both graphs the coefficient decreases with increasing Mach number (after the transonic regime). The reason for these characteristics is that in fully supersonic/hypersonic flow, the shock wave becomes stronger and the change in density is dominant and makes it easier for the spaceplane to squeeze through. In the bottom right figure, the pitch moment coefficient ($dC_m/d\alpha$) shows the strongest static stability at Mach 1.1 for all angle-of-attack lower than 18 degrees. The configuration becomes unstable when the Mach number is higher than 3. At Mach 3 the spaceplane is only statically stable with an angle-of-attack of 12 degrees or higher. The angle-of-attack increases to 23 degrees for higher Mach numbers to become statically stable. These curves are the untrimmed aerodynamic behaviour.

The lateral static stability coefficients of the Space Shuttle Orbiter are presented in Figure 2.6a and 2.6b which can be found in [Weiland, 2014]. In these figures the coefficient is plotted against the Mach number. The angle-of-attack is 0 for both graphs and the sideslip angle is linearised between 0 and 6 degrees. The yaw moment derivative (static directional) C_{n_β} is positive for Mach numbers below 8, which indicates static stability. For good flight characteristics it is desirable to have static stability, because than the angle-of-sideslip causes a moment about the top axis trying to reduce the sideslip. Above Mach 8 the derivative is slightly below 0 and therefore not stable. This characteristic explains why the controller is continuously using the deflection surfaces and thrusters to control the yaw motion. The roll moment derivative (effective dihedral) C_{l_β} is negative over the whole Mach regime, which indicates static stability because a negative C_{l_β} causes a rolling moment trying to return to an even keel.

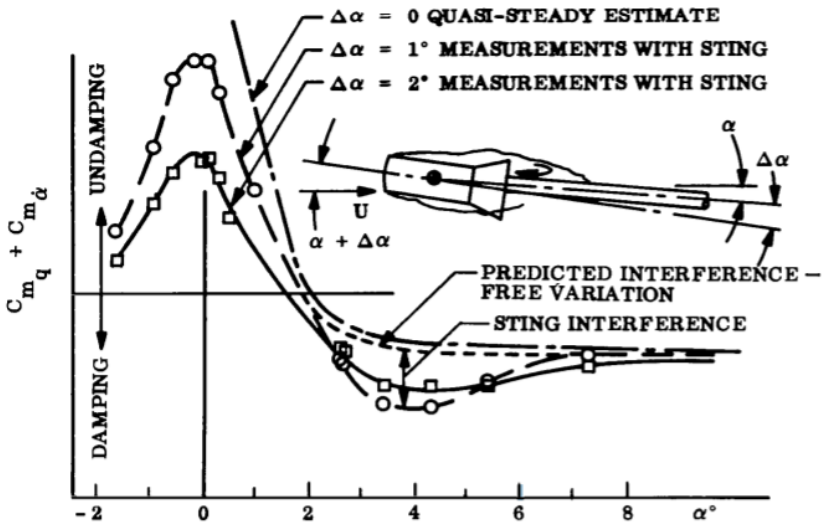

Figure 2.4: Effect of the angle-of-attack number on the dynamic pitch motion of blunt Flared cylinder (M = 0.65) [Ericsson and Reding, 1969].

2.2.3. Shape optimisation

From this point, the understanding in the aerodynamic characteristics and related stability is established, and the next step is the shape optimisation. The design of a spaceplane is very complex. In 1969 the first studies of the Space Shuttle shape were conducted. Many concept iterations were made based on manufacturing possibilities, costs, payload capacities, counteracting heat related shape features and flying qualities [Scott, 1978]. Subsequently, the main shape was largely determined. In [Surber and Olsen, 1978], more specific aerodynamic shape features are investigated with the use of wind tunnel testing. These different aerodynamic shape trade-offs are summarised in Table 2.1. Some of these results are discussed below, to give a better understanding and context:

Vertical tail design The different configurations: vertical tail, vertical tail plus ventral (small wings on the bottom of the fuselage), wing tips and butterfly configuration are investigated. For the Space Shuttle design, the vertical tail was chosen, which from the aerodynamic data in the previous section resulted in weak yaw static stability. In this decision making the minimum weight is more important than the yaw stability. The extensive attitude thrusters implemented in the Space Shuttle create artificial controlled stability and is preferable above the extra weight of the additional or enlarged wings. Thus, the propellant mass required for creating this artificial stability while re-entering is less than the extra wing weight. With a point of view where the flying qualities are desired to be improved this spaceplane shape part has potential.

This vertical tail feature is debatable looking at different spaceplane designs. The smaller X-20, Hermes and HORUS design have wing tips, whereas X-37 has the butterfly configuration. And the more recent spaceplanes, the X-38 and the dream chaser (descendant of the HL-20), have the horizontal wings mounted at an angle, which give partial yaw stability. In these designs the fuselage is more integrated and combined with the wings which leads to a larger surface area to create the required lift force. In the case of the dream chaser there is an additional vertical tail on top of the fuselage. Hence, these wing configurations give multiple options for creating yaw stability. The deflecting surface area needs to be sufficient to stabilize the yaw motion.

Nose camber Instead of designing the Space Shuttle with a relatively large nose camber, the bottom shape contour from the fuselage till the nosecone is almost linear (see Table 2.1). This shape feature reduces the lift created by the nose and therefore results in a smaller needed elevon size to provide the desired trim range. Another effect is that this nose is less blunt and affects the heat load.

Nose cross section For the nose cross section, the triangular shape was selected. This improves the hypersonic directional stability and reduces sidewall heating. For the heating this result is logical, because

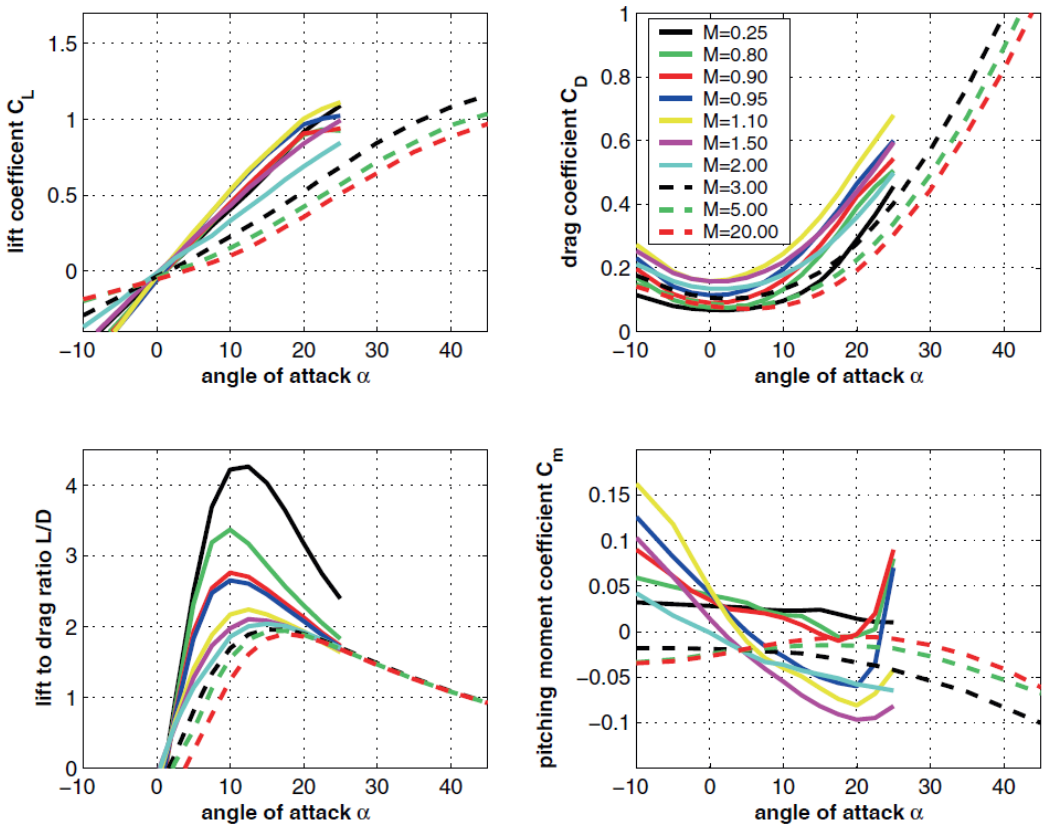

Figure 2.5: Untrimmed aerodynamic characteristics of the Space Shuttle Orbiter [Hirschel and Weiland, 2009].

with increasing angle-of-attack the side walls move away from the incoming air flow. The hypersonic (also subsonic) directional stability is improved, because there is more air deflection on the nose if there is a non zero angle-of-sideslip. Therefore the spaceplane is forced to reduce the sideslip. Also the center of pressure is displaced which helps to meet the trim requirements.

Wing-body integration For the vehicle to be stable and trimmable for both hypersonic and subsonic velocities, it is necessary that the wing is located such that for the required center of gravity range the elevens can provide enough center of pressure control to meet the upper and lower attitude requirements at both the fore and aft centers of gravity. With the wing in this location, it is also required that the subsonic aerodynamic center can still provide longitudinal stability.

The lateral characteristics of the Space Shuttle Orbiter are presented in Figure 2.7, for corresponding angle-of-attack and surface deflection angles along the trajectory. The static stability derivatives are similar as the ones presented in Figure 2.6. The difference is due to the angle-of-attack and the slightly changed pressure distribution caused by the deflection surface. Now, with this configuration the directional stability derivative (C_{n_β}) is worse and only stable at Mach 2 or lower. However, the dihedral stability derivative (C_{l_β}) is sufficiently negative (stable) that the dynamic derivative ($C_{n_{\beta\,\mathrm{dyn}}}$) is positive along the entire trajectory. The parameters is indicating the change in the yaw moment coefficient due to the yaw rate. This dynamic derivative is required to be positive for adequate stability in the Dutch roll flight mode.

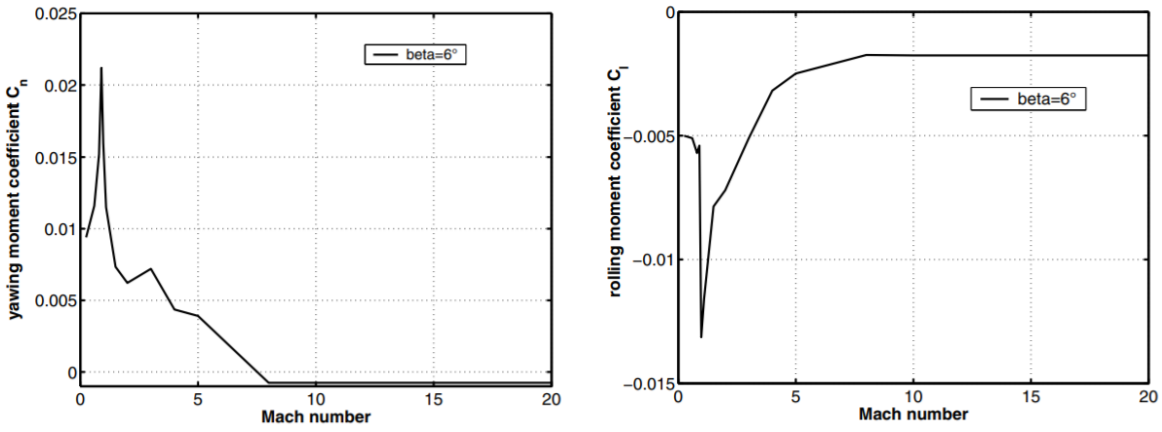

(a) Yaw coefficient

(b) Roll coefficient

Figure 2.6: The lateral coefficients of the Space Shuttle Orbiter at a constant angle-of-attack of 0 degrees and linearised sideslip angle between 0 and 6 degrees [Weiland, 2014].

Table 2.1: Summary of aerodynamic trade-off studies of the Space Shuttle Orbiter [Surber and Olsen, 1978].

TRADE ELEMENT	ALTERNATIVES OR RANGE OF VARIABLES	BASELINE SELECTION	RATIONALE
VERTICAL TAIL DESIGN	TAIL TYPE ℄ VERTICAL ℄ PLUS VENTRAL WING TIP BUTTERFLY	℄ VERTICAL	MINIMUM WEIGHT FOR STABILITY AND HANDLING QUALITIES
	AIRFOIL WEDGE VS. SYMMETRIC WITH 8% AND 12% THICKNESS RATIO	10° WEDGE	MINIMUM WEIGHT FOR REQUIRED STABILITY LEVEL
TAIL SCRAPE ATTITUDE	17° TO 21°	18°	REDUCED WING SIZE COMPROMISE BETWEEN REDUCED WING WEIGHT AND INCREASED GEAR WEIGHT
SPEED BRAKE LOCATION	VERTICAL TAIL VS. BODY VS. WING	VERTICAL TAIL	MULTIPLE USE WITH FLARED RUDDER; MINIMUM WEIGHT APPROACH
FOREBODY GEOMETRY	NOSE CAMBER 0.075 0.030	0.030	• REDUCED ELEVON SIZE TO PROVIDE DESIRED TRIM RANGE • IMPROVED INTERNAL PACKAGING AND NOSE GEAR INSTALLATION
	NOSE CROSS SECTION A B C	C	• IMPROVED HYPERSONIC DIRECTIONAL STABILITY AND REDUCED SIDEWALL HEATING • ADJUSTED PLANFORM HYPERSONIC C.P. TO MEET TRIM REQUIREMENT
WING DESIGN	SWEEP 50° VS. 60° ASPECT RATIO 1.8 TO 2.4 TAPER RATIO 0.10 TO 0.30 THICKNESS 8% TO 12% TWIST 0 AND -5° AIRFOIL SYMMETRIC VS. CAMBER	50° 2.19 0.21 8% -5° CAMBER	• IMPROVED MAX C_L • IMPROVED LOW-SPEED/HIGH-SPEED AERODYNAMIC BALANCE • IMPROVED LOW-SPEED LIFT • MINIMIZED TRIM LOSSES AT LANDING • REDUCED WING SIZE
WING-BODY INTEGRATION	C.G. RANGE (% BODY LENGTH) 5% VS. 3% MAX ENTRY TRIM α (FWD C.G.) 50° VS. 35° STATIC MARGIN (AFT C.G.) -1% TO 3% DIHEDRAL 7° TO 0°	3% 50° 0% 3-1/2°	• GOOD ALLOWABLE PAYLOAD ENVELOPE WITHOUT MAJOR CONFIGURATION IMPACT • MET CROSSRANGE REQUIREMENT AND ALLOWED HIGH α ENTRY • ADEQUATE HANDLING QUALITIES REDUCED WEIGHT • IMPROVED HANDLING QUALITIES

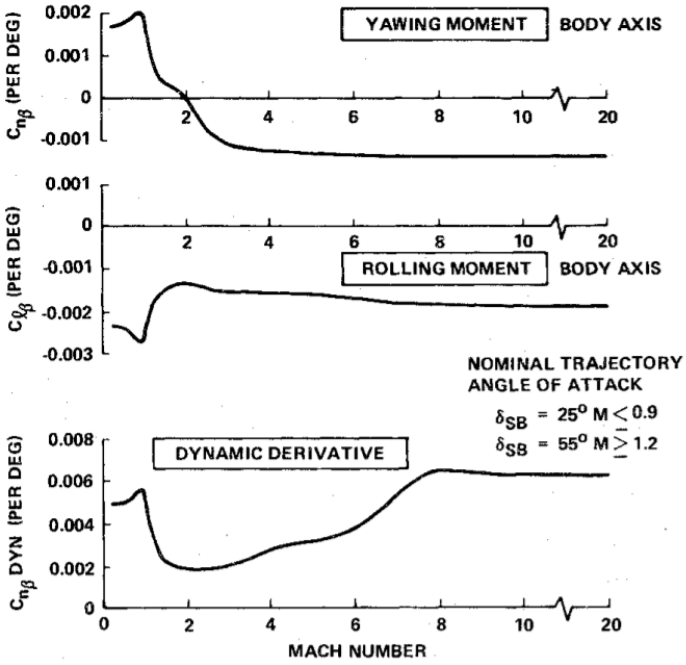

Figure 2.7: Lateral static and dynamic characteristics along the nominal trajectory [Surber and Olsen, 1978].

2.3. Hermes spaceplane

The Hermes spaceplane was designed by the Centre National D'Études Spatiales (CNES) in 1975. The maximum payload capacity to low earth orbit (LEO) is approximately 3,000 kg, which is much lower compared to the 29,000 kg of the Space Shuttle. This vehicle looks similar to the HORUS spaceplane and is therefore very relevant for this research. The Hermes spaceplane comprises two elevons, a body flap and two rudders. The rudders can deflect 35° outward and 5° inward. The nose is very blunt and the wings propagate immediately from the nose. Hereby, the wings surface has a relatively big size compared to the fuselage (a configuration of the vehicle is visualised in Figure 2.9). This design results in a relative high L/D ratio similar to the SSO, which is observable in the left bottom figure of Figure 2.8. In this same figure, the curvature of the pitching coefficient (bottom right figure), looks very similar to the SSO. Only the magnitude is slightly different. Thus, the magnitude of the pitch moment derivative (C_{m_α}) is higher. For lower angle-of-attack and high Mach number the spaceplane is unstable and visa versa at high angle-of-attack.

2.3.1. Design process

A study of the Hermes design process shows the decision making process, based on flying qualities [Raillon et al., 1992]. The mission design gave 15 control points, that have been evaluated while iterating the shape of the spaceplane. A couple of relevant control points are the thermal behaviour, subsonic instability and controllability. The computational tools that were used for the iterative process used the Euler model, which will be discussed in Chapter 4. Eventually, the Hermes 1.0 design has fulfilled several constraints. The difference is visualised in Figure 2.9. For the longitudinal stability criteria, the only problems occur at a Mach number of 2 with low angle-of-attack values. To counteract these problems, there is a restriction on the angle-of-attack. With an angle-of-attack higher than 6 degrees, there will be sufficient lift variation capabilities for the guidance.

2.3.2. Aerodynamic modeling

Another study focused on the aerodynamic modeling of the Hermes spaceplane also uses the Euler equations with real gas effects [Mallet et al., 1992]. The real gas effects are necessary for modeling the high velocity regimes (larger then Mach 5). The study shows that the gap of aerodynamic quantities between reality and simulations depends on three aspects. Firstly, the physical model, which can be viscous/inviscid, laminar/turbulent or non-reactive/reactive. Secondly, the accuracy of the numerical formulation. And thirdly, the choice of mesh and level of convergence. Ideally, for validation purposes the sensitivity of each of these parameters should be investigated. For the prediction of the aerodynamics forces in every flight condition, a lot of simulations need to be conducted, for amongst others different: Mach numbers, angles-of-attack, sideslip angles, attitudes of control deflections surfaces. Therefore, the unit cost of each simulation has to be low.

The mesh is generated by a global mesh which covers the whole spaceplane but does not account for details such as elevon/rudder gaps. In order to obtain sufficiently accurate solutions at reasonable computation costs, local meshes are implemented in the global mesh. Because of the complexity of the shape, the study uses unstructured mesh consisting of tetrahedras, prisms and hexahedras elements for the skin of the spaceplane. The volume around the spaceplane is filled with a front marching technique. A uniform flow boundary condition is initiated at the freestream condition. For the numerical solver the Galerkin finite volume method is used for the first approach, in which the inviscid fluxes are upwindend using an Osher's Riemann solver. For the second approach the Galerkin least square solver is used. Whereby the stability is taken care of by discontinuities capturing operator, which noticed the strong gradients in the flow field. The solutions are obtained in less than 200 timesteps which satisfied the accuracy demands. Overall this study shows that with an Euler equation model in combination with a mesh of 180,000 nodes, the simulation can take up to 40 hours of computation time (on a NEC SX3). The computers nowadays are better, but still these features are a very important aspect of this study. Thus, the determination of the many different aerodynamic conditions requires an efficient simulation plan.

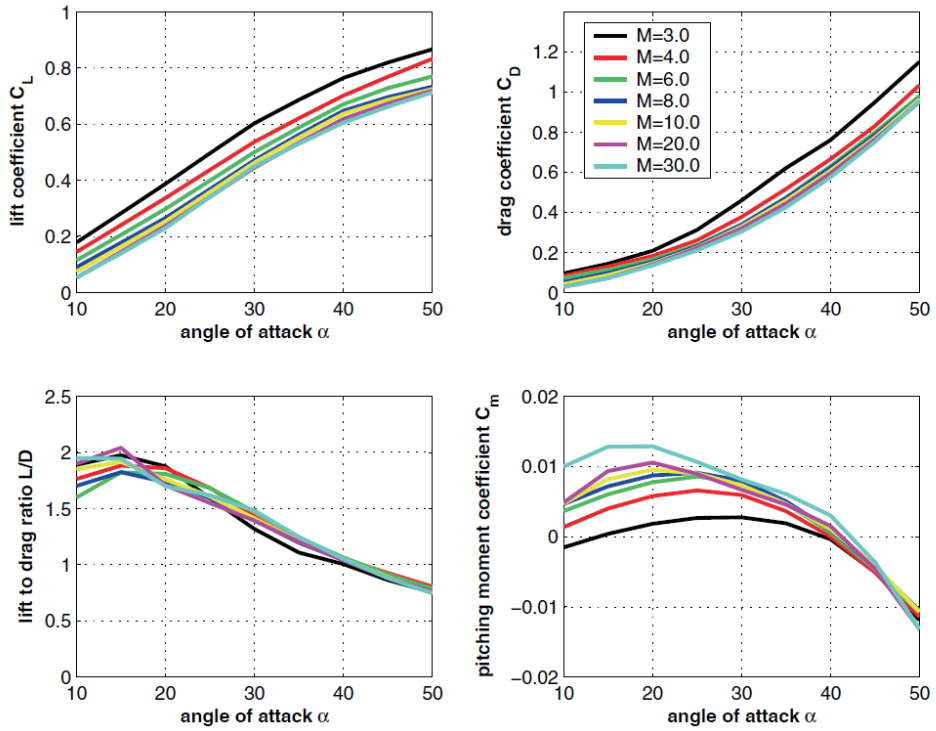

Figure 2.8: Untrimmed aerodynamic characteristics of the Hermers spaceplane [Hirschel and Weiland, 2009].

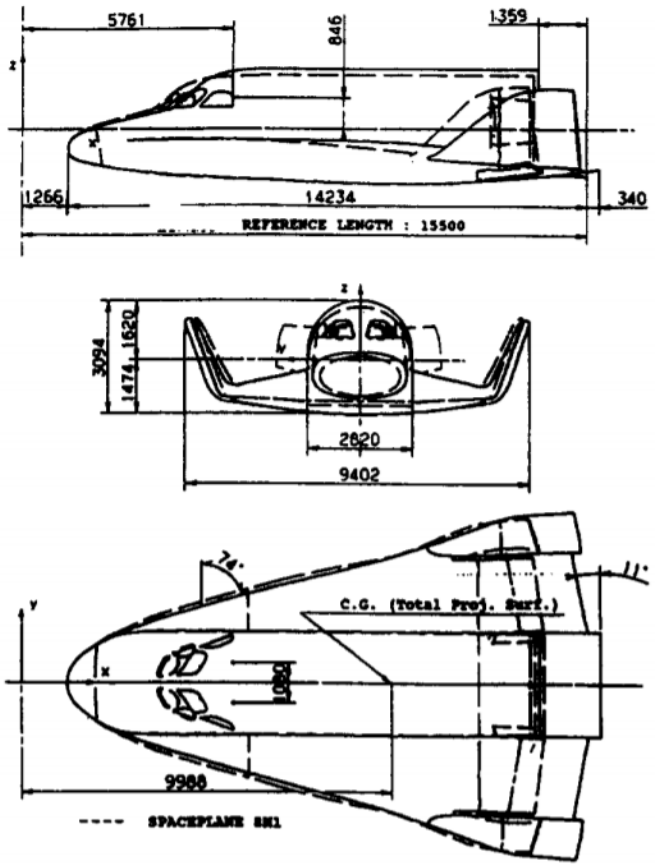

Figure 2.9: The difference between 0.0 design and 1.0 iteration design of the Hermes spaceplane [Raillon et al., 1992].

2.4. Reference vehicle and mission

As already indicated in chapter 1, the reference vehicle for this research is the HORUS-2B. This vehicle is one of the smaller designed spaceplanes with a vehicle length of 25 m [Cucinelii and Müller, 1988]. The maximum fuselage width and height are 5.4 and 4.5 m, respectively. The wingspan is 13 m and the wing area is 110 m^2. When re-entering the atmosphere the mass of the HORUS spaceplane is 26 tons. The inertia tensor of the HORUS landing configuration is 119,000, 769,000 and 806,000 kgm^2 for the I_{xx}, I_{yy} and I_{zz} respectively. A visualisation of the HORUS design is presented in Figure 2.11. As can be seen, the vehicle consists of a fuselage, nosecone and wings with relatively big winglets.

The same literature source shows the possible deflection range for which the aerodynamic data is simulated. A visualisation of the deflection surfaces is presented in Figure 2.10. The rudders can operate from 0 till 40 degrees and the deflection for both rudders is defined positive outboard. The elevons have a range from -40 till +40 degrees. A positive change is angle is a downwards deflection. At subsonic speeds these are symmetrically used for trim. Lastly, the body flap has a range from -20 till +30 degrees, similar as the elevons a positive deflection is downwards relative to the top view shown in Figure 2.10. In the subsonic regime the body flap is set to -20 degrees to trim the spaceplane. The aerodynamic data is available for these flap deflection ranges and for a Mach range of 1.2 till 20. The untrimmed aerodynamic characteristics of the original HORUS-2B design are partly presented in Figure 2.12. The aerodynamic data will be used for validation and an aerodynamic baseline for the optimisation. The aerodynamic database is constructed based on several assumptions. The first assumption is that the vehicle is a rigid body, thus no aeroelasticity phenomena are modelled, and there is no interference effects of the flaps. A second assumption is that the aerodynamic coefficients are a function of the Mach number M, angle-of-attack α, altitude h, angle-of-sideslip β, and the deflection surface angles. Hence, the definition of the aerodynamic coefficients are the following:

$$C_D = C_{D_0} + \Delta C_{D_{r,l}} + \Delta C_{D_{w,l}} + \Delta C_{D_b} + \Delta C_{D_{w,r}} + \Delta C_{D_{r,r}} - \Delta C_{D_h} \tag{2.1}$$

$$C_S = \Delta C_{S_{r,l}} + \Delta C_{S_{w,l}} + \Delta C_{S_{w,r}} + \Delta C_{S_{r,r}} + \left[\left(\frac{\partial C_S}{\partial \beta}\right)_0 + \Delta\left(\frac{\partial C_S}{\partial \beta}\right)_{w,l} + \Delta\left(\frac{\partial C_S}{\partial \beta}\right)_{w,r}\right]\beta \tag{2.2}$$

$$C_L = C_{L_0} + \Delta C_{L_{w,l}} + \Delta C_{L_b} + \Delta C_{L_{w,r}} \tag{2.3}$$

$$C_l = \Delta C_{l_{w,l}} + \Delta C_{l_{w,r}} + \left(\frac{\partial C_l}{\partial \beta}\right)_0 \cdot \beta \tag{2.4}$$

$$C_m = C_{m_0} + \Delta C_{m_{w,l}} + \Delta C_{m_b} + \Delta C_{m_{w,r}} \tag{2.5}$$

$$\text{and } C_n = \Delta C_{n_{r,l}} + \Delta C_{n_{w,l}} + \Delta C_{n_{w,r}} + \Delta C_{n_{r,r}} + \left[\left(\frac{\partial C_n}{\partial \beta}\right)_0 + \left(\frac{\partial C_n}{\partial \beta}\right)_{r,l} + \Delta\left(\frac{\partial C_n}{\partial \beta}\right)_{r,r}\right]\beta \tag{2.6}$$

where the aerodynamic force coefficients are the drag coefficient C_D, the side-force coefficient C_S, and the lift coefficient C_L, while the aerodynamic moments coefficients are the roll C_l, the pitch coefficient C_m,

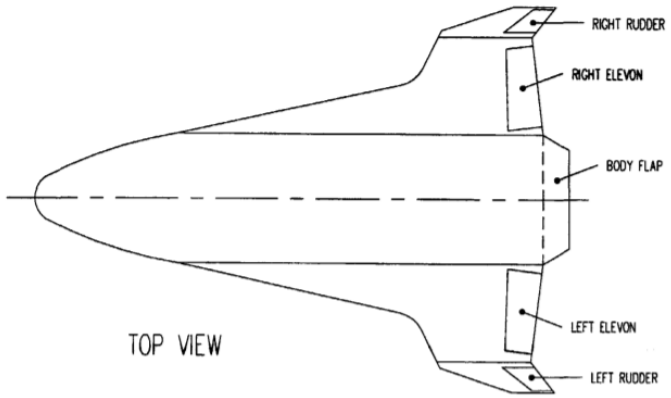

Figure 2.10: The HORUS deflection flaps [Mooij, 1995].

Table 2.2: Aerodynamic coefficients [Cucinelii and Müller, 1988].

Drag coefficients	Side-force coefficients	Lift coefficients
$C_{D_0} = f(M,\alpha)$	$\Delta C_{S_{r,l}} = f\left(M,\alpha,\delta_{r,l}\right)$	$C_{L_0} = f(M,\alpha)$
$\Delta C_{D_{r,l}} = f\left(M,\alpha,\delta_{r,l}\right)$	$\Delta C_{S_{w,l}} = f\left(M,\alpha,\delta_{w,l}\right)$	$\Delta C_{L_{w,l}} = f\left(M,\alpha,\delta_{w,l}\right)$
$\Delta C_{D_{w,l}} = f\left(M,\alpha,\delta_{w,l}\right)$	$\Delta C_{S_{w,r}} = f\left(M,\alpha,\delta_{w,r}\right)$	$\Delta C_{L_b} = f\left(M,\alpha,\delta_b\right)$
$\Delta C_{D_b} = f\left(M,\alpha,\delta_b\right)$	$\Delta C_{S_{r,r}} = f\left(M,\alpha,\delta_{r,r}\right)$	$\Delta C_{L_{w,r}} = f\left(M,\alpha,\delta_{w,r}\right)$
$\Delta C_{D_{w,r}} = f\left(M,\alpha,\delta_{w,r}\right)$	$\left(\frac{\partial C_S}{\partial\beta}\right)_0 = f(M,\alpha)$	
$\Delta C_{D_{r,r}} = f\left(M,\alpha,\delta_{r,r}\right)$	$\Delta\left(\frac{\partial C_S}{\partial\beta}\right)_{w,l} = f\left(M,\alpha,\delta_{w,l}\right)$	
$C_{D_h} = f(M,h)$	$\Delta\left(\frac{\partial C_S}{\partial\beta}\right)_{w,r} = f\left(M,\alpha,\delta_{w,r}\right)$	
Roll coefficients	**Pitch coefficients**	**Yaw coefficients**
$\Delta C_{l_{w,l}} = f\left(M,\alpha,\delta_{w,l}\right)$	$C_{m_0} = f(M,\alpha)$	$\Delta C_{n_{r,l}} = f\left(M,\alpha,\delta_{r,l}\right)$
$\Delta C_{l_{w,r}} = f\left(M,\alpha,\delta_{w,r}\right)$	$\Delta C_{m_{u,l}} = f\left(M,\alpha,\delta_{w,l}\right)$	$\Delta C_{n_{w,l}} = f\left(M,\alpha,\delta_{w,l}\right)$
$\left(\frac{\partial C_l}{\partial\beta}\right)_0 = f(M,\alpha)$	$\Delta C_{m_b} = f\left(M,\alpha,\delta_b\right)$	$\Delta C_{n_{w,r}} = f\left(M,\alpha,\delta_{w,r}\right)$
	$\Delta C_{m_{w,r}} = f\left(M,\alpha,\delta_{w,r}\right)$	$\Delta C_{n,r} = f\left(M,\alpha,\delta_{r,r}\right)$
		$\left(\frac{\partial C_n}{\partial\beta}\right)_0 = f(M,\alpha)$
		$\Delta\left(\frac{\partial C_n}{\partial\beta}\right)_{r,l} = f\left(M,\alpha,\delta_{r,l}\right)$
		$\Delta\left(\frac{\partial C_n}{\partial\beta}\right)_{r,r} = f\left(M,\alpha,\delta_{r,r}\right)$

Table 2.3: Symmetry conditions of the left and right elevons and rudders [Cucinelii and Müller, 1988].

Zero derivatives right elevon	First derivative right elevon	Zero derivatives right rudder	First derivative right rudder
$C_{D_{w,r}} = C_{D_{w,l}}$	$\left(\frac{\partial C_S}{\partial\beta}\right)_{w,r} = \left(\frac{\partial C_S}{\partial\beta}\right)_{w,l}$	$C_{D_{r,r}} = C_{D_{r,l}}$	$\left(\frac{\partial C_n}{\partial\beta}\right)_{r,r} = \left(\frac{\partial C_n}{\partial\beta}\right)_{r,l}$
$C_{S_{w,r}} = -C_{S_{w,l}}$		$C_{S_{r,r}} = -C_{S_{r,l}}$	
$C_{L_{w,r}} = C_{L_{w,l}}$		$C_{n_{r,r}} = -C_{n_{r,l}}$	
$C_{l_{w,r}} = -C_{l_{w,l}}$			
$C_{m_{w,r}} = C_{m_{w,l}}$			
$C_{n_{w,r}} = -C_{n_{w,l}}$			

and the yaw coefficient C_n. The functional arguments of the components of the aerodynamic coefficients are listed in Table 2.2. The two elevons and two rudders are located symmetrically with respect to the XZ-plane of the vehicle. Since they have identical shape, the components of the aerodynamic coefficients of the right actuator are the same as the left one, while others are equal in module and opposite in sign, as presented in Table 2.3. This is known as the symmetry condition.

This study revolves around the terminal area energy management (TAEM) phase of the re-entry trajectory, because in this phase the flight velocity is in the range where optimisation of the flying qualities is desired. The objective in the TAEM re-entry phase is to extend the flight range. Therefore, the controller is designed (and different compared to the other phases) to use the vehicle kinetic and potential energy as optimal as possible, which results in a minimized drag. This research requires a reference trajectory to obtain the corresponding flight conditions such as ambient pressure, density and temperature at different points along descent. In [Powers, 1986], the TAEM interface of the Space Shuttle Orbiter is at an altitude of 25 km, and a velocity of 760 ms^{-1}. The Mach number at that altitude is 2.55 based on the U.S. Standard Atmosphere of 1976, which is in the high supersonic regime. The end of the TAEM phase, just before the landing phase of the re-entry trajectory, is in between an altitude of 3 and 3.7 km, and a velocity of approximately 190 ms^{-1} [Moore, 1991]. Which corresponds to a Mach number of 0.58 (for a 3 km altitude) and is in the mid subsonic regime. The HORUS-2B design was later further developed by the European Space Agency (ESA) and therefore the landing location is assumed to be in Kourou (French Guiana).

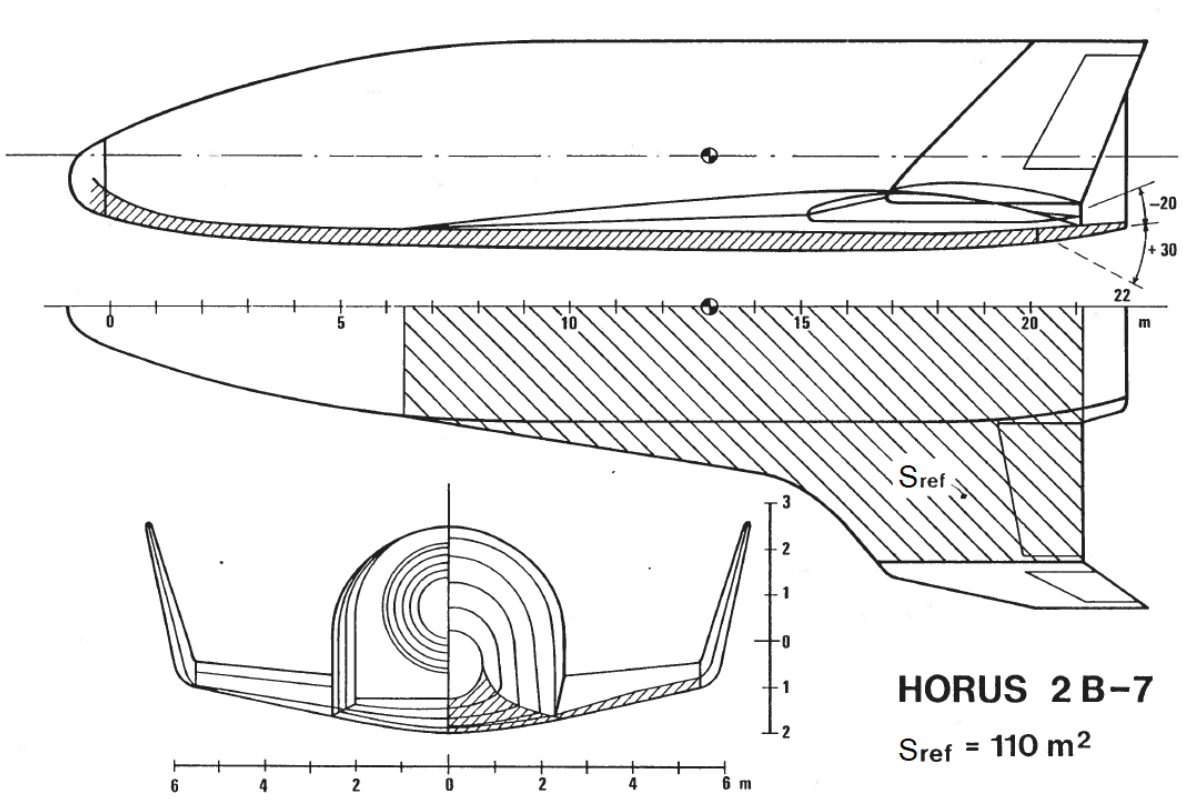

Figure 2.11: Design drawing of the HORUS-2B vehicle [Cucinelii and Müller, 1988].

For the validation of the dynamic stability and therefore the flight modes of the vehicle, the study by Mooij [2015] can be used. In this study a GNC system is used to guide the vehicle from the atmospheric interface until the TAEM interface. At the last point, the TAEM interface of the trajectory (Mach 2.5), the flight modes of the HORUS are determined along with the current flap configuration and the vehicle's attitude. This reference point is used as validation for the flight modes. When the flying qualities are improved in the lower Mach regime by changing the vehicle shape, the qualities have to be investigated for the higher Mach regime (hypersonic flow). For these dynamic stability characteristics the same literature can be used. Additionally, the research by Viavattene and Mooij [2019], gives a relation between the dynamic stability characteristics and the military requirements for aircraft. In this study, the flying qualities of the HORUS re-entry are investigated for Mach 5, 10, 15 and 20. Thus, hereby the modified HORUS spaceplane can be compared and validated with the original spaceplane.

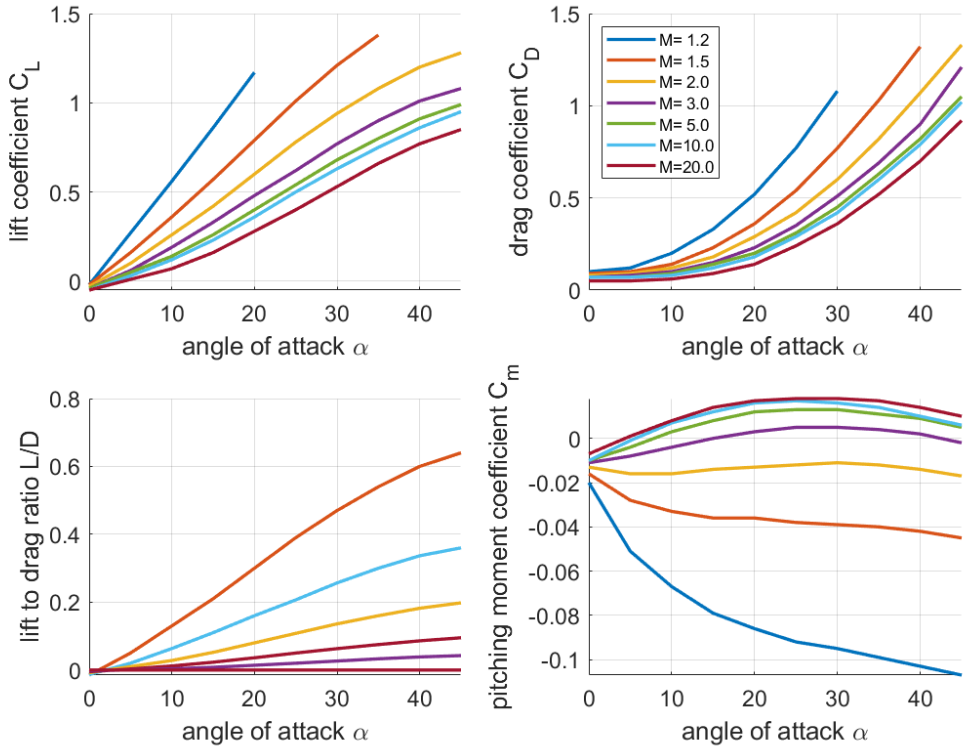

Figure 2.12: The aerodynamic coefficients of the HORUS for different Mach numbers and angle-of-attack. (plotted from data published in [Cucinelii and Müller, 1988].)

2.5. Mission and System Requirements

Before starting with the core chapters of this research, the mission and system requirements have to be determined and stated. The mission and system requirements are set based on the discoveries and conclusions of the mission heritage. The mission requirements give detailed information about which analyses have to be conducted to answer the main research questions, and the system requirements explain which specifications the model should comply with.

2.5.1. Mission Requirements

The mission requirements that are necessary to answer the main research objective are stated below.

1. A geometry shall be created which must be modifiable for the desired shape changes and flap deflection configurations.
   - 1.1. The spaceplane shape shall have an adoptable fuselage, wing, winglets and nosecone tip height. This chapter showed that the different attached wings to the fuselage configurations create opportunities in generating different spaceplane flight characteristics.
   - 1.2. The generation of different geometries must not lead to unrealistic shapes, which means that different parts of the body have to move along with the desired shape modification.
   - 1.3. The flap deflection configuration must be generate-able for all the desired shape dimensions and also combinations of these different dimensions.
2. A CFD simulation must be performed to determine the aerodynamic characteristics of the original HORUS-2B and modified spaceplane versions. These simulations must determine the forces and moments depending on different attitudes and Mach numbers.
3. An analysis of the aerodynamic characteristics shall be performed to investigate the static stability derivatives of the different spaceplanes.

3.1. The attitude and Mach ranges shall be focused on realistic conditions in the TAEM phase of the re-entry trajectory. Which is in between Mach 2.5 and 0.8, a sideslip angle between 0 and 2 degrees and an angle-of-attack lower than 20 degrees. The nominal HORUS TAEM trajectory, described in this chapter, will be discretized based on altitude and shall be simulated with the corresponding atmospheric properties.

3.2. The static stability derivatives must be determined to investigate if the spaceplane is statically stable. These stability derivatives can be compared with the benchmark (original HORUS spaceplane). The comparison shows if the spaceplane creates sufficient counter-force when the attitude is off its stable point.

4. An analysis regarding the dynamic stability of the spaceplanes at flight conditions along the TAEM trajectory must be performed. By using the obtained aerodynamic characteristics of the different spaceplanes.

4.1. The aim is to achieve dynamic stability of level 3 defined by the military in MIL-F-8785C [1980] and MIL-HDBK-1797 [1997], which implies that the vehicle has sufficient stability for a safe and controllable return from space.

4.2. The level 3 (and also level 1 and 2) dynamic stability requirements are defined with the variables: damping ratio and halve time for different eigenmotions, which will be explained in Chapter 3. These characteristics will be the outcome of the model and show the difference in the dynamic stability compared to the original HORUS spaceplane. The comparison will answer the research question: if the HORUS spaceplane's flying qualities are improved in the lower Mach regimes.

5. A static and dynamic stability analysis of the final modified spaceplane, at higher Mach regime and conditions along the reference trajectory by Mooij [2015], to ensure the stability at higher velocities. The improved shape may not deteriorate the flying qualities at higher altitudes such that the spaceplane is unstable.

2.5.2. System Requirements

The system requirements follow from the mission requirements as they are needed to satisfy the mission requirements. The following enumeration gives important requirements that must be satisfied by the model.

Reference vehicle and flight conditions related:

- The dimensions of the reference vehicle HORUS-2B shall be in compliance with the known dimensions defined by Cucinelii and Müller [1988].
- The mass and inertia properties of the reference vehicle shall be in compliance with the known properties by Cucinelii and Müller [1988].
- The environmental conditions along the flight trajectory of the spaceplane shall be used.

Simulation model related:

- An individual CFD simulation must be in the accuracy range of 30% and be completed within 60 seconds of computation time. This chapter showed that the demands for accuracy can not be too high, because the computation time would increase drastically. For this research it is important to investigate and look into the low accuracy and low computation time fluid models.
- The different software packages must be able to connect with each other for automation purposes.
- Each shape dimension modification must have a high and low value to see the influence of that individual dimension. After which an optimisation study of dimension variables will be conducted to optimize the flying qualities of the spaceplane.
- Generation of the geometry with corresponding flap configuration and mesh creation may not exceed 120 seconds.

From this point the first insight in the flying qualities of the spaceplane concept are obtained. The reference vehicle and relevant flight characteristics are discussed, which are the necessary ingredients for the shape optimisation. The mission is to achieve a safe and controllable re-entry by a re-usable modified HORUS spaceplane. The shape will be optimised for the TAEM phase and afterwards checked if the changed shape does not have disastrous stability effects in other phases of the re-entry flight. In the next couple of chapters different aspects: flight mechanics, aerodynamics and the architectural design of the model will be explained, to achieve the mission target.

3

Flight mechanics

The motion of a body under the effects of external forces and torques is one of the most fundamental problems in physics. An example of such a problem is the flight of a spaceplane in Earth's atmosphere. In this case, the vehicle is the HORUS-2B spaceplane, or a modified version of it, and the external forces and torques acting on it are generated by the gravitational field of Earth, and the aerodynamic forces and moments due to the passage of the vehicle through air. Usually, the thrust force generated by the engines is included, but in this study only the gliding trajectory is investigated. The control of the vehicle is directly linked to the motion of the spaceplane. The flight mechanics are based on the well-known Newton's laws of motion and law of gravitation, from which the equations of motion of the vehicle can be derived. To completely determine the motion, it is important to define the reference frames and the state variables, on which the description of the motion is dependent. Moreover, since sometimes it is convenient to define forces in different reference frames, it is required to transform one frame to another.

3.1. Reference frames

To properly discuss flight mechanics it is important to clearly define the reference frames that are used. The choice of reference frame depends on the scope of the investigation. This research focuses on the flow around the vehicle and the resulting effects on the stability and control while performing a gliding re-entry. The important reference frames for this study are the inertia reference frame, which is the basis for describing a motion, the planetocentric rotating reference frame for the derivation of the equations of motion, the body fixed reference frame to relate the forces to the orientation of the spaceplane and the aerodynamic reference frame for the more conventional used forces such as drag, side and lift force.

3.1.1. Rotating Earth fixed reference frame

The rotating Earth fixed reference frame is fixed to the Earth (indicated with the subscript I) and rotates with the Earth's rotation rate (ω) around the Z_R-axis [Mooij, 2013]. The origin of the reference frame is located in the Earth's centre of mass shown in Figure 3.1. The X_R-axis of the reference frame is fixed to the prime (Greenwich) meridian. (Also named zero longitude.) The Y_R-axis is as in a Cartesian coordinate system, perpendicular to the X_R and Z_R-axis. Hence, the radius vector ($\mathbf{R}_s$) towards the centre of mass of the spaceplane. This position vector can also be described by the scalar radius (R), longitude (τ) and latitude (δ), which is more convenient to point towards a location on Earth. The longitude angle is defined in the X_R and Y_R plane, from the prime meridian positive around the X_R-axis ($0° \leq \tau < 360°$). The latitude angle is defined in the Z_R plane, from the Earth's equator positive around the longitude line ($-90° \leq \delta \leq 90°$). The connection between the rotating Earth fixed reference frame and the body fixed frame, is defined by the local horizontal plane, which is a plane perpendicular to the radius vector. The angle between the velocity vector ($\mathbf{V}_s$) of the spaceplane and the local Horizontal is the flight-path angle (γ), with a range of $-90° \leq \gamma \leq +90°$. The angle between the local north and local horizontal is the heading angle χ, with a range of $-180° \leq \chi < +180°$. Hereby, the position and velocity of the spaceplane with respect to Earth can be defined. The reference frame with respect to the vehicle's local horizon is visualised in Figure 3.2.

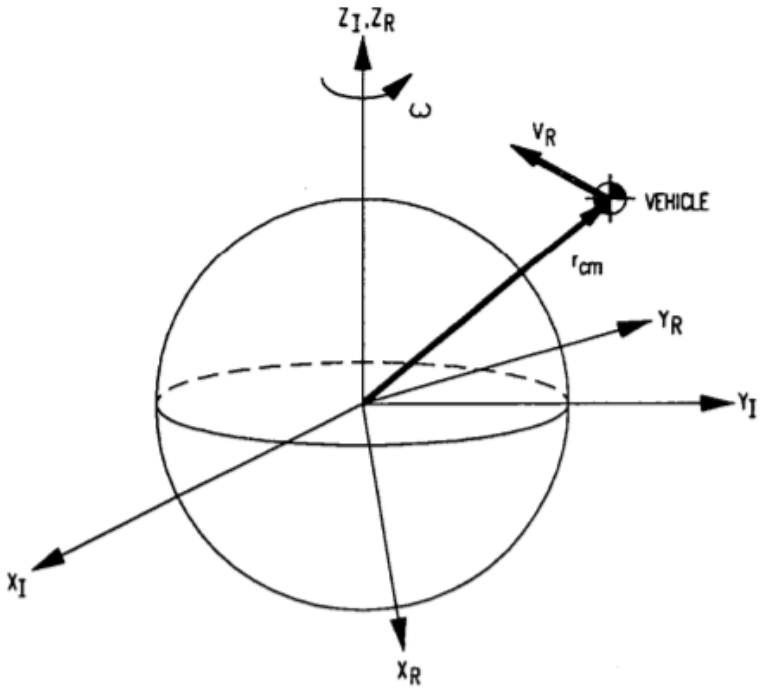

Figure 3.1: Inertial plus rotating reference frame [Mooij, 1994].

3.1.2. Body fixed reference frame

The body fixed reference frame is fixed on the spacecraft. It remains fixed to the body in all cases. The choice of axes is rather arbitrary, an often used definition can be seen in Figure 3.3. The origin of the frame is located at the centre of mass of the spaceplane. The X, Y and Z-directions are respectively directed in the longitudinal, lateral and vertical direction. With the roll ($\mathcal{L}$), pitch ($\mathcal{M}$) and yaw ($\mathcal{N}$) moment around the X, Y and Z-axis.

3.1.3. Aerodynamic reference frame

The origin of the aerodynamic reference frame is also located in the centre of mass of the spaceplane. The angles between the body fixed reference frame and the aerodynamic reference frame are the angle-of-attack (α) and the sideslip angle (β) [Mooij, 2013]. To translate between the aerodynamic reference frame and the planetocentric reference frame, the bank angle (σ) is used. The range of the angles are the following. For the bank angle $-180° \leq \sigma < +180°$ (banking towards the right is positive). For the angle-of-attack $-180° \leq \alpha < +180°$ (nose-up is is positive angle-of-attack). Lastly, the angle of sideslip range is $-90° \leq \beta \leq +90°$ (nose-right is positive angle of sideslip). The aerodynamic reference frame is shown in equation (3.4).

The transformation from the body fixed reference frame towards the aerodynamic reference frame is required for the CFD simulation. The reason for this is to improve the efficiency of the aerodynamic simulations, which will be explained in Section 4.5. Because the rotations are small and therefore no singularities occur, Euler rotations can be used. To rotate the forces from the body fixed frame (X, Y and Z-force) to the forces of the aerodynamic frame (D, S and L-force) the following rotation matrix is required. To obtain the rotation matrix written in equation (3.1.3), there is rotated around the Y and Z-axis of the body fixed frame,

$$\begin{pmatrix} F_D \\ F_S \\ F_L \end{pmatrix} = \begin{bmatrix} \cos\alpha\cos\beta & -\sin\beta & \sin\alpha\cos\beta \\ \cos\alpha\sin\beta & \cos\beta & \sin\alpha\sin\beta \\ -\sin\alpha & 0 & \cos\alpha \end{bmatrix} \begin{pmatrix} F_X \\ F_Y \\ F_Z \end{pmatrix} \tag{3.1}$$

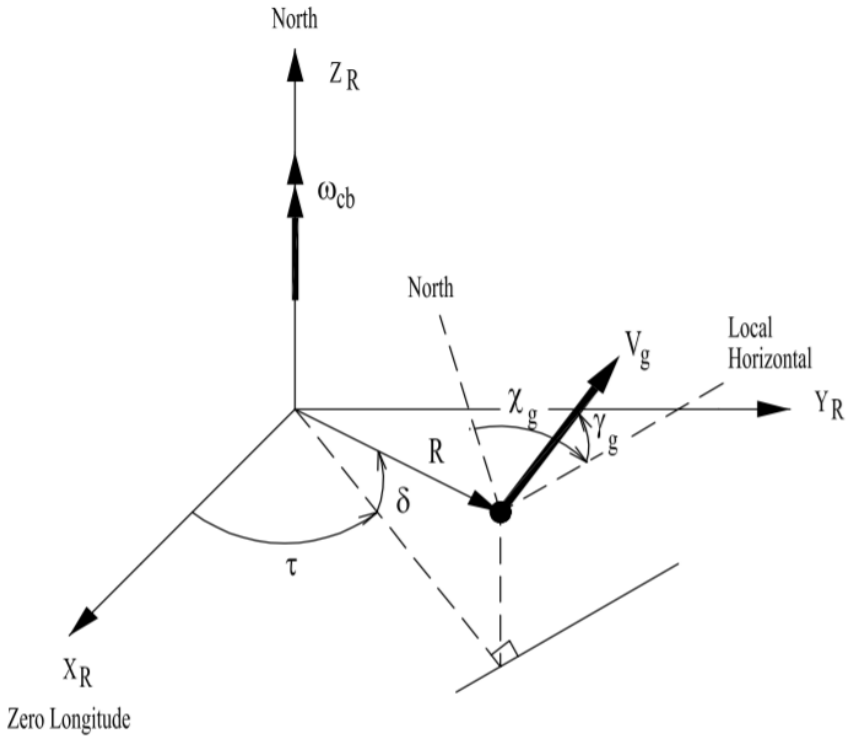

Figure 3.2: Rotating Earth fixed reference frame [Mooij, 2013].

Because the flow will be rotated in the CFD simulation, the velocity vector has to be decomposed in different components. Hence, a simple vector translation from the aerodynamic frame to the body fixed reference frame is determined. Here, the same angles are required namely; the angle-of-attack (α) and sideslip angle (β). The equations of the velocity components in the body fixed reference frame are stated in equation (3.2) till (3.4),

$$V_X = |V| \cos\alpha \sin\beta \tag{3.2}$$

$$V_Y = |V| \sin\alpha \tag{3.3}$$

$$\text{and } V_Z = |V| \cos\alpha \cos\beta \tag{3.4}$$

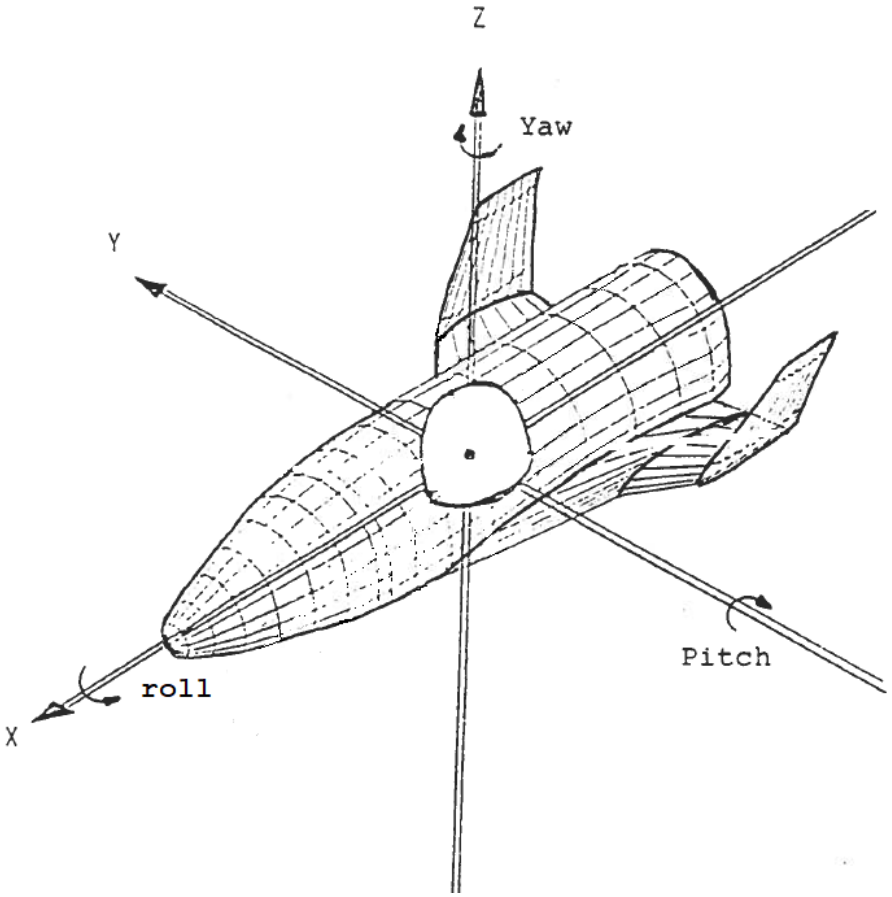

Figure 3.3: The body fixed reference frame [Cucinelii and Müller, 1988].

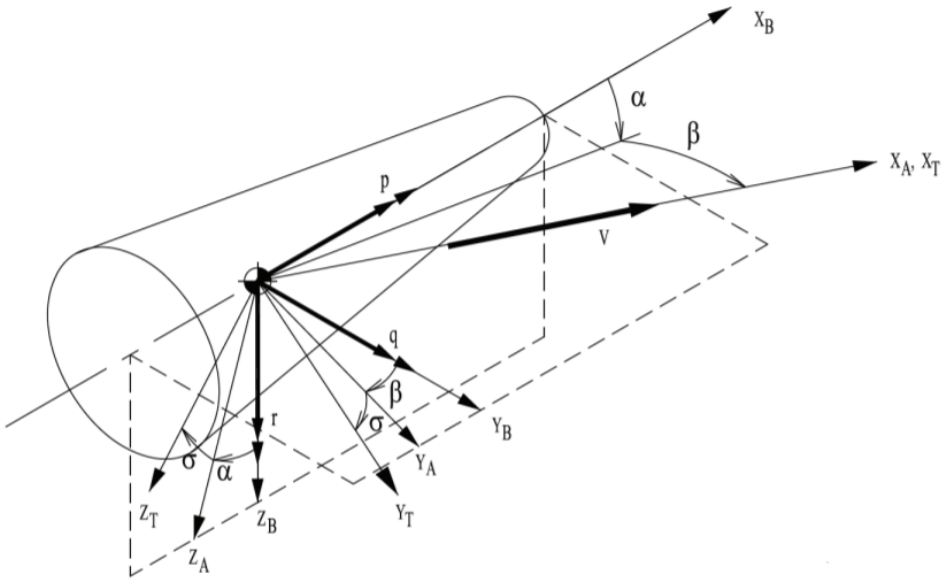

Figure 3.4: Aerodynamic reference frame [Mooij, 2013].

3.2. Equations of motion

The equations of motion are formulated using the theory of classical mechanics, more specified by Newton's well-known three laws of motion. The motion of a rigid body, such as a spaceplane, can be divided into the motion of its centre of mass and the rotation around the centre of mass. In total there are 6 degrees of freedom of which 3 for translational motion and 3 for the rotational motion. The equations of translational motion describe the position and velocity of the body and the equations of rotational motion describe the angular rate and attitude of the vehicle.

3.2.1. Equations of transitional motion

From Newton's second law, the transitional motion with respect to the inertial Earth-centred reference frame is determined as follows:

$$\tilde{\mathbf{F}}_{\mathbf{I}} = \mathbf{F}_{\mathbf{I}} = m\frac{d^2\mathbf{r_{cm}}}{dt^2} \tag{3.5}$$

where $\tilde{\mathbf{F}}_{\mathbf{I}}$ is the pseudo external force vector [N] and $\mathbf{F}_{\mathbf{I}}$ is the sum of the external forces acting on the vehicle [N]. These two forces are equal because the Coriolis force and relative force are zero. The term $m\frac{d^2\mathbf{r_{cm}}}{dt^2}$, is the acceleration of the vehicle's centre of mass with respect to the inertial reference frame [m/s^2], where $\mathbf{r_{cm}} = (x_{cm}, y_{cm}, z_{cm})$ represents the position of the vehicle's centre of mass with respect to the inertial frame's origin in Cartesian components [m].

Describing the vehicle's motion with respect to the inertial reference frame is not convenient in case of control system design, and for the stability and controllability analyses. In this case, it is preferable to express the equations of motion with respect to the rotating Earth fixed reference frame. These can be derived from the general equation for the translational motion (3.5). In this case it is considered that the Earth fixed reference frame rotates with respect to the inertia Earth centered reference frame with an angular velocity equal to the Earth's angular velocity $\boldsymbol{\omega}_{\mathbf{R}} = (0, 0, \omega_{cb})^T$.

Mooij [1994] states the full set of translational motion equations. For a vehicle with constant mass m that is subjected to external forces of aerodynamic, propulsion and gravity, written in the spherical coordinates in the rotation Earth fixed reference frame. In these equations the effects of the wind are not considered and because there is no propulsion required in the re-entry phase, the equations are slightly rewritten:

$$\dot{V} = -\frac{D}{m} - g\sin\gamma + \omega_{cb}^2 R\cos\delta\,(\sin\gamma\cos\delta - \cos\gamma\sin\delta\cos\chi) \tag{3.6}$$

$$\begin{aligned} V\dot{\gamma} = &\frac{L\cos\sigma}{m} - g\cos\gamma + 2\omega_{cb}V\cos\delta\sin\chi + \frac{V^2}{R}\cos\gamma \\ &+ \omega_{cb}^2 R\cos\delta\,(\cos\gamma\cos\delta + \sin\gamma\sin\delta\cos\chi) \end{aligned} \tag{3.7}$$

$$\begin{aligned} \text{and } V\cos\gamma\dot{\chi} = &\frac{L\sin\sigma}{m} + 2\omega_{cb}V\,(\sin\delta\cos\gamma - \cos\delta\sin\gamma\cos\chi) \\ &+ \frac{V^2}{R}\cos^2\gamma\tan\delta\sin\chi + \omega_{cb}^2 R\cos\delta\sin\delta\sin\chi \end{aligned} \tag{3.8}$$

Whereas the kinematic position equations are given by:

$$\dot{R} = \dot{h} = V_g\sin\gamma_g \tag{3.9}$$

$$\dot{\tau} = \frac{V_g\sin\chi_g\cos\gamma_g}{R\cos\delta} \tag{3.10}$$

$$\text{and } \dot{\delta} = \frac{V_g\cos\chi_g\cos\gamma_g}{R} \tag{3.11}$$

In these equations the D, S and L are the aerodynamic forces, i.e., the drag force, side force, and lift force, respectively [N]. The position is given by the distance R, longitude τ and latitude δ. The symbol V is the groundspeed and there are two direction angles, i.e., flight-path angle γ and heading angle χ. From the kinematic equations a singularity for the latitude $\delta = \pm 90°$ exists (which is the north and south pole). However, these conditions are not encountered in our flight conditions.

3.2.2. Equations of rotational motion

The rotational motion is defined as follows:

$$\tilde{\mathbf{M}}_{\mathbf{cm}} = \mathbf{M}_{\mathbf{cm}} = \int_m \tilde{\mathbf{r}} \times \left(\frac{d\boldsymbol{\omega}}{dt} \times \tilde{\mathbf{r}} \right) dm + \int_m \tilde{\mathbf{r}} \times [\boldsymbol{\omega} \times (\boldsymbol{\omega} \times \tilde{\mathbf{r}})] dm \tag{3.12}$$

where $\tilde{\mathbf{M}}_{\mathbf{cm}}$ is the pseudo external moment about the vehicle's centre of mass [Nm] and $\mathbf{M}_{\mathbf{cm}}$ is the sum of external moments about the vehicle's centre of mass [Nm]. These two moments are again equal because the Coriolis and relative moment are equal to zero. The first term on the right-hand side of equation (3.12) is the apparent moment due to the angular acceleration of the body with respect to the Earth fixed reference frame and the second term is the apparent moment due to the angular velocity of the body with respect to the Earth fixed reference frame.

Solving the equation of the rational motion stated in equation (3.12), can be expressed in the components along the body axes. The resulting set of non-linear equations are the Euler equations. This set of equations describes the rotational motion of the vehicle with respect to the body fixed reference frame.

Thus, the vehicle moves with respect to the Earth rotating reference frame. The vehicle has a constant mass, located at $\mathbf{r}_{\mathbf{cm}}$ from the Earth's centre of mass. The spaceplane moves with a velocity $\mathbf{V}_{\mathbf{R}}$ with respect to the Earth's reference frame, with an angular velocity $\boldsymbol{\omega}$ with respect to the inertial reference frame and is subjected to external forces $\mathbf{F}_{\mathbf{R}}$ and moments $\tilde{\mathbf{M}}_{\mathbf{cm}}$. The rational motion of this vehicle can be described through the Euler equations, defined as:

$$\dot{\boldsymbol{\omega}} = \mathbf{I}^{-1} \left(\tilde{\mathbf{M}}_{\mathbf{cm}} - \boldsymbol{\omega} \times \mathbf{I}\boldsymbol{\omega} \right) \tag{3.13}$$

with,

$$\mathbf{I} = \begin{bmatrix} I_{xx} & -I_{xy} & -I_{xz} \\ -I_{yx} & I_{yy} & -I_{yz} \\ -I_{zx} & -I_{zy} & I_{zz} \end{bmatrix} \tag{3.14}$$

being a symmetric matrix that contains the products of inertia of the vehicle. The sum of external moments about the centre of mass is expressed in $\tilde{\mathbf{M}}_{\mathbf{cm}} = (M_x, M_y, M_z)^T$. The $\boldsymbol{\omega} = (p, q, r)^T$, represents the angular rotation vector of the body fixed reference frame with respect to the inertial frame. The Euler equations can be written showing the relation between the $\dot{p}, \dot{q}, \dot{r}$ on p, q, r and the inertia moments and products.

Assuming that the body is rotational symmetric in mass, the Euler equations can be simplified because the products of inertia are zero, i.e., $\mathbf{I} = \text{diag}\,[I_{xx},\ I_{yy},\ I_{zz}]$. This assumption is valid for our reference vehicle since the products of inertia are much smaller than the moments of inertia. Thus, the rotational equations of motion become:

$$\dot{p} = \frac{M_x}{I_{xx}} + \frac{I_{yy} - I_{zz}}{I_{xx}} qr \tag{3.15}$$

$$\dot{q} = \frac{M_y}{I_{yy}} + \frac{I_{zz} - I_{xx}}{I_{yy}} pr \tag{3.16}$$

$$\text{and } \dot{r} = \frac{M_z}{I_{zz}} + \frac{I_{xx} - I_{yy}}{I_{zz}} qp \tag{3.17}$$

From here on, equation (3.6) till (3.8) represent the translational motion in spherical components in the rational Earth fixed reference frame. For the rotational motion, the Euler equations are used, describing the orientation and its evolution in time of the vehicle. These steps result in equation (3.15) till (3.17), which describe the rotational motion in aerodynamic angles, and roll, pitch, yaw rate with respect to the body fixed reference frame. These equations are essential for the linearisation and the definition of the state-space model, which is necessary for the control system design and stability and controllability analyses. The state-space model is provided in the next section.

3.3. State-space form

The equations of motion are derived based on the reference frames in the previous section. These equations describe the motion of the spaceplane and therefore connect the aerodynamic forces and moments with the velocity and angular rates. The stability of a vehicle can be analysed by studying these equations of motion. The characteristic motion of a vehicle can be determined by evaluating the eigenvalues and eigenvectors of state-space form.

However, the eigenvalues and eigenvectors can only be obtained when the time derivatives of the states are given as linear combinations of the states. Thus, the non-linear equations of motion derived in the previous section have to be linearised. By linearising and discretising the equations of motion, the overall system is transformed into a sequence of so-called linear time-invariant (LTI) systems. The linearised equations of motion describe the cation of the state variables as function of the parameters that influence the system, i.e., state variables and control variables. These equations are generally written in matrix form, which is known as the state-space form equations. Before deriving the formulas for the control algorithm, the assumptions that are used to determine the state-space equations need to be discussed.

- The Earth will be considered to be non-rotating ($\omega_{cb} = 0$ rad/s), which is allowed since the angular velocity of the Earth's atmosphere is negligible compared to the velocity of the spaceplane. Whereby, the Coriolis and centrifugal accelerations are zero as well.
- The atmospheric winds will not be implemented in the equations of motion.
- The HORUS-2B is mass symmetrical in body fixed x and y plane. Which means that the inertia (I_{xy} and I_{yz}) is equal to zero. Another related assumption is that the I_{xz} is approximately equal to zero, because the vehicle is rotationally mass symmetric around the x-axis of the body-fixed frame. This assumption is also valid for the modified spaceplanes.
- A spherical Earth is assumed.

The first assumption is valid because the rotational rate of Earth is much smaller than the rotational rate of the vehicle. The second assumption can be justified, since the products of inertia are much smaller than the moments of inertia. With these assumptions the equations for χ, τ and δ are decoupled from the other equations, so the linearised equation of motion in state-space form can be defined by 9 equations for V, γ, R, p, q, r, α, β and σ. For the linearisation procedure of the non-linear equations of motion, the derivation is derived by Mooij [1998]. The resulting simplified and linearised equations are stated in equation (3.18) through (3.26),

$$\Delta\dot{V} = -\frac{\Delta D}{m} + 2\frac{g_0}{R_0}\sin\gamma_0\Delta R - g_0\cos\gamma_0\Delta\gamma \tag{3.18}$$

$$\begin{aligned}\Delta\dot{\gamma} = &\left(-\dot{\gamma}_0 + \frac{2V_0}{R_0}\cos\gamma_0\right)\frac{\Delta V}{V_0} + \left(\frac{2g_0}{R_0} - \frac{V_0^2}{R_0^2}\right)\frac{\cos\gamma_0}{V_0}\Delta R - \left(\frac{V_0^2}{R_0} - g_0\right)\frac{\sin\gamma_0}{V_0}\Delta\gamma + \\ &- \frac{L_0}{mV_0}\sin\sigma_0\Delta\sigma + \frac{\cos\sigma_0}{mV_0}\Delta L - \frac{\sin\sigma_0}{mV_0}\Delta S\end{aligned} \tag{3.19}$$

$$\Delta\dot{R} = \sin\gamma_0\Delta V + V_0\cos\gamma_0\Delta\gamma \tag{3.20}$$

$$\Delta\dot{p} = \frac{\Delta M_x}{I_{xx}} \tag{3.21}$$

$$\Delta\dot{q} = \frac{\Delta M_y}{I_{yy}} \tag{3.22}$$

$$\Delta\dot{r} = \frac{\Delta M_z}{I_{zz}} \tag{3.23}$$

$$\begin{aligned}\Delta\dot{\alpha} = &\Delta q - \frac{1}{mV_0}\Delta L - \frac{g_0}{V_0}\cos\gamma_0\sin\sigma_0\Delta\sigma + \left(\frac{L_0}{mV_0^2} - \frac{g_0}{V_0^2}\cos\gamma_0\cos\sigma_0\right)\Delta V + \\ &- \frac{g_0}{V_0}\sin\gamma_0\cos\sigma_0\Delta\gamma - \frac{2g_0}{R_0V_0}\cos\gamma_0\cos\sigma_0\Delta R\end{aligned} \tag{3.24}$$

$$\Delta\dot{\beta} = \sin\alpha_0\Delta p - \cos\alpha_0\Delta r - \frac{\Delta S}{mV_0} - \frac{g_0}{V_0}\cos\gamma_0\cos\sigma_0\Delta\sigma + \frac{g_0}{V_0^2}\cos\gamma_0\sin\sigma_0\Delta V + \\ + \frac{2g_0}{R_0V_0}\cos\gamma_0\sin\sigma_0\Delta R + \frac{g_0}{V_0}\sin\gamma_0\sin\sigma_0\Delta\gamma \tag{3.25}$$

$$\text{and } \Delta\dot{\sigma} = -\cos\alpha_0\Delta p - \sin\alpha_0\Delta r - \left(\frac{L_0}{mV_0} - \frac{g_0}{V_0}\cos\gamma_0\cos\sigma_0\right)\Delta\beta + \frac{L_0}{mV_0}\sin\sigma_0\Delta\gamma + \\ + \frac{\tan\gamma_0}{mV_0}\left(\sin\sigma_0\Delta L + \cos\sigma_0 L_0\Delta\sigma + \cos\sigma_0\Delta S - \frac{L_0}{V_0}\sin\sigma_0\Delta V\right) \tag{3.26}$$

The initial states of $V, \gamma, R, \alpha, \beta$ and σ are known. But, the initial states for the body roll, pitch and yaw rate (p_0, q_0 and r_0) are not known yet. However, the relations can be determined from the equilibrium angular rates, because for the nominal control no perturbations are desired. Resulting in the following equations:

$$p_0 = \frac{g_0}{V_0}\cos\gamma_0\sin\sigma_0\sin\alpha_0 + \frac{L_0}{mV_0}\tan\gamma_0\sin\sigma_0\cos\alpha_0 \tag{3.27}$$

$$q_0 = \frac{L_0}{mV_0} - \frac{g_0}{V_0}\cos\gamma_0\cos\sigma_0 \tag{3.28}$$

$$\text{and } r_0 = -\frac{g_0}{V_0}\cos\gamma_0\sin\sigma_0\cos\alpha_0 + \frac{L_0}{mV_0}\tan\gamma_0\sin\sigma_0\sin\alpha_0 \tag{3.29}$$

These equations of motion can be written in state-space form ($\dot{\mathbf{x}} = \mathbf{Ax} + \mathbf{Bu}$). Whereby the $\mathbf{x}$ is the state vector and $\mathbf{u}$ the control vector, and $\mathbf{A}$ and $\mathbf{B}$ the system and the control coefficient matrix. Before obtaining the final system and control coefficient matrix, the force and moment variations need to be evaluated. For example, the change in drag force can be expressed as dependencies of the drag forces (stated in equation (3.30)). Whereby the smaller contributions can be neglected, resulting in equation (3.31). For these derivatives it is also assumed that higher order derivatives are negligible. These relations describing the forces and moments in most relevant dependencies are fully explained by Mooij [1998],

$$\Delta D = \frac{\partial D}{\partial M}\Delta M + \frac{\partial D}{\partial\alpha}\Delta\alpha + \frac{\partial D}{\partial h}\Delta h + \frac{\partial D}{\partial\delta_e}\Delta\delta_e + \frac{\partial D}{\partial\delta_a}\Delta\delta_a + \frac{\partial D}{\partial\delta_r}\Delta\delta_r + \frac{\partial D}{\partial\delta_b}\Delta\delta_b \tag{3.30}$$

$$\text{Rewritten to, } \Delta D = \frac{\partial D}{\partial M}\Delta M + \frac{\partial D}{\partial\alpha}\Delta\alpha. \tag{3.31}$$

The full state-space description is stated below. All the full expressions of a_{ij} and b_{ik} terms are represented in Appendix A. The reason why the body flap deflection is not visible in the equations is because the body flap is only used for trim, so it has a nominal deflection angle ($\Delta\delta_b = 0$),

$$\begin{pmatrix}\Delta\dot{V}\\ \Delta\dot{\gamma}\\ \Delta\dot{R}\\ \Delta\dot{p}\\ \Delta\dot{q}\\ \Delta\dot{r}\\ \Delta\dot{\alpha}\\ \Delta\dot{\beta}\\ \Delta\dot{\sigma}\end{pmatrix} = \begin{bmatrix} a_{VV} & a_{V\gamma} & a_{VR} & 0 & 0 & 0 & a_{V\alpha} & 0 & 0\\ a_{\gamma V} & a_{\gamma\gamma} & a_{\gamma R} & 0 & 0 & 0 & a_{\gamma\alpha} & a_{\gamma\beta} & a_{\gamma\sigma}\\ a_{RV} & a_{R\gamma} & 0 & 0 & 0 & 0 & 0 & 0 & 0\\ 0 & 0 & 0 & 0 & 0 & 0 & 0 & a_{\rho\beta} & 0\\ a_{qV} & 0 & 0 & 0 & 0 & 0 & a_{q\alpha} & 0 & 0\\ 0 & 0 & 0 & 0 & 0 & 0 & 0 & a_{r\beta} & 0\\ a_{\alpha V} & a_{\alpha\gamma} & a_{\alpha R} & 0 & a_{\alpha q} & 0 & a_{\alpha\alpha} & 0 & a_{\alpha\sigma}\\ a_{\beta V} & a_{\beta\gamma} & a_{\beta R} & a_{\beta p} & 0 & a_{\beta r} & 0 & a_{\beta\beta} & a_{\beta\sigma}\\ a_{\sigma V} & a_{\sigma\gamma} & 0 & a_{\sigma p} & 0 & a_{\sigma r} & a_{\sigma\alpha} & a_{\sigma\beta} & a_{\sigma\sigma}\end{bmatrix}\begin{pmatrix}\Delta V\\ \Delta\gamma\\ \Delta R\\ \Delta p\\ \Delta q\\ \Delta r\\ \Delta\alpha\\ \Delta\beta\\ \Delta\sigma\end{pmatrix} \\ + \begin{bmatrix} 0 & 0 & 0 & 0 & 0 & 0\\ 0 & 0 & 0 & 0 & 0 & 0\\ 0 & 0 & 0 & 0 & 0 & 0\\ 0 & b_{pa} & 0 & b_{px} & 0 & 0\\ b_{qe} & 0 & 0 & 0 & b_{qy} & 0\\ 0 & b_{ra} & b_{rr} & 0 & 0 & b_{rz}\\ 0 & 0 & 0 & 0 & 0 & 0\\ 0 & 0 & 0 & 0 & 0 & 0\\ 0 & 0 & 0 & 0 & 0 & 0\end{bmatrix}\begin{pmatrix}\Delta\delta_e\\ \Delta\delta_a\\ \Delta\delta_r\\ \Delta T_x\\ \Delta T_y\\ \Delta T_z\end{pmatrix}. \tag{3.32}$$

Overall the state-space form describes the equations of motion of the spaceplane, with respect to the defined reference frames and is thereby the plant of the control system. With this representation the motion and aerodynamic forces due to the shape and deflection surfaces are related to each other.

3.4. Stability

With the explained vehicle dynamics, the static and dynamic stability can be discussed. The static stability depends only on the aerodynamic most relevant derivatives and the dynamic stability can be analysed by investigating the eigenvalues and eigenvectors of the vehicle dynamics and therefore the flight modes.

3.4.1. Stability and controllability coefficients

There are several aerodynamic derivatives that indicate the static stability/instability of the vehicle. The most relevant are already used in the state-space form stated above. In these derivatives, the C_D, C_L and C_S represent the drag, lift and sideslip coefficients. The C_l, C_m and C_n indicate the roll, pitch and yaw moment coefficients. And, the δ_a, δ_e and δ_r are the deflection angles for the ailerons, elevons and rudder.

- The coefficients only dependent on the base vehicle:
  $C_{D_M} = \frac{\partial C_D}{\partial M}$, $C_{D_\alpha} = \frac{\partial C_D}{\partial \alpha}$, $C_{S_\beta} = \frac{\partial C_S}{\partial \beta}$, $C_{L_M} = \frac{\partial C_L}{\partial M}$, $C_{L_\alpha} = \frac{\partial C_L}{\partial \alpha}$, $C_{l_\beta} = \frac{\partial C_l}{\partial \beta}$ and $C_{n_\beta} = \frac{\partial C_n}{\partial \beta}$.
- The coefficients based on the base of the vehicle combined with the body flap and the elevons deflections:
  $C_{m_M} = \frac{\partial C_m}{\partial M}$ and $C_{m_\alpha} = \frac{\partial C_m}{\partial \alpha}$.
- The coefficient based on only the elevons deflection:
  $C_{l_{\delta_a}} = \frac{\partial C_l}{\partial \delta_a}$, $C_{m_{\delta_e}} = \frac{\partial C_m}{\partial \delta_e}$ and $C_{n_{\delta_a}} = \frac{\partial C_n}{\partial \delta_a}$.
- The coefficients based on the rudder deflection:
  $C_{n_{\delta_r}} = \frac{\partial C_n}{\partial \delta_r}$.

The first bullet point shows the stability indicators of the base part of the spaceplane. The second bullet point is a combination of the base, the body flap and the elevons and is therefore a combination of a stability and controllability derivative. The body flap and elevon are set to the trim condition. The last two bullet points are the control derivatives which indicate the effectiveness of the attitude deflection surfaces. Each implemented derivative in the state-space form will be chronologically explained below:

C_{D_M} This derivative is the drag coefficient depending on the Mach number. Because there is no rotation between the body fixed reference frame and the aerodynamic reference, the X-force is aligned with the drag force. The sign will be positive because an increment in velocity will lead to more drag force.

C_{D_α} This coefficient deals with the effect of the angle-of-attack on the drag coefficient (which is along the X-axis of the aerodynamic reference frame). A change in angle-of-attack is obtained by varying the velocity direction in the aerodynamic simulation, and the X, Y and Z-forces will be converted to the drag, side and lift force by equation (3.1.3). An increase in angle-of-attack will lead to an increase in the drag coefficient, thus the sign of this derivative is positive.

C_{S_β} The derivative C_{S_β} shows the effect of the side force with respect to the angle-of-sideslip. An increase sideslip angle causes an increase in the side force and the coefficient is negative because of the definition of the reference frames. Similar as the α variation, the sideslip angle will be simulated by changing the direction of the velocity vector with the use of equation (3.2) till (3.4).

C_{L_M} This is the lift coefficient effected by the Mach number. In this case, because there is no rotation between the body fixed reference frame and aerodynamic reference frame, the lift force is aligned with the Z-force of the body fixed frame. The lift force is perpendicular to the flow direction. The sign of the coefficient depends on the geometry. At zero angle-of-attack the sign is negative for the HORUS. Therefore a positive angle-of-attack is required to create lift.

C_{L_α} This coefficient indicates the effect of the angle-of-attack on the lift coefficient. The sign of this coefficient is positive with a positive angle-of-attack until stall occurs. At the moment of stall the lift force decreases rapidly with increasing angle-of-attack.

C_{l_β} This is a moment coefficient around the X-axis (roll moment) of the body fixed reference frame. The coefficient deals with the roll moment due to change of variation in the angle-of-sideslip. For static stability, a negative sign for this coefficient is preferred, because in that case the sideslip generates an opposite moment. This means that the spaceplane wants to rotate back towards zero degree sideslip angle after a disturbance in angle-of-sideslip. The largest contributions to the C_{l_β} are the dihedral and sweep angle of the wing, and the wing-fuselage interaction with the flow. This coefficient is one of the primary lateral stability derivatives.

C_{n_β} The C_{n_β} coefficient is the moment about the Z-axis of the body fixed reference frame due to a change in the angle-of-sideslip. Also known as the static directional or weathercock suitability derivative. This derivative is another important stability indication parameter, and is preferred to be positive. A positive value indicates that there is a moment created for non-zero sideslip angle that wants to rotate back towards zero degrees. Hence, there is a resistance against the yaw rotation.

C_{m_M} This derivative is the pitch moment due to the change in Mach number. The moment is around the Y-axis of the body fixed reference frame. The pitch moment should increase with increasing Mach number because the forces are increased by the increasing Mach number. As already explained above, this derivative is a contribution of the main body, body flap and elevons. These flaps are set at the trim condition.

C_{m_α} The C_{m_α} is one of the most important stability coefficients, as it expresses the pitch moment (which is the moment around the Y-axis of the body fixed reference frame) influenced by the angle-of-attack. If stability is not achieved for this parameter, an increase in pitch moment would increase the angle-of-attack and this process would be repeated until stall occurs, because the lift force is not in equilibrium with the gravity force anymore. Thus, the condition $C_{m_\alpha} < 0$ is very important. This can be achieved by placing the aerodynamic centre behind (negative x-axis) the centre of mass. The aerodynamic centre is the position where the lift force will not produce a moment around the y-axis. Hereby, the increase in angle-of-attack, will have a moment balancing the lift force. Thus, for longitudinal static stability the derivative needs to be negative.

$C_{l_{\delta_a}}$ This is the roll moment due to the aileron deflection angle. Hence, the effectiveness of the aileron. The function of the aileron is to create an additional moment around the X-axis of the body fixed reference frame. In this reference frame the coefficient is negative and changing for different Mach numbers because of the change in the lift force.

$C_{m_{\delta_e}}$ With symmetrical moving the left and right flaps, i.e. elevons, are creating an additional pitch moment. This derivative describes the pitch moment due to the elevon deflection angle and is negative based on the reference frame. According to [Cucinelii and Müller, 1988] the effectiveness increases with decreasing Mach number in the supersonic flight regime.

$C_{n_{\delta_a}}$ This derivative is the aileron (asymmetrically moving of the left and right flaps) effectiveness on the yaw moment . The sign is negative based on the defined axis.

$C_{n_{\delta_r}}$ The $C_{n_{\delta_r}}$ is the effectiveness of the rudders. The primary task of the rudder is to create an additional yaw moment . An increase in rudder deflection angle will increase the yaw moment and therefore the sign is positive.

$C_{m_{\delta_b}}$ Lastly, the pitch moment due to the body flap deflection. This derivative is not in the state-space form because this is included in the pitch moment effected by the angle-of-attack. In the TAEM phase of the re-entry the body flap is set to -20 degrees for trim purposes. The sign of the derivative is negative.

3.4.2. Dynamic stability

Next, the dynamic stability can be investigated by analysing the flight modes. The modes of motion of a hypersonic spaceplane are similar to those of a subsonic aircraft, presented by [Etkin and Reid, 1996], with one additional flight mode because of the hypersonic flight regime. By using the $\dot{\mathbf{x}} = \mathbf{A}\mathbf{x}$ without the $\mathbf{B}$ matrix (control part) the flight modes can be investigated, which is called the open-loop behaviour. The longitudinal modes are the short-period and phugoid mode (which is long period). For hypersonic flight another longitudinal long-period mode, called height mode is added. For the lateral directions there are the lateral oscillation (or Dutch roll), the rolling convergence and the spiral mode. For these modes a general description of each mode of motion is provided:

- Phugoid (longer period) oscillations: Performing the phugoid manoeuvre large amplitude variations in the velocity, pitch angle, altitude, but almost no angle-of-attack variation. The manoeuvre is a slow interchange of kinetic energy and potential energy about an equilibrium energy level, as the spaceplane attempts to re-establish the level flight condition from which it has been disturbed.
- Short period oscillations: The short period oscillations mode is basically the shorter period version of the longer period oscillations. The motion is a rapid pitching movement about the centre of gravity of the spaceplane which is essentially an angle-of-attack variation. Whereby the motion becomes heavily damped in a short period of time. The initial HORUS-2B design has two aperiod modes at a Mach number below 3 and a bank angle of 55 degrees of which one of them is unstable according to [Mooij, 1998].
- Height mode: The height mode is a lightly damped aperiodic motion in which the altitude is changed. This mode is relevant from Mach 3 and higher. It includes drag changes by means of variations in the speed and altitude. This is different compared to the phugoid mode because the phugoid mode is mainly dependent on altitude variations.
- Lateral oscillation: The lateral oscillation mode is based on a strong roll rate and yaw rate of the spaceplane. The roll rate does not effect the motion that much. For this mode the velocity and flight path angle have almost constant values. As already known, this mode is unstable for the initial HORUS design due to the lack in yaw motion capabilities. But for the TAEM phase of the re-entry this is very important to steer the vehicle to the right location.
- Aperiodic roll motion: For the roll manoeuvre there are two versions: a fast and a slow one which both have the bank angle as main contributor to the motion. Hence, the motion is a pure rotation around the X-axis of the aerodynamic reference frame. The motion is aperiodoc because it is only dependent on one moment.
- Spiral mode: This mode consists mainly of the yawing motion and has almost a zero sideslip angle. This mode is a slow motion that is aperiodic and is present mostly when flying with a non-zero bank angle.

All the flying qualities are valued by the response characteristics. Which consist of the damping ratio, halving time and natural frequency or the eigenvectors as explained in the next section. These modes can be conducted at certain points along the trajectory to have different flight conditions.

3.5. Response Characterisation

The response characteristics of the state-space form can be valued by eigenvectors. The different response outputs are represented in Figure 3.5. As can been seen in the figure, if the eigenvalue has a positive real part, the the solution becomes unstable. The imaginary part results in more oscillation behaviour, and is therefore less desired. If the eigenvalue is located on the imaginary axis, the response will not increase nor decrease [D'Souza, 1988]. Another representation is expressing the eigenvalues with an angle and magnitude,

$$z = \sqrt{Re(\lambda)^2 + \mathrm{Im}(\lambda)^2}, \tag{3.33}$$

$$\text{and } \theta = \arctan\left(\frac{\mathrm{Im}(\lambda)}{\mathrm{Re}(\lambda)}\right). \tag{3.34}$$

The eigenmotions can also be characterized by the following parameters: the period (P), halving time ($T_{1/2}$), doubling time (T_2), damping ratio (ζ) and the natural frequency (ω_n). The period indicates what the period is of the output frequency response and is represented in equation (3.35). The half time gives a time interval when the amplitude of the motion has become half its original value (equation (3.36)). If the halving time has a positive real part, the halving time becomes negative. Therefore, the formula changes to the doubling time equation of the diverging motion (equation (3.37)). The damping ratio is an important indication of dynamic stability. If the ζ is positive the eigenmotion is damped. If the ζ is not defined (because the real part is zero) the motion is aperiodic. The formula for the damping ratio is expressed in equation (3.38). Furthermore, as can be seen in equation (3.5), if the eigenvalue has an imaginary part there is a frequency in the signal, this natural frequency can be calculated with equation (3.39),

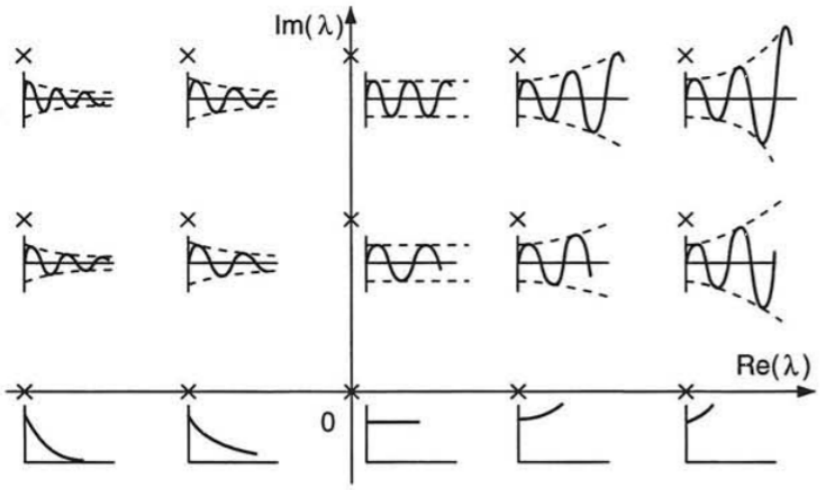

Figure 3.5: Impulse responses for various eigenvalues with different real and imaginary part [D'Souza, 1988].

$$P = \frac{2\pi}{\mathrm{Im}(\lambda)} = \frac{2\pi}{\omega_n\sqrt{1-\zeta^2}}, \tag{3.35}$$

$$T_{1/2} = \frac{\ln 1/2}{\mathrm{Re}(\lambda)}, \tag{3.36}$$

$$T_2 = \frac{\ln 2}{\mathrm{Re}(\lambda)}, \tag{3.37}$$

$$\zeta = -\frac{\mathrm{Re}(\lambda)}{\sqrt{\mathrm{Re}(\lambda)^2 + \mathrm{Im}(\lambda)^2}}, \tag{3.38}$$

$$\text{and } \omega_n = \sqrt{\mathrm{Re}(\lambda)^2 + \mathrm{Im}(\lambda)^2}. \tag{3.39}$$

3.6. Military requirements

By Viavattene and Mooij [2019], flight manoeuvres/modes are preformed and investigated by comparing them with military specifications. Because the flying qualities of aircraft were very important for the U.S. military, multiple studies were conducted. By MIL-F-8785C [1980], the qualities are presented for subsonic aircraft and the report was later adapted and extended because of the development of more advanced aircraft technology. Thus, a more complete version was published in [MIL-HDBK-1797, 1997]. The MIL-spec requirements are considered as a starting point for identifying the flying qualities of the spaceplanes. These requirements differ depending on the vehicle type and flight phase category. Aircraft are classified in four groups depending on size, weight and manoeuvrability. Group three consists of large, heavy, low-to-medium manoeuvrability aircraft which presents characteristics that are similar to those of vehicles flying in the high-supersonic and hypersonic regime. So, the flying characteristics of group three aircraft will be used.

There are different levels of flying qualities in the MIL-requirements. The levels of flying qualities are stated by MIL-HDBK-1797 [1997] and presented here:

Level 1: The flying qualities clearly adequate for the mission flight phase.

Level 2: Flying qualities adequate to accomplish the mission flight phase, but some increase in pilot workload or degradation in mission effectiveness, or both, exists.

Level 3: Flying qualities such that the aircraft can be controlled safely, but pilot workload is excessive or mission effectiveness is inadequate, or both. However, Category B flight phases can be completed. Which is defined as: "non-terminal flight phases that are normally accomplished using gradual manoeuvres and without precision tracking, although accurate flight-path control may be required".

Table 3.1: Phugoid damping requirements [MIL-HDBK-1797, 1997].

Phugoid	
Level 1	$\zeta_{ph} \geq 0.04$
Level 2	$\zeta_{ph} \geq 0$
Level 3	$T_{2_{ph}} \geq 55s$

Table 3.2: Short period damping ratio limits [MIL-HDBK-1797, 1997].

Short period	
Level 1	$0.30 \leq \zeta_{sp} \leq 4.00$
Level 2	$0.20 \leq \zeta_{sp} \leq 2.00$
Level 3	$0.15 \leq \zeta_{sp}$ [1]

Table 3.3: Lateral oscillation requirements with undamped natural frequency ω_{n_d} and damping ratio ζ_{n_d} [MIL-HDBK-1797, 1997].

Lateral Oscillation			
	Min. ζ_{n_d}	Min. $\zeta_{n_d}\omega_{n_d}$ [rad/s]	Min. ω_{n_d} [rad/s] [2]
Level 1	0.08	0.15	0.4
Level 2	0.02	0.05	0.4
Level 3	0	Not specified	0.4

An aircraft must be designed to satisfy the level 1 requirements when all the systems operate normally. The probability of failure of the system is related to the probability of degradation of the flying quality levels. The MIL-requirements establish this criteria by defining level 2 and level 3 which corresponds with failure less than 10^{-2} and 10^{-4} respectively in operating flight envelope. In service envelope, the probability of failure should be less than 10^{-2} for level 3. When the aircraft meets the MIL-requirements, the aircraft provides a suitable control effort to stabilise and control the vehicle.

3.6.1. Longitudinal requirements

In MIL-F-8785C [1980] and MIL-HDBK-1797 [1997] the flying quality requirements for the longitudinal direction are presented. As mentioned before, the phugoid is a long-period airspeed oscillation that is experienced when there is a sudden disturbance during a stable airspeed flight. The requirement for the phugoid damping ratio or the doubling time of the amplitude is presented in Table 3.1. The time to halve the amplitude is an important parameter and is already defined in equation (3.36), but can be rewritten as:

$$T_{1/2_{ph}} = \frac{\ln \frac{1}{2}}{-\zeta_{ph}\omega_{n_{ph}}}. \tag{3.40}$$

When the damping ratio is negative, the eigenmotion is amplified and the equation changes to the doubling time presented in equation (3.37).

The short period mode requirements are also defined and these are presented in Table 3.2. To have adequate flight performance, the short period oscillation has more strict requirements compared to the long longitudinal oscillation. The necessary damping ratio for this flight mode is higher, resulting in higher damped oscillation.

3.6.2. Lateral requirements

MIL-F-8785C [1980] and MIL-HDBK-1797 [1997] also specify the lateral requirements for adequate flying quality. One of the lateral direction modes is the lateral oscillation, as explained above. The MIL-requirements for the lateral oscillation can be expressed by the undamped natural frequency ω_{n_d}, the damping ratio ζ_{n_d} and their product. The values are presented in Table 3.3.

From this point all the flight mechanics features are discussed. This involved the derivation of the equations of motion, linearisation of these equations and creating the state-space form. This system lead to the

[1] The limit can be reduced for altitude higher than 6.1 km.
[2] This requirement (and defined levels) may not be valid for class three.

static and dynamic stability of the spaceplane. The importance of static stability which is defined by the aerodynamic characteristic parameters and the investigation of the flight modes was shown. The different flight modes which represents the eigenmotion of the vehicle, lead to the analysis of the eigenvalues and eigenvectors. For the dynamic motion there are military requirements which give reference values for a stable and controlled flight.

The control analysis initiated one important subject of this research namely: the aerodynamics. To conduct this control analysis the aerodynamic behaviour of the spaceplane needs to be determined. For each spaceplane the relevant aerodynamic parameters are required to complete the dynamic stability analyses.

4

Aerodynamics

The stability and control of any flying vehicle are determined indirectly by the airflow around the vehicle, i.e., aerodynamics. How the flow behaves in different Mach regimes is very important because it influences the shape. This chapter begins with explaining the assumptions related to the medium which is atmospheric air. Secondly, the analytical formulation of fluid dynamics will be expressed. Followed by simplification assumptions which are required to derive the flow field in an efficient manner. Next, the mathematical relations in combination with different flow phenomena will be discussed. Then, because the analytical formulation is limited for complex fluid dynamics, the conversion is made to numerical simulation. This will be the start of showing flow behaviour, simulation establishment and accuracy of an example CFD object. The importance of mesh generation in combination with fluid models and discretisation schemes is highly relevant and will be explained in detail. Lastly, these features of CFD simulation will be applied to the complex HORUS spaceplane.

4.1. Assumptions and validity

The aerodynamics described in this chapter rely on a number of assumptions. The assumptions will also be noted when appropriate in this chapter, but in this section the most important assumptions will be stated:

No chemical reactions The flow will not be chemically reactive. By Dobrov et al. [2021], the influence of chemical reactions are simulated by ANSYS Fluent and studied. The chemical reactions influence the aerodynamic results and are highly relevant in the region of the shock layer. The effects become more important with increasing Mach number in the hypersonic regime. In the TAEM phase of the re-entry these effects can be neglected.

Flow is a continuum The flow is assumed to be a continuum. A continuum flow can be treated as continuous, even though, on a microscopic scale, they are composed of molecules. With the continuum assumptions, the macroscopic properties such as density, pressure and temperature are assumed to be defined at infinitesimal volume. This assumption is related to the Knudsen number Kn, which is a dimensionless number that defines the ratio of the molecular mean free path length to the representative physical length scale. (The length scale in this case is the length of the spaceplane.) For $Kn < 0.01$ continuum flow can be assumed. If the number increases, the regime will change to slip flow, transitional flow and free-molecular flow. The assumption is true for altitudes lower than 75 km [Brykina et al., 2009]. Because the TAEM phase is lower than 25 km this assumption is true, but in the beginning of the hypersonic re-entry this assumption is invalid. The equation for the Knudsen number is stated here,

$$Kn = \frac{k_B T}{\sqrt{2}\pi d^2 p L} \tag{4.1}$$

with k_B the Boltzmann constant, T the thermodynamic temperature, d the particle hard-shell diameter, p the total pressure and L the representative length scale.

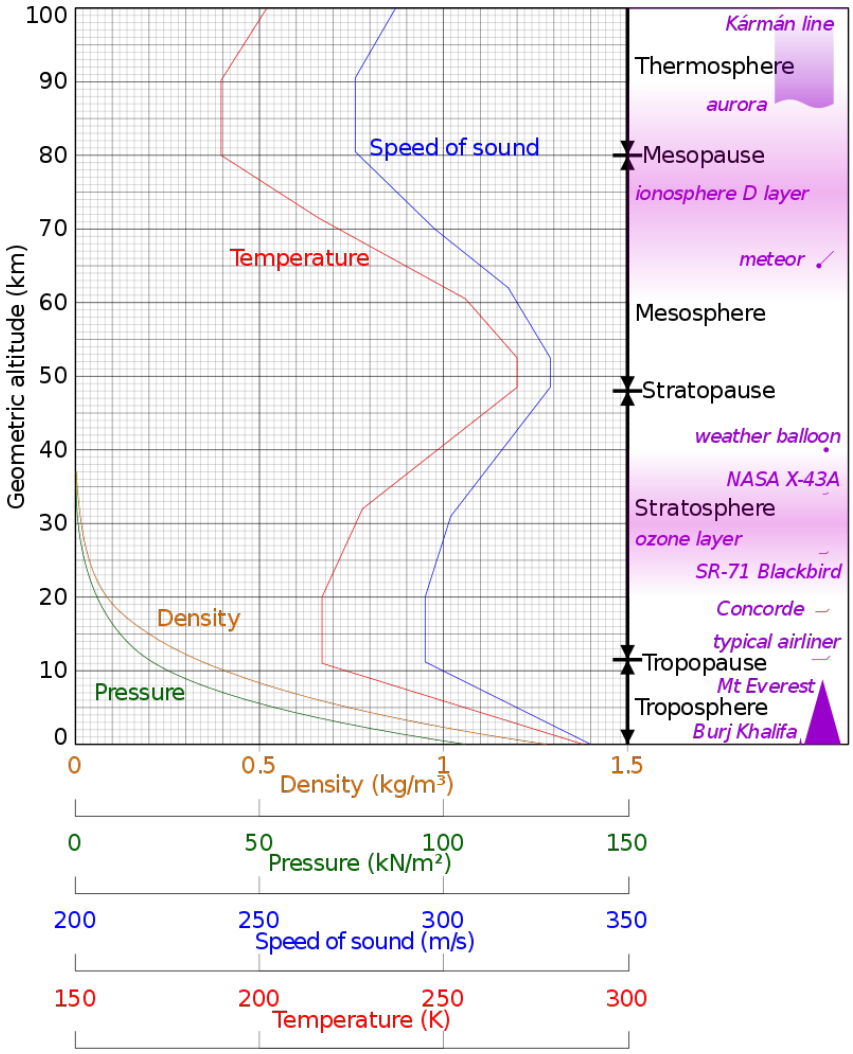

Figure 4.1: The U.S. Standard atmosphere model of 1976 [NASA, 1976].

Atmospheric properties For the atmospheric properties the U.S. standard atmosphere of 1976 is used. The ambient pressure, density, temperature and speed of sound are defined by that model. For the CFD model the same values will be used. The values of the ambient properties are visualised against the altitude in Figure 4.1. The corresponding properties along the re-entry trajectory are stated in Table 4.1. These discrete points with their ambient conditions will be used for the simulations.

Ideal gas The ideal gas law assumes that the medium behaves as a perfect gas. This means that the gas particles interact elastically when they collide [White, 1974]. To check the validity of this assumption, a graphical method is visualised in Figure 4.2. When the compressibility factor (Z) is approximately equal to 1 the ideal gas assumption is valid. If Z is higher then 1, oxygen dissociation, nitrogen dissociation and ionization occur. The ideal gas law is defined as: $p = \rho RT$, with pressure p, density ρ, gas constant R and temperature T.

To determine the compressibility factor, the pressure reduction factor ($p_r = p_t/p_c$) and temperature reduction factor ($T_r = T_t/T_c$) need to be determined (the subscript letter t stands for the total quantity which is the sum of the dynamic and static values). The critical pressure and temperature for air are 132.2 K and 3.688×10^6 Pa, respectively. The total pressure and temperature during flight are in the order of 1.8×10^6 Pa and 650 K by using the NASA simulation calculators[1]. Resulting in a $p_r = 0.48$ and $p_r = 4.9$, which leads to a Z value of approximately 1. Thus, the ideal gas law is valid.

[1]NASA AtmosModeler Simulator, website: https://www.grc.nasa.gov/www/k-12/airplane/atmosi.html, accessed on 05/03/2021.

Table 4.1: Atmospheric conditions along the re-entry trajectory.

M [-]	h [m]	P [Pa]	T [K]
25	75000	2.06792	206.650
20	70000	4.63422	217.650
15	60000	20.3143	245.450
10	53000	51.8668	265.050
7.5	48000	97.7545	270.650
5.0	38000	365.455	245.450

M [-]	h [m]	P [Pa]	T [K]
2.5	25000	2511.02	221.650
2.0	22500	3699.54	219.150
1.5	20000	5474.89	216.650
1.2	18000	7504.84	216.650
1.0	16000	10287.5	216.650
0.8	13000	16510.4	216.650

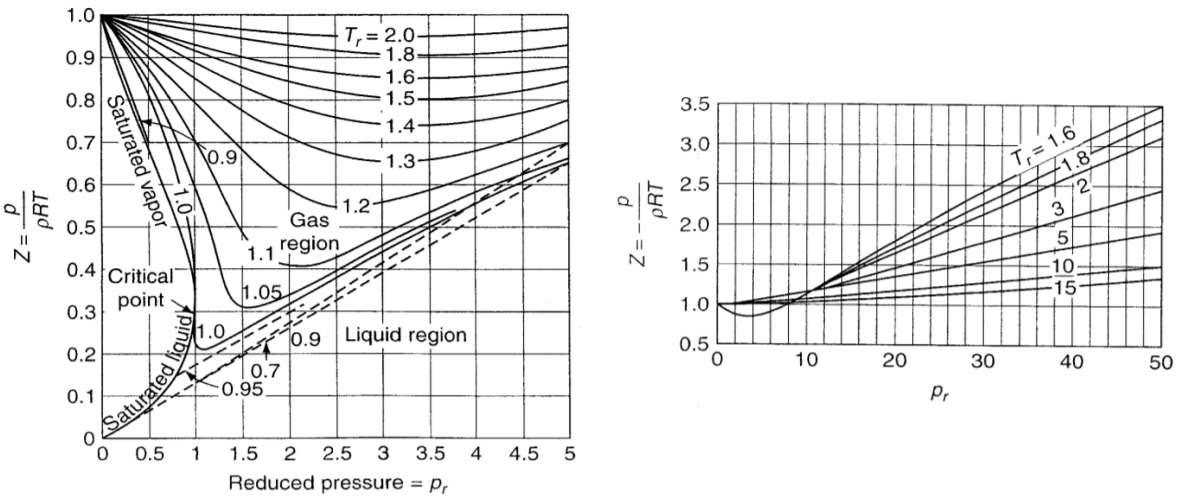

Figure 4.2: Compressibility factor for gasses left graph for the low reduced pressure range ($0 \geq p_r \geq 5$) and right graph the high range ($0 \geq p_r \geq 50$) [White, 1974].

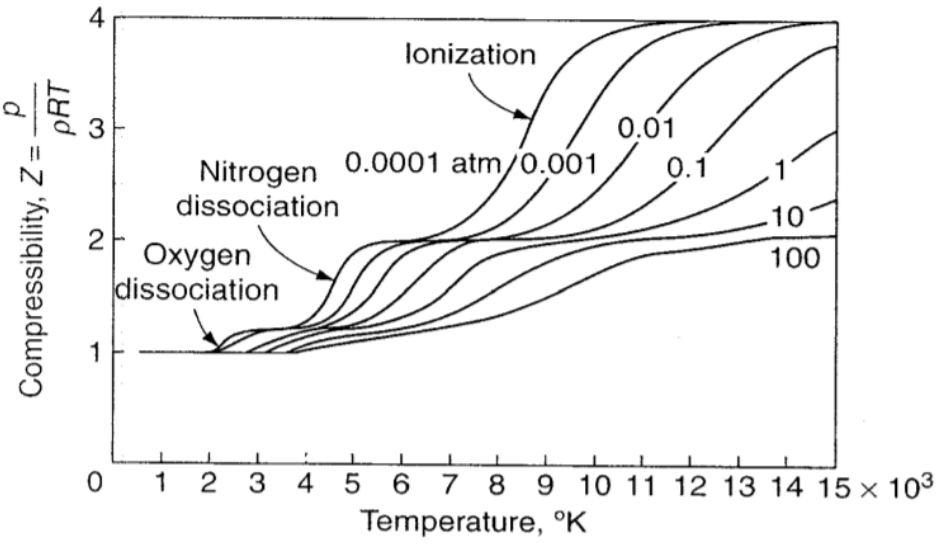

Figure 4.3: The compressibility factor due to dissociation and ionization of air [White, 1974].

In the hypersonic regime, the ideal gas law is no longer valid, because the amount of energy driving chemical reactions is significant [Filippone, 2006]. In this regime dislocation and ionization occur because the temperatures become extremely high. For the chemical components in atmospheric air the dislocation and ionization and their influence on the compressibility factor as a function of temperature are visualised in Figure 4.3.

4.2. Governing equations

The field of fluid dynamics is described by three conservation equations: conservation of mass, conservation of momentum and conservation of energy. These equations are derived and stated in the book Kundu et al. [2016], or in any other fluid dynamics book for that matter. These governing equations are vector differential equations, and are still analytical unsolvable, unless the problem is extremely simplified. Therefore, a numerical approach is required to solve the flow field for most general cases. However, the calculation time needed to solve the flow field exceeds present computing capabilities. To perform these simulations in a reasonable time frame, it is necessary to simplify the governing equations.

The equation of mass conservation for fluid flows, also known as continuity equation, is expressed in equation (4.2). The first term represents the time rate of change of the fluid density. The second term is a flux divergence term, also called a transport term. The equation indicates that the result of mass flow changes is equal to zero, i.e. conservation,

$$\frac{\partial \rho}{\partial t} + \frac{\partial}{\partial x_i}(\rho u_i) = 0 \tag{4.2}$$

The Navier-Stokes (NS) vector equation describes the conservation of momentum for a Newtonian fluid and is expressed in equation (4.3). In essence, the NS momentum equation is a form of Newton's second law ($F = m \cdot a$). The term on the left-hand side indicates the change in momentum. The first term on the right-hand side of the equation indicates the change of pressure over the distance of the volume. The second term is the change of momentum due to the gravity. The last term is the change of momentum due to the deformations in the fluid. Whereby the δ_{ij} is the Kronecker delta, which is equal to 1 if $i = j$ and equal to 0 if $i \neq j$. The μ and μ_s are the dynamic viscosity and bulk viscosity respectively.

$$\rho\left(\frac{\partial u_j}{\partial t} + u_i\frac{\partial u_j}{\partial x_i}\right) = -\frac{\partial p}{\partial x_j} + \rho g_j + \frac{\partial}{\partial x_i}\left[\mu\left(\frac{\partial u_j}{\partial x_i} + \frac{\partial u_i}{\partial x_j}\right) + \left(\mu_s - \frac{2}{3}\mu\right)\frac{\partial u_m}{\partial x_m}\delta_{ij}\right] \tag{4.3}$$

The last equation, the energy conservation law is stated in equation (4.4). This equation is derived from the first law of thermodynamics. Which states that the change in energy of a system equals the work put into the system minus the heat lost by the system. The term on the left-hand side is the change in time of internal energy per unit of mass. The first term on the right-hand side is the contribution of the pressure change to the energy change of the system. The second and third term indicate the dissipation of energy due to viscous stresses. The last term expresses the heat flow into or out of the system. In the equation e, S_{ij} and k represent the internal energy, strain rate tensor and fluid's thermal conductivity.

$$\rho\frac{De}{Dt} = -p\frac{\partial u_m}{\partial x_m} + 2\mu\left(S_{ij} - \frac{1}{3}\frac{\partial u_m}{\partial x_m}\delta_{ij}\right)^2 + \mu_v\left(\frac{\partial u_m}{\partial x_m}\right)^2 + \frac{\partial}{\partial x_i}\left(k\frac{\partial T}{\partial x_i}\right) \tag{4.4}$$

These field equations and thermodynamic equations provide: 1 + 3 + 3 = 7 scalar equations. The dependent variables in these equations are ρ, e, p, T, and u_j, a total of 1 + 1 + 1 + 1 + 3 = 7 unknowns. The number of equations is equal to the number of unknown field variables; therefore, solutions are in principle possible for suitable boundary conditions.

4.3. Euler equations

Because solving the full governing equations is too time consuming, the equations are simplified. If the viscous effects are negligible, which is commonly true in exterior flows away from solid boundaries, the equations are simplified to the Euler equations [Kundu et al., 2016]. The mass conservation law in equation (4.2), can be rewritten with the use of the material derivative expressed in equation (4.5) and the mathematical rule stated in equation (4.6). Furthermore, the mass equation has no viscous terms and therefore stays as it is.

$$\frac{D\rho}{Dt} \equiv \frac{\partial \rho}{\partial t} + u_i\frac{\partial \rho}{\partial x_i} \tag{4.5}$$

$$\text{and } \frac{\partial(\rho u_i)}{\partial x_i} = \frac{u_i\partial\rho}{\partial x_i} + \frac{\rho\partial u_i}{\partial x_i} \tag{4.6}$$

The momentum equation displayed in equation (4.3), has one major viscous term, the one between square brackets. The term will be equal to zero and disappears from the equation. Finally, the energy equation from equation (4.4), also has viscous terms. The second and the third term will be equal to zero. The inviscid assumption leads to the Euler equations stated in equation (4.7) till (4.9). Instead of using the index-based notation, the Euler equations are presented with the more recognizable bold vector notation,

$$\frac{D\rho}{Dt} = -\rho\nabla \cdot \mathbf{u} \tag{4.7}$$

$$\frac{D\mathbf{u}}{Dt} = -\nabla\left(\frac{p}{\rho}\right) + \mathbf{g} \tag{4.8}$$

$$\text{and } \rho\frac{De}{Dt} = -p\nabla \cdot \mathbf{u} + \nabla \cdot (k\nabla T) \tag{4.9}$$

As already stated above, these equations are accurate for non-viscous flows, which is flow far away from the solid boundaries. However, these equations also become appropriate for high-Reynolds-number applications, where inertial forces tend to dominate the viscous forces. Since this is the case for high-speed aerodynamic analysis like this one, the Euler equations become applicable. Here, the pressure forces on the body will dominate the viscous forces. Hence, an inviscid analysis will give a quick estimate of the primary forces acting on the body [ANSYS, 2009]. After the body shape has been modified to optimize the flying qualities, another more accurate viscous analysis can be performed to include the effects of the fluid viscosity and turbulent viscosity on the lift, drag and side forces. Such a more accurate simulation model, which includes viscous effect, is possible with the Spalart-Allmaras model. This is applicable for low-Reynolds-number flows and is very useful for aerospace applications. However, more advanced models will not be discussed further, due to the simulation time considerations. The inviscid approach is also a must because of the complicated vehicle geometry, because for these simulations the numerical solver has difficulties converging and the inviscid model is sometimes the only way to get the calculation started. However, the viscous effects in the boundary layers result in an unavoidable error.

4.4. Flow regimes

To give a better understanding of the flow types that are involved while re-entering the Earth's atmosphere, the different flow regimes will be explained. Not only the subsonic, transonic and supersonic regimes will be discussed, but also the hypersonic regime because of sub-research question 3. The shape may not deteriorate the flying qualities such that the spaceplane becomes unstable and uncontrollable in the beginning of the re-entry.

4.4.1. Subsonic flow

The subsonic flow regime itself is divided into two parts, the incompressible and compressible flow. The incompressible flow is much easier to work with due to the disappearing density derivative from the governing equations. It disappers because for incompressible flow, the density is constant in time and space. The incompressible condition is only applicable up to a Mach number of 0.3. Above Mach 0.3 the flow is generally considered compressible, which means that the fluid density changes throughout the flow. The upper limit of the subsonic flow is approximately Mach 0.8. The major difference between subsonic flow and other flow regimes is the absence of discontinuities in the form of shocks. Because the flow velocity is lower than the speed of sound, disturbances propagate in all directions. In the case of incompressible flow this would happen at the same velocity in all directions, while for compressible flow the velocities would be different.

If the viscosity effects are neglected, the flow is also isentropic, or an adiabatic reversible process. Adiabatic means that there is no heat added or distracted from the surroundings into the process. The only heat source that can occur is heat due to friction from the fluid flow itself. However, because the flow is inviscid there is no friction and therefore it is an adiabatic process. A reversible process is a process in which the entropy does not increase, which means that in an enclosed system with adiabatic walls the direction of the process can be reversed after any change of state. In subsonic flow there are no non-isentropic shockwaves and because there is no entropy production trough friction, the flow is reversible.

Thus, in inviscid subsonic flow the flow is also isentropic. Thus, the isentropic flow equations can be used to relate different quantities throughout the flow. In equation (4.10), the ratio between static and total pressure is expressed as a function of Mach and specific heat ratio. Similarly, the ratio for temperature and density are expressed in equation (4.11) and (4.12),

$$\frac{p}{p_t} = \left(1 + \frac{\gamma - 1}{2} M^2\right)^{\frac{-\gamma}{\gamma - 1}} \tag{4.10}$$

$$\frac{T}{T_t} = \left(1 + \frac{\gamma - 1}{2} M^2\right)^{-1} \tag{4.11}$$

$$\text{and } \frac{\rho}{\rho_t} = \left(1 + \frac{\gamma - 1}{2} M^2\right)^{\frac{-1}{\gamma - 1}} \tag{4.12}$$

Because in the subsonic flow regime the Reynolds number (due to the decrease in velocity) is lower, the accuracy of CFD results with the use of the Euler inviscid method becomes less. The viscous forces located in the boundary layer will be neglected, resulting in a deviation. To visualise these effects an aerodynamic simulation of the flow around a sphere is performed. By Loth et al. [2021], the drag coefficient of a sphere is determined by different means such as experimental wind tunnel tests and CFD simulations. This data will be used as comparison and validation of the CFD model settings.

A steady compressible CFD model is made of a sphere with similar flow conditions as the reference data [Loth et al., 2021]. To reduce the computation time, the mesh structure has been carefully handled. Instead of making a three dimensional sphere, a two dimensional semicircle geometry is used. Combined with the axis symmetric flow assumption, this converts to a sphere. The only difference is that the number of mesh elements is significantly reduced, allowing flow simulation with more advanced fluid models, discretisation schemes and posting more mesh elements in important flow regions. The mesh density is higher closer to the cylinder and lower in outer regions. These improvements increase the computation time, but also the accuracy of the results. Shortly, these settings make the simulation efficiently and as accurately as the computational capabilities allow.

The inlet, outlet and upper boundaries are placed 5, 15 and 7 times the diameter of the sphere away of the sphere (visually displayed in Figure 4.4). Therefore, the boundaries have a negligible influence on the flow. The solver is density-based, which will be explained in more detail later in this chapter in Section 4.5. The mesh quality is sufficient to use more advanced and accurate turbulence models by checking the y^+ value. The y^+ is a dimensionless number, which defines the number of mesh elements close to the wall boundary. The definition of y plus is stated in equation (4.13). Where the y is the absolute distance from the wall, the u_τ the friction velocity and the ν kinematic viscosity. The physical interpretation of this formula is that, if the value is satisfied, there are enough mesh elements inside the viscous dominant boundary layer for the fluid model to determine flow properties accurately. The required y^+ differs for different fluid models. Furthermore, the flow is assumed to be an ideal gas as explained in Section 4.1,

$$y^+ = \frac{y u_\tau}{\nu} \tag{4.13}$$

In Figure 4.4, the dynamic pressure of a Mach 0.5 flow around the sphere is visualised. In this figure, and all other sphere flow visualization figures, the flow moves from the left to the right side. In front of the sphere there is a stagnation point and therefore the velocity is low and the stagnation pressure is high. Between 45 and 95 degrees of the sphere a boundary layer starts to arise where the flow velocity and dynamics are increasing. At the back, flow separation occurs, which has low dynamic pressure and velocity flow properties. When the Mach number increases, and therefore also the flow velocity, the wake increases. This behaviour is typical for subsonic flow.

In Figure 4.5, the drag coefficient is plotted for different Reynolds numbers at a constant Mach number of 0.5 [Loth et al., 2021]. The line shows the numerical behaviour and the icons indicate different experiments as validation. In Figure 4.6 a similar presentation is used for Mach 0.8. The Reynolds number equation is stated in equation (4.14), and is defined by the velocity u, diameter D, density ρ and dynamic viscosity μ. Or rewritten towards the kinematic viscosity ν, with the use of the density and dynamic viscosity relation. The Reynolds number from the simulation at different Mach numbers of 0.5 and 0.83 is roughly equal to $5.8{\times}10^5$ and $9.6{\times}10^5$ respectively. The corresponding drag coefficients from the figures are 0.5 and for

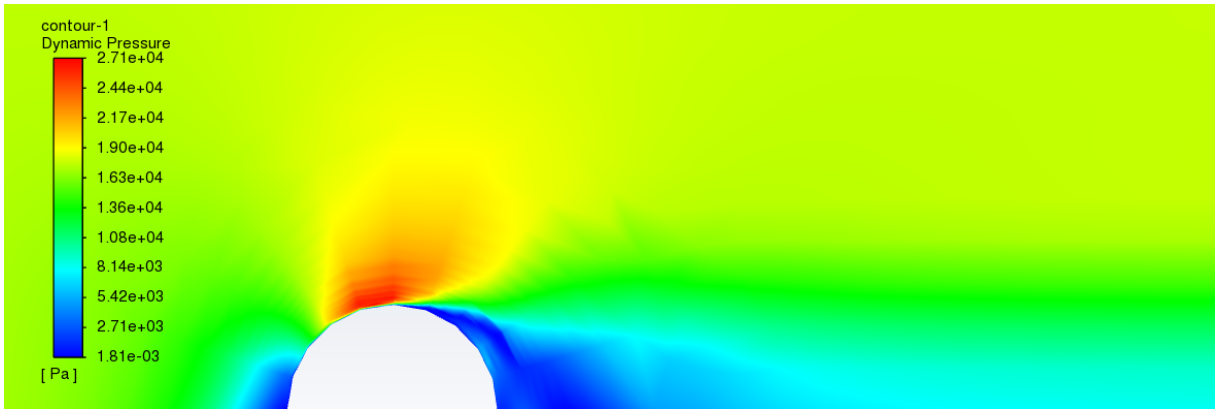

Figure 4.4: Flow around a sphere at Mach 0.5 and Reynolds number of $6{\times}10^5$.

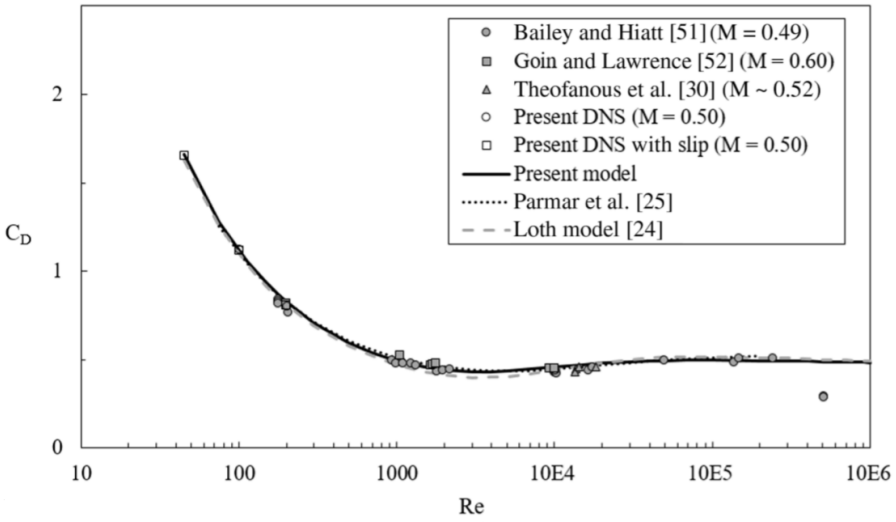

Figure 4.5: Drag coefficient of a sphere for different Reynolds numbers at Mach ~0.5 [Loth et al., 2021].

Mach 0.83 slightly higher approximately 0.75. In Table 4.2 the simulation results for different fluid models can be found. The inviscid method has for both Mach numbers a lower estimation of the drag coefficient because it neglects the viscous drag. The error is within the 30%, which is the requirement of this research. The turbulence model k-omega has a better estimation of the drag coefficient, but still a deviation of 0.1 (and slightly better accuracy), a more dense mesh and advanced model gives a better estimation of the drag coefficient as expected,

$$Re = \frac{uD\rho}{\mu} = \frac{uD}{\nu} \tag{4.14}$$

4.4.2. Transonic flow

The transonic regime is the transition between the subsonic and supersonic flow. The range of the transonic regime is approximately in between Mach 0.8 and 1.2. The flow is characterised by partly subsonic flow and in other areas supersonic flow. This means that the shock associated with the supersonic flow will occur somewhere on the body because locally along the body the Mach number will be higher than 1 [Mooij, 2015]. This causes the formation of subsonic and supersonic pockets, leading to large pressure gradients. This phenomenon causes an increase in drag. At the regions where the Mach number is lower than 1, there is parasitic drag. For the regions where the Mach number is higher than 1, shock waves start to occur. The parasitic drag which is driven by the shape, is dependent on viscosity. Whereas the wave drag due to the shock waves is independent on viscosity. The shock wave patterns are strongly dependent on the state of the boundary layer [Liepmann, 1946]. For instance a change from laminar to turbulent boundary layer at

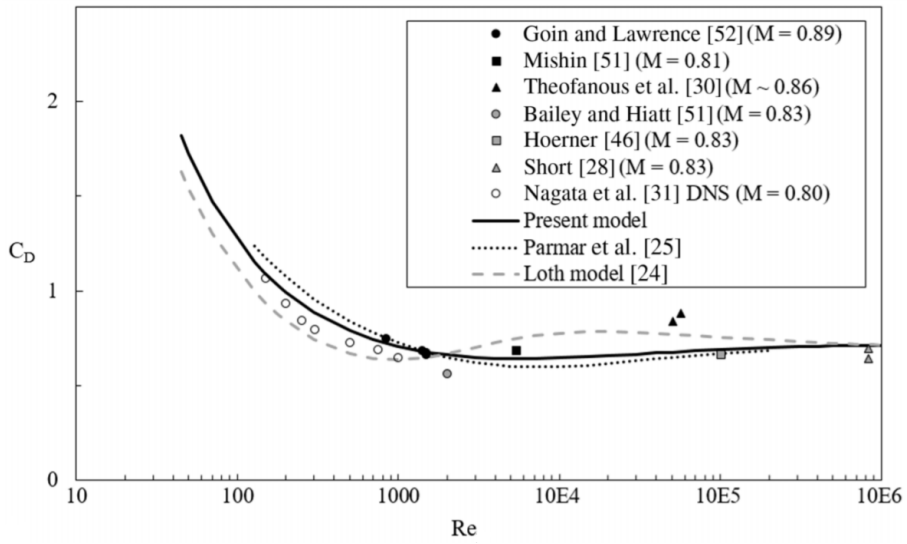

Figure 4.6: Drag coefficient of a sphere for different Reynolds numbers at Mach ~0.83 [Loth et al., 2021].

Table 4.2: Drag coefficient results of subsonic CFD simulations around a sphere.

Fluid model	**discretisation scheme**	**Number of mesh elements [#]**	**Reynolds [-]**	**Mach [-]**	**Maximum y^+ [-]**	**Drag coefficient [-]**
Inviscid	Second order upwind	15526	N.D.[2]	0.5	N.D.	0.43
Standard k-omega	Second order upwind	15526	577372	0.5	0.047	0.47
Inviscid	Second order upwind	15526	N.D.	0.83	N.D.	0.55
Standard k-omega	Second order upwind	15526	957957	0.83	0.038	0.65

the same free stream Mach number, changes the flow pattern and pressure distribution considerably. The shockwaves can interact with the boundary layer in a similar manner as in a reflection of the shock wave from a free surface. In contrast with the boundary layers of the subsonic flow, the pressure gradient normal to the boundary layer is of the same order as the pressure gradient parallel to the boundary layer.

The transonic flow is difficult to simulate because of the formation of these pockets. An automatic mesh refinement is added to the CFD sphere simulation. This refinement checks the Mach gradient in between the mesh elements while iterating the governing equations. At every 50 iterations the mesh will be refined in areas where the gradient exceeds 0.05 Mach. Hereby, the mesh elements located in the shock wave, which have similar mesh density as the free stream flow, will be refined. This increases the accuracy of the results because the flow properties are determined more refined. A visualisation example of such a mesh element refinement can be seen in Figure 4.7. This refinement feature contributes to the efficiency and accuracy of the CFD simulations.

The sonic condition (Mach equal to 1) is simulated. Even with the use of the automatic mesh refinement, converging the governing equations is difficult. A step by step approach is required to get converging results. Starting with the first order discretisation scheme and followed by a second order discretisation scheme, this gives a better start solution for the more advanced scheme. And similarly from the inviscid model towards a turbulent model. The Reynolds number for these conditions is equal to 1.3×10^6, which is just outside of the graph presented in Figure 4.8. However, the regression seems to behave linear for a higher Reynolds number. The corresponding drag coefficient for Mach 1 is approximately 0.8 based on Loth et al. [2021]. The inviscid method, with a second order upwind discretisation scheme, resulted in a simulated drag coefficient of 0.77 (error of 3.75%). This result is well within the required accuracy demands, the reason for the accuracy

[2]N.D. is short for not defined. The Reynolds number and y-plus are not defined because there is no viscosity (dividing by zero).

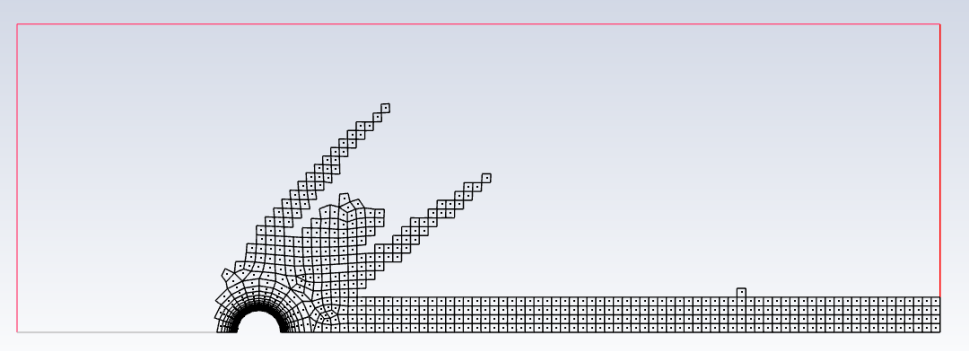

Figure 4.7: Visualisation example of the automatic mesh refinement. The mesh elements that are exceeding a Mach gradient of 0.05 are shown.

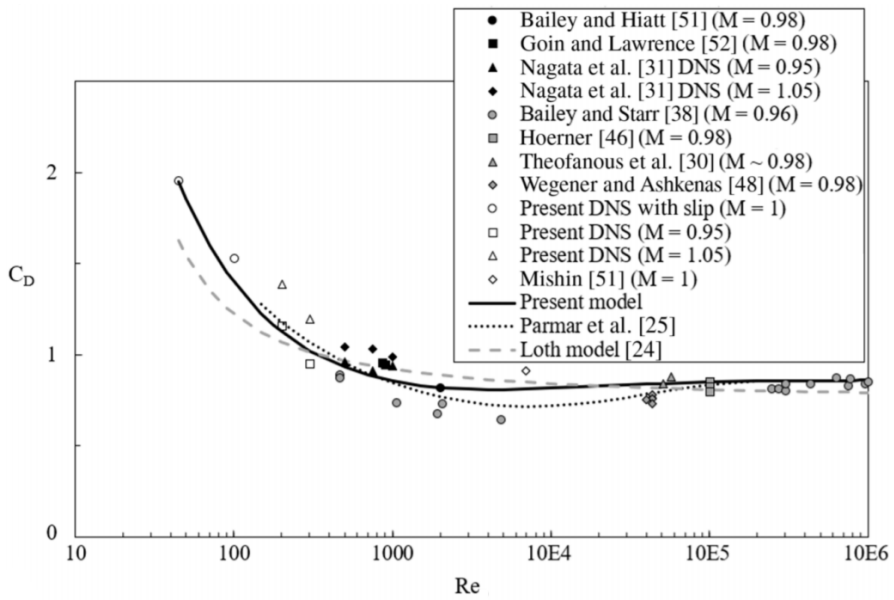

Figure 4.8: Drag coefficient of a sphere for different Reynolds numbers at Mach ~1 [Loth et al., 2021].

improvement compared to Mach 0.5 is that the Reynolds number is slightly increased and the model has an adapted and more advanced mesh (higher density mesh). The standard k-omega, with second order upwind scheme fluid model resulted in approximately 0.80. The accuracy in the drag coefficients becomes closer with more advanced fluid models.

4.4.3. Supersonic flow

In the supersonic flow regime, the Mach waves combine and create a so called shock wave. This occurs when the velocity of the flow is higher than the velocity of sound. The supersonic flow regime is from Mach 1.2 until Mach 5, at Mach 5 the flow becomes hypersonic. Flow across the shock wave strongly differs in fluid properties. In the supersonic flow regime the flow is irreversible and thereby not isentropic due to these shock waves. The shock wave will arise from the leading edge of the sphere and the shock will be detached. If the shock wave is perpendicular to the flow direction, the shock wave is called normal shock wave. If there is an inclination angle with respect to the upstream flow, the shock is called an oblique shock wave. Such a bow shock wave is also clearly visible in the CFD simulation of the sphere. In Figure 4.9, the dynamic pressure is visualised for a flow of Mach 3. For the oblique bow shock the following fluid property equations are derived by Kundu et al. [2016],

$$M_2^2 = \frac{(\gamma - 1)M_1^2 + 2}{2\gamma M_1^2 - (\gamma - 1)} \tag{4.15}$$

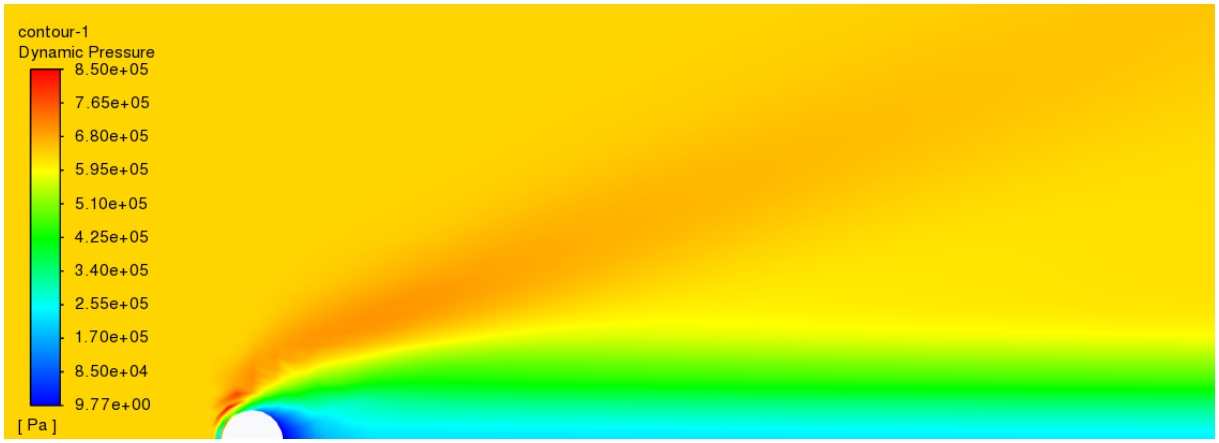

Figure 4.9: Flow around a sphere at Mach 3 and Reynolds number of 3.5×10^6.

$$\frac{p_1}{p_0} = \frac{2\gamma M_1^2 - (\gamma - 1)}{\gamma + 1} \tag{4.16}$$

$$\frac{T_1}{T_0} = \frac{\left[2\gamma M_1^2 - (\gamma - 1)\right]\left[(\gamma - 1)M_1^2 + 2\right]}{(\gamma + 1)^2 M_1^2} \tag{4.17}$$

$$\text{and } \frac{\rho_1}{\rho_0} = \frac{(\gamma + 1)M_1^2}{(\gamma - 1)M_1^2 + 2} \tag{4.18}$$

The sphere CFD simulation in between Mach 1.5 and 2 had a slight over estimation of the drag coefficient. This is due to the converging issues, similar as in the transonic regime. If there is less convergence, the flow properties are less accurately determined, which interferes with the pressure distribution and therefore the drag coefficient. However, at Mach 3 and again a slightly higher Reynolds number, the inviscid method and the turbulent models both became more accurate. The drag coefficient is approximately 1 at this condition shown in Loth et al. [2021], and the simulated inviscid method had 0.99 whereas the k-omega had 1.05. Overall, with increasing Reynolds number the inertial force becomes more important than the viscous force. Still, the inviscid method is well within the accuracy demands of the model.

4.4.4. Hypersonic flow

For this research the subsonic till supersonic regime is the most important. However, because of research question 3., the flying qualities in the hypersonic regime also have to be satisfied after optimizing the flying qualities for the lower regimes. From the assumptions stated in Section 4.1, it became clear that hypersonic flow is difficult to simulate because the chemical reactions occur. In this regime the temperatures become extremely high leading to dissociation and ionization of the molecules (as shown in Figure 4.3). The hypersonic regime starts from Mach 5 until re-entry speeds Mach 25.

Because a real gas simulation requires too much research time, a simulation with the current settings is performed to see the deviation. For a Mach 10 simulation at altitude and therefore flow conditions along the re-entry trajectory of the HORUS, the converging process has difficulties. The discretisation scheme is lowered to a first order upwind scheme, the mesh elements are decreased and the automatic refinement is not initiated. For the inviscid method, after 5000 iterations the drag coefficient is equal to 1.0258. There are some mesh elements which have outliers in the flow properties which create difficulty for the solution to converge. These outliers can be seen in Figure 4.10 and create an error in the solution. To make the solution converge, a hypersonic solution steering option is required which starts initiation of the flow field with a hypersonic flow. This reduces the iteration number and results in a less deviated start solution. (More details about solution steering will be explained later in this chapter.) The more advanced CFD setting resulted in a converged drag coefficient of approximately 0.95 (Figure 4.11). (This results in an accuracy error of 12%.) Both simulations with or without enabling the solution steering setting result in the same outcome, the only difference is that less often divergence occurs and less computation power is required. The error between the literature and the simulated hypersonic results is overseeable, but the difficulty is the converging part

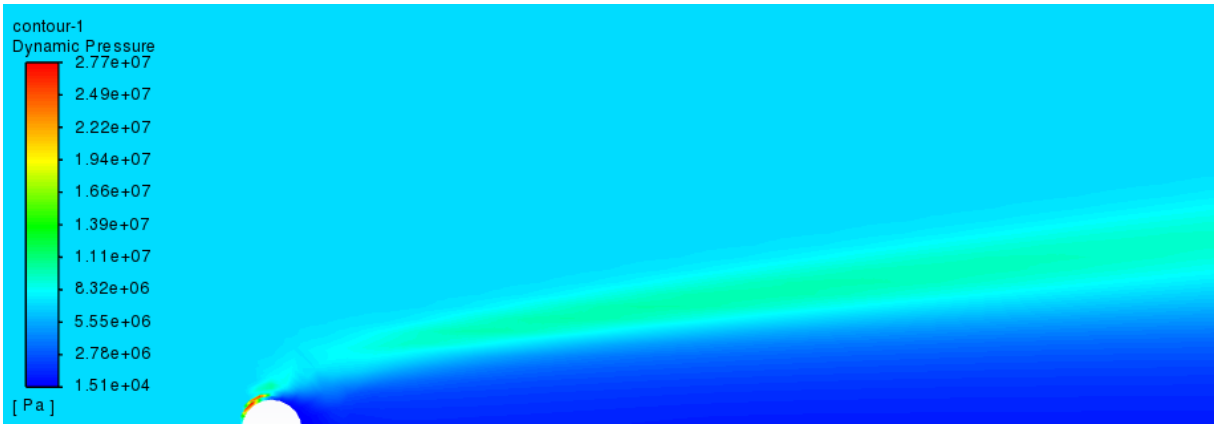

Figure 4.10: Flow around a sphere at Mach 10 and Reynolds number of 12.1×10^6.

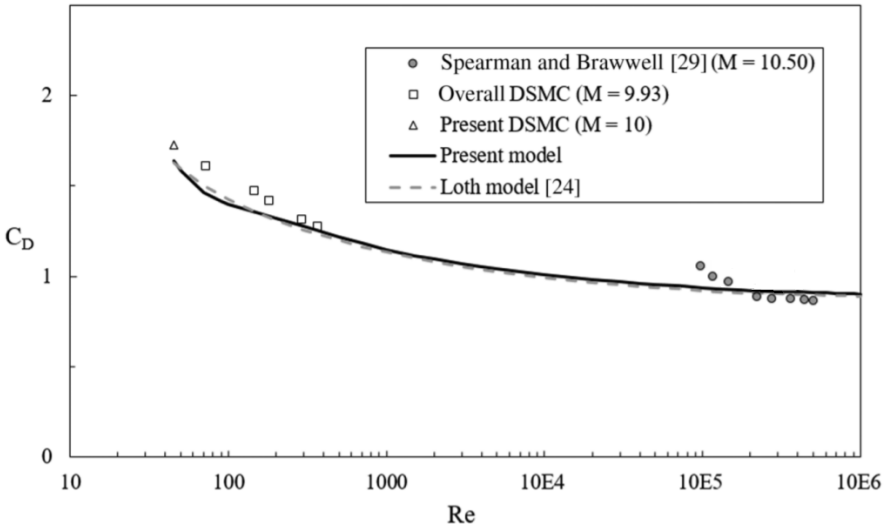

Figure 4.11: Drag coefficient of a sphere for different Reynolds numbers at Mach ~ 10 [Loth et al., 2021].

of the hypersonic simulation and this is even with a very simplistic geometry. Thus, creating accurate and converging hypersonic solutions for the complex three dimensional HORUS geometry will be challenging.

At this high Mach number, the flow separates at just upstream of 90 degrees and leads to a weak recompression shock at this location. At higher Mach numbers where the flow is hypersonic, the standoff shock becomes very close to the particle; it begins to interact with the boundary layer and to create a shock layer. Further downstream, a oblique shock with a very shallow angle forms while the flow separation shear layer becomes steadier, because it is more controlled by gas dynamics than turbulent instabilities. The result of this compressibility is a higher contribution of the pressure drag generally leading to a higher drag coefficient [Loth et al., 2021]. In Figure 4.12, the difference between supersonic flow and hypersonic flow is visualised, these results correspond to the flow fields features of the CFD simulations shown in Figure 4.9 for Mach 3 and Figure 4.10 for Mach 10. The shockwave becomes more narrow with increasing Mach number. In the figures it is also visible that the separation occurs further downstream.

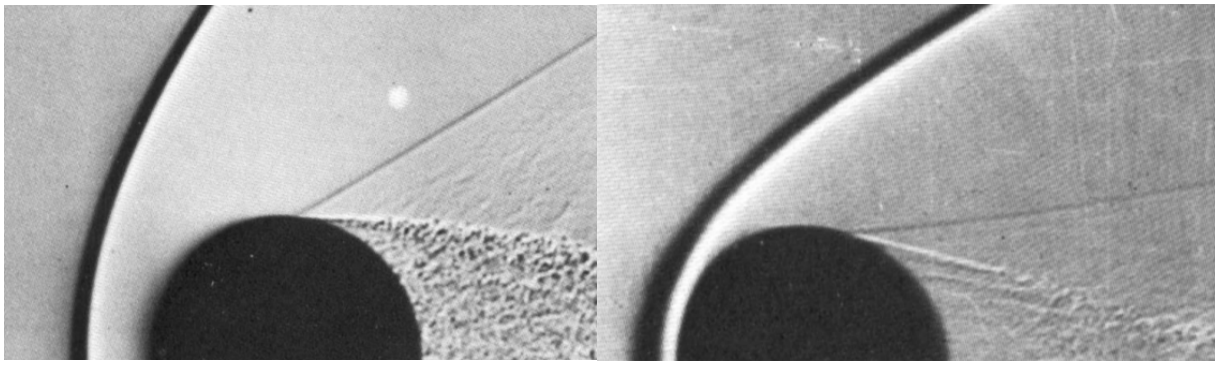

Figure 4.12: Shadowgraphs showing flow around spheres, the left figure is at supersonic conditions ($M \sim 2.5$), and the right figure hypersonic conditions ($M \sim 7.6$) [Loth et al., 2021].

4.5. HORUS simulation

From this point the flow assumptions, analytical formulation, flow regimes and numerical simulation are discussed and studied. In this section the simulation of the HORUS-2B will be performed. The section starts with the geometry, followed by the mesh generation and finally there are the CFD simulation settings.

4.5.1. Geometry

To satisfy the system requirements, the HORUS dimensions should correspond with the reference sketch of Figure 2.11. With the use of the program SolidWorks the HORUS-2B design is created, the solid body is presented in Figure 4.14 and the design drawing is shown in Figure 4.13. The most complex part of the design is the curvature of the wing, winglet and nosecone, and the intersection between the wing and the fuselage. Because the three dimensional contours require more dimensions to fully define the curves. Especially the creation of the winglet which has no clear reference coordinates due to the already three dimensional curved wing. The only straight part of the body is the fuselage until the start of the nosecone. That is why the creation of this complex body starts by making the fuselage. To create the smooth wing and winglet the choice is made to create them as one solid part, which leads to a smooth transition of curves between the wing and winglet. The intersection between the wing and the fuselage, more specifically the intersection between the wing and the nosecone, is challenging because the different parts are three dimensional curved and need to align perfectly. The program requests fully aligned pieces with no gaps to create a single solid body. A solution is found by making the parts overlap and trim the overlapping volume.

Thus, the starting point of the creation of the HORUS geometry is making the fuselage, which is referenced by the origin. Because the geometry is symmetrical in the XZ-plane of the body fixed reference frame, the choice is made to create only halve the body and use the mirroring feature to generate the whole body. This tool reduces the time required to design the HORUS spaceplane. Usually for simplifying the CFD simulation the boundary condition symmetry is used. Therefore, only half the body and mesh volume/elements is required leading to a significantly decrease in simulation time. Similarly, as the axis-symmetric function to simulate the sphere in the previous section. However, these features assume that the flow is plane-symmetric or axis-symmetric, and because the aerodynamic simulations require angle-of-attack and angle-of-sideslip variations this assumption does not hold. If only the longitudinal forces/moments were required, the plane-symmetric CFD function could be used and would simplify the problem significantly. The simulations could be separated into two models, whereby the longitudinal requires halve the mesh volume, but a separate creation of such an automatic model requires more time than the increase in simulation time.

After the creation of halve the fuselage, the nosecone is attached by creating a three dimensional design drawing which curved contours are approximately the same as in the reference sketch. The next part is the nose tip which is axis-symmetrical around the x-axis and is therefore pretty simple to design by a two dimensional sketch. The following part is the creation of the wing and winglet in one piece. To be able to do so, one design sketch is created with in total more than 150 elements, which consist of reference lines, design lines and curved three dimensional lines. These lines are all fully defined by dimensions and relation constraints between lines and nodes. This sketch is the most computational power demanding part of the design. With the function boundary boss/base the outer curvature lines are used to create a solid part. The final part that has to be created is the body flap which is mostly straight and easy to implement. For the

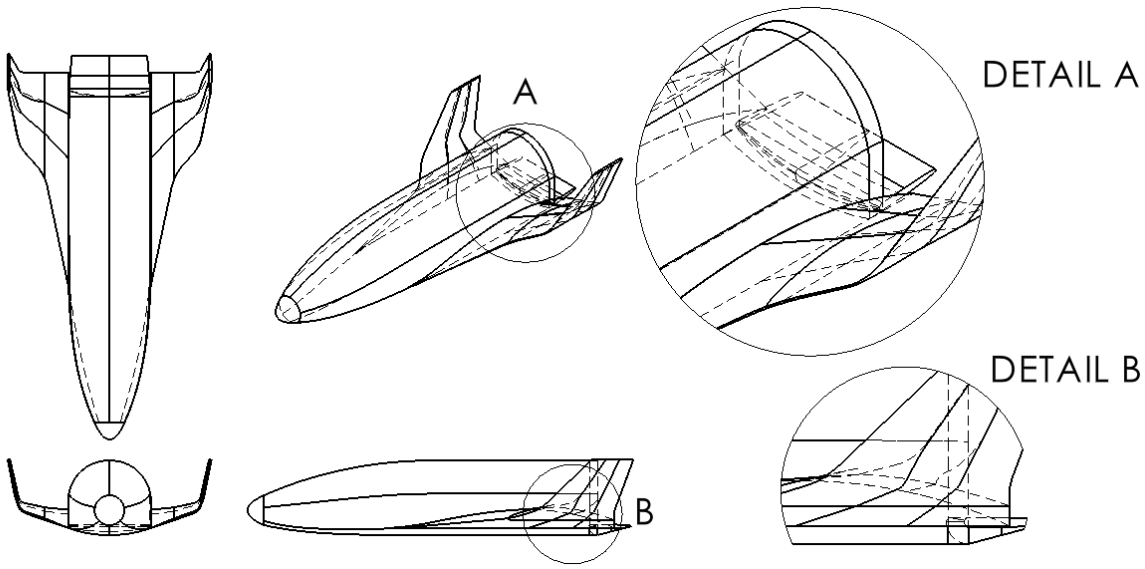

Figure 4.13: The HORUS-2B design drawing based on the reference sketch.

elevons and rudders, the bodies are cut out of the wing/winglet and are defined as a part on their own, to create a smooth overlap between these parts (similarly as the reference sketch). The parts have some additional volume in the area where the rotation-axis of the deflection surfaces are located, which makes sure that there is no gap when rotating. Overall, the creation of HORUS-2B geometry is almost identical as the reference sketch.

The HORUS generated body is subtracted from the fluid volume, because there is no investigation required of the stresses acting on the vehicle itself. This leads to a volume without the vehicle volume, which is basically the space where the fluid is flowing. At this point the volume and surfaces are named because they are identified as boundary conditions and type of volume (fluid/solid) later. One important aspect of defining the fluid volume is the size. There should be enough space in front and after the object related to the flow direction, because the flow initiation at the boundary conditions may not affect the flow field and therefore the aerodynamic forces. For the sphere simulation in the previous section, similar dimensions as the literature where used. For the HORUS simulations, the distance between the boundary conditions and the centre of the spaceplane is 30 meter upwards and sidewards (Z and Y-axis body fixed reference frame). In front of the spaceplane 40 meters and afterwards 80 meters (X-axis body frame). This makes sure that the flow is not forced in a certain direction due to the boundary layer. These volume dimensions are validated by simulating an oversized volume and comparing the aerodynamic forces, to make sure that the mesh volume is efficient. An even more efficient mesh volume can be generated by changing the beam-shaped volume into a coned volume which is aligned with the shockwave leading to less required mesh elements. However, in that case the mesh volume needs to be modified for each Mach number, because these variations lead to variations in shock angle. This adds unnecessary complexity and more computation time would be required for generation of the mesh volume than the decrease of computation time due to the CFD simulation.

4.5.2. Mesh generation

Mesh generation is a complex process. A mesh can be structured or unstructured or a combination of both which makes it essentially structured but until a certain level. The difference is that a structured mesh has settings which create more or less mesh elements in specific areas. This is a more efficient way to generate a mesh, because important areas where large gradients in the field variables are located will be determined more detailed and vice versa. Leading to a relatively low number of mesh elements required to visualise and determine the important details. This is important because more accuracy in the flow properties leads to more accuracy in the aerodynamic characteristics. A choice was made for the combination, any structured mesh feature that can be applied is used given that the automation process will not be interfered (more details in Chapter 5). Hereby, the mesh is as efficient as possible for this research. Before going into the details of the mesh functions applied at the mesh generation process, the difficulties of mesh generation will be explained. To be able to generate a mesh, the volume must satisfy the following requirements:

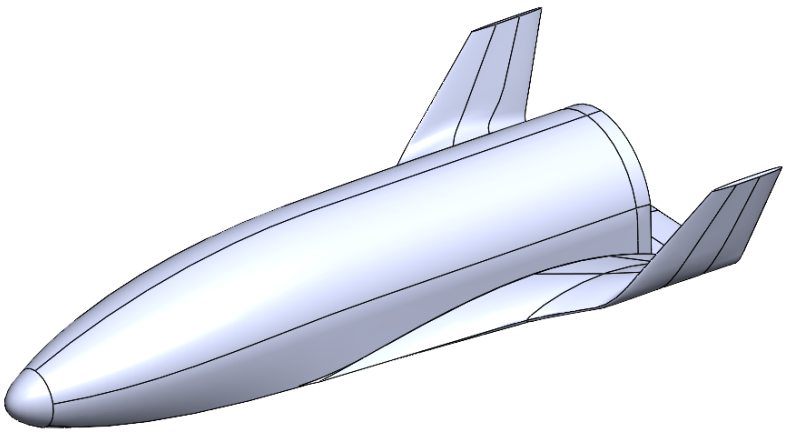

Figure 4.14: The HORUS-2B design in SolidWorks based on the reference sketch.

- The fluid volume must not contain small cracks. If there are small cracks, the mesh is not able to generate mesh elements inside the infinite small areas. Hence, these cracks need to be filled up with solid material. Or, if it is desired to have fluid in that area, the crack needs to be increased until a reasonable sized space is created (relative to the body). Filling up the crack is allowed, because a small area like that creates a negligible influence on the flow field properties. If the area is increased, the initiated mesh element size needs to be small enough to place mesh elements in that area.

  The HORUS design has such cracks in the area of the deflection surfaces. When rotating the flaps these difficult areas arise. Because many simulations of different flow conditions and shapes are required, it was chosen to make the areas larger. Thus, making sure the mesh elements can be placed inside the cracks. Due to the fact that the mesh generation needs to be automated, there is no time to adjust every single geometry (filling up the cracks). This automated process will be explained extensively in Chapter 5.

- Another mesh feature is that mesh generation does not prefer (almost) infinite sharp edges. This is because the surface mesh of the spaceplane cannot create good mesh elements around the edge. This can be solved by cutting of a bit off the edge, leading to more blunt edges which solves this problem. At the trailing edge these effects are small, but in the direction of the incoming flow this affects the results significantly. Another solution to this problem is to tune the edge proximity value which makes smaller mesh elements in these critical areas.

  Again the HORUS design has many of these areas. The winglets for instance have sharp edges on both the leading and trailing edges. Also, the transition from the fuselage to the wing has a really sharp corner. Another area is the trailing edge of the wing. The choice was made to solve these mostly with the proximity value which can be seen clearly in Figure 4.15, but also with less sharp corners.

If the mesh requirements above are satisfied, the focus can be shifted to the mesh efficiency. As already briefly indicated, the mesh is efficient when there is a high density of mesh elements in the areas where high gradients in the flow field properties are likely to occur. This would be in the area of the boundary layers, which is around the spaceplane, in the shockwave area, especially at the nose tip and in the wake of the spaceplane. In Figure 4.16, the left image is the total mesh volume and the right side is an enlarged version of the area where the spaceplane is located. In the figure the small elements are indicating the highly dense mesh and visa versa. The mesh quality is not perfect because in the shockwave area, except for the nosecone region, the mesh density is not that high. Similarly for the wake, further downstream the number of mesh elements decreases. In the perfect world the number of mesh elements would be high downstream behind the spaceplane and also in the shockwave region. And, ideally, rotating and area increasing/decreasing with angle-of-attack variation (for the wake region) and changing with shock angle with increased/decreasing velocity (for the shockwave region). The region why this mesh is a compromise is due to the limitation of the automation possibilities, see Chapter 5. However, in the boundary layer region, nosecone, nose tip and in the beginning of the wake this is accomplished. Also, a low density of mesh elements in less important regions is accomplished. Lastly, for accuracy reasons it is preferable that the mesh elements are aligned. If the mesh

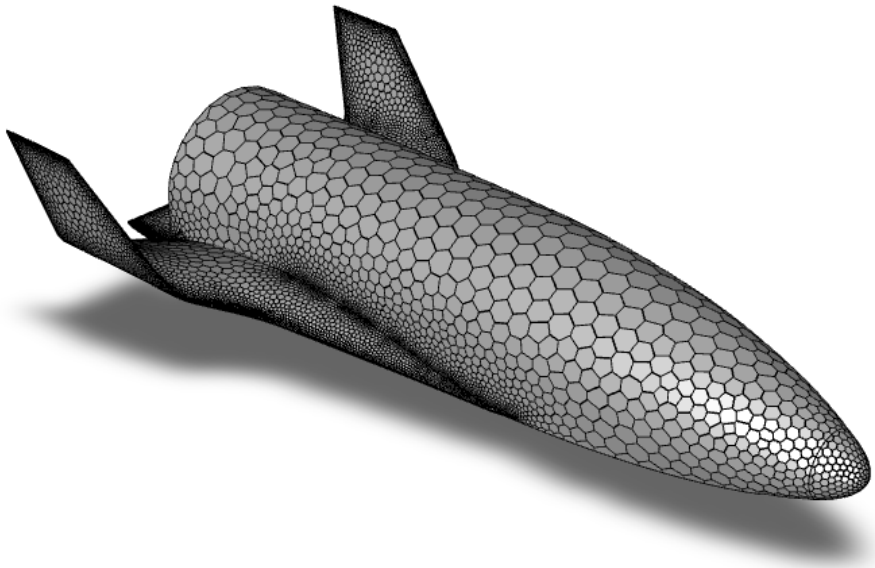

Figure 4.15: The surface mesh of the HORUS spaceplane design.

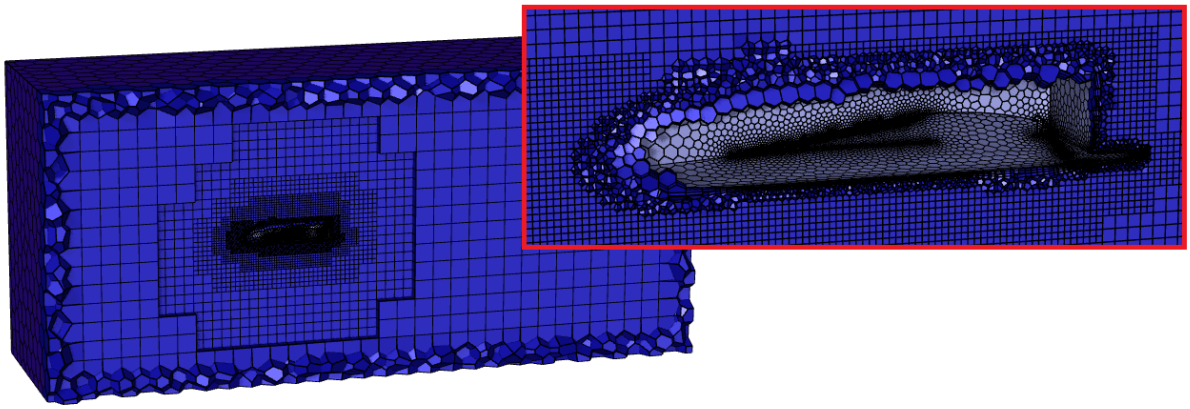

Figure 4.16: A cross section in the XZ-plane of the body fixed reference frame of the fluid volume mesh.
(The right picture is an enlarged visualisation of the spaceplane area.)

elements are stacked as fine and consistent as possible, there are less peaks in the flow properties between different mesh nodes because of varying mesh note distance.

To obtain the mesh visualised in Figure 4.16, the following settings are used. The poly-hexcore mesh element type is used. This type is specialised in generating the best quality mesh elements in the shortest generation time by using the relatively new Mosaic meshing technology[3]. It accelerates the meshing process with a reduced face count, higher quality cells and efficient parallel scalability. Several settings are used for the cracks and sharp edges. In the settings the proximity for curves is initiated and special features to create elements in the gap are used. After which the creation of the surface mesh is generated with a defined mesh surface element size (Figure 4.15). From this point, the named of boundary conditions are used to define a refinement at the wall (which is the spaceplane). There are 10 layers applied at the wall boundary and an increase in layers in the nose tip area. Lastly, the bulk volume mesh is generated after defining the mesh element size.

4.5.3. CFD simulation

The CFD simulation basically solves the governing equations in a numerical manner by iteration. As explained in the beginning of this chapter, certain simplifications are applied. Based on the purpose of this

[3]The ANSYS Fluent official website: https://www.ansys.com/products/fluids/ansys-fluent/mosaic-meshing, accessed at 29/11/2021.

research and the results shown in the example sphere simulation, the choice was made to use the most simplistic available models. All the settings for the HORUS simulation are stated below:

- Density-based solver: Traditionally the density-based solver is preferred over the pressure-based solver for compressible flows. Nowadays the schemes are updated and both can be used for a wide range of conditions. However, because in this research the velocities are extremely high, the density-based solver is selected. The difference is that the density-based solver solves the coupled set of equations such as continuity, momentum, and energy in a coupled manner. This is slower and more memory intensive to solve because it solves all equations in one iteration. The pressure-based solver solves them in a segregated approach. First it decouples the equations, then it solves the pressure-velocity coupling problem by applying various models.
- Steady solution: The governing equations will be iterated until a steady converged solution is found. In time the wake will fluctuate behind the spaceplane, but this is not relevant for this research.
- Euler modes: The Euler equations are selected for the fluid model, which is explained extensively. Therefore, the viscous effects are neglected which is one of the most simplistic fluid models.
- Energy equation: The energy equation is added to the governing equations because the flow has compressibility effects due to the high simulation Mach numbers.
- Fluid properties: The chemical composition of air is selected, with constant molecular weight. For the specific heat C_p a piecewise-polynomial is selected, the temperature slightly changes the specific heat. For the density the ideal-gas is selected, which is explained in Section 4.1.
- Boundary conditions: Obviously the spaceplane surface is a wall boundary. The inflow boundary conditions are selected as pressure-far-field boundary conditions which is specialised for aerodynamic simulations with high Mach numbers. These boundary conditions require ambient temperature, pressure and the free stream Mach number. The direction of the flow is initialised by a vector notation, which is defined by equation Equation 3.2 till 3.4, which requires the implemented angle-of-attack and angle-of-sideslip. There is also a pressure outlet boundary condition as a flow outlet.
- Spatial discretisation method: Gradients are needed not only for constructing values of a scalar at the cell faces, but also for computing secondary diffusion terms and velocity derivatives. For the gradient the Least Squares Cell-Based method is used instead of the Green Gauss Cell-Based method, because the accuracy is slightly better. On the other hand, it requires a bit more computation power. This is combined with the first order Upwind discretisation scheme, which is required to make sure the solutions converge. The downside is however the lower accuracy compared to a second order scheme.
- Solution steering initialisation: The FMG initialisation solves the problem on the coarsest grid first, then interpolates that onto the next finer grid, solves that, and so on. The basic idea here is to give successively better initial guesses to the solver, making the systems easier and faster to solve. This initialisation process is enabled to improve the convergence. This initialisation process is key to create convergence for complex shapes like the HORUS, given that there is not much available simulation time. Normally, for high Mach numbers a step-by-step increase of the Mach number is required to reach convergence. However, FMG initialisation helps this process significantly.
- Iterations and convergence: For the HORUS simulations in the TAEM phase around 75 iterations are required to converge. The simulation settings are set to maximum 100 iterations before the simulation is terminated.
- Aerodynamic output: The aerodynamic forces in the body fixed reference frame are translated to the forces in the aerodynamic reference frame by Equation 3.1.3. The moments require the aerodynamic reference point which is implemented. Both the forces and moments are converted to coefficients with the use of the reference values (referencevehicledata). The equations are state below:

$$\mathbf{M}_B = \begin{pmatrix} \mathcal{L} \\ \mathcal{M} \\ \mathcal{N} \end{pmatrix} = \bar{q} S_{ref} \begin{pmatrix} b_{ref} C_l \\ c_{ref} C_m \\ b_{ref} C_n \end{pmatrix}, \tag{4.19}$$

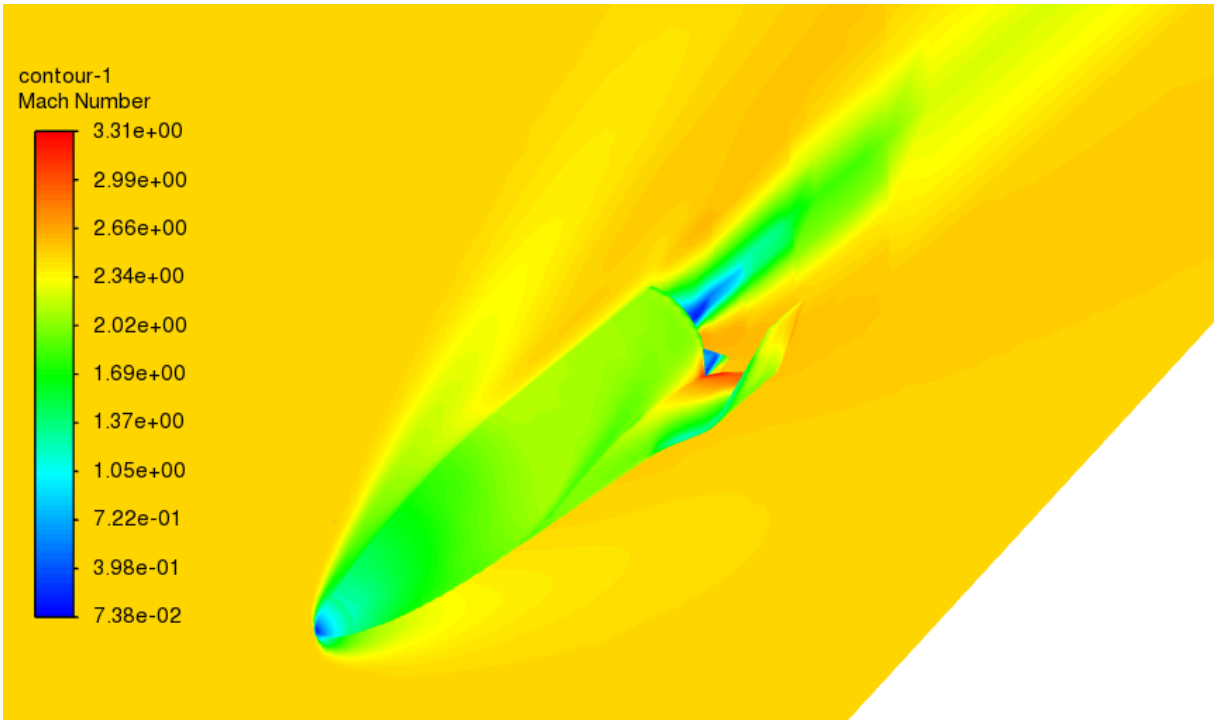

Figure 4.17: HORUS CFD simulation for a Mach 2.5 flow. With an additional cross section at the XZ-plane of the body fixed reference frame to give a better flow visualisation. On the left side the local Mach number. In the picture there can be seen that at the nosecone a stagnation point arises, large deviations in fluid properties in the shockwave and an increase in velocity in between the fuselage and the winglet. The wake is another larger stagnation point in the flow where flow separation occurs.

$$\text{and } \mathbf{F}_A = \begin{pmatrix} D \\ S \\ L \end{pmatrix} = \bar{q} S_{ref} \begin{pmatrix} C_D \\ C_S \\ C_L \end{pmatrix}. \tag{4.20}$$

with $\bar{q}$ the dynamic pressure, S_{ref} the reference area, b_{ref} the width reference and the c_{ref} the length reference.

As an example, the simulation of Mach 2.5 is simulated with conditions along the trajectory. In Figure 4.17, the local Mach number in the flow field can be seen. In this view an XZ-plane is added to see the flow around the HORUS spaceplane. As expected there is a stagnation point at the nose tip and just after the fuselage. From the nose tip there is a shockwave similarly as in the simulations of the sphere. The local Mach number starts to increase at the back of the wing because of the low pressure. Further away from the spaceplane the properties are less accurate because the mesh density is low. This is visible in Figure 4.18 where the dynamic pressure is visualised, in the wake of the vehicle the gradients between elements increase and the solution is less smooth.

4.5.4. Mesh density influence

From this moment all the settings to perform a CFD simulation, as well as the difference between fluid models and their accuracy, have been explained. However, for this study an optimised mesh with the desired balance between computation time and accuracy must still be achieved. The system requirements state that one CFD simulation must not exceed 60 seconds of simulation time and achieve the most optimal result accuracy. This last part is already established with the most optimal mesh settings given the automation requirement. For this short mesh study, which is already a small validation of the CFD model, 4 conditions for different meshes will be simulated. The Mach number is varied between 1.5 and 2.5, and the angle-of-attack is varied between 0 and 20 degrees. The used CFD settings for this study and for all the HORUS simulations in the future are stated in Subsection 4.5.3 unless indicated otherwise.

The results are presented in Table 4.3. The first two meshes are with the settings used in Subsection 4.5.2 and the last mesh is with slightly modified geometry and mesh which was required for the automation of the

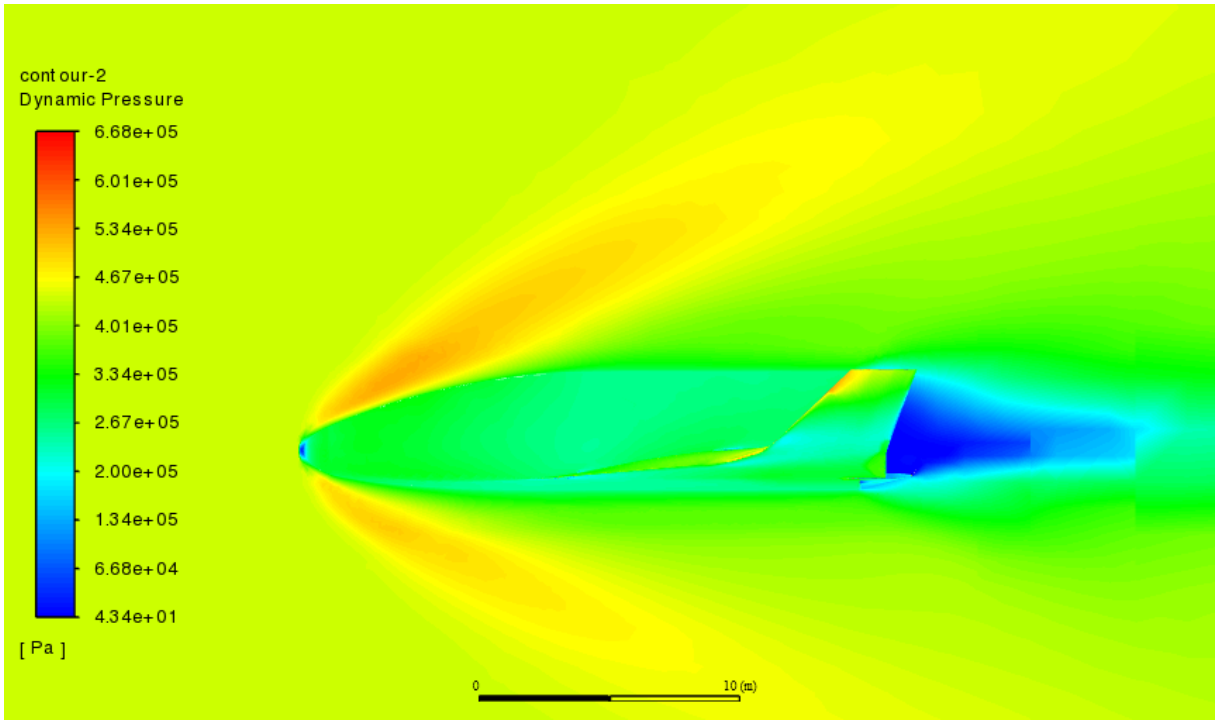

Figure 4.18: HORUS flow simulation for a Mach 2.5 flow. With an additional cross section at the XZ-plane of the body fixed reference frame to give a better flow visualisation. On the left side the local dynamic pressure. In this visitation the shockwave and the wake region becomes more clear. There are large deviations in dynamic pressure visualised by the blue colored area.

model (see Chapter 5). The meshes are from high density and quality till low. Even lower meshes are created but resulted to less convergence and therefore a lower accuracy. The simulation time for each iteration decreases with mesh density which is as expected. The mesh used for the final model is below 0.5 seconds (fourth row of the table) and leads to a total simulation time for 100 iterations of 50 seconds. Thus, the system requirement is satisfied.

The results are compared with the reference data from Cucinelii and Müller [1988], the last two rows in the table represent the relative error between the reference and simulation results. For the first two meshes the accuracy does not differ much, for some conditions the first mesh is better and for other conditions the second mesh is better. Only for 0 angle-of-attack the high density is slightly better. This is logical because the cell number is still in the same order, the mesh elements are structured slightly different, and the final iteration number can be different (because every mesh is unique). However, from this comparison it can be concluded that the high density mesh is unnecessary (in this order of mesh elements) because the accuracy improvement is small. Lastly, the mesh used in the automation model with even less mesh nodes has a slightly worse accuracy and lower simulation time. In this simulation the mesh element size and the mesh element type is changed due to the change in software program that is required for the automation process explained in Chapter 5. The objective of this section is to show that the target CFD simulation time is achieved and what the effects are on the accuracy of the aerodynamic characteristics due to the number of mesh elements. Overall, the result accuracy is reasonable given the initiated mesh, CFD settings and simulation time. Only at zero angle-of-attack (last two rows and, first and third columns of each mesh grid), the results deviate more than desired, a deviation of approximately -200% for the lift coefficient and 40% for the drag coefficient. The reason for the deviation is due to the details in the design. The nosecone design and the wing leading edge bluntness, are not defined accurately in the reference sketch, a small deviation in nosecone tip height is leading to large deviations in the lift coefficient. The SolidWorks nosecone tip height should have been lower leading to more lift, this is especially important at zero angle-of-attack. With a non-zero angle-of-attack the air is flowing at the correct side (over and under the fuselage), and is less influenced by the correct point direction of the nosecone. In Chapter 7, this behaviour is observed and therefore validated when influencing the nosecone height dimension parameter. For the drag coefficient it is due to the slight deviation of the nosecone bluntness, which is also not perfectly defined, shown in Figure 2.11. When increasing the angle-of-attack, the bottom reference area becomes more important and the fuselage bluntness is less dominant.

Table 4.3: Mesh optimisation results for three different mesh grids.

	Mesh 1				**Mesh 2**				**Mesh 3**[4]			
# Cells	**406264**				**147207**				**160731**			
# Faces	1744804				875817				326801			
# Nodes	1016472				684151				225162			
t [s]	**1.596**				**0.839**				**0.494**			
M [-]	1.5	1.5	2.5	2.5	1.5	1.5	2.5	2.5	1.5	1.5	2.5	2.5
α [deg]	0	20	0	20	0	20	0	20	0	20	0	20
$C_{D_{sim}}$ [-]	0.11	0.34	0.07	0.23	0.13	0.35	0.08	0.23	0.13	0.35	0.09	0.24
$C_{L_{sim}}$ [-]	0.02	0.66	-0.02	0.46	0.02	0.68	-0.02	0.47	0.03	0.67	-0.02	0.47
$C_{D_{ref}}$ [-]	0.09	0.36	0.08	0.26	0.09	0.36	0.08	0.26	0.09	0.36	0.08	0.26
$C_{L_{ref}}$ [-]	-0.02	0.79	-0.04	0.44	-0.02	0.79	-0.04	0.44	-0.02	0.79	-0.04	0.44
$C_{D_{err}}$ %	**24.5**	**6.7**	**2.6**	**12.8**	**41.8**	**1.7**	**1.0**	**10.9**	**47.8**	**2.2**	**10.5**	**6.2**
$C_{L_{err}}$ %	**-191.6**	**16.4**	**-48.3**	**4.7**	**-214.1**	**14.3**	**-48.5**	**6.2**	**-236.0**	**15.6**	**-47.0**	**6.8**

[4]The mesh that has been used for the automation process is explained in Chapter 5.

5

Architectural design

The architectural design that will fulfill the system requirements and therefore the needs of this research is presented in this chapter. The flight mechanics and aerodynamics will be integrated and automated such that the system requirements are satisfied. The architectural design will be explained step-by-step in chronological order. In the explanation of the model, the focus is on the inputs and outputs of each individual part. Wherefore, the files or parameters of the in and outflow of each program in the block chain become clear.

5.1. Geometry

As explained in the Section 2.5, the objective is to automate the process of aerodynamic modeling such that different spaceplane shapes can be easily implemented. After determining the aerodynamics, the flying qualities have to be determined by investigating the flight modes. Thus, the whole sequence starts with the spaceplane shape. There are certain requirements for the shape design:

- The spaceplane shape has to be adjustable, as a result of which different designs can be investigated.
- The design file has to be implementable by the meshing software program.
- The geometry and adjusted geometries have to be suitable for mesh generation.
- A feedback connection has to be established, such that the shape can be optimised.

5.1.1. SolidWorks

These requirements are satisfied by the software program Solidworks. This software package has many extra functions, which makes the creation of the design easier. Also for connection purposes the program offers opportunities. Thus, the starting point is a geometry file created by SolidWorks that defines the contours of the spaceplane shape. The geometry used in Section 4.5, needs to be adjusted so that the requirements stated above are met. The adjustable feature of the geometry is complex, because if there is an adjustment in some dimension, the whole design and therefore multiple drawings have to be adjusted. These drawings contain hundreds of constraints each which also have to be satisfied. Additionally, there are also curved three dimensional lines, because of the smooth curvatures in the HORUS design, which are less convenient to move along with the changing shape. Lastly, the most difficult demand, a combination of multiple dimension modifications. There are many possible combinations and checking for design errors is a time consuming process.

To be able to perform these shape adjustments, the different drawings had to be connected to each other by the means of equations and dimensions defined by the origin. Some adjustable dimensions required extra dimension features, which are solved by simple equations. For instance, for the fuselage length modification, the wing attached to the fuselage has to move along with the fuselage. Otherwise unrealistic designs will be made, where the wing sticks out in front of the fuselage. The small overlap of the different bodies (nose, fuselage and wing) are trimmed away.

Table 5.1: Adjustable spaceplane parameters and there ranges.

Parameter name	Original value	Upper limit	Lower limit
1. Fuselage width	2.5 m	>4.5 m	2 m
2. Fuselage height	1.57 m	>3 m	1 m
3. Nosecone height	1.5 m	2.0 m	1.0 m
4. Fuselage length	10 m	>15 m	5 m
5. Fuselage bottom curvature width	5.5 m	6.6 m	4.5 m
6. Fuselage bottom curvature height	1.5 m	2 m	1 m
7. Wing width	3.1 m	3.9 m	2.8 m
8. Wing corner width	1.5 m	2.5 m	1.2 m
9. Wing corner length	4.8 m	5.5 m	4.6 m
10. Wing thickness	0.2 m	0.3 m	0.18 m
11. Winglet bottom length	4.5 m	4.7 m	4 m
12. Winglet top length	2.5 m	3.5 m	2.2 m
13. Winglet length	3.2 m	4.5 m	2.5 m
14. Winglet angle	12 deg	25 deg	5 deg
15. Winglet angle back	20 deg	30 deg	10 deg
16. Elevon length	1.4 m	2 m	1.3 m
17. Rudder length	1.2 m	1.4 m	1.1 m
18. Rudder height bottom	0.8 m	1.2 m	0.6 m
19. Bodyflap length	2 m	2.5 m	1.8 m

Thus, the input of the geometry file are parameters which are shape dimensions. These adjustable parameters and their range are stated in Table 5.1. These adaptable dimensions are assumed to have no impact on the thermo-mechanical load limits in the beginning of the re-entry trajectory. Most of the parameters are straightforward, but some parameters need extra explanation. The fuselage bottom curvature width and height, are indirectly related to the angle at which the wing is positioned. For example, if there is zero height, the wings and fuselage are horizontally aligned. The wing corner width and length are parameters related to the location of the corner in the wing. The winglet bottom and top length, defines the wideness of the winglet, at the bottom where the winglet is attached to the wing and at the tip. The winglet angles are the orientation of the winglet, defined backwards and outwards. The parameters related to the base of the spaceplane are presented in Figure 5.4 till 5.18 and the parameters related to the deflection surfaces are presented in Figure 5.19 till 5.22. A visualisation of these adjustable parameters inside the SolidWorks drawings are shown in Figure 5.1 for the wing, and in Figure 5.2 for the fuselage parameters. In these figures the adjustable dimensions have a pink color for clarity.

5.1.2. ANSYS DesignModeler

The output of the SolidWorks program is a computer aided design (CAD) file. This file contains the main body and five smaller bodies which are the deflection surfaces (rudders, elevons and body flap). To be able to use the ANSYS environment, the bodies have to be implemented by a geometry program named ANSYS DesignModeler. In this program the mesh geometry will be created. However, firstly, the orientation angles of the deflection surfaces will be defined and added to the input parameters. The following parameters were added: body flap deflection angle δ_{bf}, left elevon deflection angle $\delta_{e,l}$, right elevon deflection angle $\delta_{e,r}$, left rudder deflection $\delta_{r,l}$ and right rudder deflection $\delta_{r,r}$. After defining the orientation of the deflection surfaces, the bodies are attached to each other and overlapping parts are trimmed away. This body is subtracted from the desired beam-shaped volume which represents the mesh. The output of this program is also a CAD file which contains a volume in which the mesh will be created. A visualisation of the volume subtracted by the spaceplane design is presented Figure 5.23.

5.1.3. ANSYS Meshing

The next program in the sequence is the meshing program. Instead of using the Fluent meshing program, which has been used in Section 4.5, the standard meshing program of ANSYS is selected. The reason for this choice is that the Fluent meshing program cannot be automated as desired. The standard meshing program is also developed for fluid models and does not impose any restrictions. To fulfill the demands of automation

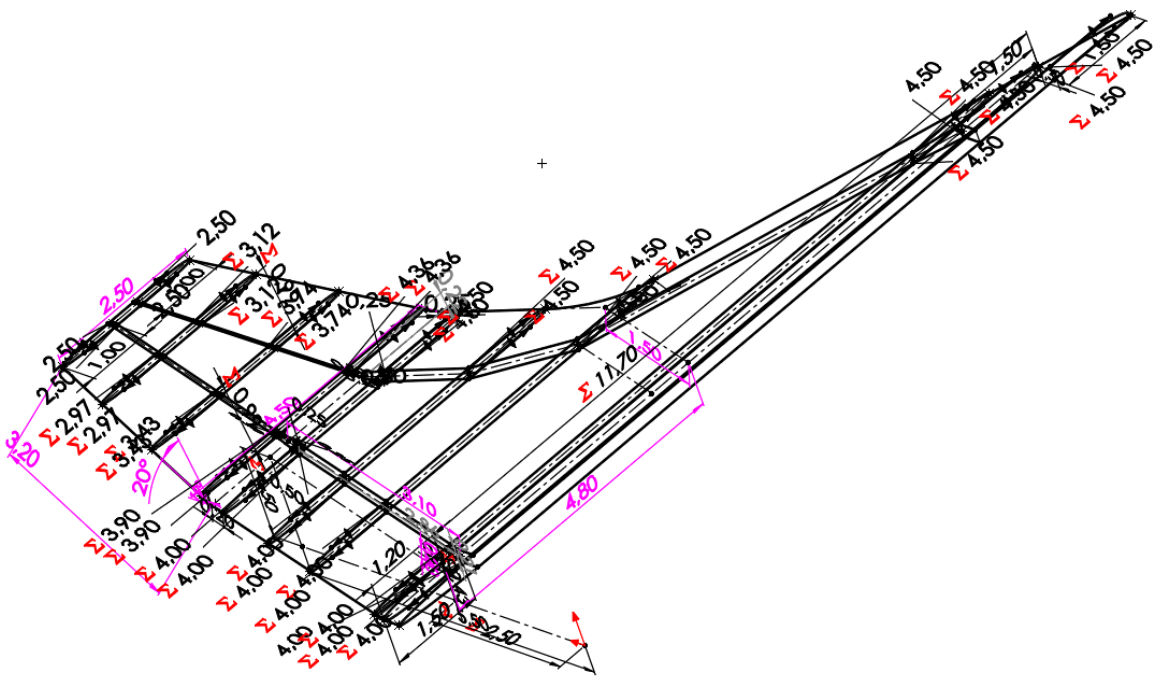

Figure 5.1: Wing design of the adjustable spaceplane. All the pink colored dimensions are the changeable parameters stated in Table 5.1.

and decreasing the simulation time, the choice was made for an unstructured mesh. Some special features are added such as refinement and alignment of mesh elements. What is different compared to the two meshes in Subsection 4.5.4, is that the element type here is tetrahedron, because in this program the poly-hexcore elements are not available. The refinement of mesh elements is used on the leading edges of the vehicle to improve the accuracy. Whereas, the automatic alignment of mesh elements reduces the distance alteration between mesh elements, and therefore also improves the accuracy of the results. Because otherwise small fluctuations will be present in the quantities of the fluid properties leading to small deviations in the aerodynamic characteristics. For every simulation the mesh settings will be the same. The mesh is obviously a little bit different for each geometry, but this is unavoidable with the adjustable shape. By using the same mesh settings, the mesh qualities will not differ very much, and therefore it is assumed that the result accuracy difference is negligible.

The automatic mesh generation is very closely connected with the geometry. To create the three dimensional mesh around the complex spaceplane shape is not simple. Because as explained before, if there are small cracks, the mesh can often not be generated. These cracks needs to be big enough to create mesh elements inside or the cracks need to be closed. However, due to the adaptable deflection angles, the cracks change and this makes it more complicated. The reference HORUS-2B sketch in Cucinelii and Müller [1988], has deflection surfaces that cannot rotate in a real-life scenario. Because the rotation axes of the elevons and rudders are at an angle with respect to the fuselage, the deflection surfaces would intersect with the fuselage or the wings (based on this sketch). When the shape intersects itself, the mesh can also not be generated. Both problems are solved by iterating the geometry of the spaceplane until the meshing program is satisfied. The final spaceplane geometry is changeable, but the shape is slightly altered from the original design to overcome these problems. The altered spaceplane version is visible in Figure 5.3. The fuselage and wings have small cuts in the flap areas to make the deflection surfaces rotational. Also, the transition between the wing and the fuselage and the complex curvature in the wing is simplified. The sharp trailing edges of the wing are slightly more blunt, to make sure that the mesh can be generated. These are all slight modifications, that will only result in small aerodynamic errors.

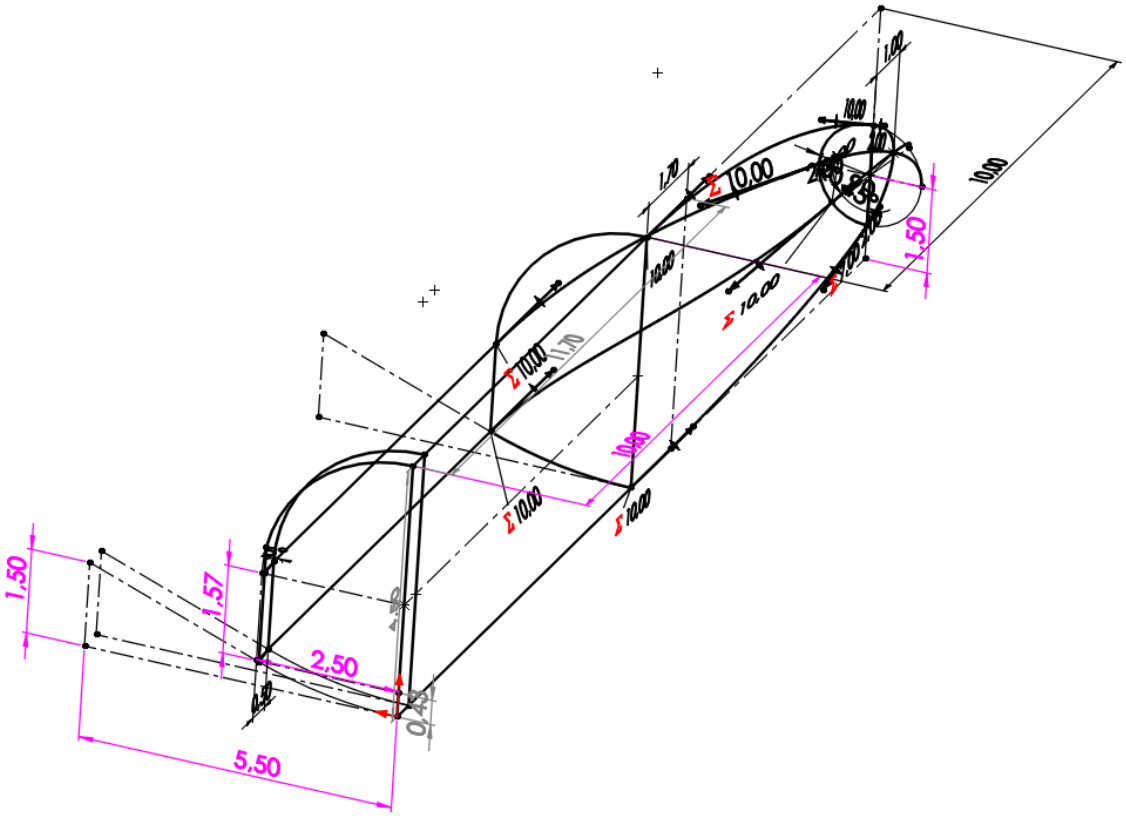

Figure 5.2: Fuselage design of the adjustable spaceplane. All the pink colored dimensions are the changeable parameters stated in Table 5.1.

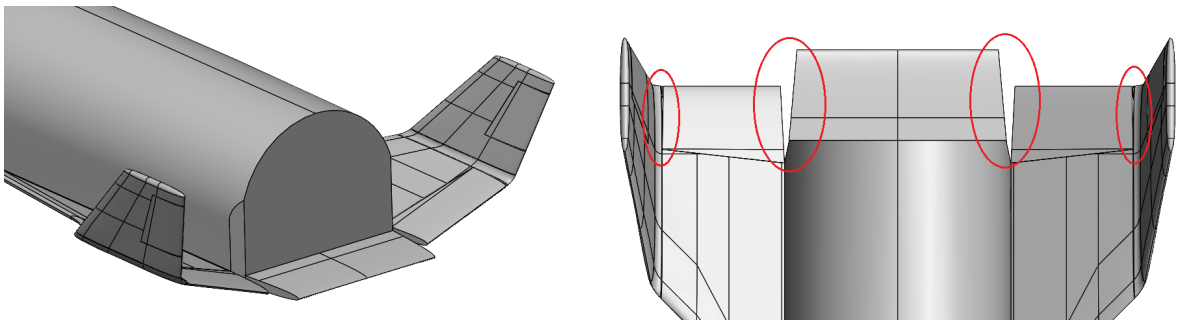

(a) Fuselage modification

(b) Elevon and body flap modification

Figure 5.3: The design changes compared to the MBB reference sketch.

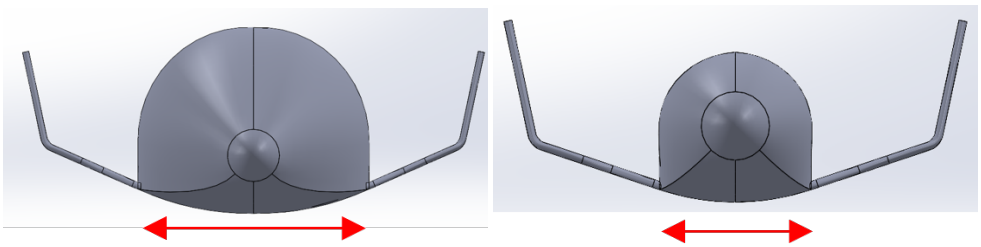

(a) Fuselage width high

(b) Fuselage width low

Figure 5.4: Adjustable spaceplane geometry parameter upper and lower limits (corresponding with Table 5.1).

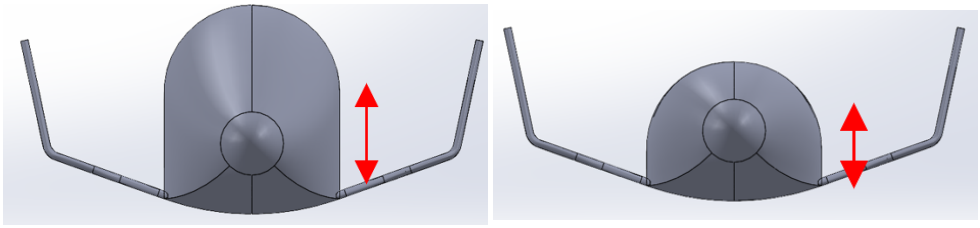

(a) Fuselage height high (b) Fuselage height low

Figure 5.5: Adjustable spaceplane geometry parameter upper and lower limits (corresponding with Table 5.1).

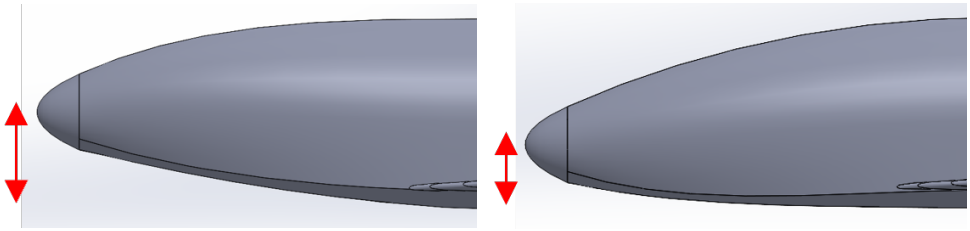

(a) Nosecone height high (b) Nosecone height low

Figure 5.6: Adjustable spaceplane geometry parameter upper and lower limits (corresponding with Table 5.1).

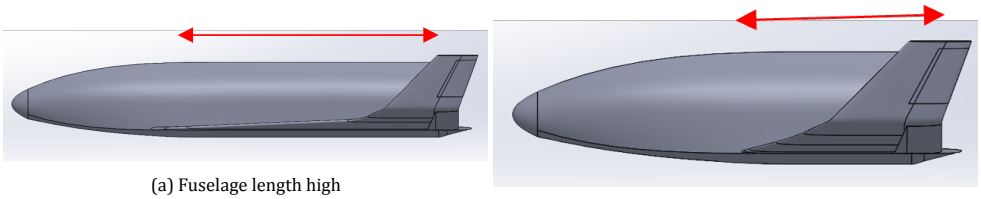

(a) Fuselage length high (b) Fuselage length low

Figure 5.7: Adjustable spaceplane geometry parameter upper and lower limits (corresponding with Table 5.1).

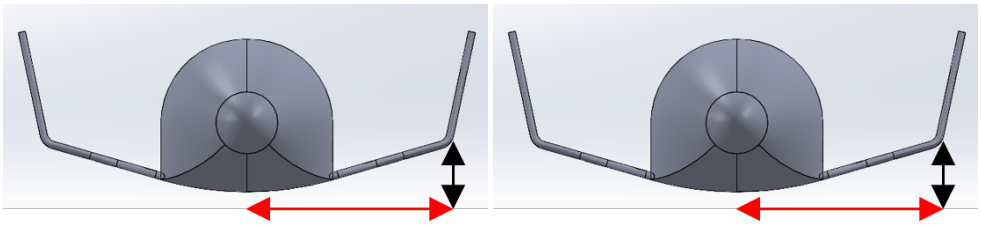

(a) Bottom curvature width high (b) Bottom curvature width low

Figure 5.8: Adjustable spaceplane geometry parameter upper and lower limits (corresponding with Table 5.1).

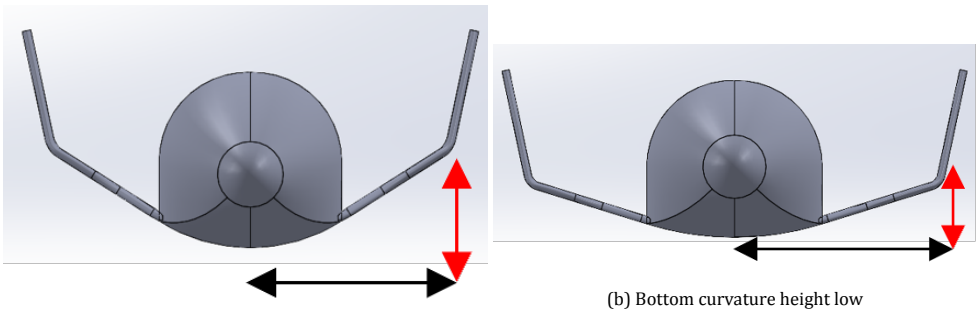

(a) Bottom curvature height high

(b) Bottom curvature height low

Figure 5.9: Adjustable spaceplane geometry parameter upper and lower limits (corresponding with Table 5.1).

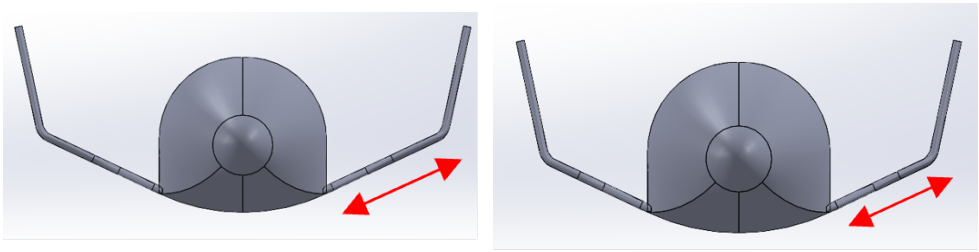

(a) Wing width high

(b) Wing width low

Figure 5.10: Adjustable spaceplane geometry parameter upper and lower limits (corresponding with Table 5.1).

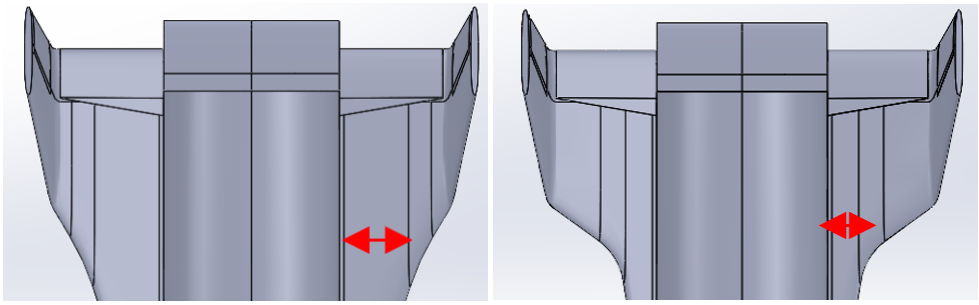

(a) Wing corner width high

(b) Wing corner width low

Figure 5.11: Adjustable spaceplane geometry parameter upper and lower limits (corresponding with Table 5.1).

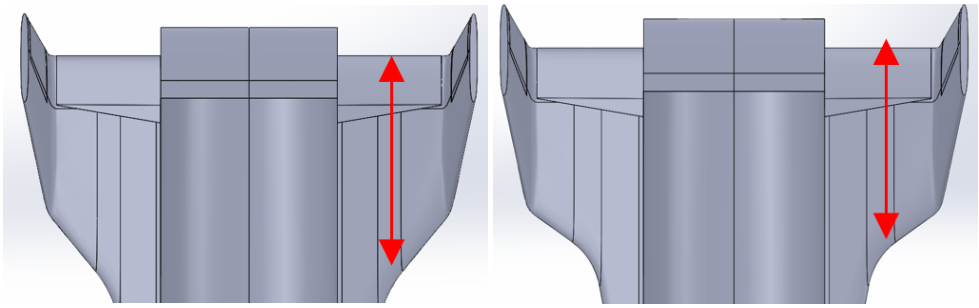

(a) Wing corner length high

(b) Wing corner length low

Figure 5.12: Adjustable spaceplane geometry parameter upper and lower limits (corresponding with Table 5.1).

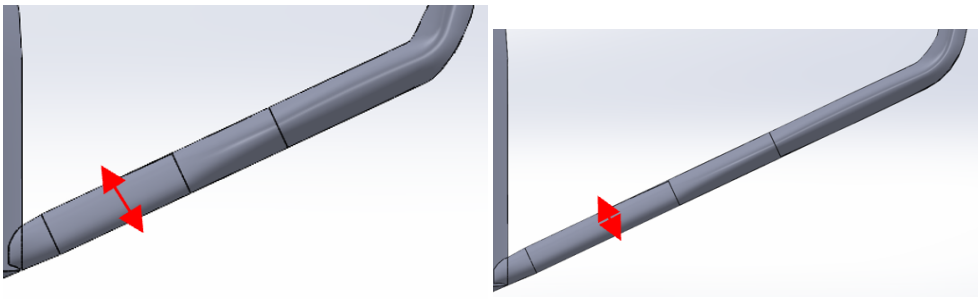

(a) Wing thickness high

(b) Wing thickness low

Figure 5.13: Adjustable spaceplane geometry parameter upper and lower limits (corresponding with Table 5.1).

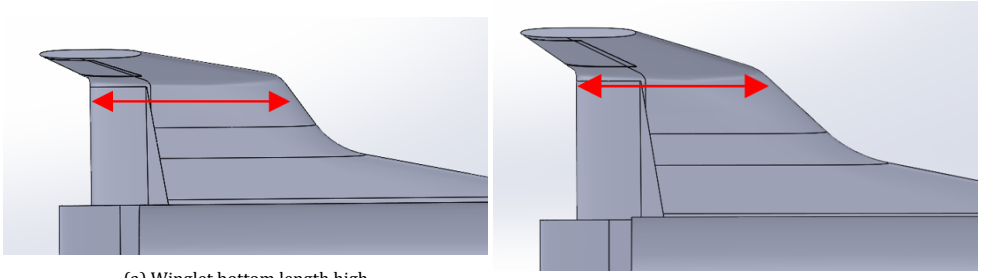

(a) Winglet bottom length high

(b) Winglet bottom length low

Figure 5.14: Adjustable spaceplane geometry parameter upper and lower limits (corresponding with Table 5.1).

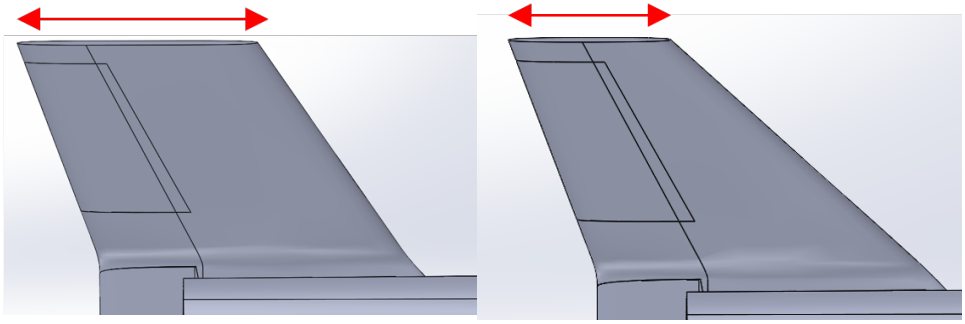

(a) Winglet top length high

(b) Winglet top length low

Figure 5.15: Adjustable spaceplane geometry parameter upper and lower limits (corresponding with Table 5.1).

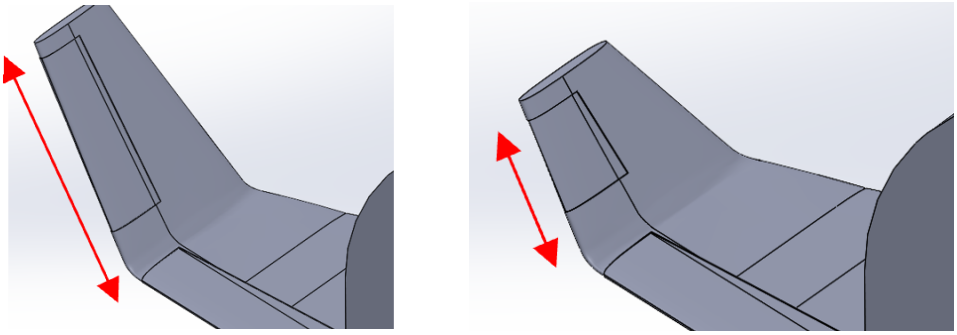

(a) Winglet height high

(b) Winglet height low

Figure 5.16: Adjustable spaceplane geometry parameter upper and lower limits (corresponding with Table 5.1).

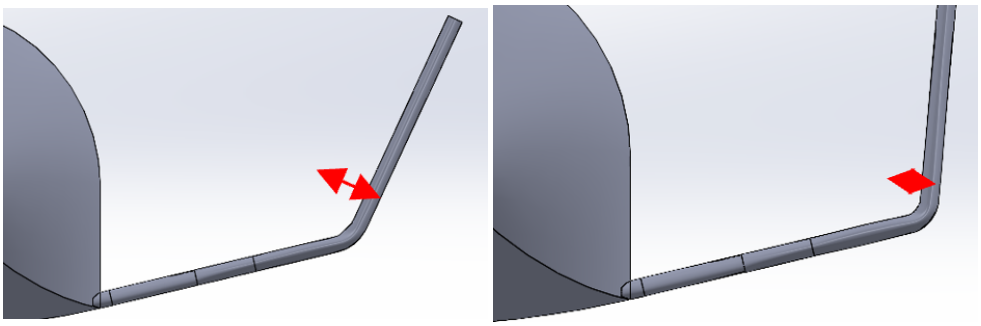

(a) Winglet angle sidewards high

(b) Winglet angle sidewards low

Figure 5.17: Adjustable spaceplane geometry parameter upper and lower limits (corresponding with Table 5.1).

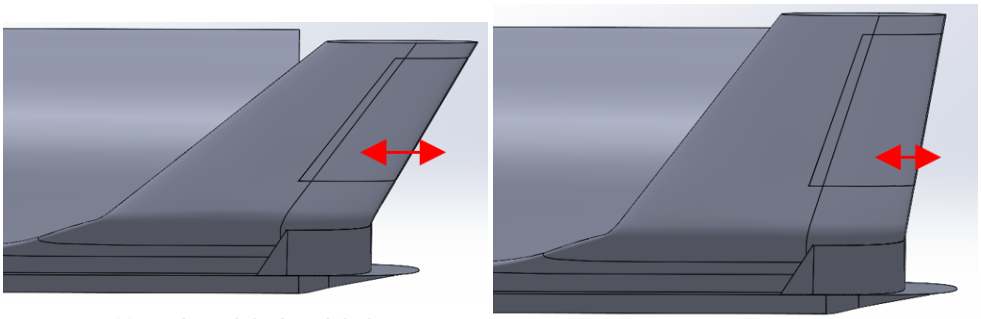

(a) Winglet angle backwards high

(b) Winglet angle backwards low

Figure 5.18: Adjustable spaceplane geometry parameter upper and lower limits (corresponding with Table 5.1).

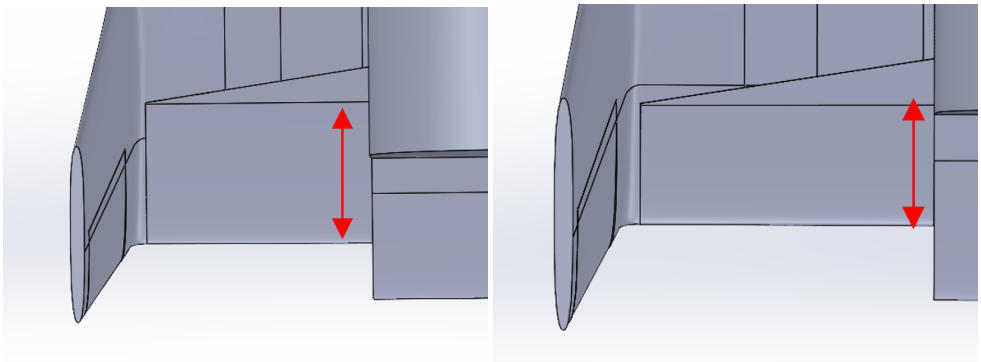

(a) Elevon length high

(b) Elevon length low

Figure 5.19: Adjustable deflection surface parameter upper and lower limits (corresponding with Table 5.1).

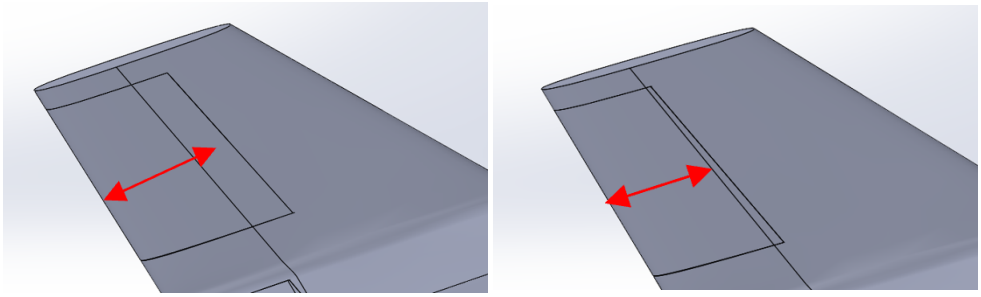

(a) Rudder length high (b) Rudder length low

Figure 5.20: Adjustable deflection surface parameter upper and lower limits (corresponding with Table 5.1).

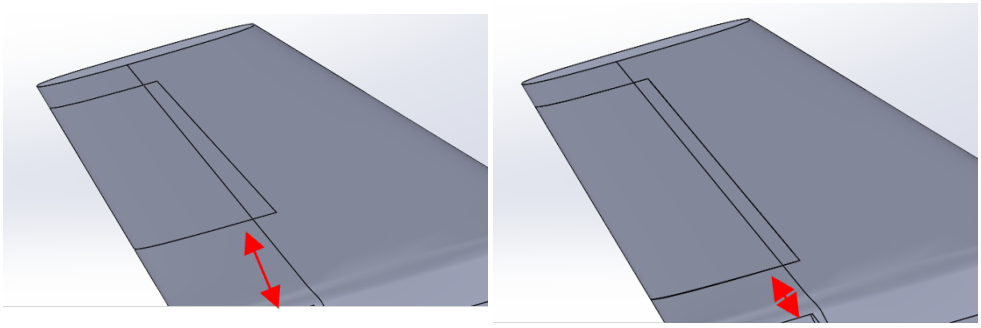

(a) Rudder bottom height high (b) Rudder bottom height low

Figure 5.21: Adjustable deflection surface parameter upper and lower limits (corresponding with Table 5.1).

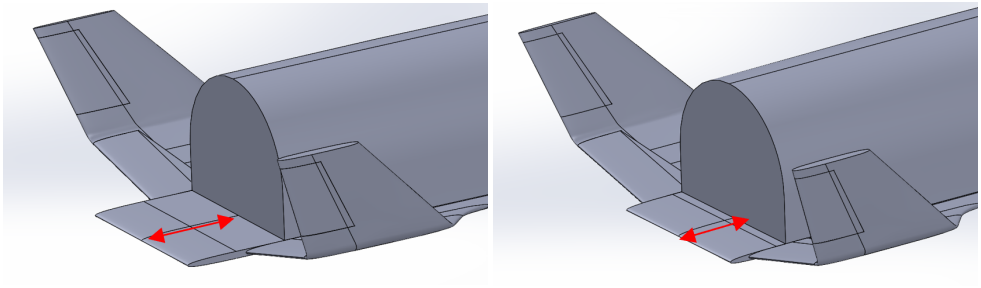

(a) Bodyflap length high (b) Bodyflap length low

Figure 5.22: Adjustable deflection surface parameter upper and lower limits (corresponding with Table 5.1).

Table 5.2: Adjustable CFD simulation parameters.

Input parameters	Unit	Output parameters	Unit
Ambient pressure	[Pa]	Drag force coefficient	[-]
Ambient temperature	[K]	Side force coefficient	[-]
Free stream Mach number	[-]	Lift force coefficient	[-]
Angle-of-attack	[deg]	Roll moment coefficient	[-]
Angle-of-sideslip	[deg]	Pitch moment coefficient	[-]
Reference width	[m]	Yaw moment coefficient	[-]
Reference length	[m]		
Reference Area	[m^2]		
Moment reference center x-distance	[m]		
Moment reference center z-distance	[m]		

5.2. ANSYS Fluent

After the mesh program, the program ANSYS Fluent will perform the CFD simulations. This process is already described in Section 4.5. The settings in the Fluent program will not be altered, hence every simulation has the same accuracy. In the program Fluent there are several parameters that will be added to the input list. These parameters are related to the flow conditions and reference values to perform the calculations of the coefficients. Also, the orientation parameters of the spaceplane are added which are required to determine the stability derivatives. The input and output parameters of ANSYS Fluent are stated in Table 5.2. The reason why the orientation is adjusted in this program is to make the simulations faster. Changing the orientation in the geometry program would lead to a mesh generation for each of the orientations, thus rotating the flow in ANSYS Fluent is faster. The change in flow orientation only required a vector rotation calculation with the use of a rotation matrix combined with the angle-of-attack and angle-of-sideslip. Additionally, the total mesh volume needs to be increased to make sure that the flow is not influenced by the boundary conditions if relatively large angle variations are used. However, this is much faster compared to geometry generation in ANSYS DesignModeler and a mesh generation in ANSYS Meshing for every desired orientation.

5.3. Result processing

The aerodynamic results from the CFD data will be implemented by Matlab. There, the flying qualities will be determined. As described in Chapter 3, a state-space model can be made by using the equations of motion. This investigates the response characteristics by of the different flight modes. The output variables are the response characteristics, which include the natural frequency, damping ratio and halve time or converted in imaginary and real values. By comparing the spaceplane shapes with each other, an iterative optimisation can be performed. Also, to see if a stable, safe and controllable flight is performed, the results will be compared with the military requirements. By evaluating these results the research questions can be answered. The process done with the use of Matlab will become more clear in the next section, where the automation process will be described. Matlab is not only for data processing and visualisation, but also as a driver of the CFD part of this model.

5.4. Automation

All the individual parts with their respective in and outputs have been explained. In this section, the automation and connection between all these programs will be described. The key of the automation is the efficiency of the programs. Similar as the spaceplane orientation which is transferred from the geometry towards the CFD simulation by not changing the geometry, but the orientation of the flow. This makes the inner loop smaller and much more efficient.

5.4.1. Connections

ANSYS programs

The overarching program of all the ANSYS programs is ANSYS Workbench. This program is used to make connections between the individual programs. By using a fluid flow building block, the programs: DesignModeler, Meshing and Fluent are connected. When the run command is triggered, all the programs will run subsequently. Each generated file will be pushed forward to the next program. The in and output parameters of each of the individual programs are exported to ANSYS Workbench. In this case, the only output parameters are the aerodynamic characteristics. And the input parameters are the flow conditions, reference values, the orientation of the spaceplane and the flaps. The parameters are merged and a table of design points can be made.

SolidWorks with ANSYS

The SolidWorks geometry parameters are connected with ANSYS DesignModeler. In ANSYS DesignModeler, an inner loop is made with SolidWorks. The parameters of SolidWorks are exported to ANSYS DesignModeler. In this program, if the value is adjusted, SolidWorks will be started. The program changes the shape and checks if the modification of the dimensions is allowed. This means that all the constraints of the sketches and the usage of the features and functions are satisfied. Then the CAD file will be implemented in ANSYS DesignModeler and the sequence continues. The parameters that are exported to ANSYS DesignModeler are exported again to the overarching program ANSYS WorkBench.

ANSYS with Matlab

Because Matlab is desired to be the driver of the model, because Matlab is preferred for data processing and result visualisation capabilities. Therefore, a connection has to be established between ANSYS Workbench and Matlab. To establish the connection, the batch mode of ANSYS is used, instead of using the ANSYS Workbench interface. In this window a simple command line sends a file with a task list that has to be executed by ANSYS Workbench. This command combined with another command in the Matlab script, which starts the ANSYS Workbench and delivers that task command, make the connection.

A task can be given to ANSYS Workbench with the use of a journal file. This file contains code in the ANSYS language that specifies what ANSYS Workbench needs to do. In this case, the task for ANSYS is pretty simple. The task is to fill the table of design points with the desired values and starts the sequence of programs for each of the design points. By making multiple design points, the command of starting ANSYS has to be used only once for each spaceplane design. After the imported aerodynamic data and determining the flying qualities, another spaceplane design can be created based on the observations. By creating the table of design points, the efficiency of the model is improved. There is another Matlab script that automatically writes the task journal with the desired values for the parameters.

5.5. Overview

To make the model more structured and visual, a schematic block chain is presented in this section. The first figure shows the Matlab part which is data processing, directing the model and determining the flying qualities. The second figure is the CFD simulation block chain.

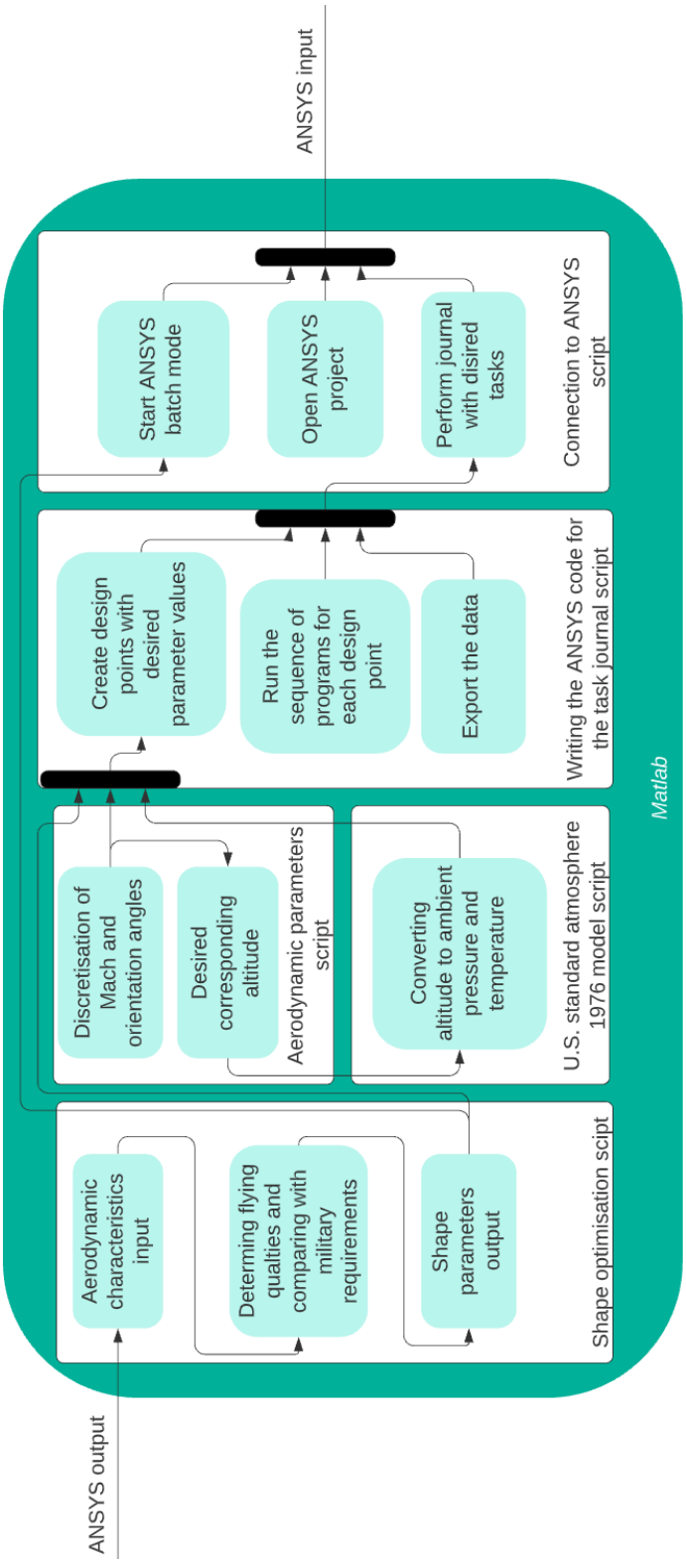

Figure 5.23: The Matlab block chain.

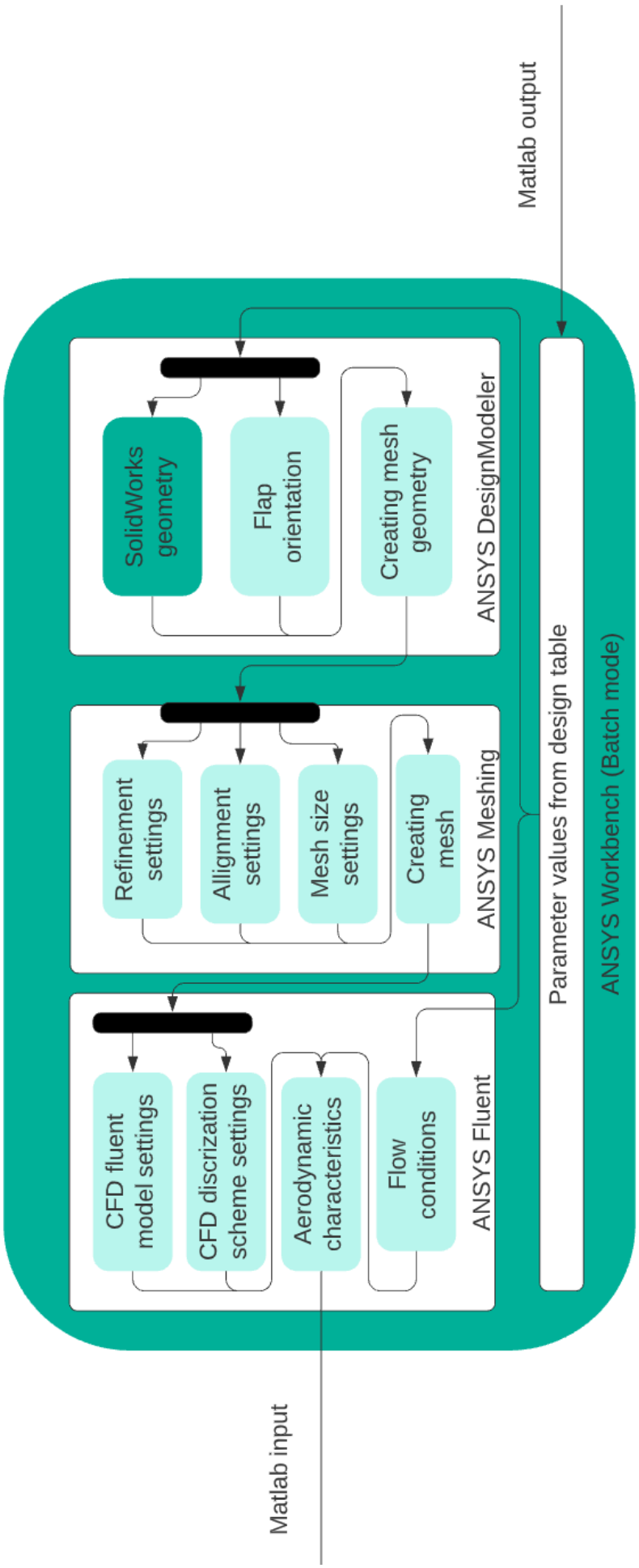

Figure 5.24: The ANSYS block chain including SolidWorks.

6

verification and validation

In this chapter the verification and validation of the model are executed. It starts with a verification of the geometry used in Chapter 4 and the adjustable geometry created in Chapter 5. Followed by the aerodynamic characteristics of the final HORUS spaceplane, which are determined by the aerodynamic simulation part of the model. The aerodynamic verification and validation will have two parts, one in the supersonic regime and one in the hypersonic regime. The second part is the verification and validation of the eigenmotion and therefore the flight dynamics i.e. the dynamic stability.

6.1. Geometry verification

In Subsection 4.5.4 the mesh optimisation was presented. The mesh density variation made sure that the best accuracy was obtained with the constraint of maximum simulation time. This section covers the validation of the geometry, which is slightly changed compared to the original design in Chapter 4, as explained in Chapter 5. To see the influence of the adapted geometry, both geometries are simulated with the same mesh settings. A comparison in aerodynamic characteristics is performed for the TAEM phase flight conditions: Mach 1.5, 2.0 and 2.5. The aerodynamic characteristics are for the nominal condition, which means all the deflection surfaces are set to zero angle of deflection. In Figure 6.1 the results are visualised for the lift and drag coefficients as a function of angle-of-attack. For the sideforce, roll moment, pitch moment and yaw moment coefficients see Appendix B. The results show that there is a small offset between the two geometries. The offset increases at zero angle-of-attack, and is based on the validation between the aerodynamic database which will be explained in the next section an improvement [Cucinelii and Müller, 1988]. Thus the aerodynamic results are slightly artificially improved at zero angle-of-attack. This has to be taken into consideration when discussing the final results of this research.

Looking at the variables in the flow field, the increased deviation at zero angle-of-attack can be clarified. Because at zero angle-of-attack the small changes in the bluntness of the wing leading edge and nosecone, create slightly more airflow downwards or upwards. The wing of the original design is smoother compared to the wing of the modifiable geometry, and therefore guides more air downwards, leading to an increase in lift. For the drag, this is due to the thicker and more curved wing in the original design, which blocks more air compared the modifiable geometry. When the angle-of-attack is increased till 20 degrees, the slight bluntness deviation of the geometries do not influence the flow very much. Because in this condition, the flow deflection is more determined by the bottom area, which is identical to each other. Thus, the decreasing offset in aerodynamic characteristics is clarified. For the lateral direction (angle-of-sideslip related) a similar explanation can be found, only now other parts of the wing (for example the corner in the wing) also lead to small deviations. The deviation in the lateral direction and moment in longitudinal direction are shown in Figure B.1 and B.2 in Appendix B. For the lateral direction the accuracy is slightly worse, because the determination of lateral forces is more sensitive to lower order field variables variations.

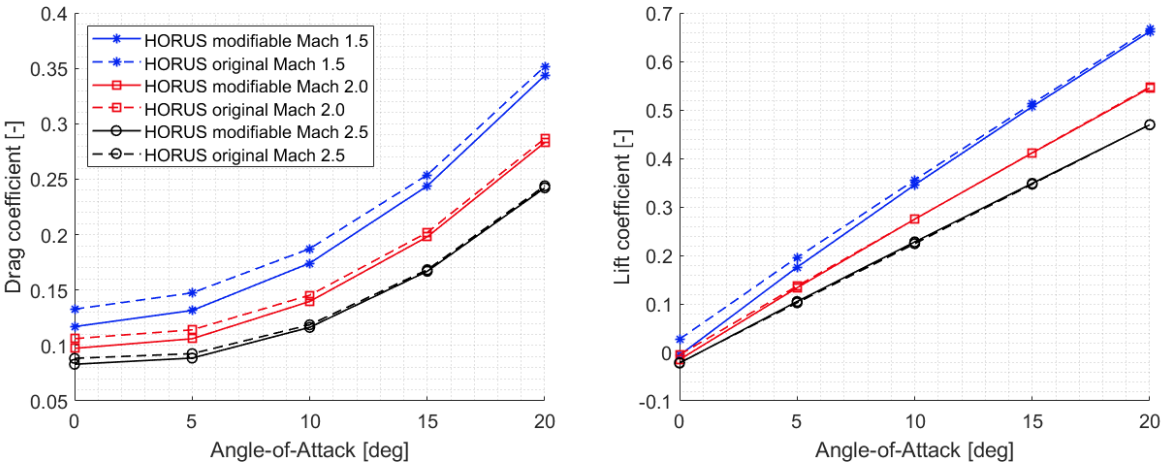

(a) Nominal drag coefficient

(b) Nominal lift coefficient

Figure 6.1: The comparison between the original (most similar to reference sketch) and modifiable geometry.

6.2. Aerodynamic characteristics verification

In the previous section there is established that there is not much difference in aerodynamic characteristics due to the change in geometry (for automation purposes). In this section the aerodynamic data will be compared with the reference data. The first intermediate results are presented in this section. For the lower flight regime, Mach 1.2 till 3, aerodynamic reference data are available from Cucinelii and Müller [1988] and Mooij [1995]. The reference data is discretized for the following Mach numbers: 1.2, 1.5, 2.0 and 3.0, and will be used as comparison for the CFD simulations. Because the transonic conditions are difficult to simulate, as shown in Subsection 4.4.2, the choice was made to simulate from Mach 1.5 till 2.5. (The chosen Mach 2.5 upper limit is the TAEM interface point.) For the Mach 2.5 simulation, the reference data is linearised between Mach 2.0 and 3.0. The CFD results are presented similarly as in the literature, the forces and moments in the longitudinal direction are shown depending on the angle-of-attack. And, the forces and moments in the lateral direction are shown depending on the angle-of-attack and the angle-of-sideslip. The angle-of-sideslip is linearised between 0 and 2 degrees (which corresponds to the reference data). A higher angle-of-sideslip is not relevant because the controller keeps the angle below 2 degrees [Mooij, 2017]. Similar as in the previous section, the aerodynamic characteristics are shown in the nominal configuration, hence zero degrees deflection angle.

The aerodynamic forces are plotted in Figures 6.2a, 6.2b and 6.3a which are the forces in the X, Y, and Z-direction of the aerodynamic reference frame. The relative deviation in drag coefficient at zero angle-of-attack is in between 20.6% for Mach 2.5 and 37.1% for Mach 1.5, which is the highest deviation over the whole simulated angle-of-attack range. At 20 degrees angle-of-attack the deviations are 4.8% and 5.9% for Mach 2.5 and 1.5 respectively. This behaviour is due to the uncertainty in the bluntness of the nosecone. In Figure 2.11, where the HORUS design is presented, the curvature of the nosecone is not fully defined and this causes the deviation in the results at zero angle-of-attack. When the angle-of-attack increases, the bottom surface of the HORUS spaceplane is more dominant in deflecting the flow. Therefore the results become more accurate for higher angle-of-attack. A similar accuracy percentage can be seen for the lift coefficient. The highest relative error is at zero angle-of-attack, which is 38.0% for Mach 2.5. At 20 degrees angle-of-attack the error decreases towards 1.6%. The reason for this behaviour is again related to the uncertainty in the nosecone design for zero angle-of-attack. At higher angle-of-attack the lift coefficient is slightly underestimated, which is due to the fact that the wake behind the spaceplane increases, and the flow properties in this flow region are determined with the lowest accuracy. The reason for this is that the wake is created by the flow separation, which is viscous dominated and currently neglected by the Euler method. For the side force coefficient, the CFD simulations are inaccurate. The trend of the curves and the order of magnitude are correct, but the influence of the different Mach numbers is almost invisible. The largest deviation is 65.3% (visible in Figure 6.2b). The reason for the deviation is that the lateral direction is more difficult to simulate, because the order of magnitude of the forces is much smaller than the longitudinal direction. The lateral direction requires much more mesh elements and advanced fluid model, leading to more details in the flow variables

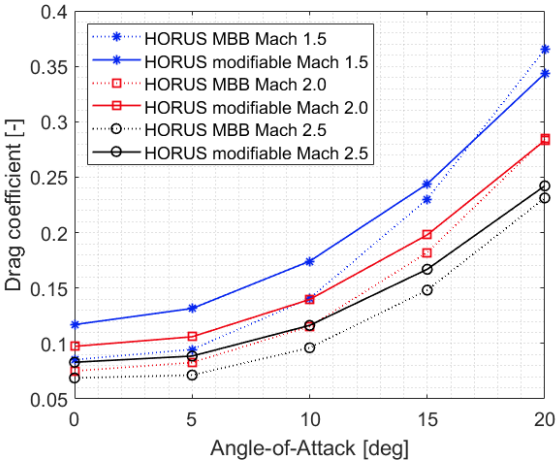

(a) Nominal drag coefficient

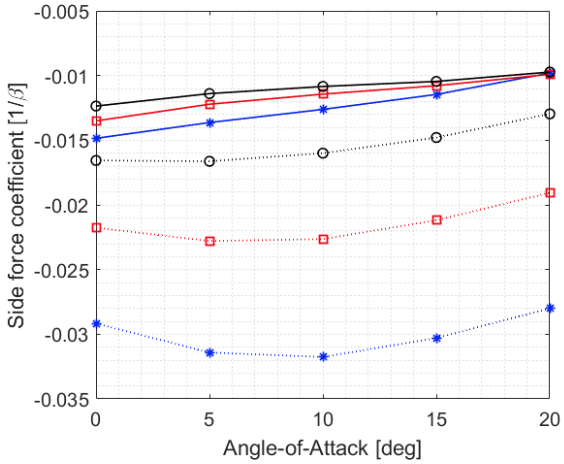

(b) Nominal side-force coefficient differentiated to the sideslip angle

Figure 6.2: The comparison of aerodynamic characteristics between the original HORUS data [Cucinelii and Müller, 1988] and the CFD model part 1 of 3.

and therefore resulting in more accurate lateral results. But, due to computational power and the available research time of this research the mesh quality could not be generated at that level. Also, the spikes in the flow properties (for instance in gaps) have more impact on this direction as discussed in the previous section. The inaccurate prediction of the side force coefficient also leads to inaccurate results for the lateral moment coefficients.

The moment coefficients are plotted in Figures 6.3b, 6.4a and 6.4b. These are the moment coefficients around the X, Y and Z-axis of the body fixed reference frame, respectively. The momentums are depended on the distance from the reference center which is chosen similarly as the reference [Cucinelii and Müller, 1988] and visible in Figure 2.11. Starting with the roll moment coefficient, the curve trend and order of magnitude are correct, but there are some deviations especially at 0 angle-of-attack. The error at an angle-of-attack of 20 degrees is between 11.2 and 30.5%. The reason for the error is again associated with the simulation accuracy of the lateral direction. The order of magnitude is much smaller and harder to determine accurately with this mesh quality/density. For the yaw moment coefficient, similar results can be seen. The yaw coefficient is closely related to the side force coefficient and therefore the trends look the same. However, because the sign is negative instead of positive, the static stability changes from stable to slightly unstable ($C_{n_\beta} > 0$ is statically stable). For the pitch moment the results look pretty accurate, only for the lower Mach of 1.5 the results start to deviate more, because of transonic flow simulation difficulties. Overall, the coefficients for the longitudinal direction are within the mission requirements, but for the lateral direction the results require more advanced meshing, which is beyond the capabilities and available time of this research. The deviations will lead to errors in the lateral eigenmotions. However, a shape improvement will still be noticeable with respect to the original spaceplane.

6.2.1. Bodyflap and elevon

Because the pitch moment derivative in the state-space form includes the effect of the bodyflap and elevons (see Subsection 3.4.1), the increment in pitch moment due to the bodyflap and elevons has to be determined. Instead of determining all the configurations, the most relevant flap deflections are investigated. Mooij [2015] shows, the flap configuration of a realistic flight control system of the HORUS spaceplane can be found. At the TAEM interface the bodyflap is set to -20 degrees and the elevons are set to -17.5 which is required to be able to trim the vehicle. The elevon angle will decrease further when the altitude decreases to maintain trim conditions. In Figure 6.5 the pitch moment increment due to the bodyflap and both elevons (left and right elevon) is simulated. The reference data is linearised between Mach 2 and 3, similarly as above. Also for the elevon the deflection angle is linearised between -10 and -20 degrees. Both results are quite accurate, the errors are in the order of 15%. For Mach 1.5 the accuracy is slightly lower in the order of 30%. For higher deflections of the elevons the results become more accurate as can be seen in Figure 6.6.

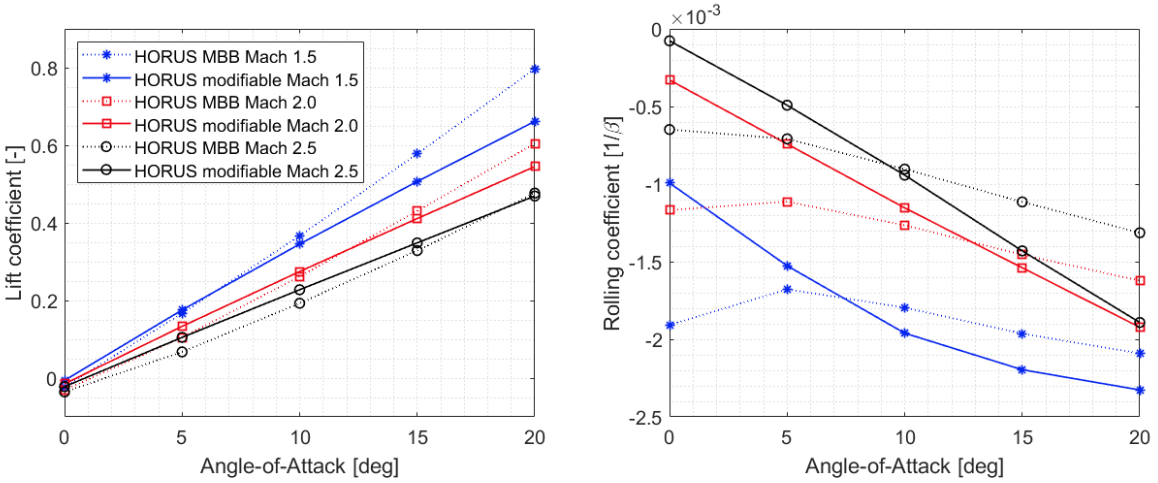

(a) Nominal lift coefficient

(b) Nominal roll moment coefficient differentiated to the sideslip angle

Figure 6.3: The comparison of aerodynamic characteristics between the original HORUS data [Cucinelii and Müller, 1988] and the CFD model part 2 of 3.

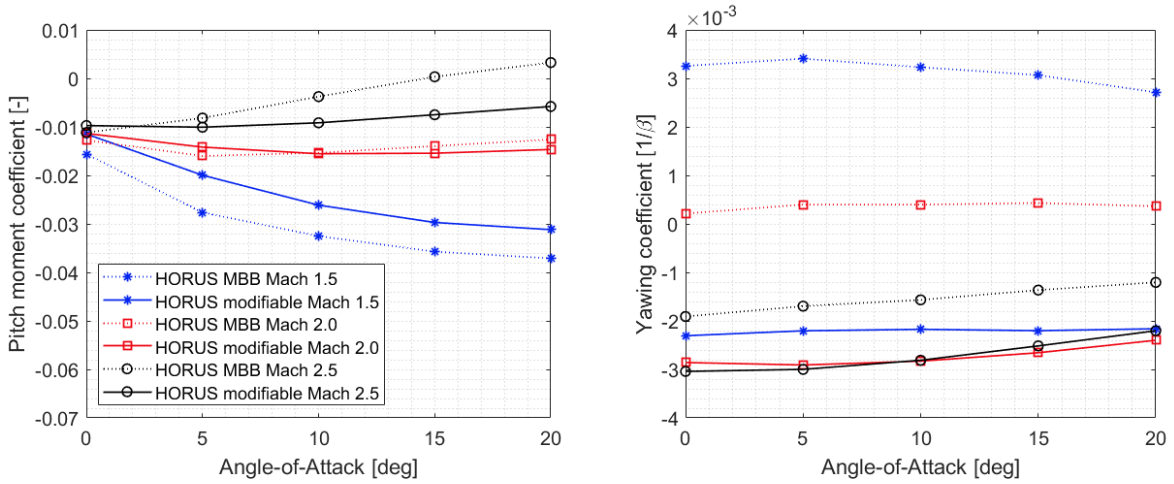

(a) Nominal pitch moment coefficient

(b) Nominal yaw moment coefficient differentiated to the sideslip angle

Figure 6.4: The comparison of aerodynamic characteristics between the original HORUS data [Cucinelii and Müller, 1988] and the CFD model part 3 of 3.

6.2.2. Hypersonic regime

Because the spaceplane concept needs to deal with different flow conditions, the aerodynamic characteristics at higher flow velocities need to be determined after the optimisation study. These will be used to investigate the eigenmotions in the beginning of the re-entry trajectory. As already discussed in Chapter 4, the hypersonic regime is more difficult to simulate. The iterations of the governing equations converge less and sometimes even result in divergence due to the spikes in the field variables. These spikes arise mostly at the tip of the nosecone in the stagnation area. For the validation, Mach 5, 10 and 15 (with nominal flap conditions) are simulated and compared with the data in Cucinelii and Müller [1988]. Since in the reference data Mach 15 is not simulated, it is linearised between Mach 10 and 20. The accuracy of the higher Mach numbers: 5, 10 and 15 is quite good. Similar accuracy percentages can be seen as for the TAEM phase shown above. The results are shown in Figures 6.7, 6.8 and 6.9. The longitudinal results have a maximum accuracy percentage of approximately 35%, similar as the results shown in the TAEM phase of the re-entry. The lift and pitch coefficient at zero angle-of-attack are slightly worse. The velocity is increased, which leads to an increased error in the lift force due to the already explained uncertainty in the nosecone dimensions. The lateral direction is more accurate than the results in the TAEM phase of the re-entry. The reason for this behaviour is that viscous effects become negligible and therefore the inertia effects become dominant with

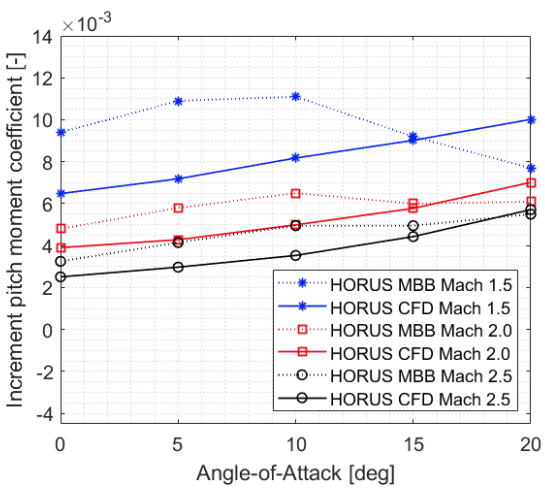

(a) Increment in pitch moment coefficient due to the bodyflap at -20 degrees

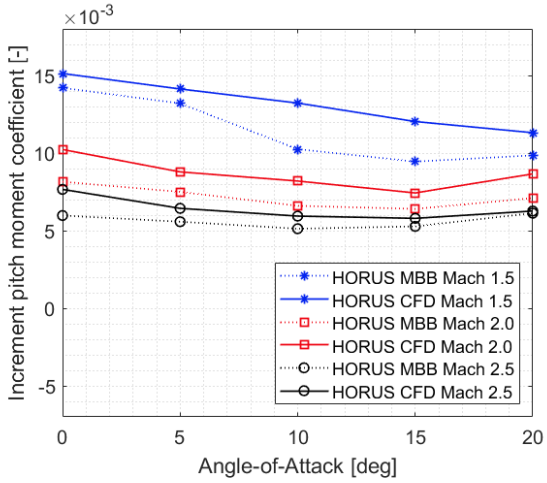

(b) Increment in pitch moment coefficient due to both elevons at -12.5 degrees

Figure 6.5: The comparison of aerodynamic characteristics between the original HORUS data [Cucinelii and Müller, 1988] and the CFD model.

increasing Mach number. Because the side force is more accurate, the roll and yaw moment become more accurate. The lowest accuracy of the yaw moment coefficient is 32.9% at zero angle-of-attack which is a significant improvement. To conclude, the longitudinal accuracy results are similar as for the lower speeds, the simulation outcome for the lateral direction is improved, but the simulation complexity and therefore difficulty is increased.

6.2.3. Geometry uncertainties

The original HORUS spaceplane design is created based on the reference sketch Figure 2.11. As already explained, the reference sketch is not precise and is more of an aerodynamic concept drawing. In a real life scenario, the deflection surfaces cannot even rotate the full designated range due to the intersection of the flaps with the base of the vehicle. Also, some dimensions are doubtful, for instance the curvature dimensions which are not precisely stated and had to be approximated by other dimensions available in the reference sketch. These uncertainties in the curvatures have a small effect on the longitudinal direction, but for the lateral direction where the forces are order of magnitude lower, the accuracy is within the details. Thus, a small part of the deviation is due to these curvature uncertainties. The aerodynamic deviations are not due to the cracks created to make the deflection surfaces rational, because that is excluded by the geometry validation in the previous section. The most precise geometry had no cracks to investigate this influence, therefore the small deviation in the flow field variables due to the cracks is negligible.

6.2.4. Fluid model and mesh setting uncertainties

Obviously, the settings of the CFD model are a simplification of the real life scenario which led to errors in the results. However, also the overall level of simulation is low, because the most simplistic fluid model and discretization schemes are used. As already explained, the viscous dominated region which is close to the wall is oversimplified. The turbulent and boundary layer effects are neglected. Because not only the CFD settings require more simulation also the mesh y^+ value needs to be satisfied for those simulations as explained in Section 4.4 which adds unrealistic complexity for this three dimensional geometry. Also, a decrease of mesh surface element size would increase the details of the shape captured by the mesh. Thus, these settings in combination with the geometry deviation itself are the reason for the relative big error in the lateral direction. To obtain the order of magnitude of the lateral forces, the mesh density needs to be increased extensively.

6.2.5. Reference data reliability

The reference data by Cucinelii and Müller [1988] are determined in a simplistic manner. The target was to get a quick estimate of the aerodynamic characteristics of the HORUS to see the potential of this design. The

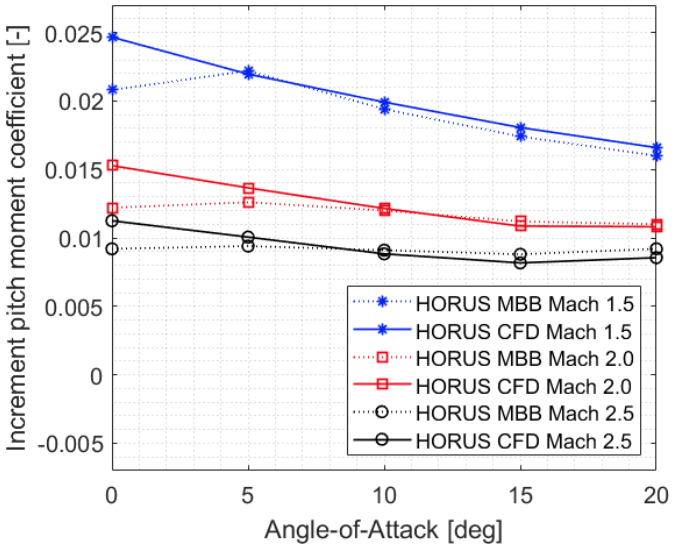

Figure 6.6: Increment in pitch moment coefficient due to both elevons at -20 degrees.

data are determined based on simple calculation methods like, linearised potential theory (which is based on inviscid and irrotational flow assumption), semiempirical methods and hypersonic impact and shadow flow methods. Also, there were no experimental tests done to validate the data. The reference data also neglected the real gas effects, bow-shock-wing-interaction, flow separation, and are therefore very simplistically obtained. Thus, because the aerodynamic data were obtained in 1988 and in that time computers had less computational capabilities, the data cannot be assumed to be 100% correct. But, that does not mean that the data generated by this research is correct. Hence, the real percentage error in aerodynamic data is still uncertain.

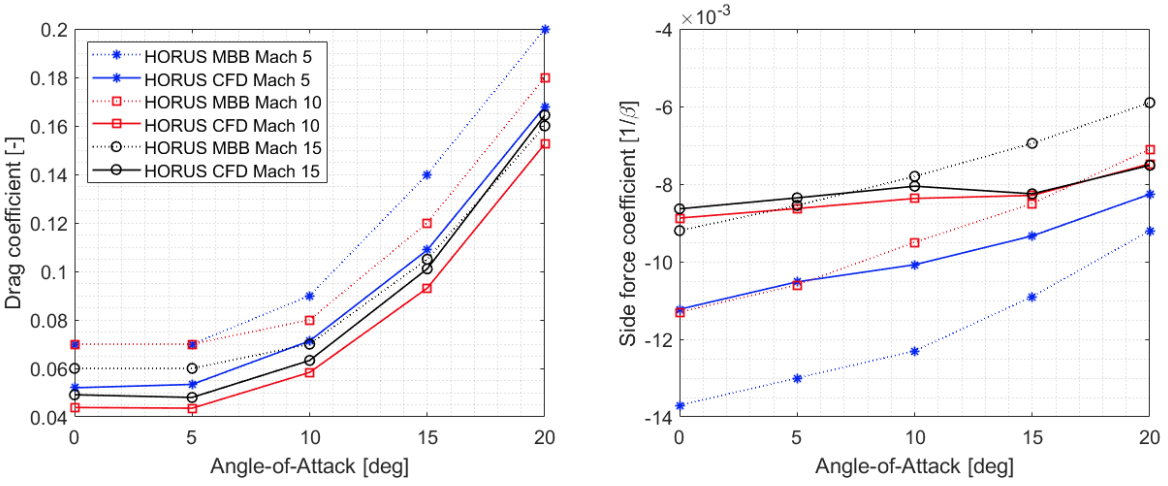

(a) Nominal drag coefficient

(b) Nominal side-force coefficient differentiated to the sideslip angle

Figure 6.7: The comparison of aerodynamic characteristics between the original HORUS data [Cucinelii and Müller, 1988] and the CFD model for hypersonic speeds part 1 of 3.

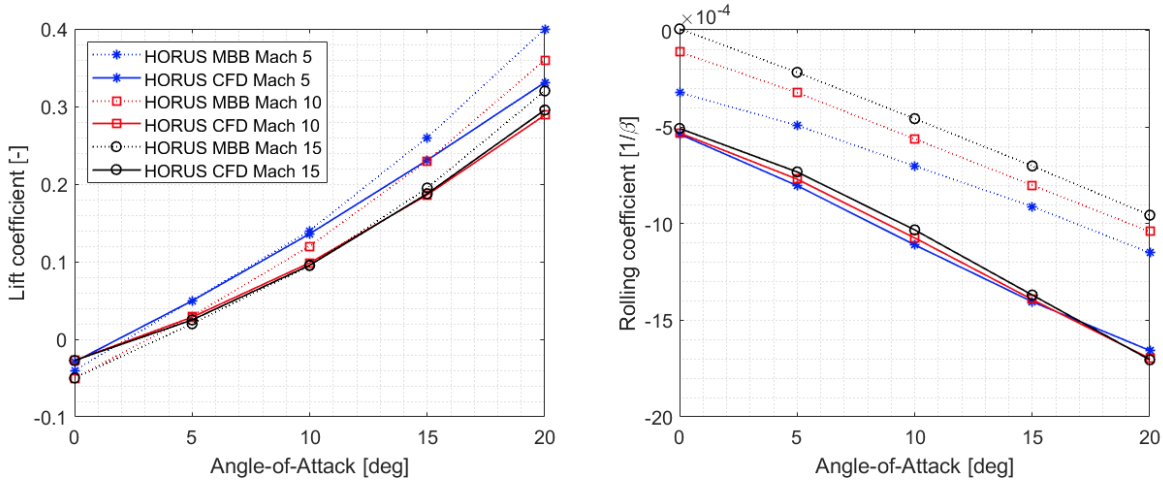

(a) Nominal lift coefficient

(b) Nominal roll moment coefficient differentiated to the sideslip angle

Figure 6.8: The comparison of aerodynamic characteristics between the original HORUS data [Cucinelii and Müller, 1988] and the CFD model for hypersonic speeds part 2 of 3.

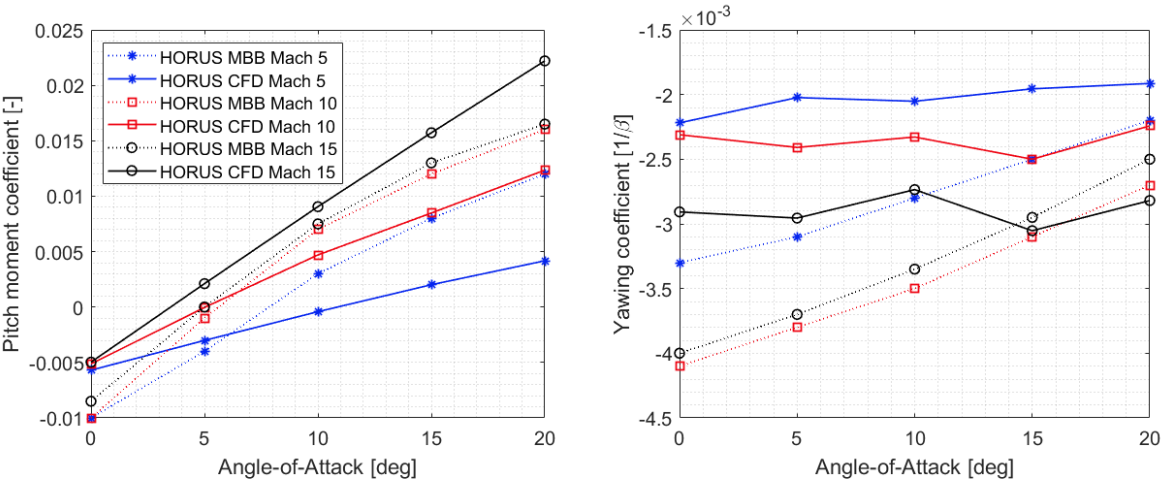

(a) Nominal pitch moment coefficient

(b) Nominal yaw moment coefficient differentiated to the sideslip angle

Figure 6.9: The comparison of aerodynamic characteristics between the original HORUS data [Cucinelii and Müller, 1988] and the CFD model for hypersonic speeds part 3 of 3.

6.3. Dynamic stability calculations

As indicated in Section 2.4, the validation of the dynamic stability is possible at the TAEM interface point. Stated by Mooij [1998], there is a simple equilibrium system which determines the attitude and flap deflection angles to trim the vehicle. At this point the bodyflap has an angle of -20 degrees and the elevon angle is -12.5 degrees. The rest of the conditions along the trajectory and corresponding aerodynamic characteristics from Cucinelii and Müller [1988] are stated in Table 6.1. At this point along the trajectory the eigenmotions are determined and presented in Table 6.3. Mooij [2015] states the eigenmotions at similar conditions are determined. These results are presented in Table 6.2.

The different flight modes are presented in the first row of the tables with their corresponding eigenvalues. These eigenvalues result in the period, halve time, damping ratio and natural frequency which are shown in the next rows. The lower part of the tables show the eigenvectors in magnitude and phase angle. The results show a similar response of real and complex values. The deviation in the eigenvalues for the spiral mode 1 and 2, pitch roll/divergence, lateral oscillation, periodic pitch/roll mode and former short-period oscillation are 16.4%, 30.2%, 12.8%, 61.0%, 4.3%, 87.7% and 85.6%, respectively. The former short period oscillation and the lateral oscillation, which have higher in eigenvalues (in magnitude), have more deviation

Table 6.1: Input variables for the dynamic stability validation (trimmed condition -20 degrees bodyflap and -17.5 degrees).

Variable	Value	Unit
M	2.5	-
h	26.7	km
P_s	2511.02	Pa
T_s	221.650	K
S_{ref}	110	m^2
c_{ref}	23	m
b_{ref}	13	m
α	16.6	deg
γ	-8.4	deg
σ	55	deg

Variable	Base	Increment bodyflap	Increment left elevon[1]	**Total**	Unit
C_{D_α}	0.019	-0.0007	-0.0002	**0.0179**	-
C_{L_α}	0.033	-0.0003	-0.0002	**0.0323**	-
C_{m_α}	0.0004	0.00011	0.0001	**0.00071**	-
C_{S_β}	-0.01725	-	-	**-0.01725**	-
C_{l_β}	-0.00139	-	-	**-0.00139**	-
C_{n_β}	-0.00048	-	-	**-0.00048**	-
C_{D_M}	-0.045	-0.0005	0.002	**-0.0415**	-
C_{L_M}	-0.105	0.0065	0.001	**-0.0965**	-
C_{m_M}	0.015	-0.00165	-0.0007	**0.01195**	-

than the others. The deviation is due to the small differences in input variables of the state-space matrix **A**. Such as, atmospheric properties, dynamic pressure, height and aerodynamic forces. These values are not exactly known from the reference and are leading to these errors in the eigenmodes. The signs are still correct only the magnitude is slightly off, which indicates still the same stability behaviour only not by the same level. For instance a higher imaginary eigenvalue will lead to a lower damping ratio and higher natural frequency, which is by the military requirements worse. Thus, for the highest deviation eigenvalues (former short-period oscillation and lateral oscillation), the slight negative offset in eigenvalues is artificially decreasing the stability for the former short-period oscillation and increasing the stability for the lateral oscillation. This offset has to be taken into account when discussing the results of this research.

[1]The increment due to the elevon has to be doubled because of the symmetric condition, see Table 2.3.

Table 6.2: The reference eigenmotion characteristics of the HORUS spaceplane at the TAEM interface conditions [Mooij, 1998].

	former short-period oscillation		periodic pitch/roll mode		lateral oscillation		pitch/roll divergence	spiral mode	
λ_i Re	-1.0884	0.9518	-0.0213		0.0392		0.0401	$-0.1059 \cdot 10^{-3}$	$-0.9138 \cdot 10^{-15}$
Im	-	-	±0.0146		±1.343		-	-	-
P (s)	∞	∞	430.4		4.7		∞	∞	∞
$T_{½}$ (s)	0.6	-0.7	32.6		-17.7		-17.3	6,544.1	$0.759 \cdot 10^{15}$
ζ (-)	-	-	0.825		-0.029		-	-	-
ω_n (rad/s)	-	-	0.026		1.343		-	-	-
μ_i	z	z	z	θ (°)	z	θ (°)	z	z	z
ΔV	**0.9895**	**0.8871**	$\mathbf{0.6586 \cdot 10^{-2}}$	**52.8**	0.0268	339.8	**0.0419**	$0.3379 \cdot 10^{-4}$	$0.1613 \cdot 10^{-4}$
$\Delta\gamma$	$0.1275 \cdot 10^{-2}$	$0.1111 \cdot 10^{-2}$	$0.3613 \cdot 10^{-4}$	68.9	$0.1815 \cdot 10^{-2}$	72.9	$0.4591 \cdot 10^{-4}$	$0.1498 \cdot 10^{-6}$	$0.3187 \cdot 10^{-8}$
ΔR	**1.0000**	**1.0000**	**1.0000**	**35.0**	**1.0000**	**341.4**	**1.0000**	**1.0000**	**1.0000**
Δp	$0.3547 \cdot 10^{-4}$	$0.3566 \cdot 10^{-4}$	$0.1380 \cdot 10^{-5}$	305.5	**0.1259**	**74.5**	$0.1785 \cdot 10^{-5}$	$0.3427 \cdot 10^{-8}$	$0.6985 \cdot 10^{-9}$
Δq	**0.0266**	**0.0220**	$0.5895 \cdot 10^{-6}$	343.9	$0.3583 \cdot 10^{-3}$	336.1	$0.4785 \cdot 10^{-5}$	$0.8551 \cdot 10^{-8}$	$0.3164 \cdot 10^{-8}$
Δr	$0.1701 \cdot 10^{-5}$	$0.1710 \cdot 10^{-5}$	$0.6617 \cdot 10^{-7}$	305.5	$\mathbf{0.6041 \cdot 10^{-2}}$	**74.5**	$0.8561 \cdot 10^{-7}$	$0.1644 \cdot 10^{-9}$	$0.1977 \cdot 10^{-8}$
$\Delta\alpha$	**0.0267**	**0.0210**	$\mathbf{0.7066 \cdot 10^{-5}}$	**52.8**	$0.4624 \cdot 10^{-3}$	71.3	$\mathbf{0.4525 \cdot 10^{-4}}$	$0.3632 \cdot 10^{-7}$	$0.1734 \cdot 10^{-7}$
$\Delta\beta$	$0.5123 \cdot 10^{-5}$	$0.4504 \cdot 10^{-5}$	$0.4726 \cdot 10^{-8}$	339.9	**0.0225**	**346.2**	$0.9498 \cdot 10^{-8}$	$0.4817 \cdot 10^{-13}$	$0.1735 \cdot 10^{-22}$
$\Delta\sigma$	$\mathbf{0.2715 \cdot 10^{-3}}$	$\mathbf{0.2695 \cdot 10^{-3}}$	$\mathbf{0.4661 \cdot 10^{-4}}$	**298.7**	**0.0911**	**342.9**	$\mathbf{0.3464 \cdot 10^{-4}}$	$\mathbf{0.3238 \cdot 10^{-6}}$	$\mathbf{0.2104 \cdot 10^{-6}}$

Table 6.3: Eigenmotion validation

	Former short period oscillation				Periodic pitch/ roll mode		Lateral oscillation		Pitch/roll divergence		Spiral mode			
λ_i Re	-0.15667		0.11686		-0.022228		0.015307		0.034959		$-8.8493 \cdot 10^{-5}$		0	
Im	0		0		±0.014393		±0.18501		0		0		0	
$P(s)$	Inf		Inf		436.5		34.0		Inf		Inf		Inf	
$T_{1/2}(s)$	4.4		-5.9		31.2		-45.3		-19.9		7832.8		Inf	
$\zeta(-)$	-		-		0.839		-0.083		-		-		-	
$\omega_n(rad/s)$	0.157		0.117		0.027		0.186		0.0350		$8.849 \cdot 10^{-5}$		0	
μ_i	Z	$\theta(^\circ)$	Z	$\theta(^\circ)$	Z	$\theta(^\circ)$	Z	$\theta(^\circ)$	Z	$\theta(^\circ)$	Z	$\theta(^\circ)$	Z	$\theta(^\circ)$
ΔV	0.12142	0	0.10869	0	0.00759	167.65	0.01511	-179.24	0.03499	180	$3.56 \cdot 10^{-5}$	180	$1.94 \cdot 10^{-5}$	180
$\Delta\gamma$	0.00012	180	0.00014	180	$3.71 \cdot 10^{-5}$	147.89	0.00025	85.949	$4.03 \cdot 10^{-5}$	0	$1.26 \cdot 10^{-7}$	180	$3.83 \cdot 10^{-9}$	180
ΔR	0.99214	0	0.99387	180	0.99997	0	0.99988	0	0.99939	0	1	0	1	180
Δp	$4.33 \cdot 10^{-6}$	180	$4.20 \cdot 10^{-6}$	180	$1.51 \cdot 10^{-6}$	94.088	0.00052	-102.95	$1.40 \cdot 10^{-6}$	0	$3.02 \cdot 10^{-9}$	180	$6.76 \cdot 10^{-10}$	0
Δq	0.004615	180	0.00240	180	$1.14 \cdot 10^{-5}$	129.59	0.00011	136.86	$7.54 \cdot 10^{-5}$	0	$7.82 \cdot 10^{-9}$	0	$3.03 \cdot 10^{-9}$	180
Δr	$2.21 \cdot 10^{-7}$	180	$2.14 \cdot 10^{-7}$	180	$7.68 \cdot 10^{-8}$	94.088	$2.66 \cdot 10^{-5}$	-102.95	$7.15 \cdot 10^{-8}$	0	$1.54 \cdot 10^{-10}$	180	$1.94 \cdot 10^{-9}$	180
$\Delta\alpha$	0.02977	0	0.02026	180	0.00043	-14.764	0.00073	58.828	0.00210	0	$2.01 \cdot 10^{-6}$	0	$1.19 \cdot 10^{-6}$	0
$\Delta\beta$	$4.80 \cdot 10^{-6}$	180	$3.47 \cdot 10^{-6}$	0	$2.82 \cdot 10^{-7}$	61.164	0.00069	162.32	$3.47 \cdot 10^{-7}$	180	$1.89 \cdot 10^{-12}$	180	$3.89 \cdot 10^{-22}$	180
$\Delta\sigma$	$2.94 \cdot 10^{-5}$	0	$4.56 \cdot 10^{-5}$	0	$4.87 \cdot 10^{-5}$	101.38	0.00275	-8.6055	$2.80 \cdot 10^{-5}$	180	$3.08 \cdot 10^{-7}$	0	$2.04 \cdot 10^{-7}$	180

7

Results

In this second to last chapter the results of the model will be presented. First, the aerodynamic derivatives representing the static stability of the spacecraft are discussed. Next, the consequences of the modified spaceplane shapes are shown. In the second part, the dynamic stability will be evaluated to give the full stability characteristics. This explains which flight modes are improved and which have become worse. Followed by stating which shape features have the potential to improve the military requirements of the HORUS spaceplane. This chapter will be concluded with the improved shape, this shape will be simulated for a higher Mach number.

7.1. Aerodynamics

To answer the research question, several points along the reference trajectory were chosen to be investigated. One just below the transonic regime at Mach 0.8, and the others above the transonic regime into the supersonic regime at Mach 1.5 and 2.5. The flap configuration is assumed to be at a realistic -20 degrees for the bodyflap and -17.5 degrees for both elevons, to trim the vehicle. The atmospheric properties are set as defined in Table 4.1. The chosen Mach range will show the stability effects in the TAEM phase of the re-entry trajectory. The shape modifications are compared with the original spaceplane which is extensively discussed in Chapter 6. Instead of discussing each flow field, the magnitude of the aerodynamic derivatives will be discussed. Because the flow field will only show the pressure/density/velocity distribution for a single situation whereas the aerodynamic derivatives show the change in the flow field and therefore the vehicle's aerodynamic behaviour. The reference aerodynamic derivatives which are the derivatives of the original modifiable spaceplane are presented in Table 7.1.

In Table 7.1 the derivatives required for the **A** matrix of the state-space model are shown. The three columns represent the three different Mach numbers along the trajectory. The angle-of-attack variation is linearised between the current state and an increment of 5 degrees, for the side-slip angle the increment is 2 degrees and for the Mach number its an increment of 1. This leads to 12 CFD simulations to obtain one spaceplane aerodynamic database. The outcome of the aerodynamic simulations will be discussed starting with the moments. As can be seen in the table, the C_{m_α} is close to zero as it should be to trim the vehicle and is therefore quite accurate. The small offset from zero is due to the chosen flap deflection. The C_{n_β} is positive which indicates static instability for the yaw moment. Thus, instead of creating a counter moment when there is a non-zero angle-of-sideslip, the spaceplane wants to rotate more. This is also visible in Table 6.1 where the reference aerodynamic derivatives are shown from the source by Cucinelii and Müller [1988]. However, the instability is slightly higher in the simulations compared to the reference. The C_{l_β} is stable and becomes more stable with decreasing Mach number. For the other derivatives, the drag is slightly underestimated due to the simplicity of the model and due to the extra 5 degrees in elevon deflection which leads to less drag and lift at the current attitude. Overall the aerodynamic simulation and flow properties satisfy the accuracy demands.

All the shape modification with their lower and upper limits as described in Table 5.1 and visualised in Figure 5.4 till Figure 5.22 are simulated. The whole database is presented in Appendix C (for reference purposes). Because we are interested in the differences between the original shape and the modified shape, the relative derivatives deviation is presented in Figure 7.1 till **??** for Mach 0.8, 1.5 and 2.5. For the C_{m_α},

Table 7.1: The aerodynamic derivatives of the original modifiable spaceplane.

M	0.8	1.5	2.5
C_{D_α}	0.0091	0.0123	0.0092
C_{L_α}	0.0350	0.0334	0.0241
C_{m_α}	$1.2919 \cdot 10^{-5}$	-0.0010	0.0004
C_{S_β}	-0.0129	-0.0131	-0.0107
C_{l_β}	-0.0032	-0.0020	-0.0008
C_{n_β}	-0.0023	-0.0020	-0.0029
C_{D_M}	0.0208	-0.1598	-0.0253
C_{L_M}	0.1164	-0.1567	-0.0460
C_{m_M}	-0.0543	0.0283	0.0028

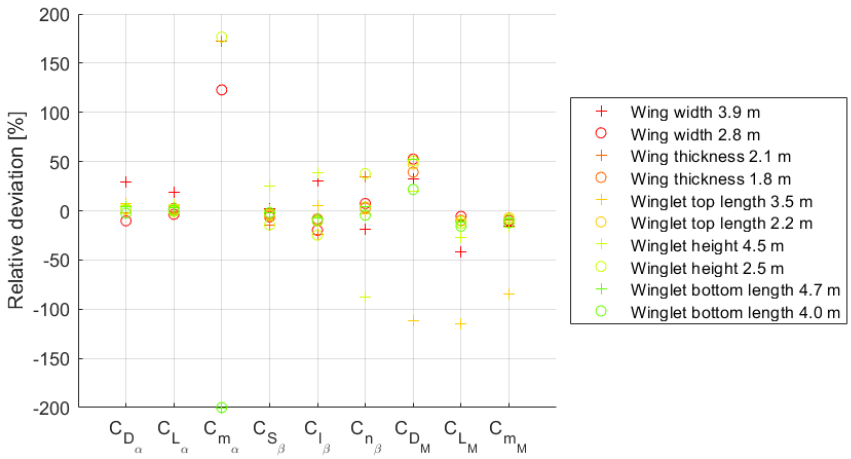

Figure 7.1: The aerodynamic derivatives for the modified spaceplane at Mach 0.8 part 1 of 3.

the deviation is close to zero (due to trim condition), which would blow up the relative derivative deviation. Therefore, it is expressed in the Relative Percent Difference (RPD) which is defined as:

$$\text{RPD} = \frac{x - y}{(|x| + |y|)/2} = 2\frac{x - y}{|x| + |y|}, \tag{7.1}$$

The RPD value is another way to represent the deviation percentage and is slightly better. However, the results of the C_{m_α} are still less convenient to present, because a small deviation compared to zero is still very large. To make the comparison as equivalent as possible, the moment reference point is scaled. For example, for the increase in fuselage length the x-reference length is moved along with a percentage of the increased length. Similarly in the z-direction. For the y-direction this is not necessary because of symmetry. The displacement of the reference center is a realistic estimation and obviously leads to small deviations for the moment coefficients.

In this chapter there will be only focused on the most relevant or negligible shape modification. The wing width (Figures 7.1, 7.4 and 7.7) of the spaceplane increases/decreases the deflection area. This leads to a higher lift coefficient with increasing angle-of-attack and Mach number. Additionally, the pitch moment depending on Mach increases, because of similar reasoning. The thickness of the wing (Figures 7.1, 7.4 and 7.7) does have much impact on the derivatives. For Mach 2.5 all the derivative deviations are within a range of 10%. The only difference is in the drag coefficient depending on the Mach number for lower Mach numbers. This is due to increased/decreased sharpness of the leading edge which has to move along with the thickness of the wing. The change due to the wing thickness is therefore negligibly small and will be used to improve the spaceplane shape. The two parameters which change the location of the corner in the base of the wing (Figures 7.2, 7.5 and 7.8) do not effect the outcome much and are therefore also negligible. This is because the range of the parameter is limited by design limitations. There is a small increase in the side force depending on the side-slip-angle and also less drag depending on how streamlined shape becomes.

Increasing the wing top length (Figures 7.1, 7.4 and 7.7) makes the winglet less streamlined, because

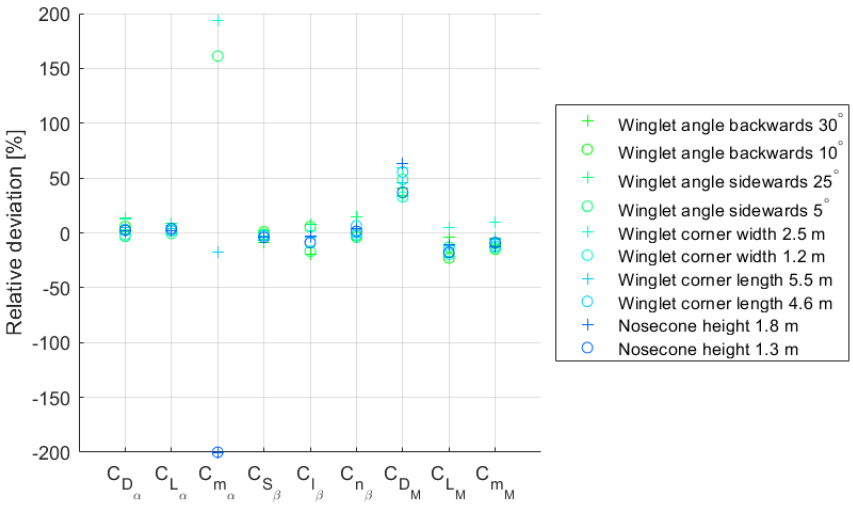

Figure 7.2: The aerodynamic derivatives for the modified spaceplane at Mach 0.8 part 2 of 3.

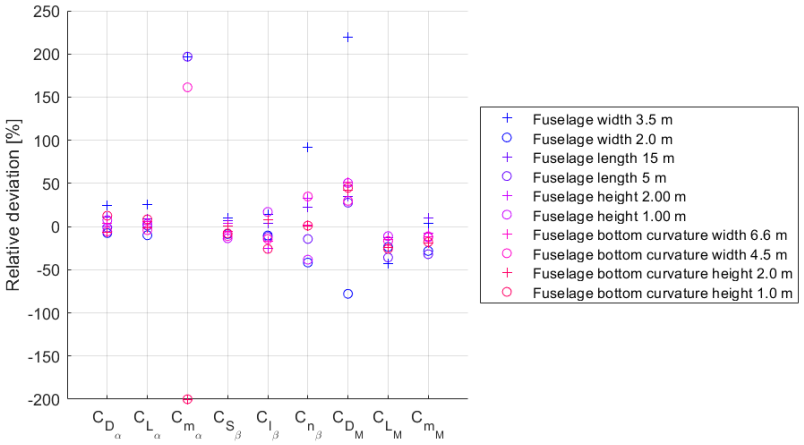

Figure 7.3: The aerodynamic derivatives for the modified spaceplane at Mach 0.8 part 3 of 3.

the back reference point is fixed and therefore the winglet is moving forwards. This affects the lift, drag and pitch coefficients depending on Mach significantly because the spaceplane becomes less streamlined. Hence, increasing the winglet top length reduces the negative lift force and increases the drag force. For the winglet height, which basically increases the winglet, the lateral derivatives change. For instance the C_{n_β} decreases (more statically stable) with increasing winglet and vice versa. Also, the roll coefficient depending on the angle-of-attack is more stable with an increased winglet size. For the bottom length (Figures 7.1, 7.4 and 7.7) of the winglet, which makes the wing less streamlined after the corner, the C_{D_M} also increases, because of similar reasoning as the winglet top length parameter. The backwards angle (Figures 7.2, 7.5 and 7.8) of the winglet is interesting, this shape feature mainly affects the side-slip-angle related derivatives. By moving the vertical reflecting area more backwards, the moment arm is increased which improves the C_{n_β} but decreases the C_{l_β} performance. (These two derivatives counteract each other.) The winglet sideways angle (Figures 7.2, 7.5 and 7.8) is a shape feature which mostly affects the C_{l_β}. An increase in sidewards angle increases the C_{l_β} value.

The nose height (Figures 7.2, 7.5 and 7.8) influences the lift, drag and pitch coefficients related to the angle-of-attack. This makes sense, because the forces on the nosecone will be more upwards or downwards, depending on the pointing direction. For the drag it depends on whether the streamlining is improved, when the angle-of-attack is changed. The effects due to the change in Mach number remain similar.

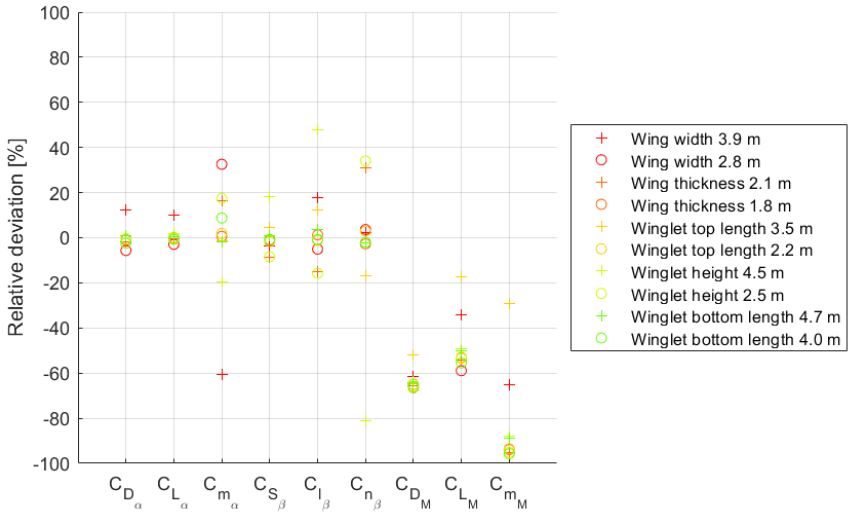

Figure 7.4: The aerodynamic derivatives for the modified spaceplane at Mach 1.5 part 2 of 3.

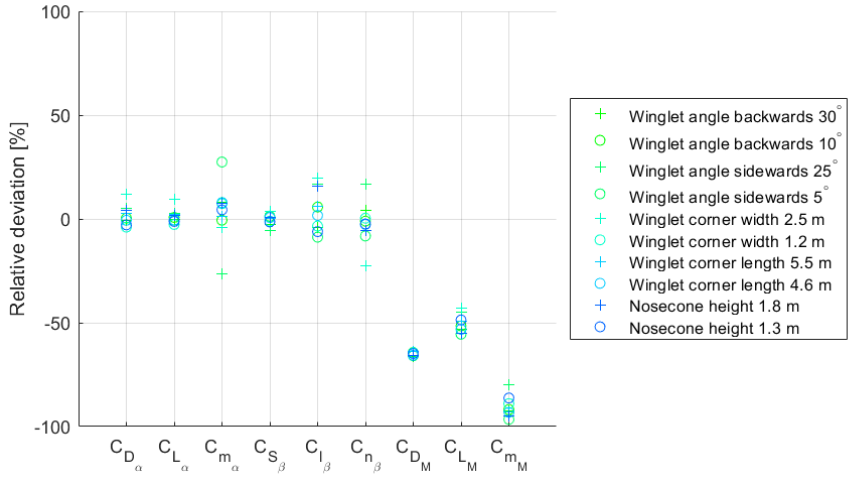

Figure 7.5: The aerodynamic derivatives for the modified spaceplane at Mach 1.5 part 2 of 3.

The fuselage width (Figures 7.3, 7.6 and 7.9) increases the curvature of the nosecone from the nose tip until the start of the fuselage, which leads to much more force in the lateral direction and therefore improves the lateral stability derivatives. In the longitudinal direction a similar response can be seen. A wider base of the vehicle increases the drag forces and also the lift forces because the deflection area becomes larger. Therefore, all the derivatives increase with increasing fuselage width and vice versa. Unlike the fuselage width parameter, the fuselage height (Figures 7.3, 7.6 and 7.9) parameter does not increase all the derivatives. This is due to the fact that the expansion/reduction does not change the reference area for the lift force. Thus, the impact for the angle-of-attack related parameters is not influenced significantly. For the lateral direction, however, the roll derivative becomes lower and the yaw derivative becomes higher with increasing height. Hence, for static stability for both parameters a higher fuselage is desired. The change in height affects the derivatives depending on Mach number the most in a similar manner as the fuselage width. The change in fuselage length (Figures 7.3, 7.6 and 7.9) is one of the parameters which is important if the derivatives related to the angle-of-attack need to be modified. Because the reference area becomes larger, there is more lift and drag gain with increasing angle-of-attack.

Lastly, the curvature of the bottom fuselage and wing depending on height and width (Figures 7.3, 7.6 and 7.9) dimensions as explained in Chapter 5 are discussed. This parameter effects all the coefficients and changes significantly with different Mach numbers. The parameters change the whole design: the fuselage,

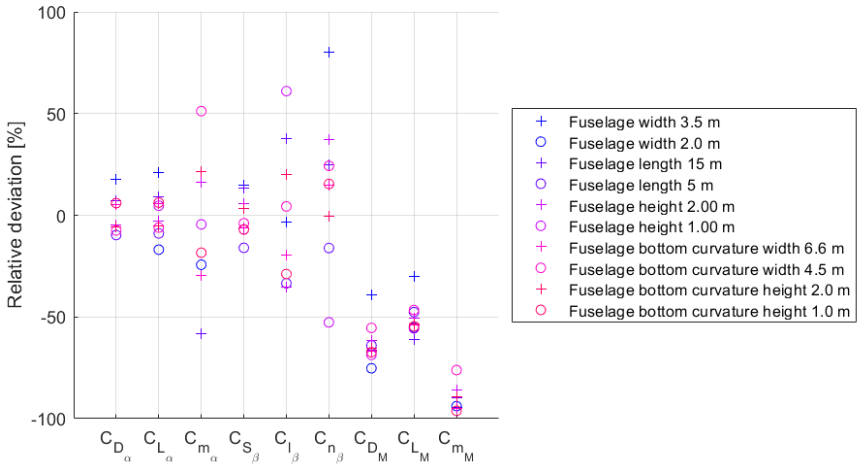

Figure 7.6: The aerodynamic derivatives for the modified spaceplane at Mach 1.5 part 3 of 3.

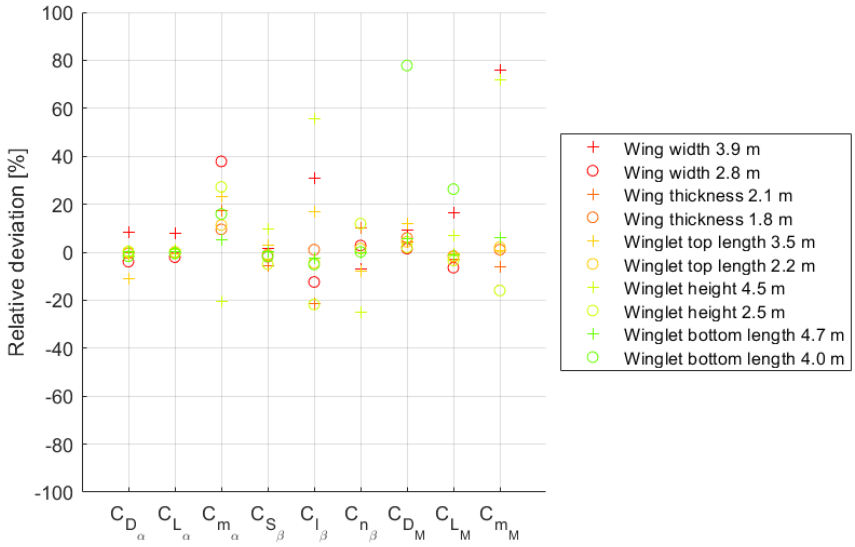

Figure 7.7: The aerodynamic derivatives for the modified spaceplane at Mach 2.5 part 1 of 3.

wings and the wing and winglet interaction. The shape parameters can be compared with the wing folding of birds. When the curvature height is increased, the lift and drag becomes less. Thus, the parameters related to the drag and lift change the most. For the lateral direction, small changes can be seen due to the increase or decrease of the angle of the wing, which causes more vertical forces to act on this part of the vehicle.

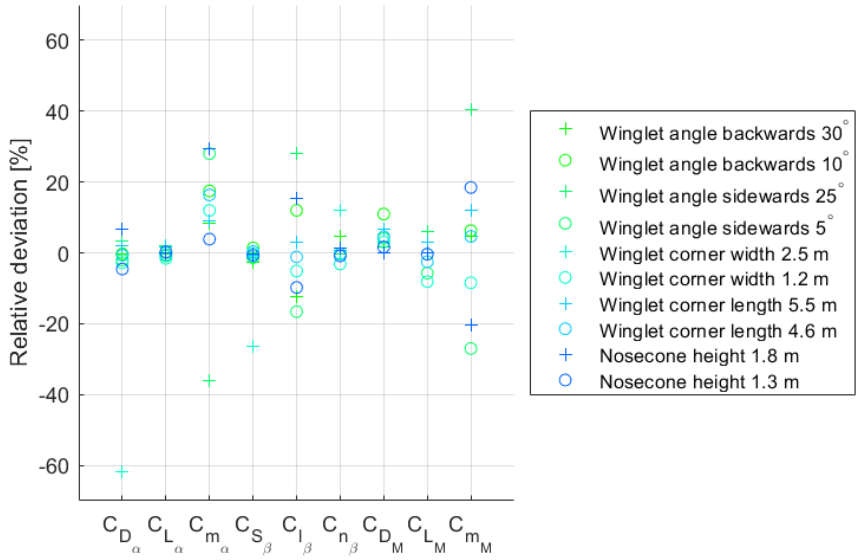

Figure 7.8: The aerodynamic derivatives for the modified spaceplane at Mach 2.5 part 2 of 3.

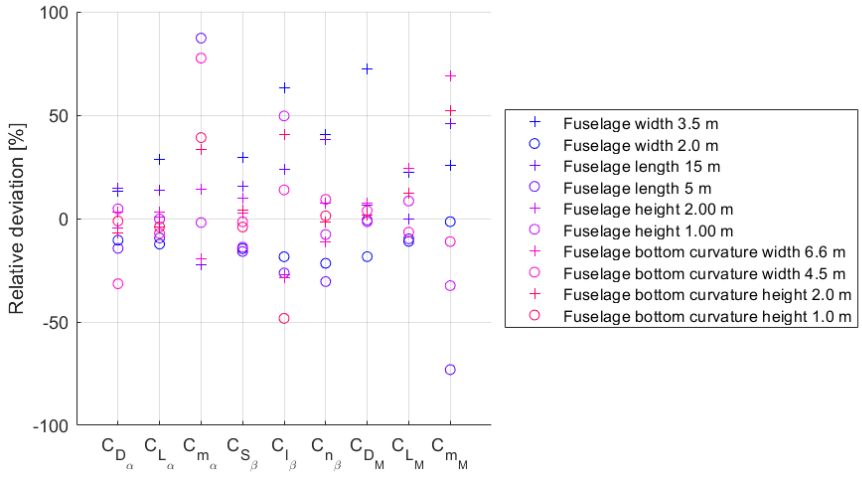

Figure 7.9: The aerodynamic derivatives for the modified spaceplane at Mach 2.5 part 3 of 3.

7.2. Flight modes

The flight modes of the original spaceplane are determined and presented in Tables 7.2, 7.3 and 7.4 for Mach 0.8, 1.5 and 2.5 respectively. Comparing Mach 2.5 with the reference eigenmodes created by the reference data by Cucinelii and Müller [1988] in Table 6.3, the results look similar. The longitudinal short period oscillation is damped for all the Mach numbers. The phugoid however, which is the longer period oscillation, is unstable. The eigenvalue has a positive real part which indicates the instability. When the Mach number is lowered, the phugoid flight modes becomes less unstable. The lateral oscillation, which has a large imaginary part and a small real part, is close to zero and is therefore on the edge of unstable/stable. The periodic pitch/roll mode is stable, but has a long period and high halve time. The pitch/roll divergence determined at Mach 2.5 is slightly unstable. Lastly, the spiral modes are very small and the real part is close to zero. The halve time is very high which means that it takes a long time to become damped again. Overall, the different Mach numbers show similar responses, except that for lower Mach numbers the phugoid will have an imaginary eigenvalue pair. The eigenvalues are more clearly presented in Figure 7.10 which shows the eigenvalues in the complex plane. To improve the spaceplane it is important to make the unstable eigenvalues become stable by changing the real part from positive to negative or less positive.

Instead of showing all the tables with the eigenvalues of different shapes or all the values in the complex plane, the focus will be on the maximum unstable flight mode, which is the eigenvalue of the phugoid mode. By plotting the maximum real part of the eigenvalues, the improvement or deterioration of the stability can be shown. In Figures 7.11, 7.12 and 7.13 the maximum real eigenvalues are shown for Mach 0.8, 1.5, and 2.5 respectively. For the different Mach numbers, the results show similar parameters which improve the eigenvalue. An increase in winglet height decreases the real value by 53% for Mach 2.5. The only difference is that the eigenvalue gains a complex part. This again effects the damping ratio, but not the doubling time. For lower Mach numbers, the percentage is approximately the same. The starting eigenvalue at this Mach number already has an imaginary part and the parameters increase this value slightly. Another parameter which improves the eigenvalue is the fuselage height, by decreasing this parameter the real part lowers with 45% for Mach 2.5. The parameter that does not create an imaginary part when decreasing the real part is the wing width (increasing the wingspan), this lowers the eigenvalue by 36% for Mach 2.5. For the lower Mach numbers, the improvement percentages are a bit lower and they all have an imaginary part as can be seen in Figures 7.11 and 7.12.

The full eigenmotion eigenvalues are presented in Table 7.5. The downside is that the short period oscillation, periodic pitch/roll rate and the second spiral mode became a little less stable. However, the improvement on the phugoid mode is definitely worth the deterioration in the others. For the fuselage height, the outcome is slightly worse for the first spiral mode and slightly better for the second spiral and periodic pitch/roll mode. By increasing the wing width, the improvement in the phugoid mode is less, but the upside is that the (negative) impact on the other eigenvalues is also less.

Different parameters are relevant to improve the other flight modes. Starting with the short period oscillation, the best option for improving the eigenvalue is by increasing the fuselage height and fuselage width. For the lateral oscillation also an increase in fuselage width is desired. The periodic pitch/roll mode is improved by increasing the nosecone height or the wingspan. Finally, the spiral modes are improved by the winglet top length. These results are similar for all the different Mach numbers. Only the percentage improvements for the lower Mach numbers are lower compared to Mach 2.5.

Table 7.2: The eigenmodes of the modifiable spaceplane at Mach 0.8.

		Short period oscillation	Phugoid	Lateral oscillation	Periodic pitch/ roll mode	Spiral mode	
λ_i	Re	-0.1975	0.0975	-0.0044	-0.0186	$3.652 \cdot 10^{-5}$	0
	Im	0	±0.2248	±0.5617	±0.0453	0	0
$P(s)$		Inf	28.0	11.2	138.6	Inf	Inf
$T_{1/2}(s)$		3.5	-7.1	157.9	37.3	$-1.9 \cdot 10^{4}$	Inf
$\zeta(-)$		-	-0.398	0.008	0.379	-	-
$\omega_n(rad/s)$		0.198	0.245	0.562	0.049	$3.652 \cdot 10^{-5}$	0

Table 7.3: The eigenmodes of the modifiable spaceplane at Mach 1.5.

		Short period oscillation	Phugoid	Lateral oscillation	Periodic pitch/ roll mode	Spiral mode	
λ_i	Re	-0.1562	0.0765	0.0003	-0.0074	$3.824{\cdot}10^{-5}$	0
	Im	0	±0.1549	±0.6088	±0.0267	0	0
$P(s)$		Inf	40.6	10.3	235.4	Inf	Inf
$T_{1/2}(s)$		4.4	-9.1	-2480.4	93.8	$-1.8{\cdot}10^{4}$	-Inf
$\zeta(-)$		-	-0.443	-0.001	0.267	-	-
$\omega_n(rad/s)$		0.156	0.173	0.609	0.028	$3.824{\cdot}10^{-5}$	0

Table 7.4: The eigenmodes of the modifiable spaceplane at Mach 2.5.

		Short period oscillation	Phugoid	Lateral oscillation	Periodic pitch/ roll mode	Pitch/roll divergence	Spiral mode	
λ_i	Re	-0.2111	0.1715	-0.0006	-0.0062	0.0378	$1.091{\cdot}10^{-4}$	0
	Im	0	0	±0.6231	±0.0149	0	0	0
$P(s)$		Inf	Inf	10.1	421.3	Inf	Inf	Inf
$T_{1/2}(s)$		3.3	-4.0	1231.5	111.2	-18.3	$-6.4{\cdot}10^{3}$	Inf
$\zeta(-)$		-	-	0.001	0.386	-	-	-
$\omega_n(rad/s)$		0.211	0.172	0.623	0.016	0.038	$1.091{\cdot}10^{-4}$	0

Table 7.5: The eigenmodes of the spaceplane with winglet height of 4.5 m at Mach 2.5.

		Short period oscillation	Phugoid	Lateral oscillation	Periodic pitch/ roll mode	Spiral mode	
λ_i	Re	-0.1643	0.0813	-0.0005	-0.0020	$1.461{\cdot}10^{-5}$	0
	Im	0	±0.0787	±0.6532	±0.0155	0	0
$P(s)$		Inf	79.8	9.6	404.6	Inf	Inf
$T_{1/2}(s)$		4.2	-8.5	1476.3	349.1	$-4.7{\cdot}10^{4}$	-Inf
$\zeta(-)$		-	-0.718	0.001	0.127	-	-
$\omega_n(rad/s)$		0.164	0.113	0.653	0.016	$1.461{\cdot}10^{-5}$	0

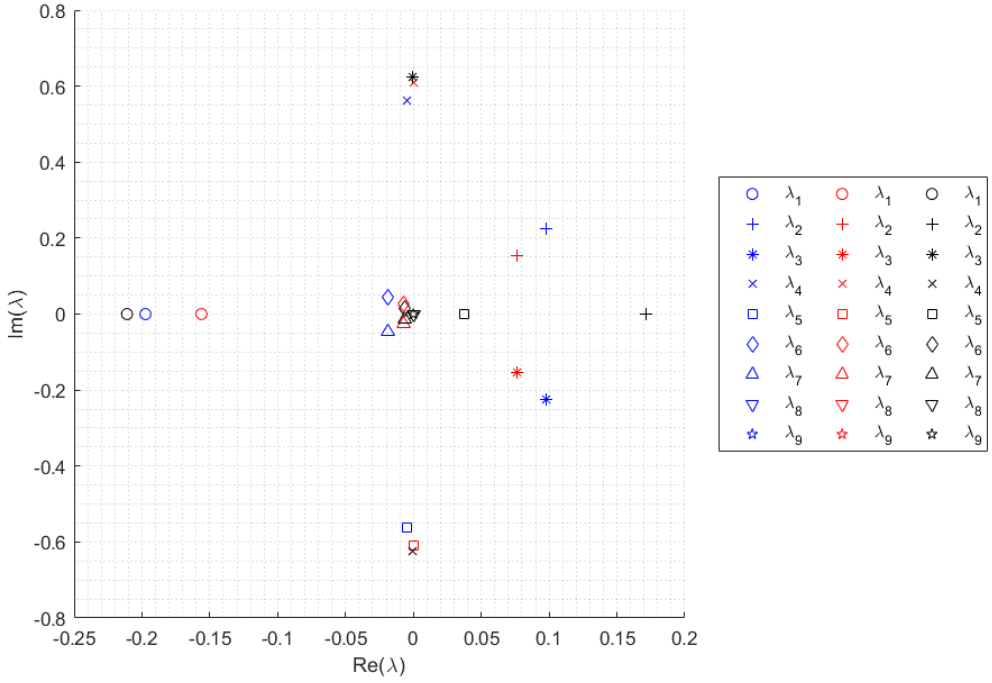

Figure 7.10: The eigenvalues of the modifiable spaceplane for Mach 0.8 (blue), 1.5 (red) and 2.5 (black).

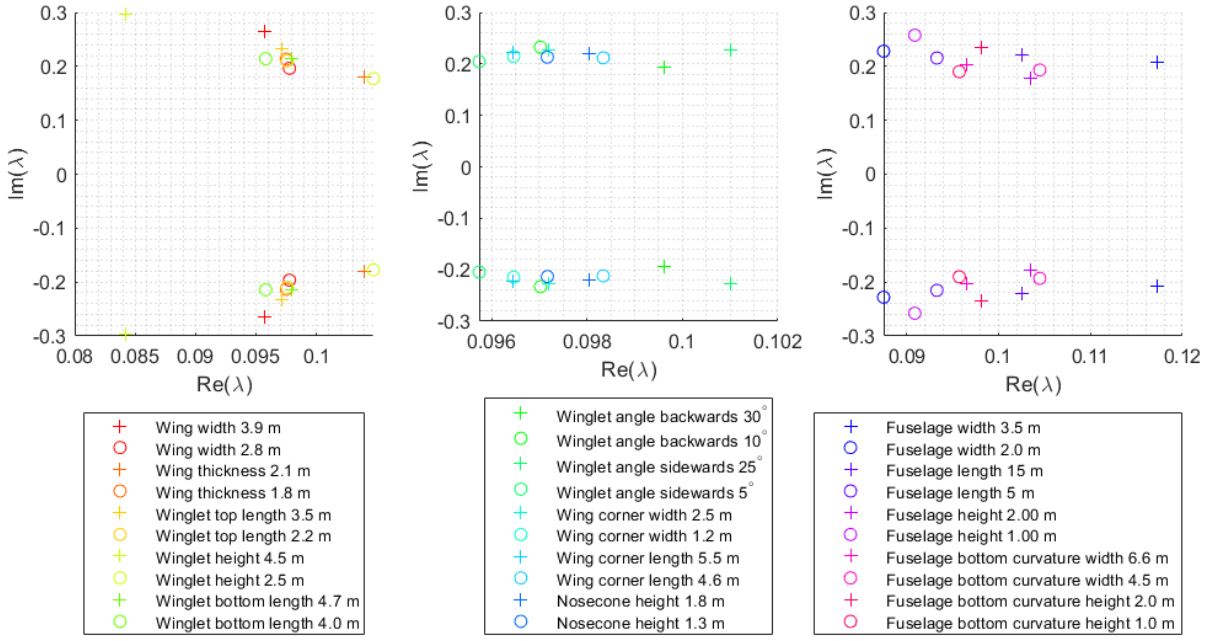

Figure 7.11: The complex eigenvalue of the phugoid flight mode at Mach 0.8.

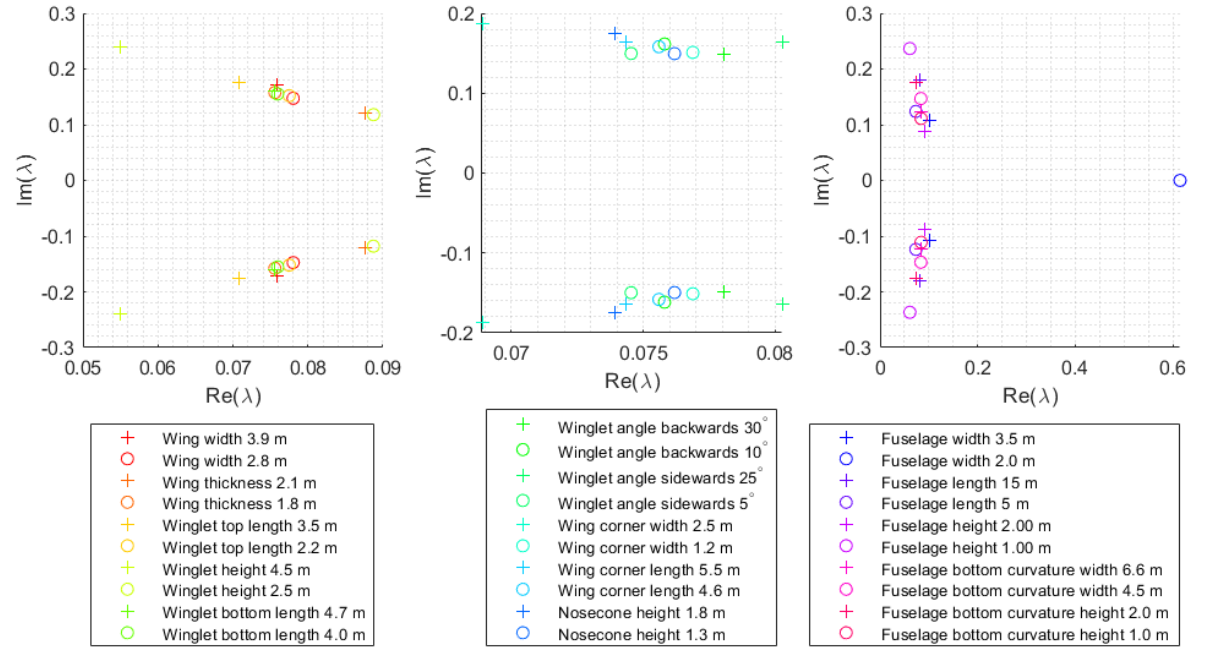

Figure 7.12: The complex eigenvalue of the phugoid flight mode at Mach 1.5.

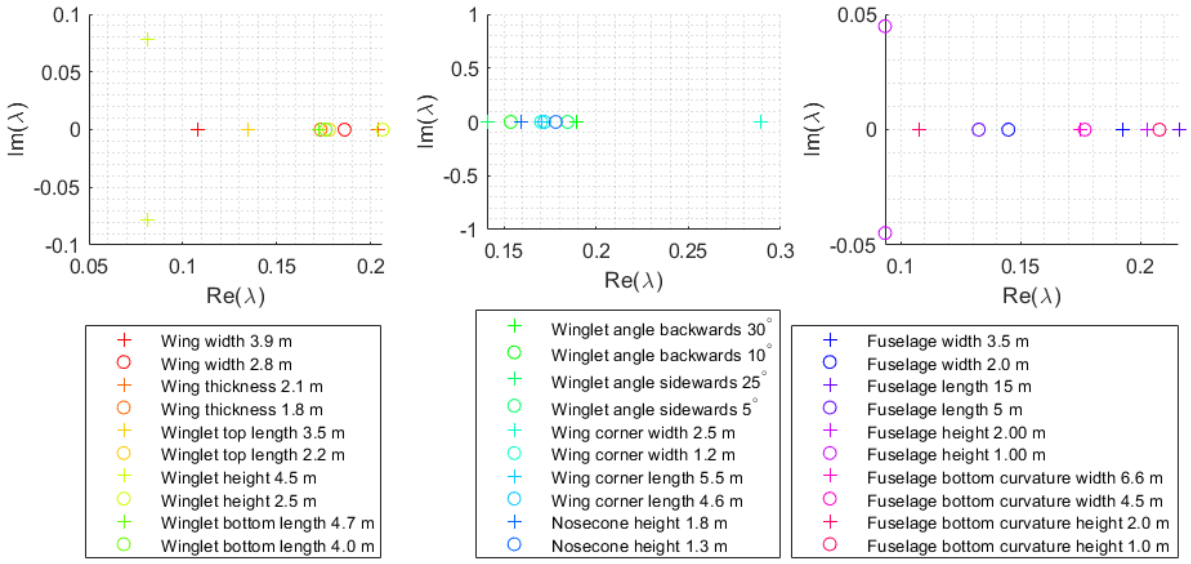

Figure 7.13: The complex eigenvalue of the phugoid flight mode at Mach 2.5.

7.3. MIL standards

In this section, the results of the eigenmotions will be compared with the military requirements. As explained earlier, there are military requirements that give confirmation for a save flight. These requirements are stated for the short period, the phugoid and the lateral oscillation.

- The longitudinal short period oscillation, has a requirement based on the damping ratio for this particular eigenmotion. For level 1, a damping is required between 0.30 and 2.00. For level 2 (which is worse), the damping ratio may be lowered to 0.20 and for level 3 (which is the worst case), the damping may be lowered to 0.15. However, because the eigenvalue of this motion only has a real part, the motion is aperiodic and therefore the damping ratio is not defined. Not only is this the case for the original spaceplane, but also for all the modified simulated spaceplanes. Stated by Mooij [2015], this eigenmotion of the original spaceplane will only have an imaginary part at an altitude of approximately 70 kilometers or higher where the Mach number is in between 15 and 20 and upwards. (For these calculations the corresponding parameters along that point in the trajectory are used, similar to this research.) With the shape modifications, the input parameters are kept similar except of the aerodynamic derivatives. Therefore, the eigenvalue results for this eigenmotion are also similar. Thus, the military requirements for the longitudinal direction can not be compared with the generated results. Only if higher velocities are simulated this might be the case. Overall, the short period oscillation has a high real value which means that this mode is most stable compared to the others.

- The phugoid flight mode, also has requirements depending on the damping ratio and the doubling time. For level 1 the damping ratio must be higher than 0.04, for level 2 the damping must be at least higher than 0 and for level 3 the doubling time (which means unstable motion) must be at least higher than 55 seconds. The phugoid mode is already discussed above and has a negative real value which indicates instability. The eigenvalues for Mach 2.5 of most of the modified spaceplanes and the original spaceplane again have only a real part (this is shown in Figure 7.13). This again means that the damping ratio cannot be determined. For the lower Mach numbers, 1.5 and 0.8, all the spaceplanes will have a conjugate eigenvalue pair with a negative real value. However, because the real part is negative the damping ratio is negative, which means that the damping ratio becomes an amplification ratio and the halve time becomes doubling time. Thus, without doing any calculations it can be determined that the first and second military requirement levels will not be satisfied for these Mach numbers and shape modifications. The only option is to decrease the real part of the eigenvalue, which makes the eigenmotion less unstable, (but still unstable), and increases the doubling time. This was already investigated in the previous section.

  The lowest real value for Mach 2.5 is the increased winglet height, this results in a real part of -0.0813 which gives a doubling time of 8.53 seconds (as can be seen in Table 7.5. The doubling time is not high enough to satisfy the level 3 requirement of the military requirements. However, the doubling time has improved from the starting value of 4.04 seconds shown in Table 7.4. For Mach 1.5, the winglet height increases the doubling time to 12.62 seconds and for Mach 0.8 this decreases again to 8.23 seconds. This individual shape modification does not lead to satisfying the military requirements

- The lateral oscillation has military requirements based on the damping ratio, natural frequency and a combination of both. For each level, all three requirements have to be satisfied (the natural frequency requirement may not be valid for this type of vehicle). For level 1 the minimum damping ratio has to be 0.08, the product of damping ratio and natural frequency has to be higher than 0.15 and the natural frequency has to be higher than 0.4. Level 2 requires a minimum damping of 0.02, the product has to be higher than 0.05 and the natural frequency has to be higher than 0.4. Finally, the level 3 requirement, requires a damping higher than 0, the combination is not specified and the natural frequency higher than 0.4.

  Because for this flight mode all the spaceplane modifications are within the potential to satisfy the requirement, the results are plotted for Mach 0.8. The damping ratio, natural frequency and the product of both are visualised in Figures 7.14a, 7.14b and 7.15, respectively. For the damping ratio all the spaceplane modifications and also the original spaceplane are just within the level 3 requirement. For the natural frequency all the spaceplanes (including the original) are far above the level 1 requirement and for the multiplication of the natural frequency and damping ratio most of the spaceplanes are below the level 2 requirement. Some modification such as: the increased wing width, fuselage width and

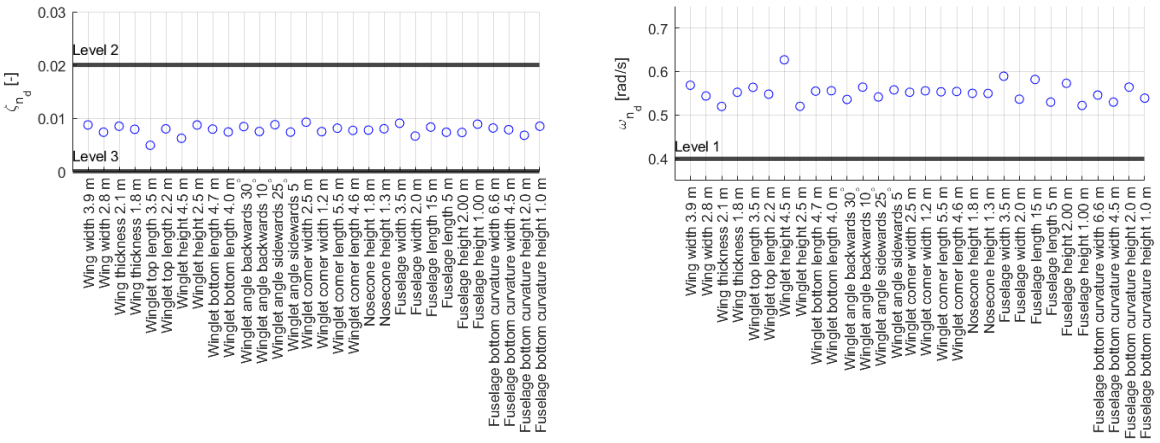

(a) the damping ratio

(b) the natural frequency

Figure 7.14: The lateral oscillation results of different spaceplanes compared with the military requirements for Mach 0.8.

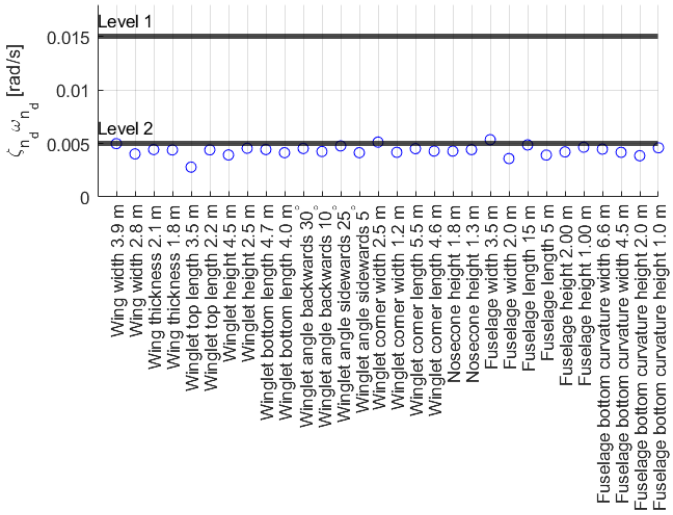

Figure 7.15: The lateral oscillation results of different spaceplanes compared with the military requirements for Mach 0.8.

wing corner width the values are barley in the level 2 requirement. The results combined for all the modified spaceplanes, lead to a satisfied level 3 requirement for the lateral oscillation, which is not very good. Additionally, as can be seen in the results, a single change in shape parameter cannot lead to satisfying the level 2 requirements, due to the low damping ratio. The best option to improve this flight mode is to decrease the fuselage height, increase the fuselage width and length and increase the wing width. There are also some parameters such as increasing the winglet height and increasing the backwards and sidewards angle of the winglet. However, each of these parameters or combined will probably not lead to level 2, because each of these parameters do not effect damping ratio significantly. Unless changing the parameters until unrealistic shape would be generated, which would not be possible within the bounds of this model. For Mach 2.5, the damping ratio and the product of the damping and natural frequency become a little lower. But, overall the results for Mach 1.5 and 2.5 look the same.

7.4. Optimising the spaceplane shape

To optimise the shape based on the knowledge gained in the previous sections we must do the following shape modifications. To improve the static stability for the yaw moment coefficient depending on the side-

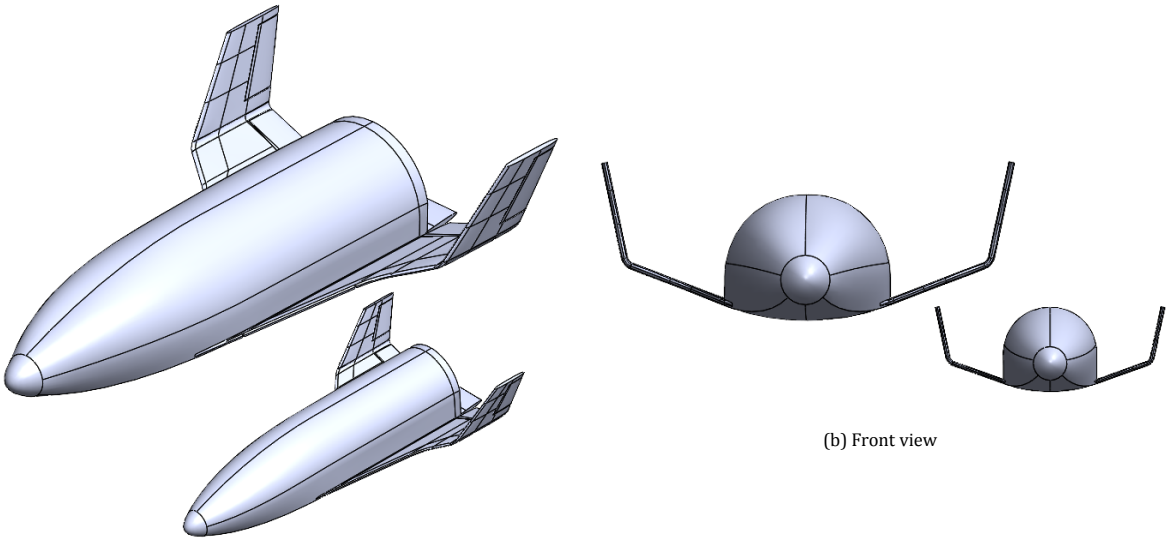

(a) 3-Dimensional view

(b) Front view

Figure 7.16: The final optimised shape configuration on the left upper side and the original on the right lower side. The fuselage wider and less high, the winglet and wingspan in increased explained in Section 7.4.

slip-angle we desire to increase the winglet height. This parameter is also desired to increase the dynamic stability, in particular for the phugoid flight mode. The fuselage height is preferred to be lowered for the eigenvalue of the phugoid eigenmode, but this will decrease the short period oscillation and the lateral oscillation. Therefore, this parameter cannot be used to improve the phugoid eigenvalues. Another positive effect for the phugoid mode is to increase the wing width and therefore the wingspan. The last parameter which will improve this mode is to increase the fuselage width. For the spiral mode, the winglet top length is desired to be enlarged, but this will decrease the pitch/roll divergence performance.

Thus, for the next simulation the parameters are set to:

- The winglet height is increased from 3.2 to 4 meters.
- The straight part of the fuselage height is decreased from 1.57 to 1 meter.
- The fuselage width (one side) is increased from 2.5 to 3 meters.
- The wing width is increased from to 3.1 to 3.9 meters.
- The winglet top length is increased from to 2.5 to 3 meters.

These shape modifications result in the following shape, as can be seen in Figure 7.16. For the fuselage and the nosecone there are not that many differences compared to the original. In contrast, the wing and winglet are enlarged significantly. The changes in aerodynamic characteristics are shown in Table 7.6. The fuselage width and wing expansion created more deflecting area and therefore more lift with increasing angle-of-attack. Also, the increased winglet creates more deflection when the angle-of-sideslip is non-zero. The drag is reduced because of a lower fuselage and can be noticed when adjusting the angle-of-attack. The static stability of the yaw coefficient is improved, especially for Mach 1.5, but still slightly statically unstable. These derivatives are implemented in the state-space form and the eigenmotions are determined. The results for Mach 0.8, 1.5 and 2.5 are stated in Table 7.7. For this optimised shape the military requirements and the behaviour in higher Mach regimes will be determined in the next couple of sections.

Table 7.6: Aerodynamic coefficients of the optimised spaceplane shape.

	optimised spaceplane		
M	0.8	1.5	2.5
C_{D_α}	0.0113	0.0145	0.0105
C_{L_α}	0.0405	0.0387	0.0274
C_{m_α}	0.0005	-0.0008	0.0007
C_{S_β}	-0.0146	-0.0147	-0.0116
C_{l_β}	-0.0057	-0.0039	-0.0017
C_{n_β}	-0.0011	-0.0008	-0.0027
C_{D_M}	0.0406	-0.0684	-0.0333
C_{L_M}	0.0465	-0.0925	-0.0559
C_{m_M}	-0.0391	-0.0004	0.0024

7.4.1. Satisfying the MIL standards

The dynamic stability of the different flight modes is discussed here:

- For the longitudinal short period oscillation the real part of the eigenvalue is increased, which indicates that the eigenmotion is still less dynamically stable (as predicted). However, because the eigenvalue is still negative, the motion is still stabilising. This is a side effect of optimizing the shape such that the phugoid manoeuvre becomes less unstable. The eigenvalue still does not contain an imaginary part and therefore this eigenmotion can still not be compared with the military requirements from the source MIL-F-8785C [1980] and MIL-HDBK-1797 [1997].
- For the phugoid eigenmotion the overall doubling time is improved from approximately 4 seconds to 8 seconds for Mach 2.5. This is not spectacular, but based on our findings in the previous section, it is difficult to achieve a large improvement with the shape parameters and their scopes which are available in this model. The result is still unstable and far from the level 3 requirement (which is the lowest). The spaceplane is still very unstable for this eigenmotion.
- The lateral oscillation is stable and slightly improved for Mach 2.5, 1.5 and 0.8. This requirement meets the required level 3 demands for all three Mach numbers. The damping ratio is above 0 (which is level 3) and becomes closer to the level 2 requirement, but is not level 2 yet. The natural frequency is above 0.4 (which is level 1) and therefore very good. The combination of the damping ratio multiplied with the natural frequency is in the level 2 requirement. This leads to a total level 3 for this eigenmotion. But, the behaviour on this flight mode is significantly improved.
- The periodic pitch has negative imaginary parts as well for all three different Mach numbers, indicating stability.
- The spiral modes are slightly positive, but is so small that the doubling time is extremely large. Therefore these modes are negligible and can be easily anticipated.

7.4.2. Behaviour hypersonic regime

To make sure that for higher Mach numbers the spaceplane still has reasonable dynamic stability, the aerodynamic derivatives for Mach 5 and 10 are determined and presented in Table 7.8, leading to the eigenmotions visualised in Table 7.9. For these results the input parameters are changed to the corresponding atmospheric properties stated in Table 4.1. The imaginary part of the phugoid disappeared again, similar as seen above for some Mach 2.5 shapes. The flight modes of the higher Mach numbers look similar, except for the unstable pitch/roll divergence. Compared to the eigenmotions at these Mach numbers determined by Mooij [2015], the outcome looks similar. In these results the longitudinal phugoid and the pitch/roll divergence are unstable. However, for the optimised spaceplane the lateral oscillation is still negative and therefore stable. Thus, the lateral oscillation is also improved for higher Mach regimes. Overall, the modified spaceplane has no stability downside in the hypersonic flight regime. In Figure 7.17 a hypersonic flow (Mach 5) simulation of the optimised shape with 10° angle-of-attack is visualised.

Table 7.7: Eigenmotions for different Mach numbers of the optimised spaceplane shape.

		Mach 2.5					
		Short period oscillation	Phugoid	Lateral oscillation	Periodic pitch/ roll mode	Spiral mode	
λ_i	Re	-0.1715	0.0847	-0.0007	-0.0072	0.0001	0
	Im	0	±0.1010	±0.6481	±0.0148	0	0
$P(s)$		Inf	62.2	9.7	423.5	Inf	Inf
$T_{1/2}(s)$		4.0	-8.2	1013.2	96.7	-5574.8	-Inf
$\zeta(-)$		-	-0.643	0.001	0.435	-	-
$\omega_n(rad/s)$		0.171	0.132	0.648	0.016	0.0001	0
		Mach 1.5					
		Short period oscillation	Phugoid	Lateral oscillation	Periodic pitch/ roll mode	Spiral mode	
λ_i	Re	-0.1228	0.0595	-0.0016	-0.0144	$7.9057 \cdot 10^{-5}$	0
	Im	0	±0.2626	±0.6450	±0.0259	0	0
$P(s)$		Inf	23.9	9.7	242.3	Inf	Inf
$T_{1/2}(s)$		5.6	-11.7	428.8	48.2	-8767.7	Inf
$\zeta(-)$		-	-0.221	0.003	0.485	-	-
$\omega_n(rad/s)$		0.123	0.269	0.645	0.030	$7.905 \cdot 10^{-5}$	0
		Mach 0.8					
		Short period oscillation	Phugoid	Lateral oscillation	Periodic pitch/ roll mode	Spiral mode	
λ_i	Re	-0.1911	0.0931	-0.0043	-0.0219	$3.462 \cdot 10^{-5}$	0
	Im	0	±0.3173	±0.5957	±0.0497	0	0
$P(s)$		Inf	19.8	10.5	126.5	Inf	Inf
$T_{1/2}(s)$		3.6	-7.4	159.7	31.7	-20020	-Inf
$\zeta(-)$		-	-0.282	0.007	0.403	-	-
$\omega_n(rad/s)$		0.191	0.331	0.596	0.054	$3.462 \cdot 10^{-5}$	0

Table 7.8: Aerodynamic coefficients for higher Mach numbers of the optimised spaceplane shape.

	optimised spaceplane	
M	10	5
C_{D_α}	0.0066	0.0077
C_{L_α}	0.0178	0.0199
C_{m_α}	0.0010	0.0010
C_{S_β}	-0.0088	-0.0095
C_{l_β}	-0.0014	-0.0012
C_{n_β}	-0.0027	-0.0029
C_{D_M}	0.0009	-0.0075
C_{L_M}	-0.0027	-0.0167
C_{m_M}	0.0007	0.0009

Table 7.9: Eigenmotions for high Mach regime of the optimised spaceplane shape.

		Mach 5						
		Short period oscillation	Phugoid	Lateral oscillation	Pitch/roll divergence	Periodic pitch/ roll mode	Spiral mode	
λ_i	Re	-0.1417	0.0980	-0.0001	0.0434	-0.0016	$1.368 \cdot 10^{-4}$	0
	Im	0	0	±0.4470	0	±0.0064	0	0
$P(s)$		Inf	Inf	14.1	Inf	979.4	Inf	Inf
$T_{1/2}(s)$		4.9	-7.1	4972.3	-16.0	427.5	$-5.069 \cdot 10^{3}$	Inf
$\zeta(-)$		-	-	0.0003	-	0.245	-	-
$\omega_n(rad/s)$		0.142	0.098	0.447	0.043	0.007	$1.368 \cdot 10^{-4}$	0
		Mach 10						
		Short period oscillation	Phugoid	Lateral oscillation	Pitch/roll divergence	Periodic pitch/ roll mode	Spiral mode	
λ_i	Re	-0.0910	0.0520	0	0.0389	-0.0006	$1.575 \cdot 10^{-4}$	0
	Im	0	0	±0.3236	0	±0.0029	0	0
$P(s)$		Inf	Inf	19.4	Inf	2180.5	Inf	Inf
$T_{1/2}(s)$		7.6	-13.3	23675	-17.8	1165.9	$-4.402 \cdot 10^{3}$	Inf
$\zeta(-)$		-	-	0	-	0.202	-	-
$\omega_n(rad/s)$		0.091	0.052	0.324	0.039	0.003	$1.575 \cdot 10^{-4}$	0

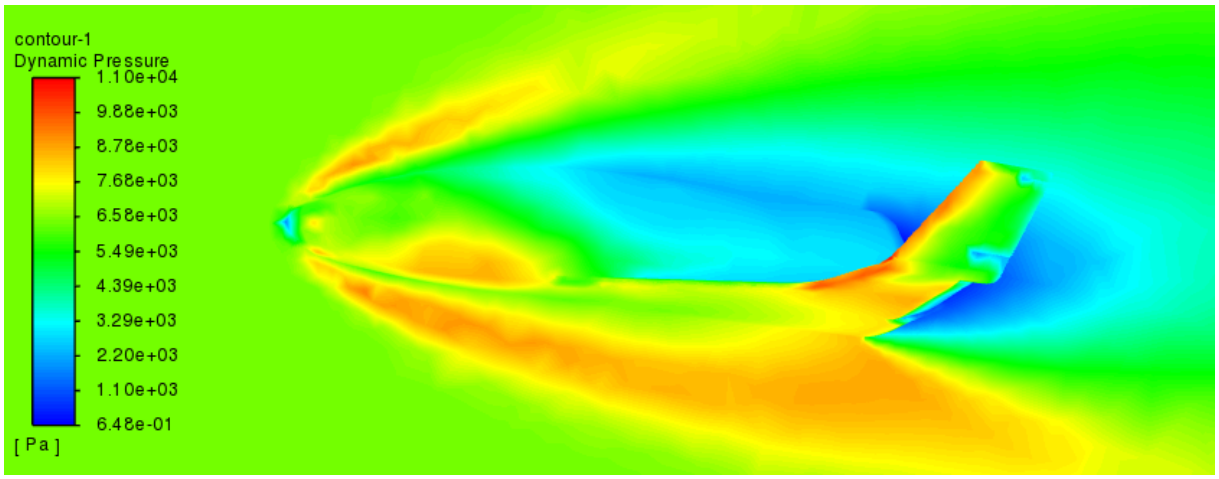

Figure 7.17: A Mach 5 flow simulation of the optimised spaceplane shape with an angle-of-attack of 10° (trimmed condition). On the right side the dynamic pressure is shown.

8

Conclusion and Recommendations

In this chapter the conclusions and recommendations of this research will be stated and discussed. To begin with stating the influences of the spaceplane modification parameters. Leading to the most important optimisation parameters to improve the flying qualities. Followed by comparing these parameters with the military requirements. At that point all the research questions are answered. This chapter will be concluded with the recommendations for further research. Which involve controllability performance, data reliability and a better optimisation process.

8.1. Conclusions

8.1.1. Shape optimisation

From the 15 modification parameters which were investigated, some are more interesting than others. Parameters which had a small modification range did not change the aerodynamic characteristic much, leading to negligible small influence on the flying qualities. These parameters are the wing thickness, winglet bottom length, changing the location of the wing corner and the parameters related to the bottom fuselage/wing curvature. Other parameters such as: fuselage, the wing and winglet design had more influence on the static and dynamic stability.

To improve the yaw moment static stability derivative, which is a problem for many spaceplanes, the winglet height and winglet top length are enlarged. This increases the flow deflection when a non-zero angle-of-sideslip occurs, leading a counter moment pushing the spaceplane back towards the desired zero angle-of-sideslip equilibrium. The downside of this modification is that the longitudinal short period oscillation and periodic pitch/roll eigenmodes decreased in dynamic stability.

The phugoid flight mode is one of the most (and only) unstable eigenmodes of the HORUS spaceplane. Increasing the winglet height and decreasing the fuselage height improved the stability of the phugoid flight mode. The real eigenvalue becomes closer to zero and the imaginary part becomes non-zero. The downside of this modification is again an increase in the short-period oscillation, but this is still a stable eigenmode after the modifications.

To improve the lateral oscillation eigenmode the fuselage width, wing width and the winglet height are increased. The increased nose curvature length due to the increased fuselage width creates more deflection which is able to damp the oscillation in the lateral direction. Similar, reasoning can be used for the increased winglet height. The results showed an increase in natural frequency as well as for the damping ratio. The increase in damping ratio and natural frequency increased the lateral dynamic stability, with these improvements the lateral eigenmode almost became level 2. The downside of these modifications is again a slight decrease in stability for the short period oscillation. The other modification parameters were also investigated, but the effects on the flying qualities due to these parameters are significantly smaller, and are therefore not further analysed. These include the nosecone height, winglet backwards and sidewards angle.

For the optimisation process all the parameters, which significantly improved the unstable eigenmodes were used. The final optimisation led to: a winglet height increase from 3.2 m to 4 m, fuselage height (straight part) decrease from 1.57 m to 1 m, fuselage width (one side) increase from 2.5 m to 3 m, a wing width increase from 3.1 m to 3.9 m and a winglet top length increase from 2.5 to 3 m. The optimised spaceplane shape led to: an improved yaw static derivative by 7.4% (slightly statically unstable), an improved phugoid flight mode

real eigenvalue by 45.6% (slightly dynamically unstable), a deteriorated short period oscillation real value by 9.5% (dynamically stable) and increased lateral oscillation real eigenvalue by 16.7% (dynamically stable) for Mach 2.5. The other static stability derivatives and eigenmodes are not effected significantly such that they become unstable. Overall, the compromise in the short period eigenmode is worth the improvement in the other stability characteristics. These improvements almost resulted in a level 2 dynamic stability for the lateral oscillation. The military requirements of the longitudinal direction could not be compared with the requirements, because the eigenvalues only consisted of a real part and not an imaginary part. But, based on the definition of the eigenvalues, which indicate that an negative eigenvalue is stable, conclusions can still be made. The short period oscillation is stable and the phugoid eigenmode is slightly unstable and has to be artificially controlled by the flaps to create stability. For the other Mach numbers: Mach 0.8 and Mach 1.5 the numbers are similar and therefore the conclusions about static and dynamic stability are the same. The only difference is that the improvement percentage is a little lower for lower Mach numbers. These results and conclusions are answered the main research question. The geometry dimensions which influence the spaceplane's flying qualities the most (Sub research question 2.) are the fuselage dimensions, the wing width and the size of the winglet.

However, there is not a single parameter or combination of parameters that could have made such a difference that all the military requirements would have been satisfied. With the shape modification parameters and their scope which were available in this model, the level 1 military requirements for the lateral oscillation cannot be reached for the TAEM phase of the re-entry. With a full optimisation and more computational power there might be a shape that satisfies the level 2 military requirement. Also, creating dynamic stability for the phugoid flight mode appeared to be not possible. For the former short period oscillation no modification are required, this flight mode was already stable and will still be stable with the modifications. Other shape modifications were in contradiction with the limitations set by the thermo-mechanical load limits (sub research question 1.), such as: nosecone and sharpness of the leading edges. This makes satisfying the military requirements difficult. The blunt nosecone leads to bad dynamic stability and has a dominant effect as shown by the results. Other spaceplanes, such as the Space Shuttle Orbiter, have similar problems and solve these by artificially stabilising the spaceplane with control surfaces or thrusters. But, if these control surfaces and thrusters fail, and the spaceplane is in such an unstable eigenmode, this will have disastrous effects. Than, the manoeuvre will be amplified until the spaceplane crashes. This is one of the biggest problematic consequence of the spaceplane design.

8.1.2. Hypersonic behaviour

For research question 3., the optimised spaceplane is simulated for hypersonic conditions. The modified spaceplane did not effect the flight modes in a negative manner. At these speeds the positive pitch roll divergence flight mode appears, with a positive real eigenvalue (indicating unstable). But, this behaviour is also showing in the eigenmodes from the original spaceplane. The final results show actually still an improvement in the lateral oscillation eigenmode compared to the original spaceplane. For other eigenmodes the results look similar and therefore the modified spaceplane did not negatively effect the spaceplane's performance in the higher flow regimes.

8.2. Recommendations

8.2.1. Controllability

The model is also able to study and modify the effects of the deflection surfaces. The control characteristics/derivatives can be determined by the CFD model and be implemented into the $\mathbf{B}$ matrix of the state-space model. These changes can be studied by comparing the control effort required for artificially stabilising the spaceplane. For this investigation a complete control model is required, instead of only the plant (system) matrix which described the motion of the spacecraft. However, these shape modifications and necessary control effort were not studied due to the time constraints of this research. For investigating the full flying qualities of a spaceplane, both the stability and controllability has to be investigated. Therefore, for further research it is desired to take a look into the controllability of these modified spaceplanes. With an improvement in dynamic stability due to the base of the vehicle, less control effort is required to keep the spaceplane stable for a controlled and safe flight. This investigation would lead to a complete overview of the flying qualities.

8.2.2. Data reliability

The data of the CFD simulations are quite accurate as shown in the validation chapter. All the results made sense, except for the parameters affecting the corner of the wing and also the curvature of the bottom of the spaceplane. These parameters sometimes gave extreme derivatives and might be incorrect. The reason for this behaviour is that these parameters are the most complex shape modifications. For each of these four parameters, a bunch of adjustments in the design must be performed to correctly generate the shape. This is likely the reason for the sometimes odd behaviour in the derivatives.

Another recommendation is to simulate the spaceplane with a more advanced mesh and fluid model. This would answer if the forces and moments in the lateral direction can be determined more accurately. If these are determined more accurately the overall research accuracy would be improved.

8.2.3. Optimisation

In this research the computational capabilities were limited leading to a simplistic optimisation and rough estimate of the aerodynamic characteristics. The model is able to perform a full optimisation by creating an algorithm in Matlab. This will find the optimal performance in flight modes or static stability derivatives. For instance, a Monte Carlo simulation would show the best parameter and the individual capabilities of the parameters to improve the flight modes. A computer with more capabilities would improve the outcome of this research significantly and show the full capability of the model and therefore the potential of each shape modification parameter.

But, if a full optimisation study will be performed, the results would probably not create full dynamic stability. The results showed that one or a combination of multiple parameters would likely not create full stability. This research was based on small shape modifications while preserving the original style of the HORUS-2B spaceplane. However, to further improve the stability, other shape implementation features are required, such as: a different wing/fuselage design or an additional wing. Thus, more promising stability improvements would likely be outside the scope of these modification parameters.

Bibliography

ANSYS Inc. ©. ANSYS FLUENT 12.0 Theory Guide. January 2009.

Brykina I.G., Rogov B.V., and Tirskiy G.A. The applicability of continuum models in the transitional regime of hypersonic flow over blunt bodies. *Journal of Applied Mathematics and Mechanics*, 73(5): 502–513, January 2009. ISSN 00218928. doi: 10.1016/j.jappmathmech.2009.11.003.

Camarda C. J. Space Shuttle Design and Lessons Learned. 2014. doi: 10.13140/RG.2.1.2635.2405.

Cucinelii G. and Müller W. Study on Re-entry Guidance and Control (HORUS-2B vehicle). Final Report Vol. 2, MBB, Germany, April 1988.

Detra R. W. and Hidalgo H. Generalized Heat Transfer Formulas and Graphs for Nose Cone Re-Entry Into the Atmosphere. *ARS Journal*, 31(3): 318–321, January 1961. ISSN 1936-9972. doi: 10.2514/8.5471.

Dobrov Y., Gimadiev V., Karpenko A., and Volkov K. Numerical simulation of hypersonic flow with non-equilibrium chemical reactions around sphere. *Acta Astronautica*, page S009457652100549X, October 2021. ISSN 00945765. doi: 10.1016/j.actaastro.2021.10.008.

D'Souza A. F. *Design of control systems*. Prentice-Hall, Englewood Cliffs, N.J, 1988. ISBN 978-0-13-199951-0.

Ericsson L. E. and Reding J. P. Aerodynamic effects of bulbous bases. Contractor Report 19690026143, NASA, Washington, D. C., August 1969.

Etkin B. and Reid L. D. *Dynamics of flight: stability and control*. Wiley, New York, 3rd ed edition, 1996. ISBN 978-0-471-03418-6.

Filippone A. *Flight Performance of Fixed and Rotary Wing Aircraft*. Elsevier Science & Technology Books, Jordan Hill, 2006. ISBN 978-0-08-046103-8.

Heracleous L., Terrier D., and Gonzalez S. NASA's Capability Evolution Toward Commercial Space. *Space Policy*, 50: 101330, November 2019. ISSN 02659646. doi: 10.1016/j.spacepol.2019.07.004.

Hirschel E. H. and Weiland C. *Selected Aerothermodynamic Design Problems of Hypersonic Flight Vehicles*. Springer, Berlin, Heidelberg, 2009. ISBN 978-3-540-89973-0. doi: 10.1007/978-3-540-89974-7.

Kazemba C., Braun R., Clark I., and Schoenenberger M. Survey of Blunt Body Dynamic Stability in Supersonic Flow. In *AIAA Atmospheric Flight Mechanics Conference*, Minneapolis, Minnesota, August 2012. American Institute of Aeronautics and Astronautics. ISBN 978-1-62410-184-7. doi: 10.2514/6.2012-4509.

Kundu P.K., Cohen I. M., Dowling D. R., and Tryggvason G. *Fluid mechanics*. Elsevier/AP, Amsterdam; Boston, sixth edition edition, 2016. ISBN 978-0-12-405935-1.

Liepmann H. W. The Interaction Between Boundary Layer and Shock Waves in Transonic Flow. *Journal of the Aeronautical Sciences*, 13(12): 623–637, December 1946. ISSN 1936-9956. doi: 10.2514/8.11473.

Loth E., Tyler Daspit J., Jeong M., Nagata T., and Nonomura T. Supersonic and Hypersonic Drag Coefficients for a Sphere. *AIAA Journal*, Vol. 59: 3261–3274, 2021. ISSN 0001-1452, 1533-385X. doi: 10.2514/1.J060153.

Mallet M., Periaux J., Rostand P., and Stoufflet B. Validation of aerodynamic simulation methods for Hermes spaceplane and future hypersonic vehicles. In *AIAA 4th International Aerospace Planes Conference*, 78, Orlando, FL, December 1992. American Institute of Aeronautics and Astronautics. doi: 10.2514/6.1992-5065.

MIL-F-8785C. Military Specification Flying Qualities of Piloted Airplanes, NASA, 1980.

MIL-HDBK-1797. Flying Qualities of Piloted Airplanes, Handbook, Department of Defence, NASA, 1997.

Mooij E. *The motion of a vehicle in a planetary atmosphere*. Delft University of Technology, Faculty of Aerospace Engineering, Delft, 1994. ISBN 978-90-5623-003-6.

Mooij E. The Horus-2B reference vehicle. memorandum m-692, Delft University of Technology, Faculty of Aerospace Engineering, 1995.

Mooij E. *Linear quadratic regulator design for an unpowered, winged re-entry vehicle*. Delft University Press, Delft, 1998. ISBN 90-407-1597-1.

Mooij E. Characteristic Motion of Re-entry Vehicles. In *AIAA Atmospheric Flight Mechanics (AFM) Conference*, AIAA-13-4603, Boston, MA, August 2013. American Institute of Aeronautics and Astronautics. doi: 10.2514/6.2013-4603.

Mooij E. *Re-entry Systems*. Delft University of Technology, Delft, lecture notes (2019-2020) edition, 2015.

Mooij E. Simple Adaptive Control System Design Trades. In *AIAA Guidance, Navigation, and Control Conference*, Grapevine, Texas, January 2017. American Institute of Aeronautics and Astronautics. ISBN 978-1-62410-450-3. doi: 10.2514/6.2017-1502.

Mooij E. Simple adaptive bank-reversal control for non-linear winged re-entry vehicles. *Mathematics in Enginering, Science and Aerospace*, Vol. 9(No. 1): pp. 85–110, February 2018.

Mooij H. A. Criteria for Low-Speed Longitudinal Handling Qualities: of Transport Aircraft with Closed-Loop Flight Control Systems, 1985. ISBN: 9789401711937 OCLC: 1159711730.

Moore T. Space shuttle entry terminal area energy management. Technical Memorandum 19920010688, NASA, TX, United States, November 1991.

NASA. U.S. Standard Atmosphere, 1976. Technical Memorandum (TM) 19770009539, October 1976.

Powers B. G. Space Shuttle longitudinal landing flying qualities. *Journal of Guidance, Control, and Dynamics*, 9(5): 566–572, September 1986. ISSN 0731-5090, 1533-3884. doi: 10.2514/3.20147.

Raillon E., Parnis P., and Devaux N. Flying qualities of the Hermes spaceplane and shape definition process. *Acta Astronautica*, 26(8-10): 621–632, August 1992. ISSN 00945765. doi: 10.1016/0094-5765(92)90152-9.

Roenneke A. J. and Cornwell P. J. Trajectory control for a low-lift re-entry vehicle. *Journal of Guidance, Control, and Dynamics*, 16(5): 927–933, September 1993. ISSN 0731-5090, 1533-3884. doi: 10.2514/3.21103.

Scott H. Space Shuttle Orbiter configuration case history. Los Angeles,CA,U.S.A., August 1978. American Institute of Aeronautics and Astronautics. doi: 10.2514/6.1978-1469.

Surber T. E. and Olsen D. C. Space Shuttle Orbiter Aerodynamic Development. *Journal of Spacecraft and Rockets*, 15(1): 40–47, January 1978. ISSN 0022-4650, 1533-6794. doi: 10.2514/3.57286.

Viavattene G. and Mooij E. Flying Qualities and Controllability of Hypersonic Spaceplanes. In *AIAA Scitech 2019 Forum*, AIAA 2019-1669, San Diego, California, January 2019. American Institute of Aeronautics and Astronautics. ISBN 978-1-62410-578-4. doi: 10.2514/6.2019-1669.

Weiland C. *Aerodynamic data of space vehicles*. Springer, Heidelberg, 2014. ISBN 978-3-642-54168-1.

White F. M. *Viscous fluid flow*. McGraw-Hill, New York, third edition edition, 1974. ISBN 978-0-07-069710-2.

Young J., Perez L., Romere P., and Kanipe D. Space Shuttle entry aerodynamic comparisons of flight 1 with preflight predictions. Las Vegas, NV, U.S.A., November 1981. American Institute of Aeronautics and Astronautics. doi: 10.2514/6.1981-2476.

A

State-space expressions

For the **A** matrix of the state space form, the expressions are stated below.

$$a_{VV} = -\frac{1}{mV_0}\left(M_0 \frac{\partial C_D}{\partial M}\bar{q}_0 S_{ref} + 2D_0\right) \tag{A.1}$$

$$a_{V\gamma} = -g_0 \cos\gamma_0 \tag{A.2}$$

$$a_{VR} = 2\frac{g_0}{R_0}\sin\gamma_0 \tag{A.3}$$

$$a_{V\alpha} = -\frac{1}{m}\frac{\partial C_D}{\partial \alpha}\bar{q}_0 S_{ref} \tag{A.4}$$

$$a_{Vp} = a_{Vq} = a_{Vr} = a_{V\beta} = a_{V\sigma} = 0 \tag{A.5}$$

$$a_{\gamma V} = \frac{1}{V_0}\left(-\dot{\gamma}_0 + \frac{2V_0}{R_0}\cos\gamma_0\right) + \frac{\cos\sigma_0}{mV_0^2}\left(M_0 \frac{\partial C_L}{\partial M}\bar{q}_0 S_{ref} + 2L_0\right) \tag{A.6}$$

$$a_{\gamma\gamma} = -\left(\frac{V_0}{R_0} - \frac{g_0}{V_0}\right)\sin\gamma_0 \tag{A.7}$$

$$a_{\gamma R} = \left(\frac{2g_0}{V_0} - \frac{V_0}{R_0}\right)\frac{\cos\gamma_0}{R_0} \tag{A.8}$$

$$a_{\gamma\alpha} = \frac{\cos\sigma_0}{mV_0}\frac{\partial C_L}{\partial \alpha}\bar{q}_0 S_{ref} \tag{A.9}$$

$$a_{\gamma\beta} = -\frac{\sin\sigma_0}{mV_0}\frac{\partial C_S}{\partial \beta}\bar{q}_0 S_{ref} \tag{A.10}$$

$$a_{\gamma\sigma} = -\frac{L_0}{mV_0}\sin\sigma_0 \tag{A.11}$$

$$a_{\gamma p} = a_{\gamma q} = a_{\gamma r} = 0 \tag{A.12}$$

$$a_{RV} = \sin\gamma_0 \tag{A.13}$$

$$a_{R\gamma} = V_0 \cos\gamma_0 \tag{A.14}$$

$$a_{RR} = a_{Rp} = a_{Rq} = a_{Rr} = a_{R\alpha} = a_{R\beta} = a_{R\sigma} = 0 \tag{A.15}$$

$$a_{p\beta} = \frac{1}{I_{xx}} \frac{\partial C_l}{\partial \beta} \bar{q}_0 S_{ref} b_{ref} \tag{A.16}$$

$$a_{pV} = a_{p\gamma} = a_{pR} = a_{pp} = a_{pq} = a_{pr} = a_{p\alpha} = a_{p\sigma} = 0 \tag{A.17}$$

$$a_{qV} = \frac{M_0}{I_{yy} V_0} \frac{\partial C_m}{\partial M} \bar{q}_0 S_{ref} c_{ref} \tag{A.18}$$

$$a_{q\alpha} = \frac{1}{I_{yy}} \frac{\partial C_m}{\partial \alpha} \bar{q}_0 S_{ref} c_{ref} \tag{A.19}$$

$$a_{q\gamma} = a_{qR} = a_{qp} = a_{qq} = a_{qr} = a_{q\beta} = a_{q\sigma} = 0 \tag{A.20}$$

$$a_{r\beta} = \frac{1}{I_{zz}} \frac{\partial C_n}{\partial \beta} \bar{q}_0 S_{ref} b_{ref} \tag{A.21}$$

$$a_{rV} = a_{\gamma\gamma} = a_{rR} = a_{rp} = a_{rq} = a_{rr} = a_{r\alpha} = a_{r\sigma} = 0 \tag{A.22}$$

$$a_{\alpha V} = -\frac{g_0}{V_0^2} \cos\gamma_0 \cos\sigma_0 - \frac{1}{m V_0^2} \left(M_0 \frac{\partial C_L}{\partial M} \bar{q}_0 S_{ref} + L_0 \right) \tag{A.23}$$

$$a_{\alpha\gamma} = -\frac{g_0}{V_0} \sin\gamma_0 \cos\sigma_0 \tag{A.24}$$

$$a_{\alpha R} = -\frac{2 g_0}{R_0 V_0} \cos\gamma_0 \cos\sigma_0 \tag{A.25}$$

$$a_{\alpha q} = 1 \tag{A.26}$$

$$a_{\alpha\alpha} = -\frac{1}{m V_0} \frac{\partial C_L}{\partial \alpha} \bar{q}_0 S_{ref} \tag{A.27}$$

$$a_{\alpha\sigma} = -\frac{g_0}{V_0} \cos\gamma_0 \sin\sigma_0 \tag{A.28}$$

$$a_{\alpha p} = a_{\alpha r} = a_{\alpha\beta} = 0 \tag{A.29}$$

$$a_{\beta V} = \frac{g_0}{V_0^2} \cos\gamma_0 \sin\sigma_0 \tag{A.30}$$

$$a_{\beta\gamma} = \frac{g_0}{V_0} \sin\gamma_0 \sin\sigma_0 \tag{A.31}$$

$$a_{\beta p} = \sin\alpha_0 \tag{A.32}$$

$$a_{\beta r} = -\cos\alpha_0 \tag{A.33}$$

$$a_{\beta\beta} = -\frac{1}{m V_0} \frac{\partial C_S}{\partial \beta} \bar{q}_0 S_{ref} \tag{A.34}$$

$$a_{\beta\sigma} = -\frac{g_0}{V_0} \cos\gamma_0 \cos\sigma_0 \tag{A.35}$$

$$a_{\beta q} = a_{\beta\alpha} = 0 \tag{A.36}$$

$$a_{\sigma V} = \frac{\tan\gamma_0 \sin\sigma_0}{mV_0^2}\left(M_0 \frac{\partial C_L}{\partial M}\bar{q}_0 S_{ref} + L_0\right) a_{\sigma y} = \frac{L_0}{mV_0}\sin\sigma_0 \tag{A.37}$$

$$a_{\sigma p} = -\cos\alpha_0 \tag{A.38}$$

$$a_{\sigma r} = -\sin\alpha_0 \tag{A.39}$$

$$a_{\sigma\alpha} = \frac{\tan\gamma_0 \sin\sigma_0}{mV_0}\frac{\partial C_L}{\partial\alpha}\bar{q}_0 S_{ref} \tag{A.40}$$

$$a_{\sigma\beta} = \frac{\tan\gamma_0 \cos\sigma_0}{mV_0}\frac{\partial C_S}{\partial\beta}\bar{q}_0 S_{\text{ref}} - \frac{L_0}{mV_0} + \frac{g_0}{V_0}\cos\gamma_0 \cos\sigma_0 \tag{A.41}$$

$$a_{\sigma\sigma} = \tan\gamma_0 \cos\sigma_0 \frac{L_0}{mV_0} \tag{A.42}$$

$$a_{\sigma R} = a_{\sigma q} = 0 \tag{A.43}$$

Now, for the **B** matrix of the state space form, the expressions are the following.

$$b_{Ve} = b_{Va} = b_{Vr} = b_{Vx} = b_{Vy} = b_{Vz} = 0 \tag{A.44}$$

$$b_{\gamma e} = b_{\gamma a} = b_{\gamma r} = b_{\gamma x} = b_{\gamma y} = b_{\gamma z} = 0 \tag{A.45}$$

$$b_{Re} = b_{Ra} = b_{Rr} = b_{Rx} = b_{Ry} = b_{Rz} = 0 \tag{A.46}$$

$$b_{pa} = \frac{1}{I_{xx}}\frac{\partial C_l}{\partial\delta_a}\bar{q}_0 S_{ret} b_{ref} \tag{A.47}$$

$$b_{px} = \frac{1}{I_{xx}} \tag{A.48}$$

$$b_{pe} = b_{pr} = b_{py} = b_{pz} = 0 \tag{A.49}$$

$$b_{qe} = \frac{1}{I_{yy}}\frac{\partial C_m}{\partial\delta_e}\bar{q}_0 S_{ref} c_{ref} \tag{A.50}$$

$$b_{qy} = \frac{1}{I_{yy}} \tag{A.51}$$

$$b_{qa} = b_{qr} = b_{qx} = b_{qz} = 0 \tag{A.52}$$

$$b_{ra} = \frac{1}{I_{zz}}\frac{\partial C_n}{\partial\delta_a}\bar{q}_0 S_{ret} b_{ref} \tag{A.53}$$

$$b_{rr} = \frac{1}{I_{zz}}\frac{\partial C_n}{\partial\delta_r}\bar{q}_0 S_{ref} b_{ref} \tag{A.54}$$

$$b_{rz} = \frac{1}{I_{zz}} \tag{A.55}$$

$$b_{re} = b_{rx} = b_{ry} = 0 \tag{A.56}$$

$$b_{\alpha e} = b_{\alpha a} = b_{\alpha r} = b_{\alpha x} = b_{\alpha y} = b_{\alpha z} = 0 \tag{A.57}$$

$$b_{\beta e} = b_{\beta a} = b_{\beta r} = b_{\beta x} = b_{\beta y} = b_{\beta z} = 0 \tag{A.58}$$

$$b_{\sigma e} = b_{\sigma a} = b_{\sigma r} = b_{\sigma x} = b_{\sigma y} = b_{\sigma z} = 0 \tag{A.59}$$

B

Validation Figures

This chapter shows the extra figures used for the validation of the model (Chapter 6). Figure B.1 presents the comparison between the original design from Chapter 4 and the modifiable HORUS geometry from Chapter 5 for the sideforce coefficient and the roll moment coefficient. In Figure B.2 the pitch and yaw moment coefficient is visualised. Similar as explained in the Chapter 6 there is not much difference between the two designs based on aerodynamic data. The differences between the geometries are negligible small compared to the errors compared to the reference data. This shows that the adaptable geometry is verified to be used for the validation process with the reference data.

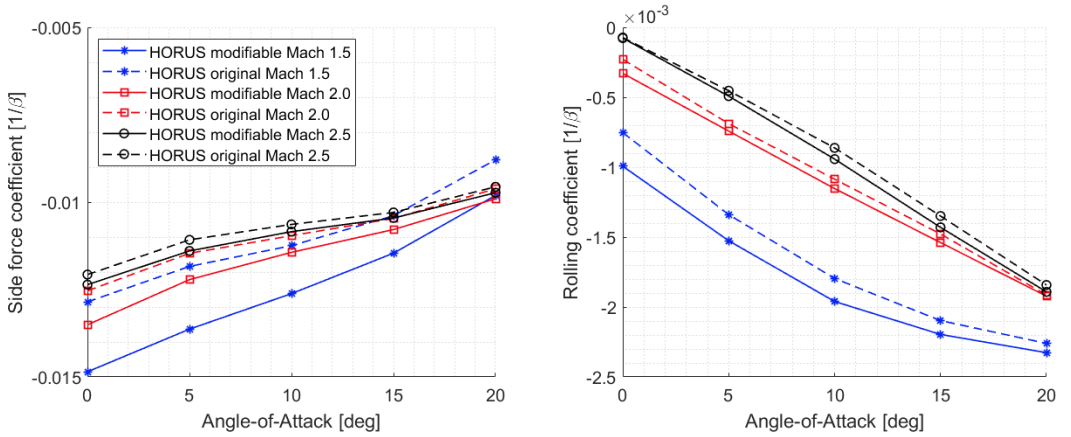

(a) Nominal side coefficient differentiated to the sideslip angle

(b) Nominal roll coefficient differentiated to the sideslip angle

Figure B.1: The comparison between the original (most similar as reference) and modifiable geometry.

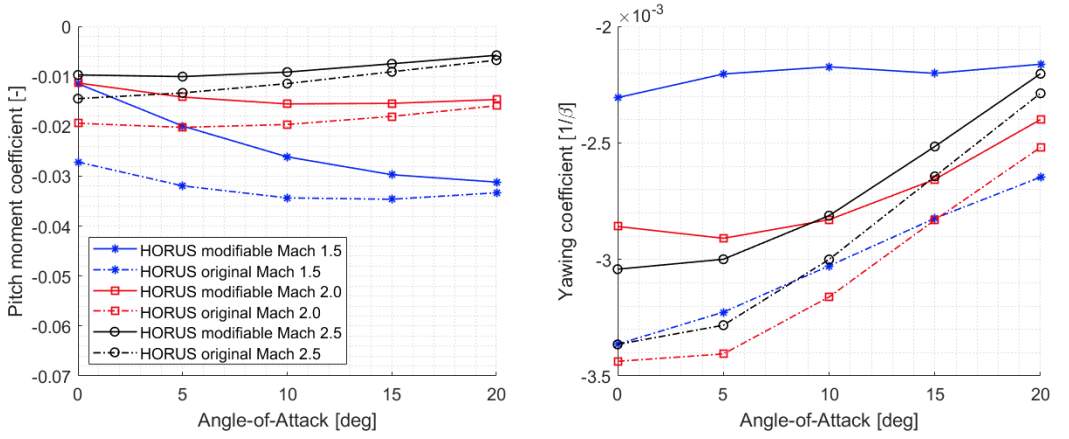

(a) Nominal pitch coefficient

(b) Nominal yaw coefficient differentiated to the sideslip angle

Figure B.2: The comparison between the original (most similar as reference) and modifiable geometry.

C

Aerodynamic characteristic tables

In this chapter the aerodynamic results of all the shape modifications are presented. In each tables the trimmed aerodynamic derivatives for different Mach numbers: 0.8, 1.5 and 2.5 along the trajectory are stated. The first column shows the original derivatives, the second column the high value of the shape modification parameter and the third the low value of the shape modification parameter. In every table's label there is linked to the shape modification visualisation of Chapter 5. These aerodynamic derivatives are used for Chapter 7, where the results of the flight modes are computed. Thus, these aerodynamic derivatives are implemented in the **A** matrix and therefore the equations stated in Appendix A. (The body flap is -20 degrees and both elevons -17.5 degrees.)

Table C.1: Influence of the wingspan by increasing the wing length, see Figure 5.10a.

	Original spaceplane (3.1 m)			Wing width 3.9 m			Wing width 2.8 m		
M	0.8	1.5	2.5	0.8	1.5	2.5	0.8	1.5	2.5
C_{D_α}	0.0091	0.0123	0.0092	0.0118	0.0139	0.0100	0.0081	0.0116	0.0088
C_{L_α}	0.0350	0.0334	0.0241	0.0418	0.0367	0.0261	0.0338	0.0325	0.0236
C_{m_α}	$1.29{\cdot}10^{-5}$	$-9.55{\cdot}10^{-4}$	$3.73{\cdot}10^{-4}$	$-1.57{\cdot}10^{-3}$	$-1.79{\cdot}10^{-3}$	$-9.88{\cdot}10^{-5}$	$5.41{\cdot}10^{-5}$	$-6.88{\cdot}10^{-4}$	$5.48{\cdot}10^{-4}$
C_{S_β}	-0.0130	-0.0131	-0.0107	-0.0133	-0.0126	-0.0109	-0.0122	-0.0130	-0.0106
C_{l_β}	-0.0032	-0.0020	-0.0008	-0.0042	-0.0024	-0.0010	-0.0026	-0.0019	-0.0007
C_{n_β}	-0.0023	-0.0020	-0.0029	-0.0019	-0.0021	-0.0027	-0.0024	-0.0021	-0.0030
C_{D_M}	0.0210	-0.1600	-0.0250	0.0270	-0.0620	-0.0280	0.0320	-0.0540	-0.0260
C_{L_M}	0.1160	-0.1570	-0.0460	0.0670	-0.1030	-0.0530	0.1100	-0.0640	-0.0430
C_{m_M}	-0.0540	0.0280	0.0030	-0.0460	0.0100	0.0050	-0.0490	-0.0000	0.0020

Table C.2: Influence of the winglet bottom length, see Figure 5.14a.

	Original spaceplane (4.5 m)			Winglet bottom length 4.7 m			Winglet bottom length 4.0 m		
M	0.8	1.5	2.5	0.8	1.5	2.5	0.8	1.5	2.5
C_{D_α}	0.0091	0.0123	0.0092	0.0094	0.0124	0.0092	0.0088	0.0120	0.0090
C_{L_α}	0.0350	0.0334	0.0241	0.0363	0.0335	0.0242	0.0352	0.0332	0.0240
C_{m_α}	$1.29{\cdot}10^{-5}$	$-9.55{\cdot}10^{-4}$	$3.73{\cdot}10^{-4}$	$-2.00{\cdot}10^{-4}$	$-9.72{\cdot}10^{-4}$	$3.93{\cdot}10^{-4}$	$-1.36{\cdot}10^{-4}$	$-8.75{\cdot}10^{-4}$	$4.38{\cdot}10^{-4}$
C_{S_β}	-0.0129	-0.0131	-0.0107	-0.0126	-0.0132	-0.0108	-0.0127	-0.0130	-0.0106
C_{l_β}	-0.0032	-0.0020	-0.0008	-0.0030	-0.0021	-0.0008	-0.0029	-0.0020	-0.0007
C_{n_β}	-0.0023	-0.0020	-0.0029	-0.0024	-0.0020	-0.0029	-0.0022	-0.0020	-0.0029
C_{D_M}	0.0208	-0.1598	-0.0253	0.0316	-0.0567	-0.0268	0.0253	-0.0545	-0.0451
C_{L_M}	0.1164	-0.1567	-0.0460	0.1025	-0.0779	-0.0456	0.0981	-0.0698	-0.0581
C_{m_M}	-0.0543	0.0283	0.0028	-0.0500	0.0032	0.0030	-0.0477	0.0012	0.0077

Table C.3: Influence of the winglet angle backwards, see Figure 5.18a.

	Original spaceplane (20°)			Winglet angle backwards 30°			Winglet angle backwards 10°		
M	0.8	1.5	2.5	0.8	1.5	2.5	0.8	1.5	2.5
C_{D_α}	0.0091	0.0123	0.0092	0.0090	0.0122	0.0092	0.0096	0.0124	0.0092
C_{L_α}	0.0350	0.0334	0.0241	0.0358	0.0333	0.0241	0.0364	0.0337	0.0241
C_{m_α}	$1.29{\cdot}10^{-5}$	$-9.55{\cdot}10^{-4}$	$3.73{\cdot}10^{-4}$	$-2.51{\cdot}10^{-4}$	$-8.83{\cdot}10^{-4}$	$4.06{\cdot}10^{-4}$	$-2.14{\cdot}10^{-4}$	$-9.61{\cdot}10^{-4}$	$4.45{\cdot}10^{-4}$
C_{S_β}	-0.0129	-0.0131	-0.0107	-0.0118	-0.0128	-0.0104	-0.0131	-0.0132	-0.0109
C_{l_β}	-0.0032	-0.0020	-0.0008	-0.0026	-0.0020	-0.0007	-0.0034	-0.0022	-0.0009
C_{n_β}	-0.0023	-0.0020	-0.0029	-0.0026	-0.0021	-0.0030	-0.0022	-0.0020	-0.0028
C_{D_M}	0.0208	-0.1598	-0.0253	0.0293	-0.0543	-0.0258	0.0284	-0.0570	-0.0281
C_{L_M}	0.1164	-0.1567	-0.0460	0.1124	-0.0734	-0.0460	0.0896	-0.0759	-0.0459
C_{m_M}	-0.0543	0.0283	0.0028	-0.0518	0.0022	0.0030	-0.0462	0.0023	0.0030

Table C.4: Influence of the winglet angle sidewards, see Figure 5.18a.

	Original spaceplane (12°)			Winglet angle sidewards 25°			Winglet angle sidewards 5°		
M	0.8	1.5	2.5	0.8	1.5	2.5	0.8	1.5	2.5
C_{D_α}	0.0091	0.0123	0.0092	0.0103	0.0129	0.0095	0.0088	0.0120	0.0090
C_{L_α}	0.0350	0.0334	0.0241	0.0382	0.0344	0.0246	0.0349	0.0331	0.0239
C_{m_α}	$1.29{\cdot}10^{-5}$	$-9.55{\cdot}10^{-4}$	$3.73{\cdot}10^{-4}$	$-8.09{\cdot}10^{-4}$	$-1.25{\cdot}10^{-3}$	$2.60{\cdot}10^{-4}$	$1.20{\cdot}10^{-4}$	$-7.25{\cdot}10^{-4}$	$4.95{\cdot}10^{-4}$
C_{S_β}	-0.0129	-0.0131	-0.0107	-0.0120	-0.0123	-0.0106	-0.0128	-0.0132	-0.0106
C_{l_β}	-0.0032	-0.0020	-0.0008	-0.0035	-0.0024	-0.0010	-0.0027	-0.0019	-0.0007
C_{n_β}	-0.0023	-0.0020	-0.0029	-0.0026	-0.0024	-0.0029	-0.0022	-0.0019	-0.0029
C_{D_M}	0.0208	-0.1598	-0.0253	0.0278	-0.0577	-0.0271	0.0309	-0.0544	-0.0264
C_{L_M}	0.1164	-0.1567	-0.0460	0.0918	-0.0860	-0.0488	0.1013	-0.0696	-0.0434
C_{m_M}	-0.0543	0.0283	0.0028	-0.0481	0.0056	0.0040	-0.0490	0.0010	0.0021

Table C.5: Influence of the wing corner width, see Figure 5.11a.

	Original spaceplane (1.5 m)			Wing corner width 2.5 m			Wing corner width 1.2 m		
M	0.8	1.5	2.5	0.8	1.5	2.5	0.8	1.5	2.5
C_{D_α}	0.0091	0.0123	0.0092	0.0102	0.0138	0.0035	0.0089	0.0119	0.0089
C_{L_α}	0.0350	0.0334	0.0241	0.0375	0.0365	0.0451	0.0359	0.0325	0.0237
C_{m_α}	$1.29{\cdot}10^{-5}$	$-9.55{\cdot}10^{-4}$	$3.73{\cdot}10^{-4}$	$8.10{\cdot}10^{-4}$	$-9.98{\cdot}10^{-4}$	$-6.28{\cdot}10^{-3}$	$-5.98{\cdot}10^{-4}$	$-8.88{\cdot}10^{-4}$	$4.21{\cdot}10^{-4}$
C_{S_β}	-0.0129	-0.0131	-0.0107	-0.0125	-0.0136	-0.0079	-0.0127	-0.0129	-0.0107
C_{l_β}	-0.0032	-0.0020	-0.0008	-0.0033	-0.0024	0.0008	-0.0029	-0.0020	-0.0007
C_{n_β}	-0.0023	-0.0020	-0.0029	-0.0022	-0.0016	-0.0032	-0.0022	-0.0020	-0.0028
C_{D_M}	0.0208	-0.1598	-0.0253	0.0331	-0.0575	-0.0550	0.0276	-0.0568	-0.0261
C_{L_M}	0.1164	-0.1567	-0.0460	0.1221	-0.0897	0.0447	0.0934	-0.0733	-0.0423
C_{m_M}	-0.0543	0.0283	0.0028	-0.0595	0.0014	-0.0306	-0.0470	0.0031	0.0026

Table C.6: Influence of the wing corner length, see Figure 5.12a.

	Original spaceplane (4.8 m)			Wing corner length 5.5 m			Wing corner length 4.6 m		
M	0.8	1.5	2.5	0.8	1.5	2.5	0.8	1.5	2.5
C_{D_α}	0.0091	0.0123	0.0092	0.0095	0.0127	0.0094	0.0093	0.0123	0.0091
C_{L_α}	0.0350	0.0334	0.0241	0.0364	0.0341	0.0245	0.0357	0.0333	0.0240
C_{m_α}	$1.29{\cdot}10^{-5}$	$-9.55{\cdot}10^{-4}$	$3.73{\cdot}10^{-4}$	$1.08{\cdot}10^{-5}$	$-9.44{\cdot}10^{-4}$	$4.09{\cdot}10^{-4}$	$-1.73{\cdot}10^{-4}$	$-8.83{\cdot}10^{-4}$	$4.40{\cdot}10^{-4}$
C_{S_β}	-0.0129	-0.0131	-0.0107	-0.0126	-0.0131	-0.0107	-0.0126	-0.0132	-0.0108
C_{l_β}	-0.0032	-0.0020	-0.0008	-0.0031	-0.0022	-0.0008	-0.0030	-0.0021	-0.0008
C_{n_β}	-0.0023	-0.0020	-0.0029	-0.0022	-0.0019	-0.0029	-0.0024	-0.0020	-0.0029
C_{D_M}	0.0208	-0.1598	-0.0253	0.0303	-0.0576	-0.0271	0.0323	-0.0549	-0.0265
C_{L_M}	0.1164	-0.1567	-0.0460	0.1032	-0.0797	-0.0474	0.0962	-0.0735	-0.0449
C_{m_M}	-0.0543	0.0283	0.0028	-0.0511	0.0020	0.0032	-0.0478	0.0019	0.0030

Table C.7: Influence of the nosecone tip height, see Figure 5.6a.

	Original spaceplane (1.5 m)			Nosecone height 1.8 m			Nosecone height 1.3 m		
M	0.8	1.5	2.5	0.8	1.5	2.5	0.8	1.5	2.5
C_{D_α}	0.0091	0.0123	0.0092	0.0092	0.0129	0.0098	0.0093	0.0120	0.0088
C_{L_α}	0.0350	0.0334	0.0241	0.0359	0.0340	0.0241	0.0364	0.0330	0.0242
C_{m_α}	$1.29{\cdot}10^{-5}$	$-9.55{\cdot}10^{-4}$	$3.73{\cdot}10^{-4}$	$-2.84{\cdot}10^{-4}$	$-8.88{\cdot}10^{-4}$	$5.03{\cdot}10^{-4}$	$-4.15{\cdot}10^{-4}$	$-9.14{\cdot}10^{-4}$	$3.88{\cdot}10^{-4}$
C_{S_β}	-0.0129	-0.0131	-0.0107	-0.0124	-0.0132	-0.0107	-0.0124	-0.0129	-0.0107
C_{l_β}	-0.0032	-0.0020	-0.0008	-0.0031	-0.0024	-0.0009	-0.0029	-0.0019	-0.0007
C_{n_β}	-0.0023	-0.0020	-0.0029	-0.0024	-0.0019	-0.0029	-0.0023	-0.0020	-0.0029
C_{D_M}	0.0208	-0.1598	-0.0253	0.0338	-0.0543	-0.0253	0.0285	-0.0561	-0.0258
C_{L_M}	0.1164	-0.1567	-0.0460	0.1042	-0.0705	-0.0461	0.0955	-0.0804	-0.0458
C_{m_M}	-0.0543	0.0283	0.0028	-0.0472	0.0014	0.0022	-0.0495	0.0039	0.0033

Table C.8: Influence of the fuselage width, see Figure 5.4a.

	Original spaceplane (2.5 m)			Fuselage width 3.5 m			Fuselage height 2.0 m		
M	0.8	1.5	2.5	0.8	1.5	2.5	0.8	1.5	2.5
C_{D_α}	0.0091	0.0123	0.0092	0.0129	0.0135	0.0070	0.0084	0.0111	0.0082
C_{L_α}	0.0350	0.0334	0.0241	0.0459	0.0394	0.0281	0.0315	0.0278	0.0211
C_{m_α}	$1.29{\cdot}10^{-5}$	$-9.55{\cdot}10^{-4}$	$3.73{\cdot}10^{-4}$	$8.67{\cdot}10^{-4}$	$2.05{\cdot}10^{-4}$	$2.35{\cdot}10^{-3}$	$-6.23{\cdot}10^{-4}$	$-1.22{\cdot}10^{-3}$	$1.16{\cdot}10^{-4}$
C_{S_β}	-0.0129	-0.0131	-0.0107	-0.0155	-0.0149	-0.0174	-0.0118	0.0134	-0.0092
C_{l_β}	-0.0032	-0.0020	-0.0008	-0.0042	-0.0020	0.0004	-0.0029	-0.0046	-0.0006
C_{n_β}	-0.0023	-0.0020	-0.0029	-0.0042	-0.0036	-0.0050	-0.0013	-0.0188	-0.0023
C_{D_M}	0.0208	-0.1598	-0.0253	-0.0363	-0.0978	-0.0498	0.0046	-0.0396	-0.0207
C_{L_M}	0.1164	-0.1567	-0.0460	-0.1029	-0.1151	-0.0618	0.0889	-0.0701	-0.0410
C_{m_M}	-0.0543	0.0283	0.0028	-0.0143	0.0033	0.0059	-0.0389	0.0017	0.0028

Table C.9: Influence of the fuselage length, see Figure 5.7a. (With scaled moment reference point.)

	Original spaceplane (10 m)			Fuselage length 15 m			Fuselage length 5 m		
M	0.8	1.5	2.5	0.8	1.5	2.5	0.8	1.5	2.5
C_{D_α}	0.0091	0.0123	0.0092	0.0101	0.0132	0.0105	0.0089	0.0111	0.0079
C_{L_α}	0.0350	0.0334	0.0241	0.0380	0.0365	0.0274	0.0355	0.0304	0.0219
C_{m_α}	$1.29{\cdot}10^{-5}$	$-9.55{\cdot}10^{-4}$	$3.73{\cdot}10^{-4}$	$-1.53{\cdot}10^{-3}$	$-1.74{\cdot}10^{-3}$	$2.98{\cdot}10^{-4}$	$1.63{\cdot}10^{-3}$	$5.65{\cdot}10^{-4}$	$9.51{\cdot}10^{-4}$
C_{S_β}	-0.0129	-0.0131	-0.0107	-0.0139	-0.0148	-0.0124	-0.0115	-0.0110	-0.0090
C_{l_β}	-0.0032	-0.0020	-0.0008	-0.0034	-0.0028	-0.0010	-0.0028	-0.0014	-0.0006
C_{n_β}	-0.0023	-0.0020	-0.0029	-0.0028	-0.0025	-0.0040	-0.0019	-0.0017	-0.0020
C_{D_M}	0.0208	-0.1598	-0.0253	0.0281	-0.0538	-0.0269	0.0265	-0.0575	-0.0252
C_{L_M}	0.1164	-0.1567	-0.0460	0.1018	-0.0610	-0.0458	0.0747	-0.0820	-0.0415
C_{m_M}	-0.0543	0.0283	0.0028	-0.0596	0.0029	0.0041	-0.0369	-0.0008	0.0008

Table C.10: Influence of the fuselage height, see Figure 5.5a. (With scaled moment reference point.)

	Original spaceplane (1.57 m)			Fuselage height 2.00 m			Fuselage height 1.00 m		
M	0.8	1.5	2.5	0.8	1.5	2.5	0.8	1.5	2.5
C_{D_α}	0.0091	0.0123	0.0092	0.0091	0.0117	0.0088	0.0097	0.0131	0.0096
C_{L_α}	0.0350	0.0334	0.0241	0.0360	0.0325	0.0243	0.0362	0.0350	0.0241
C_{m_α}	$1.29{\cdot}10^{-5}$	$-9.55{\cdot}10^{-4}$	$3.73{\cdot}10^{-4}$	$-2.56{\cdot}10^{-4}$	$-8.13{\cdot}10^{-4}$	$4.31{\cdot}10^{-4}$	$-1.27{\cdot}10^{-4}$	$-9.99{\cdot}10^{-4}$	$3.66{\cdot}10^{-4}$
C_{S_β}	-0.0129	-0.0131	-0.0107	-0.0135	-0.0138	-0.0118	-0.0112	-0.0122	-0.0093
C_{l_β}	-0.0032	-0.0020	-0.0008	-0.0024	-0.0013	-0.0006	-0.0038	-0.0033	-0.0012
C_{n_β}	-0.0023	-0.0020	-0.0029	-0.0030	-0.0028	-0.0031	-0.0014	-0.0010	-0.0027
C_{D_M}	0.0208	-0.1598	-0.0253	0.0305	-0.0613	-0.1211	0.0313	-0.0501	-0.0249
C_{L_M}	0.1164	-0.1567	-0.0460	0.0985	-0.0773	-0.5823	0.1035	-0.0695	-0.0499
C_{m_M}	-0.0543	0.0283	0.0028	-0.0499	0.0040	0.0762	-0.0475	-0.0021	0.0019

Table C.11: Influence of the fuselage bottom curve width, see Figure 5.8a.

	Original spaceplane (5.5 m)			Fuselage bottom curvature width 6.6 m			Fuselage bottom curvature width 4.5 m		
M	0.8	1.5	2.5	0.8	1.5	2.5	0.8	1.5	2.5
C_{D_α}	0.0091	0.0123	0.0092	0.0094	0.0130	0.0095	0.0167	0.0173	0.0111
C_{L_α}	0.0350	0.0334	0.0241	0.0371	0.0354	0.0249	0.0538	0.0423	0.0300
C_{m_α}	$1.29{\cdot}10^{-5}$	$-9.55{\cdot}10^{-4}$	$3.73{\cdot}10^{-4}$	$-4.38{\cdot}10^{-4}$	$-1.29{\cdot}10^{-3}$	$3.07{\cdot}10^{-4}$	$1.21{\cdot}10^{-3}$	$7.06{\cdot}10^{-5}$	$5.60{\cdot}10^{-4}$
C_{S_β}	-0.0129	-0.0131	-0.0107	-0.0122	-0.0123	-0.0110	-0.0254	-0.0227	-0.0149
C_{l_β}	-0.0032	-0.0020	-0.0008	-0.0027	-0.0016	-0.0006	-0.0051	-0.0035	-0.0014
C_{n_β}	-0.0023	-0.0020	-0.0029	-0.0023	-0.0023	-0.0026	-0.0041	-0.0036	-0.0037
C_{D_M}	0.0208	-0.1598	-0.0253	0.0316	-0.0529	-0.0273	-0.1239	-0.0733	-0.0372
C_{L_M}	0.1164	-0.1567	-0.0460	0.0986	-0.0720	-0.0572	-0.0680	-0.1097	-0.0386
C_{m_M}	-0.0543	0.0283	0.0028	-0.0480	0.0015	0.0048	-0.0288	0.0049	0.0015

Table C.12: Influence of the fuselage bottom curve width, see Figure 5.9a.

	Original spaceplane (1.5 m)			Fuselage bottom curvature height 2.0 m			Fuselage bottom curvature height 1.0 m		
M	0.8	1.5	2.5	0.8	1.5	2.5	0.8	1.5	2.5
C_{D_α}	0.0091	0.0123	0.0092	0.0085	0.0116	0.0085	0.0102	0.0131	0.0091
C_{L_α}	0.0350	0.0334	0.0241	0.0346	0.0317	0.0231	0.0380	0.0355	0.0232
C_{m_α}	$1.29{\cdot}10^{-5}$	$-9.55{\cdot}10^{-4}$	$3.73{\cdot}10^{-4}$	$-2.21{\cdot}10^{-4}$	$-7.68{\cdot}10^{-4}$	$5.23{\cdot}10^{-4}$	$-3.83{\cdot}10^{-4}$	$-1.15{\cdot}10^{-3}$	$5.55{\cdot}10^{-4}$
C_{S_β}	-0.0129	-0.0131	-0.0107	-0.0131	-0.0135	-0.0112	-0.0119	-0.0122	-0.0103
C_{l_β}	-0.0032	-0.0020	-0.0008	-0.0035	-0.0024	-0.0011	-0.0024	-0.0014	-0.0004
C_{n_β}	-0.0023	-0.0020	-0.0029	-0.0023	-0.0020	-0.0029	-0.0023	-0.0024	-0.0029
C_{D_M}	0.0208	-0.1598	-0.0253	0.0295	-0.0551	-0.0258	0.0301	-0.0521	-0.4262
C_{L_M}	0.1164	-0.1567	-0.0460	0.0879	-0.0731	-0.0517	0.0865	-0.0711	0.0622
C_{m_M}	-0.0543	0.0283	0.0028	-0.0442	0.0030	0.0043	-0.0446	0.0011	0.0074

Table C.13: Influence of the wing thickness, see Figure 5.13a.

	Original spaceplane (0.2 m)			Wing thickness 0.21 m			Wing thickness 0.18 m		
M	0.8	1.5	2.5	0.8	1.5	2.5	0.8	1.5	2.5
C_{D_α}	0.0091	0.0123	0.0092	0.0088	0.0121	0.0092	0.0092	0.0122	0.0091
C_{L_α}	0.0350	0.0334	0.0241	0.0346	0.0332	0.0240	0.0359	0.0334	0.0240
C_{m_α}	$1.29{\cdot}10^{-5}$	$-9.55{\cdot}10^{-4}$	$3.73{\cdot}10^{-4}$	$1.75{\cdot}10^{-4}$	$-8.09{\cdot}10^{-4}$	$4.44{\cdot}10^{-4}$	$-2.09{\cdot}10^{-4}$	$-9.49{\cdot}10^{-4}$	$4.11{\cdot}10^{-4}$
C_{S_β}	-0.0129	-0.0131	-0.0107	-0.0111	-0.0119	-0.0101	-0.0125	-0.0130	-0.0106
C_{l_β}	-0.0032	-0.0020	-0.0008	-0.0000	-0.0000	-0.0000	-0.0000	-0.0000	-0.0000
C_{n_β}	-0.0023	-0.0020	-0.0029	-0.0000	-0.0000	-0.0000	-0.0000	-0.0000	-0.0000
C_{D_M}	0.0208	-0.1598	-0.0253	0.0300	-0.0500	-0.0300	0.0300	-0.0600	-0.0300
C_{L_M}	0.1164	-0.1567	-0.0460	0.1000	-0.0700	-0.0400	0.1100	-0.0700	-0.0500
C_{m_M}	-0.0543	0.0283	0.0028	-0.0500	0.0000	0.0000	-0.0500	0.0000	0.0000

Table C.14: Influence of the winglet top length, see Figure 5.15a.

	Original spaceplane (2.5 m)			Winglet top length 3.5 m			Winglet top length 2.2 m		
M	0.8	1.5	2.5	0.8	1.5	2.5	0.8	1.5	2.5
C_{D_α}	0.0091	0.0123	0.0092	0.0097	0.0125	0.0082	0.0092	0.0123	0.0092
C_{L_α}	0.0350	0.0334	0.0241	0.0367	0.0336	0.0239	0.0356	0.0335	0.0241
C_{m_α}	$1.29{\cdot}10^{-5}$	$-9.55{\cdot}10^{-4}$	$3.73{\cdot}10^{-4}$	$-3.92{\cdot}10^{-4}$	$-9.70{\cdot}10^{-4}$	$4.72{\cdot}10^{-4}$	$-7.90{\cdot}10^{-5}$	$-9.38{\cdot}10^{-4}$	$4.18{\cdot}10^{-4}$
C_{S_β}	-0.0129	-0.0131	-0.0107	-0.0131	-0.0137	-0.0110	-0.0123	-0.0129	-0.0106
C_{l_β}	-0.0032	-0.0020	-0.0008	-0.0034	-0.0023	-0.0009	-0.0029	-0.0020	-0.0007
C_{n_β}	-0.0023	-0.0020	-0.0029	-0.0022	-0.0017	-0.0027	-0.0024	-0.0021	-0.0029
C_{D_M}	0.0208	-0.1598	-0.0253	-0.0025	-0.0766	-0.0283	0.0307	-0.0559	-0.0264
C_{L_M}	0.1164	-0.1567	-0.0460	-0.0177	-0.1299	-0.0457	0.1044	-0.0737	-0.0452
C_{m_M}	-0.0543	0.0283	0.0028	-0.0086	0.0201	0.0028	-0.0504	0.0018	0.0029

Table C.15: Influence of the winglet height, see Figure 5.16a.

	Original spaceplane (3.2 m)			Winglet height 4.5 m			Winglet height 2.5		
M	0.8	1.5	2.5	0.8	1.5	2.5	0.8	1.5	2.5
C_{D_α}	0.0091	0.0123	0.0092	0.0095	0.0124	0.0090	0.0092	0.0123	0.0092
C_{L_α}	0.0350	0.0334	0.0241	0.0373	0.0340	0.0244	0.0348	0.0333	0.0240
C_{m_α}	$1.29{\cdot}10^{-5}$	$-9.55{\cdot}10^{-4}$	$3.73{\cdot}10^{-4}$	$-6.46{\cdot}10^{-4}$	$-1.16{\cdot}10^{-3}$	$3.04{\cdot}10^{-4}$	$2.08{\cdot}10^{-4}$	$-8.02{\cdot}10^{-4}$	$4.91{\cdot}10^{-4}$
C_{S_β}	-0.0129	-0.0131	-0.0107	-0.0161	-0.0154	-0.0118	-0.0111	-0.0120	-0.0102
C_{l_β}	-0.0032	-0.0020	-0.0008	-0.0045	-0.0030	-0.0012	-0.0024	-0.0017	-0.0006
C_{n_β}	-0.0023	-0.0020	-0.0029	-0.0003	-0.0004	-0.0022	-0.0031	-0.0027	-0.0032
C_{D_M}	0.0208	-0.1598	-0.0253	0.0249	-0.0577	-0.0842	0.0313	-0.0538	-0.0258
C_{L_M}	0.1164	-0.1567	-0.0460	0.0844	-0.0798	-0.0492	0.1013	-0.0728	-0.0444
C_{m_M}	-0.0543	0.0283	0.0028	-0.0455	0.0035	0.0048	-0.0495	0.0014	0.0024